NTNU
Norwegian University of
Science and Technology

# Determination of AC Characteristics of Superconducting Dipole Magnets in the Large Hadron Collider Based on Experimental Results and Simulations

Sara Marie Ambjørndalen

Master of Energy and Environmental Engineering
Submission date: July 2017
Supervisor: Lars Einar Norum, IEL
Co-supervisor: Arjan Verweij, CERN

Norwegian University of Science and Technology
Department of Electric Power Engineering

# Determination of AC Characteristics of Superconducting Dipole Magnets in the Large Hadron Collider Based on Experimental Results and Simulations

Master's thesis at the Norwegian University of Science and Technology

Sara Ambjørndalen

Supervisors at NTNU: Lars Norum

Supervisor at CERN: Arjan Verweij

July 17, 2017

**Abstract**

The Large Hadron Collider (LHC) utilizes high-field superconducting Main Dipole Magnets that bend the trajectory of the beam. The LHC ring is electrically divided into eight octants, each allocating a 7 km chain of 154 Main Dipole Magnets. Dedicated detection and protection systems prevent irreversible magnet damage caused by quenches. Quench is a local transition from the superconducting to the normal conducting state. Triggering of such systems, along with other failure scenarios, result in fast transient phenomena. In order to analyze the consequence of such electrical transients and failures in the dipole chain, one needs a circuit model that is validated against measurements.

Currently, there exists an equivalent circuit of the Main Dipole Magnet resolved at an aperture level. Each aperture model takes into account the dynamic effects occurring in the magnets, trough a lossy-inductance model and parasitic capacitances to ground. At low frequencies the Main Dipole Magnet behaves as a linear inductor. Cable eddy current losses are demonstrated by a flattening of the transfer function impedance in the $30-50$ Hz range. The time constant of such losses is dictated by the parallel resistance, and the relative size of the loss is given by a scaling parameter. Capacitive effects become dominant around 10 kHz. Across the dipole magnet there is a resistor connected in parallel to dampen voltage waves.

Simulations of an Main Dipole Magnet in OrCAD Cadence PSpice, using the present parameters, and measurements from the LHC give a clear discrepancy. This necessitated an updated fit and three methods tailored to obtain each parameter were developed. Firstly, the inductance value was obtained estimated from the initial slope of the impedance plot. Secondly, the numerical method chosen for the parameter fit is Particle Swarm Optimization. The algorithm iteratively minimizes the error between measurements and the analytical impedance transfer function, making it possible to estimate the value of the parallel resistor and the scaling factor. Finally, parasitic capacitance to ground was determined with Finite Element Method in COMSOL, as it is challenging to extract parameters from high frequency measurements. Values from measurements verify this method of estimating capacitance.

The measurements of the Main Dipole Magnets were performed while connected to the rest of the dipole magnet chain, which influenced frequency response measurements. Hence a proposal on how to reduce the sensitivity to this influence is outlined. Moreover, the method of fitting was found to be modular, meaning each Main Dipole Magnet can be fitted individually. This is significant as it is not necessarily possible to perform measurements on a stand-alone magnet. To cross-check the validity of the method, Particle Swarm Optimization fits from stand-alone measurements and measurements from the dipole magnet chain were compared. Both values of the parallel aperture resistance and scaling factor were different for the two cases.

Compared to the operating point of the Main Dipole Magnet, measurements were performed at low current, resulting in 20 % lower inductance than nominal value. Through COMSOL simulations persistent magnetization was found to be the dominating cause. Furthermore, at 1 A the magnet is in the Meissner phase, which introduces non-linearities in the superconducting cable due to persistent magnetization. Simulations indicate that this distorts the mid-range frequency AC characteristics represented by the parallel aperture resistance and scaling factor. However, measurements outside the Meissner phase are expected to provide similar parameter values to that of the working point of the LHC. The approach presented has shown promising results and can be translated to a general method for fitting electrical parameters for accelerator magnets.

## Sammendrag

Partikkelakseleratoren Large Hadron Collidor (LHC) bruker superledende hoveddipolmagneter til å bøye banen til to stråler med partikler. LHC-ringen er delt elektrisk i åtte oktanter, hver bestående av en 7 km lang kjede med 154 hoveddipolmagneter. Deteksjons- og beskyttelsessystemer forhindrer irreversibel skade på magnetene forårsaket av quencher, som er en lokal overgang fra superledende til normal ledende tilstand. Utløsning av slike systemer, sammen med diverse feilscenarioer, resulterer i transienter. For å kunne analysere konsekvensene av slike utløsninger og feillscenarioer i dipolkjeden, trengs det en ekvivalentkrets som er validert mot målinger.

Den gjeldende kretsekvivalenten til hoveddipolmagneten i LHC er representert ned til aperturnivå. Hver apertur av hoveddipolmagneten består av induktanser, en parallell motstand som beskriver AC tap, og jordede kondensatorer. Ved lave frekvenser oppfører hoveddipolen seg som en lineær induktans, mens AC tap blir merkbare gjennom en flatning av transfer funksjonen til impedansen ved $30 - 50$ Hz. Tidskonstantene av slike tap er gitt av parallellmotstanden til aperturen, og den relative størrelsen på tapene som er gitt av et skaleringsparameter. Kapasitive effekter blir dominerende over 10 kHz. I tillegg, er det koblet en motstand parallelt med dipolmagneten for å dempe spenningstransienter.

Simuleringer av en hoveddipolmagnet i ORCAD Cadence PSpice, med bruk av de nåværende parametrene, og målinger fra LHC gir en klar uoverensstemmelse. Dette nødvendiggjorde en oppdatert parametertilpassing og dermed ble tre metoder skreddersydd for å estimere hvert parameter. Gjennom analytiske formuleringer ble induktansverdien funnet basert på kryssfrekvensen fra målinger. Den numeriske metoden som ble valgt for parametertilpasningen var Particle Swarm Optimization. Algoritmen minimerer iterativt forskjellen mellom målinger og den analytiske transferfunksjonen til hoveddipolmagneten. Slik var det mulig å estimere verdien av parallellmotstanden og skaleringsfaktoren. Til slutt ble parasitt kapasitans til jord beregnet med Finite Element Method i COMSOL, da det er utfordrende å estimere parametere ut ifra høyfrekvente målinger. Verdier fra målinger verifiserer denne metoden for estimering av kapasitans.

Grunnet praktiske begrensninger ble målingene av hoveddipolmagnetene utført mens de var tilkoblet resten av dipolkjeden, noe som påvirket frekvensresponsmålinger av hoveddipolene. Derfor er det skissert et forslag om hvordan redusere følsomheten for denne innflytelsen. Videre ble metoden for parametertilpasning fastslått å være modulær, hvilket betyr at hver hoveddipolmagnet kan tilpasses individuelt i dipolmagnetkjeden. Dette er et betydelig funn, da det ikke nødvendigvis er mulig å utføre målinger på en frittstående magnet. For å kryssjekke validiteten av metoden, ble Particle Swarm Optimization tilpasset frittstående og kjedetilkoblede målinger sammenlignet. Både verdien av parallellmotstanden til aperturen og skaleringsfaktoren var forskjellig for de to tilfellene.

Sammenlignet med arbeidspunktet til hoveddipolmagneten ble frekvensresponsmålingene utført ved lav strøm. Dette resulterte i 20 % lavere induktans enn nominell verdi. Gjennom COMSOL-simuleringer ble vedvarende magnetisering funnet å være den dominerende årsaken. Når hoveddipolmagneten opereres ved lav strøm, kalt Meissnerfasen, er dette en sterk effekt. Videre indikerer simuleringer at vedvarende magnetisering i denne fasen forvrenger AC-karakteristikken ved midtre frekvenser, representert ved parallellmotstanden til aperturen og skaleringsfaktoren. Samtidig forventes disse egenskapene å være likere de ved arbeidspunktet når målinger er utført utenfor Meissnerfasen. Tilnærmingen presentert har vist lovende resultater og kan brukes som en generell metode for fastsetting av elektriske parametere for akseleratormagneter.

# Acronyms

**ALICE** A Large Ion Collider Experiment
**ATLAS** A Toroidal LHC ApparatuS

**CERN** European Organisation for Nuclear Research
**CMS** Compact Muon Solenoid
**CSM** Critical State Model

**FEA** Finite Element Analysis
**FEM** Finite Element Method
**FPA** Fast Power Abort
**FRM** Frequency Response Measurement

**IFCC** Inter Filament Coupling Currents
**IFCL** Inter Filament Coupling Loss
**ISCC** Inter Strand Coupling Currents

**LHC** Large Hadron Collider
**LHCb** Large Hadron Collider beauty

**MB** Main Dipole Magnet

**Nb-Ti** Niobium-Titanium

**PDE** Partial Differential Equations
**PSO** Particle Swarm Optimization

**QPS** Quench Protection System

**RMS** Root Mean Square
**RRR** Residual Resistivity Ratio

**STEAM** Simulations of Transient Effects in Accelerator Magnets

**TVE** Total Vector Error

# List of Symbols

| | |
|---|---|
| $\mathbf{B}$ | Magnetic Induction |
| $\mathbf{B_{c1}}$ | Lower Critical Magnetic Induction |
| $C$ | Capacitance |
| $\mathbf{D}$ | Displacement Field |
| $d$ | Distance between plates in capacitor |
| $\mathbf{E}$ | Electric Field |
| $\mathbf{H_{c1}}$ | Lower Critical Magnetic Field |
| $\mathbf{H_{c2}}$ | Higher Critical Magnetic Field |
| $\mathbf{J}$ | Current density |
| $k$ | Scaling Parameter for impedance transfer function: coefficient proportional to inductance decrease as frequency increases |
| $L$ | Inductance of aperture |
| $\lambda_L$ | London depth: depth of field penetration into a bulk of superconducting material |
| $L_{diff}$ | Differential Inductance |
| $L_{\mathbf{ap}}$ | Apparent Inductance |
| $\mathbf{M}$ | Magnetization |
| $\omega_c$ | Crossover frequency |
| $\epsilon_0$ | Electric permittivity of vacuum |
| $\epsilon_r$ | Relatve permittivity to vacuum |
| $\epsilon$ | Absolute permittivity |
| $R_a$ | Average Aperture Resistance for a Dipole |
| $R_1, R_2$ | Aperture resistance for left and right aperture respectively |
| $R_p$ | Parallel resistance to dampen resonances of dipole |
| $Q$ | Charge |
| $R_{splice}$ | Splice Resistance |

| | |
|---|---|
| $S$ | Surface area of capacitor |
| $T_c$ | Absolute Critical temperature |
| $U_{mag}$ | Voltage across Main Dipole Magnet |
| $Z_a$ | Impedance of aperture of MB |
| $Z_{tf}$ | Analytical Impedance of Dipole |
| $Z_{tf,meas}$ | Measured Impedance of Dipole |
| $\mathbf{Z_n}$ | Impedance of magnet n |
| $\mathbf{mean_z}$ | Average impedance per frequency |
| $\mathbf{d_z}$ | Deviation from average impedance per frequency |

# Preface

This report is the Master's thesis and final part of the Master's Program Energy and Environmental Engineering at NTNU, the Norwegian University of Technology and Science. Furthermore, it is written to complete the course "TET4900 - Electric Power Engineering and Smart Grids, Master's Thesis" during the spring semester of 2017. The thesis has been written in collaboration and for CERN through their Technical Student Program.

The master thesis is a continuation of the specialization report "Multi-scale Analysis of Electro-Thermal Transients in the LHC Main Dipole Circuit" submitted December 2016. This thesis builds on recommendations and observations of this report. In order to make this thesis a complete document, parts of the specialization report have been included with minor changes.

# Acknowledgments

I would like to thank my supervisors and colleagues from TE-MPE-PE at CERN. Thanks to Michał Maciejewski for consciously following up my work throughout my time at CERN, as well as giving thorough feed-back on this report. Furthermore, I would like to thank Lorenzo Bortot for giving invaluable guidance on all COMSOL simulations presented. My gratitude also extends to Marco Prioli for sharing essential competence in parameter fitting and data analysis.

Also, I would like to thank my supervisor at CERN, Arjan Verweij, for his continuous interest in my work and his inputs on measurements and simulations. Thanks also goes to my supervisor at NTNU, Lars Norum for his support during this semester.

Without measurements there would be no results in this thesis, so my heartfelt appreciation goes to the Electrical Quality Assurance team at CERN, particularly Mateusz Bednarek, Giorgio D'Angelo and Szymon Michniuk who performed the frequency response measurements presented in this report and were always willing to discuss new ideas.
Apart from these main contributors, many colleagues at CERN have been kind enough to help and answer question on a spontaneous basis. A thank you to

- Zinur Charifoulline for helping me access Timber and process data
- Gerard Willering for facilitating the measurements of the stand-alone Main Dipole Magnet
- Emmanuele Ravaioli for his cross-continental interest in my work, and his input on persistent magnetization

Lastly, I want to say thank you to my friends and family, not to mention my parents Gabriella Attard and Haakon Ambjørndalen, for the support throughout my time as a student at NTNU. A special thanks to Milla Brodahl, Irina Giri, Adam Conovaloff, Kjersti Berg and Glenn Aarøen for keeping me sane during this stressful period, and to Kyrre Sjøbæk and Helga Holmestad for providing me shelter the last weeks before handing in the thesis.

# Contents

Chapter 1

# Introduction and Motivation

European Organisation for Nuclear Research (CERN), founded in 1954 in Geneva, is one of the largest particle physics laboratories in the world with the aim of probing the fundamental structures of the universe. [1] In order to do so, particles are accelerated and made to collide at close to the speed of light. The main particle accelerator at CERN, the Large Hadron Collider (LHC) accelerates protons or heavy led ions and is designed to collide two beams projected from opposite directions. [2] The beam is guided around the LHC ring by means of superconducting magnets. Among these are the Main Dipole Magnets (MBs), which through strong magnetic fields create the necessary curvature for proton beams up to 6.5 TeV, as they are accelerated through the 27 km circular tunnel. [3] In the LHC there are 8 main dipole circuits, each composed of 154 magnets. A schematic of the LHC is given in Figure 1.1.

The four points in the tunnel at which the beams collide are called experiments. These are A Toroidal LHC AparatuS (ATLAS), A Large Ion Collider Experiment (ALICE), Large Hadron Collider beauty (LHCb) and Compact Muon Solenoid (CMS). ATLAS and CMS are general purpose detectors, while LHCb specializes in the study of the asymmetry between matter and antimatter. ALICE is a detector for lead ion collisions. [4]

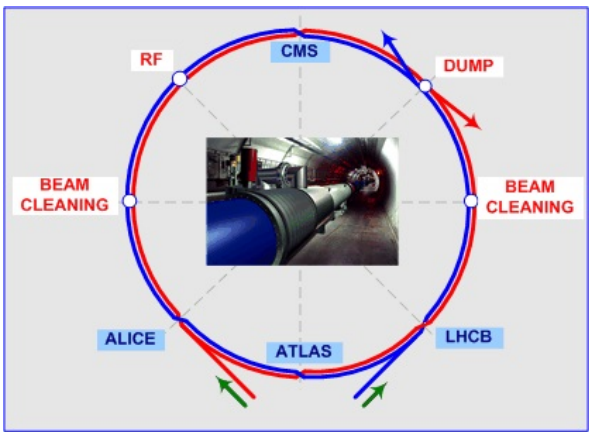


**Figure 1.1:** Schematic of LHC with experiments [2]

## 1.1 STEAM project

All research for this report has been done within the scope of the Simulations of Transient Effects in Accelerator Magnets (STEAM) project at CERN. During operation, superconducting accelerator magnets, like the ones in the LHC, experience various nonlinear transient effects such as inter-filament and inter-strand coupling currents, heat propagation between cable and coolant, mechanical response to temperature gradients and Lorentz forces, and possibly a local transition from the superconducting to the normal conducting state, to mention a few. These multi-physics transient phenomena occur at a wide range of spatial and temporal scales. Thus, the aim of the STEAM project is to establish competence for the coupling of codes using commercial, open source or academic tools. All the while creating work flows based on the recurrent needs of CERN and ensuring that the simulations are conducted in a well-maintained and flexible framework of coupling interfaces and work flows.

## 1.2 Problem description

For the purpose of studying frequency dependent behaviour, including fault scenarios and Fast Power Aborts, the Main Dipole Magnet of the LHC is modelled as an equivalent circuit based on lumped elements. The principal AC characteristics of the MBs, below 10 kHz, are captured by the lumped parameters $L$ and $C$, $k$ and $R_a$. These account for inductive and capacitive effects as well as AC losses respectively. The comparison between measurements from November 2016 and simulations incorporating the present parameter fit show a clear deviation, necessitating an updated fit. For reliable fault analysis and simulations, the thesis provides an approach to the fitting of each parameter.

The following research questions have been formulated in relation to parameter fitting:

1. Is it possible to accurately calculate parasitic capacitance to ground with a Finite Element Method approach and thus obtain the parameter $C$?
2. Is the Particle Swarm Optimization algorithm an adequate method to fit Main Dipole Magnet parameters from analytic transfer functions of impedance to Frequency Response Measurements?
    - In particular, is the method suitable for fitting Main Dipole Magnet parameters to Frequency Response Measurements performed while connected to the dipole magnet chain?
3. What requirements should be specified of measurements designed for parameter fitting?

These questions has been answered by the following studies:

1. 
    - Finite Element Analysis to determine parasitic capacitance to ground in COMSOL (see chapter 3)
2. 
    - Investigating the influence of chain impedance on dipole and aperture impedance (see section 5.1)
    - Comparing Particle Swarm Optimization fits from chained and stand-alone measurements (see section 6.2)
    - Data analysis to seek strategies for magnet groups for fitting (see section 6.3)
    - Performing Particle Swarm Optimization algorithm based on data analysis and analyzing results (see section 6.4)
3. 
    - Evaluating measurement configurations (see section 5.2)

- Investigating low inductance values from Frequency Response Measurements (see subsection 5.5.3)
- Discussing the implications of low inductance values from Frequency Response Measurements (see section 7.2)

In addressing these three overarching questions, the underlying approach will be to combine measurements and simulations, always ensuring that simulation results are validated by measurements. With this approach, methods and work flows outlined can be utilized for any superconducting accelerator magnet.

## 1.3 Scope, aim and content

The aim of this report is twofold. First of all, one wishes to outline a method to fit Frequency Response Measurements to an analytical transfer function of the MB impedance, even for measurements performed in the dipole magnet chain. The specification of a method suitable for chained magnet measurement is related to the feasibility of the measurements, as unsoldering and resoldering magnets from the dipole magnet chain is out of the question. Secondly, this thesis seeks to evaluate the method of parameter fitting by focusing on limitations and pinpoint possible solutions to such limitations. Especially considering the non-linearity of the impedance of superconducting magnets.

This thesis relies heavily on measurements to make conclusions about the parameters of the equivalent circuit of the frequency transfer function of the MB. These measurements include 8 Frequency Response Measurements from sector 1-2 of the LHC from November 2016, 41 Frequency Response Measurements from the same sector from April 2017, current and voltage measurements of Magnet A12R1 in sector 1-2 from LHC operation in May taken from the database Timber and Frequency Response Measurement from a stand-alone MB from June 2017.

Writing this thesis in collaboration with CERN puts me in the privileged position that much work has presided mine on the topic of the MB and thus this thesis bases itself upon such research. Most importantly, the COMSOL and Pspice models utilized for simulations and presented in this thesis have all been created through the STEAM project, mainly by Lorenzo Bortot, Michał Maciejewski and Marco Prioli.

### 1.3.1 Content

To sufficiently answer the research questions and reach the two aims of the thesis, the subsequent structure was created,

Chapter 2 introduces the theory of superconducting accelerator magnets necessary for the unfamiliar reader to get acquainted with the topic and understand the research conducted in this report.

Chapter 3 stands as an independent study, and utilizes a Finite Element Method approach through COMSOL to determine parasitic capacitance to ground. This result is compared to analytic and experimental results.

Chapter 4 presents a method for fitting Main Dipole parameters to Frequency Response Measurements to impedance.

Chapter 5 provides the necessary preliminary investigation for the fittings of MB parameters to be complete.

Chapter 6 demonstrate the final results from Particle Swarm Optimization analysis.

Chapter 7 and Chapter 8 discusses the main sources of error and limitations to the result presented, concludes the research questions posed in section 1.2 and recommends research for future work.

Chapter 2

# Theory of superconducting accelerator magnets

*To grapple with the challenges of modelling an MB in the LHC, the theory of superconductivity is covered. In terms of theoretical concepts within superconductivity, the emphasis will be on the Meissner effect and the existence of a critical surface. A clear distinction is made between Type I and Type II superconductors.*

*After having discussed the physical properties of superconductivity, the cable and magnet design of the MB is justified. Next, it is argued that such magnets can be modelled as an equivalent circuit composed of lumped elements. Lastly, the concept of a quench and protection systems give insight into operational challenges.*

## 2.1 Superconductivity

Superconductivity is a phenomenon where certain materials under specific conditions become perfect conductors of electricity.[5, p. 1] Below the critical values of temperature, current density and magnetic field the conductor in question abruptly changes from the normal to the superconducting state. The cable construction dictates the critical current density and critical magnetic field depends on material. Furthermore, the superconducting state is characterized by two behaviors; zero resistance and the Meissner effect.[6]

As the name indicates superconductivity allows for current to flow without any Ohmic losses. In order to evaluate zero resistance, a standard resistance measurement would be too crude. Thus a method of determining the decay rate of the produced magnetic field has been developed. The decay of the induced current is according to Equation 2.1

$$I(t) = I(0)e^{\frac{-t}{\tau}}, \qquad \text{A} \quad (2.1)$$

where the time constant $\tau$ [s] is given by the ratio between inductance and resistance, $\tau = \frac{L}{R}$. [7, p. 8] Through this method time constants up to $10^5$ years have been observed. [8]

Considering zero Ohmic losses: "[t]he only power required by a superconducting magnet is the refrigeration power needed to cool it to low temperatures and a small current supply needed to initiate the flow of current round the superconducting circuit." [5, p. 4] However, the refrigeration power is significant when the superconducting magnets of the LHC demand cryogenic temperatures of 1.9 K with a length of 27 km. On the other hand, for high energy accelerators such as the LHC superconducting magnets are an energy efficient technology, allowing the magnets to reach high magnetic fields, where conventional magnets would saturate. For further comparison between superconducting and conventional magnets, see Figure 2.1.

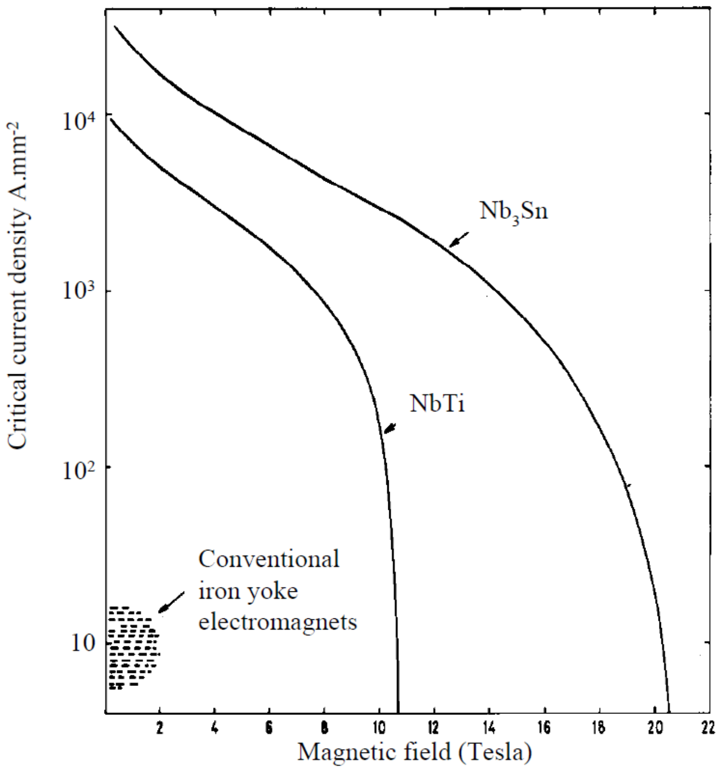


**Figure 2.1:** Comparing performance between conventional magnets and the superconducting materials Nb-Ti (alloy) and $Nb_3Sn$ (compound) [5, p.3]

### 2.1.1 Meissner effect

As mentioned, the Meissner effect is one of the two characteristics of superconductivity, which transpires as the expulsion of a small and constant external field from the bulk of the conductor. [9, p. 4] When raising a finite field, from zero to **B** on a superconducting cylinder "[a] surface current is induced whose magnetic field, according to Lenz's rule, cancels the applied field of the interior. Since the resistance is assumed to vanish, the current continues to flow with constant strength as long as the external field is kept constant, and consequently the bulk of the cylinder will stay field-free" [7, p. 10]. Figure 2.2 shows the two manners in which the Meissner effect occurs. Either case a) where a cylinder is exposed to an increasing field from zero below critical temperature (T$<T_c$). Or case b) where the cylinder has already been exposed to an increasing field from zero while over the critical temperature (T$>T_c$), as the temperature is reduced below the critical temperature surface current will appear.

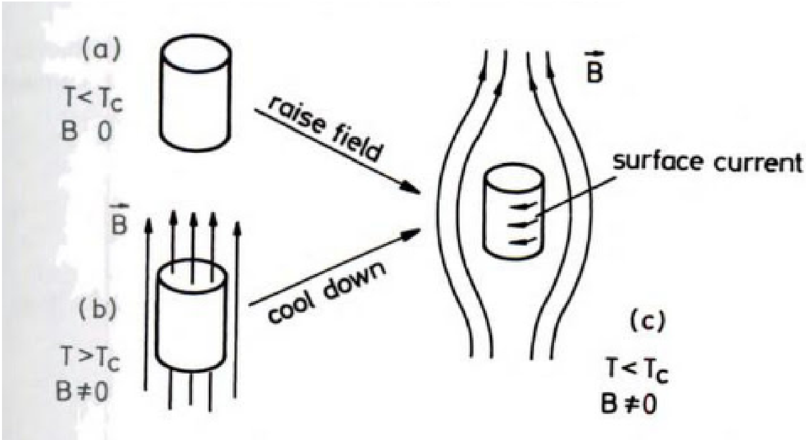


**Figure 2.2:** Meissner effect illustrated by field and surface current of superconducting cylinder [7, p.11]

### London equation

The first successful attempt to describe the Meissner effect was achieved in 1935 by Heinz and Fritz London, by assuming that only a fraction of the conduction electrons carry the supercurrent in the metal.[9, p.12] The current density is given by

$$\nabla \times \mathbf{J} = -\frac{1}{\epsilon_0 \cdot \lambda_L^2}\mathbf{B}, \qquad \mathrm{A}/m^3 \quad (2.2)$$

where $\lambda_L$ is the London depth [m], giving the depth of penetration into the bulk. [10, p.274] $\epsilon_0$ is the permittivity of vacuum [F/m], $\mathbf{J}$ the current density [A/m$^2$] and $\mathbf{B}$ the magnetic induction [T]. As illustrated in Figure 2.3 the London equation describes the current density that opposes the external field.

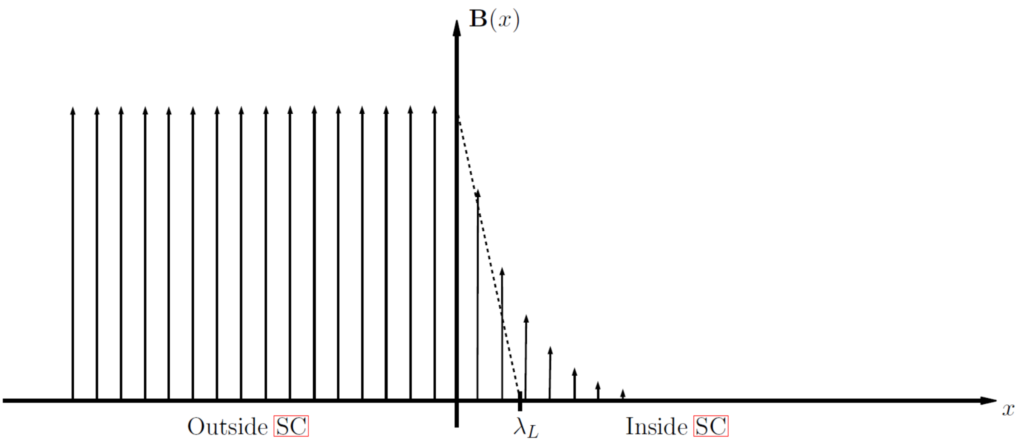


**Figure 2.3:** Illustration of the London penetration depth. The externally applied field penetrates the superconductor in the x–direction. [11, p.5]

### 2.1.2 Type I vs Type II Superconductors

In understanding superconductors and their application as magnets, there is a significant distinction between Type I and Type II. The first discovered superconductors were of Type I, also called 'soft superconductors', as they were metals such as tin, lead and mercury. [5, p. 280]. These superconductors completely expel the magnetic flux from the interior of the specimen, described by the Meissner effect. Due to their low critical fields, they are unsuitable materials for magnet construction. [9, p. 5]

However, 'hard superconductors' or Type II superconductors remain superconducting at higher magnetic fields, though in a mixed state as illustrated in Figure 2.4.

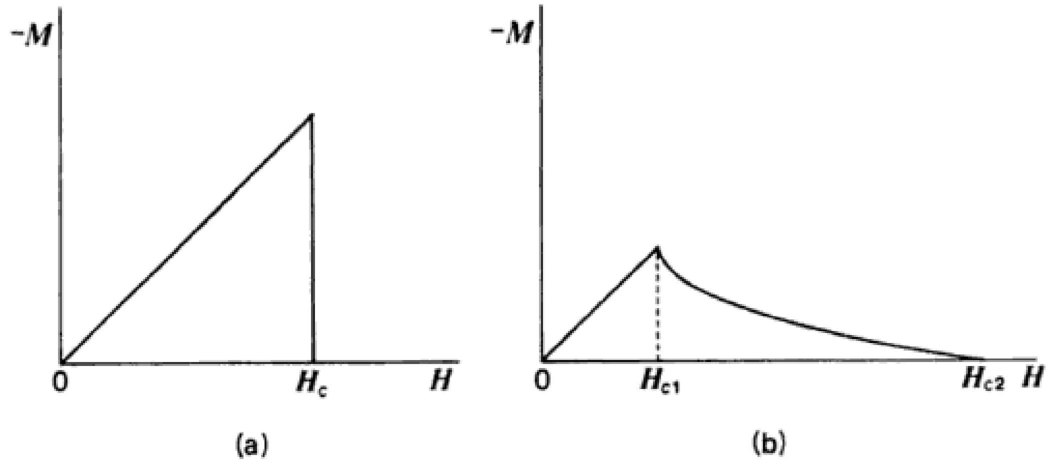


**Figure 2.4:** Comparison of magnetization of Type I and II superconductor [12, p. 23]

Up until a $\mathbf{H}_{c1}$ the Type II superconductor is in the Meissner phase and thus behaves as a Type I superconductor. Between $\mathbf{H}_{c1}$ and $\mathbf{H_{c2}}$ the Type II superconductor is in a mixed state, and thus only partially expels the magnetic flux from penetration. $\mathbf{H_{c2}}$ is usually about 100 times larger than $\mathbf{H}_{c1}$. [10, p. 264] Above $\mathbf{H_{c2}}$ the cable is no longer in the superconducting state.

### 2.1.3 Rutherford cable

The cable in the MB is made of the alloy Niobium-Titanium (Nb-Ti) and is of a Rutherford cable design, where the strands are fully transposed. This means that each strand takes every position along the cross-section of the cable. In the cable of the LHC MB, there are 28 or 36 strands of superconducting wire, in the inner or outer layer, respectively. Each strand contains approximately 6300 superconducting filaments.[13] [1] This fine subdivision has been chosen to reduce hysteresis losses. [14] Around each filament there is a 0.5 $\mu$m layer of high-purity copper, acting as an insulation material during the superconducting state and as a conductor in normal conducting state. [13] The cable, strand, and filament are illustrated in Figure 2.5, Figure 2.6a and Figure 2.6b, respectively.

[1] See Table 2.1

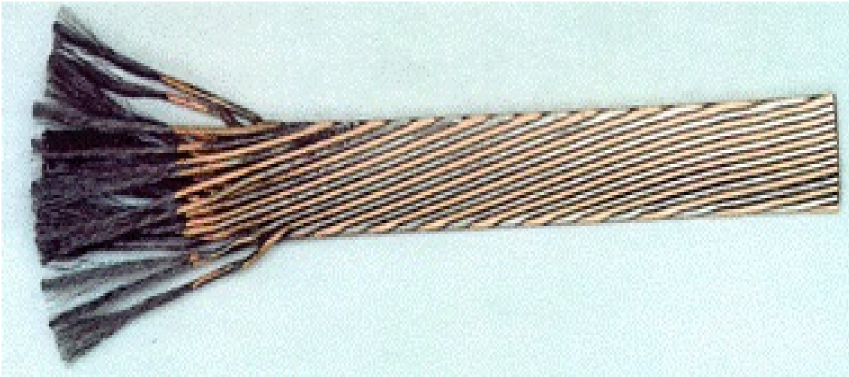

**Figure 2.5:** Rutherford cable [13]

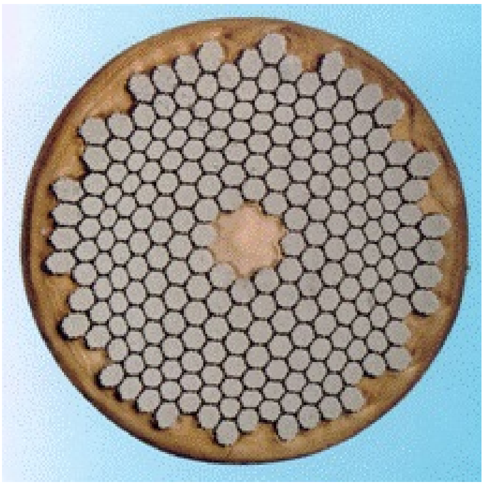

**(a)** Strand in Rutherford cable [13]

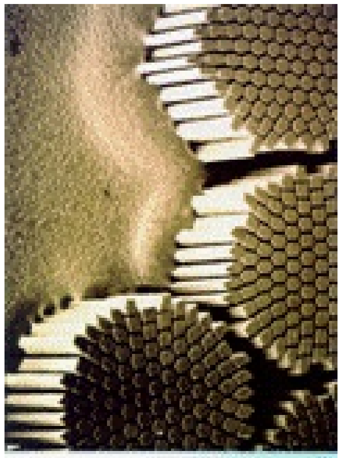

**(b)** Filament in Rutherford cable [13]

The Rutherford cable can also be described as a network model, and is illustrated in Figure 2.7.

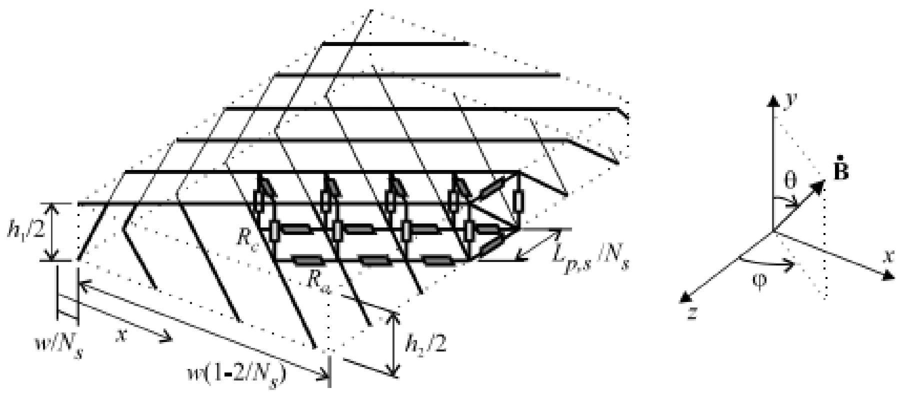


**Figure 2.7:** Network model of Rutherford cable [15, p.64]

In this model, the cable has a width $w$, height $h_1$ on one edge and height $h_2$ for the opposite edge. $N_s$ is the number of strands in the cable which has a twist pitch $L_{p,s}$, in addition to the resistances $R_a$ and $R_c$ representing the resistance between adjacent and crossing strands. All these values are available in Table 2.1. The resistive barriers and twisting function are implemented to reduce eddy current coupling losses between filaments. [14]

The insulation around the cable, does not only withstands the voltage between turns but also is porous enough to allow helium to penetrate and provide cooling. Consisting of glass-fibre tape and kapton, there is 2.5 mm spacing between insulation turns. Figure 2.8 depicts this insulation.

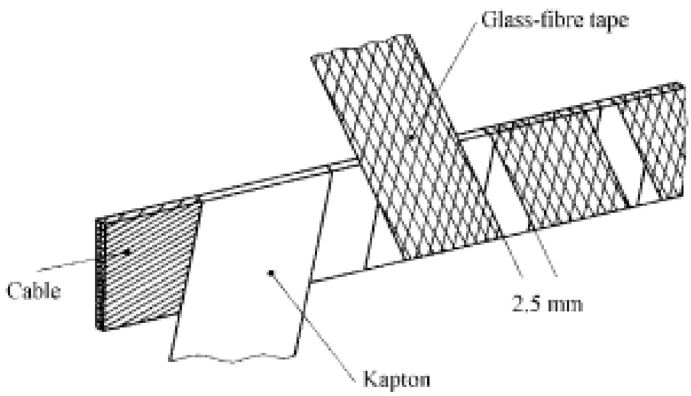


**Figure 2.8:** Insulation of Rutherford cable [15, p.37]

The main characteristics of the Rutherford cable of the MB in the LHC are summerized in Table 2.1.

| | **Inner Layer Main Dipole** | **Outer Layer Main Dipole** |
|---|---|---|
| **Strand** | | |
| Diameter after coating [mm] | 1.065 ± 0.0025 | 0.825 ± 0.0025 |
| Copper to superconductor ratio | 1.65 ± 0.05 | 1.95 ± 0.05 |
| Filament diameter [$\mu$m] | 7 | 6 |
| Number of filaments | $\sim$ 8900 | $\sim$ 6500 |
| RRR (residual resistance ratio) | $\geq$ 150 | $\geq$ 150 |
| Twist pitch after cabling [mm] | 18 ± 1.5 | 15 ± 1.5 |

| | Inner Layer Main Dipole | Outer Layer Main Dipole |
|---|---|---|
| **Cable** | | |
| Number of strands | 28 | 36 |
| Mid-thickness at 50 MPa [mm] | 1.900 ± 0.006 | 1.480 ± 0.006 |
| Thin edge [mm] | 1.736 | 1.362 |
| Thick edge [mm] | 2.064 | 1.598 |
| Width [mm] | 15.10 | 15.10 |
| Keystone angle [degrees] | 1.25 ± 0.05 | 0.90 ± 0.05 |
| Inter-strand cross contact resistance [$\mu\Omega$] | $\geq 15$ | $\geq 40$ |
| Residual Resistivity Ratio (RRR) | $\geq 70$ | $\geq 70$ |

**Table 2.1:** Strand and cable characteristics of MB [16, p. 157]

The twisting pitch described in Figure 2.7 gives the transpositional length of a strand, while RRR is a measure of the purity of copper defined by the ratio $\frac{\rho(T=293\text{K})}{\rho(T=10\text{K})}$. [16, p. 157] To facilitate the winding of the magnet, the cable has a small keystone angle which is defined as [15, p.36]

$$\alpha_k = \arctan\left(\frac{h_1 - h_2}{w}\right). \qquad \text{deg} \quad (2.3)$$

### Inter Filament and Inter Strand Coupling Currents

Due to the presence of a matrix in the strand, as depicted in Figure 2.7 there are eddy currents, specifically referred to as ISCC. When the cable is exposed to a changing field, coupling currents flow between non-insulated strands through inter-strand contact resistances $R_a$ and $R_c$. [15, p.61] Similarly, for the filaments there is a matrix of resistances that results in a flow of coupling currents called Inter Filament Coupling Currents (IFCC), given exposure to a time varying field. [15, p.51]

The characteristic time constant of the IFCC is:

$$\tau_{if} = \frac{\mu_0}{2}\left(\frac{l_f}{2\pi}\right)^2 \frac{1}{\rho_{eff}}, \qquad \text{s} \quad (2.4)$$

where $l_f$ [m] is the filament twist-pitch and $\rho_{eff}$ [$\rho m$] is the effective transverse resistivity of the strand matrix. [17, p. 26] The effective transverse resistivity depends on the absolute magnetic field in the matrix due to magneto-resistivity effects, which in turn depend on the electrical resistivity, RRR and fraction of superconducting material among others. [17, p. 26]

### 2.1.4 Critical surface of superconductivity

Superconductivity is bound by limits, creating a critical surface which relates **B**, **J** and T to each other. The critical surface for Nb-Ti is given in Figure 2.9. Notice that the surface is monotonically decreasing and thus an increase in one of the parameters necessitates a decrease in the other two in order to stay at the superconducting critical surface. Furthermore, each parameter has an absolute critical value, which is the value of the parameter when the other two are zero. Unsurprisingly, these absolute critical values have no practical application for magnet operation, but provide the limits to superconductivity. In addition, it allows the estimation of quench margins for a given operating point, also referred to as load line. [18, p. 16] Based on empirical scaling laws the critical current for Nb-Ti, as a function of **B** and $T$, can be expressed as

$$I_c = (C_1 + C_2\,|B|)\left(1 - \frac{T}{T_c}\right), \qquad \text{A} \quad (2.5)$$

$$T_c = 9.2\left(1 - \frac{|B|}{14.5}\right)^{0.59}, \qquad \text{K} \quad (2.6)$$

where $C_1$ [A] and $C_2$ [A/T] are empirically defined constants, and $T_c$ is the absolute critical temperature. [15, p.40]

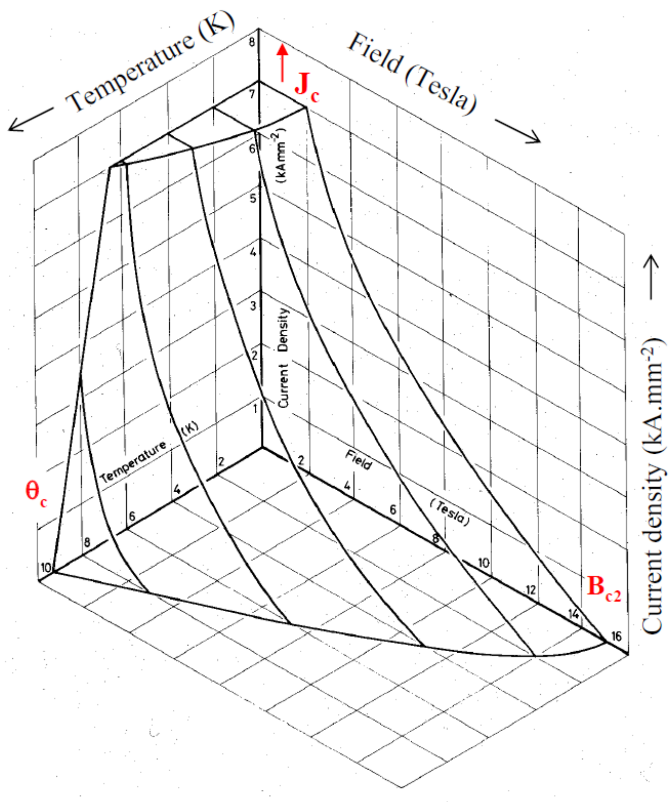


**Figure 2.9:** Critical surface for Nb-Ti [5, p.2]

### 2.1.5 Persistant Magnitization of Type II Superconductors

As a consequence of the Meissner Effect a Type I superconductor's magnetization **M** is a unique function of the external field $B_e$

$$\mathbf{M}(\mathbf{B_e}) = -\frac{\mathbf{B_e}}{\epsilon_0}. \qquad \text{A/m} \quad (2.7)$$

[7, p.19] However, a Type II superconductor will only completely expel the external field when in the Meissner phase. Above $B_{1c}$ flux enters the specimen and is captured at pinning centres. [7, p.19] If the field is subsequently reduced below $\mathbf{B_{c1}}$ again, the specimen keeps a frozen-in magnetization from bound field lines. [7, p.19] The magnetization curve for a Nb-Ti conductor can be studied in Figure 2.10.

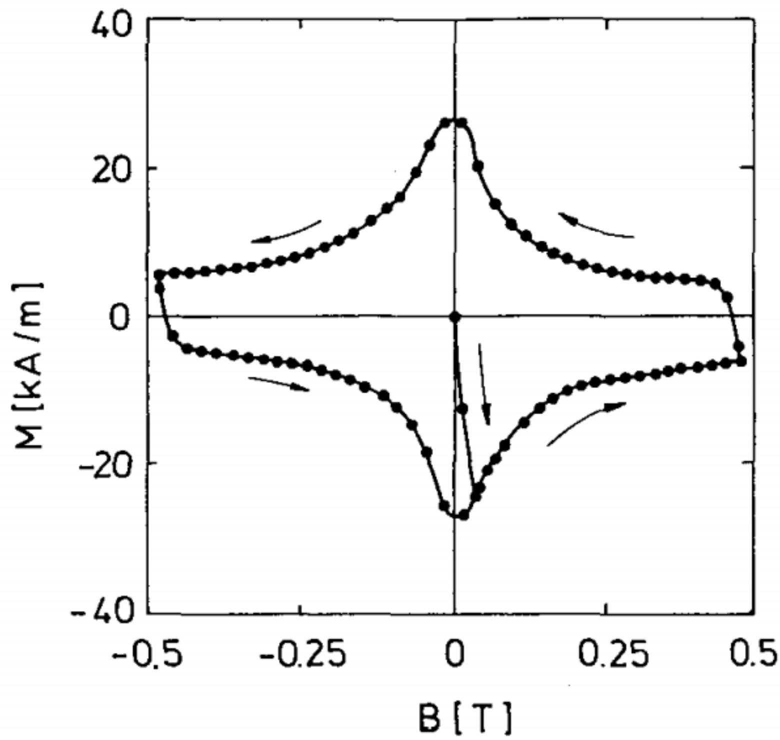


**Figure 2.10:** A typical magnetization curve for M of a multi-filamentary Nb-Ti conductor. Initial excitation starts at B = 0 and M = 0. [7, p.19]

According to Figure 2.11, magnetization is not zero at zero field after a current cycle due to residual magnetization, implying that this phenomena depends on the history of the magnet. In order to return to zero magnetization, superconductivity has to be destroyed by heating and subsequently cooling it down again. [7, p.19] Only then will the pinned flux be released.

Given the case in Figure 2.11 with a multi-filamentary Nb-Ti conductor and relatively low field, only hysteresis losses contribute to magnetization. However, during operating of superconducting magnets such as the MB, the total magnetization is due to hysteresis losses, Inter Filament Coupling Loss (IFCL), ISCC, as well as saturation of the iron yoke. [19] Moreover, magnetization of superconducting magnets has a significant effect on field quality, and at low current will cause severe field distortions. [7, p.81] Since the LHC receives the beams from Super Proton Synchrotron (SPS) at energy of 450 GeV, the MB is not operated at such a low current level with beam.

### 2.1.6 Critical current density model

The Critical State Model (CSM) describes the current distribution for Type II superconductors. It states that such a superconductor expels a varying applied field by generating a bipolar current distribution of critical current $J_c$. [20, p.513] This means that for low fields only a small current is required to expel the field. This current will be found on the edge of the conductor, while the centre is free of current. In the penetrated area the current density will equal $J_c$. Given a rectangular slab the field inside, $\mathbf{B}_\mathrm{y}$ is given by:

$$\mathbf{B}_\mathrm{y}(q) = \mathbf{B}_\mathrm{a} - \frac{\mu_0 \cdot J_c \cdot d \cdot q}{2}, \qquad \mathrm{T} \quad (2.8)$$

[20, p.513] where $q$ is the relative penetration parameter, which is zero at the horizontal edge of the conductor and 1 at the centre, $d$ is the thickness of the slab and $\mathbf{B}_\mathrm{a}$ is the applied flux density. From this equation, a penetration field $\mathbf{B}_\mathrm{p}$ is defined, which is the field at the point when the slab is fully penetrated by $\mathbf{B}_\mathrm{a}$. In other words, $q$ is equal to 1 and $\mathbf{B}_\mathrm{y}$ is zero, resulting in

$$\mathbf{B}_\mathrm{p} = \frac{\mu_0 \cdot J_c \cdot d}{2}. \qquad \mathrm{T} \quad (2.9)$$

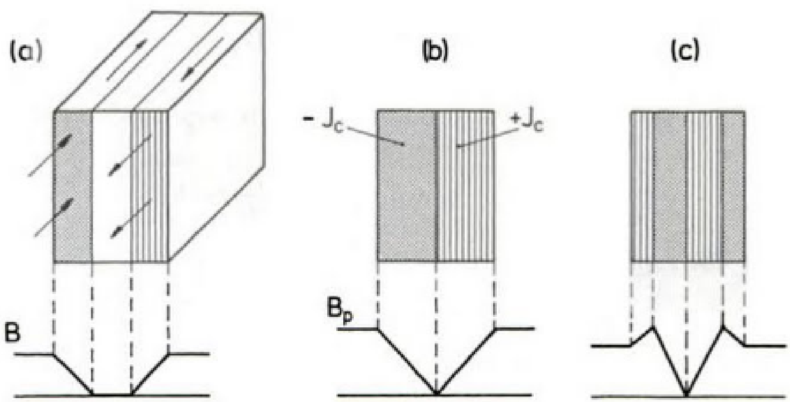


**Figure 2.11:** Current and field distribution in a slab of Type II superconductor according to CSM. (a) Initial exposition to a small external field (b) The penetrating field $\mathbf{B}_\mathrm{p}$ (c) External field first raised above $\mathbf{B}_\mathrm{p}$ and then lowered again [7, p.24]

## 2.2 Main dipole magnet design

The principle idea of the MB is to utilize the Lorentz force on the proton beam. This creates the required curvature to keep it in circulation in the beam pipe. By applying Biot-Savart's Law, it is possible to evaluate the field at any point in space and find the required current to create a transverse field. The ideal dipole magnet is based on two intersecting cylinders carrying uniform but oppositely directed current densities, such as in Figure 2.12.

Utilizing such a design, the current distribution becomes [21, p.589]

$$I(\theta) = I_0 \cos(\theta). \qquad \mathrm{A} \quad (2.10)$$

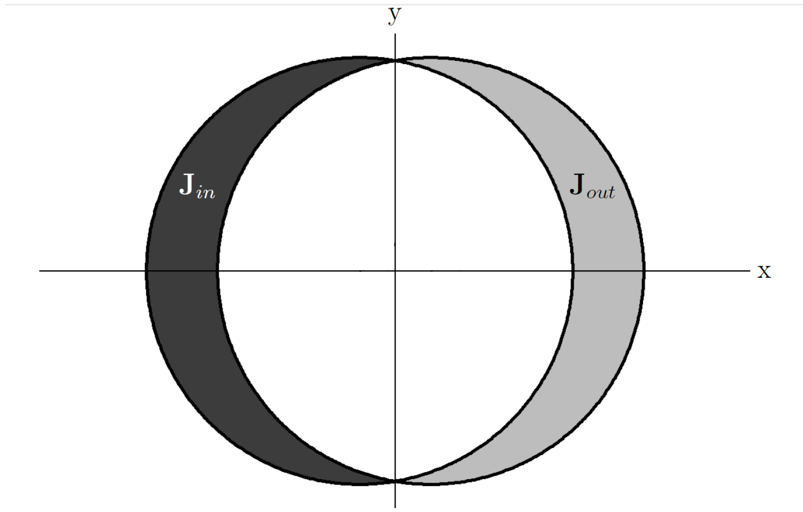


**Figure 2.12:** Cross-section of winding current distribution to produce a perfectly uniform transverse field [11, p.29]

However, approximating this ideal design by varying the current according to $\theta$, would mean having a separate current source for each winding. [11, p. 29] Obviously, this would be impractical for magnets with several hundred windings. Instead the design of the MB is optimized by using blocks and varying their size and position. [21, p.589] The resulting design of the cross-section is shown is Figure 2.13.

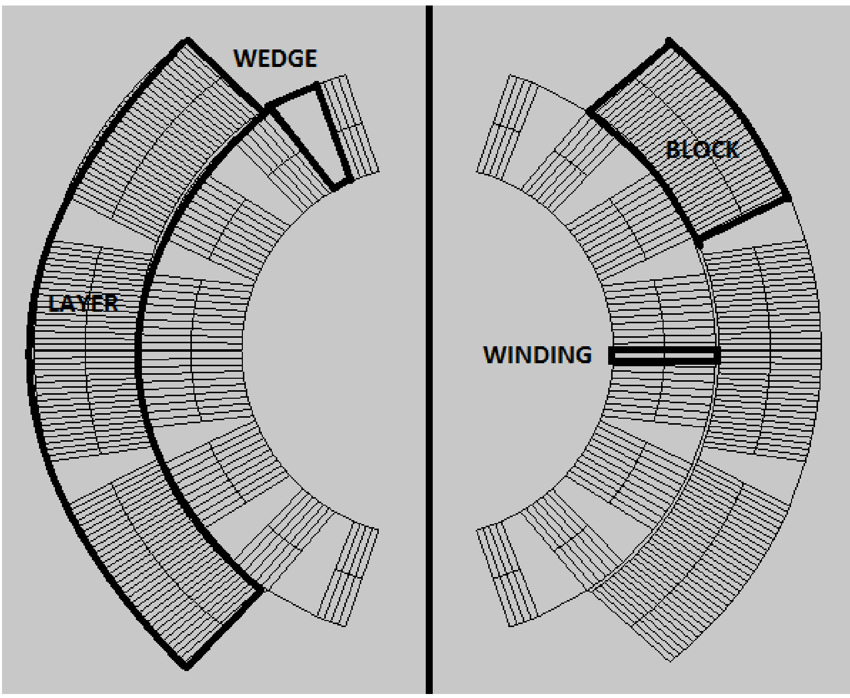


**Figure 2.13:** Cross section of the optimized aperture coil design (Taken from COMSOL model)

Figure 2.13 depicts one aperture of the twin-aperture dipole and consists of poles, turns, blocks, layers and wedges. Looking at Figure 2.13, a whole square of turns is a block, and each ring of blocks is a layer. In order for each turn to be positioned radially towards the center, there are wedges between the blocks ensuring the correct angle for the turns.

Around the coils is an iron yoke and steel collar. The iron yoke increases the central fields substantially, screens the fringe field outside the magnet and reduces the stored magnetic energy, which is advantageous in case of a quench. [7, p.3] Due to strong Lorentz forces the two halves of the dipole coil repel each other with a high force. To maintain high field precision, a steel structure called a collar is mounted around the magnet defining the exact geometry. [7, p.2] The combined cross-section is illustrated in Figure 2.14

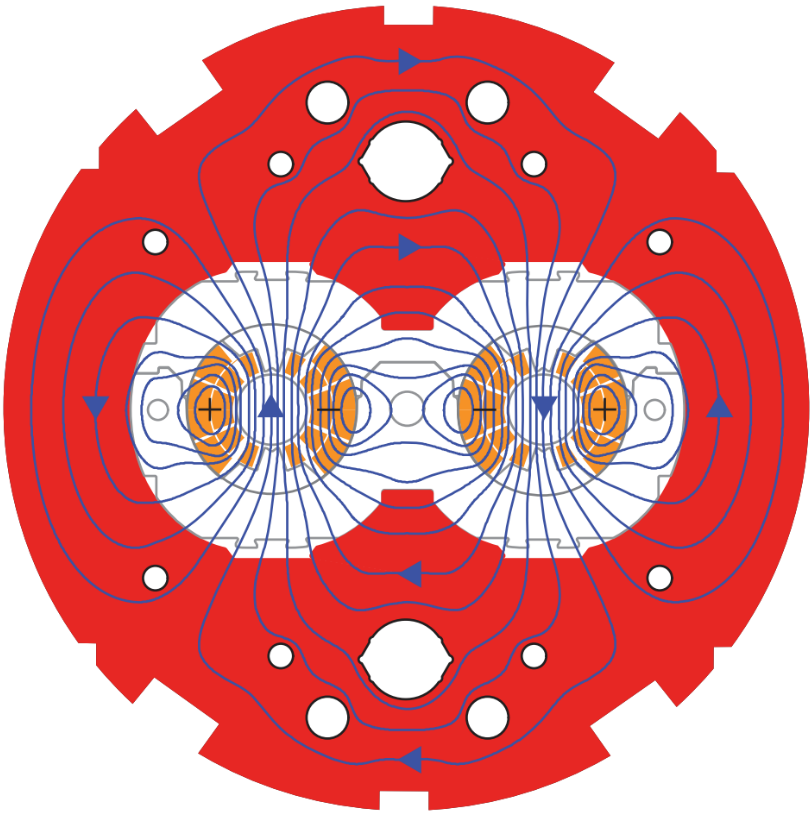

**Figure 2.14:** LHC aperture dipole with computed field lines [21, p.589]

A special winding is necessary in order to accommodate the beam pipe in accelerator magnets. There are two main options for 3D design of the coil for producing transverse fields, which are racetrack or saddle-shaped coils, with the coils in the LHC being saddle-shaped. [5, p.27] To see how the magnetic field is created with the different coil designs see Figure 2.15

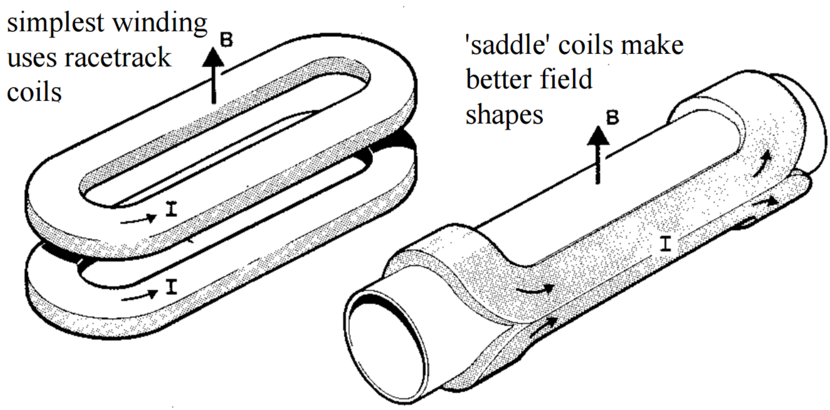


**Figure 2.15:** Transverse fields produced by racetrack coils (left) and saddle-shaped coils(right) [5, p.27]

## 2.3 Equivalent circuit of the MB and dipole magnet chain

This section discusses the circuit representation of MB and dipole magnet chain. The representation of the main dipole magnet chain consists of a power converter with a filter, quench protection systems, superconducting busbars, superconducting leads and other elements. Furthermore, the MB itself has been characterized experimentally, and due to eddy current losses and parasitic capacitances it is not purely inductive. [22] The present dipole circuit representation accounts for both these phenomena on an aperture level.

### 2.3.1 Dipole magnet

The MBs in the LHC can be represented as an equivalent circuit consisting of two apertures in series, with a parallel resistor as given in Figure 2.16. Currently, the components take the values given in Table 2.2. $R_p$, $L$ and $C$ can be measured directly through for example impedance measurements and high-voltage tests, while $R_a$ and $k$ are features of the equivalent circuit. Thus, they can only be estimated through Frequency Response Measurement (FRM).

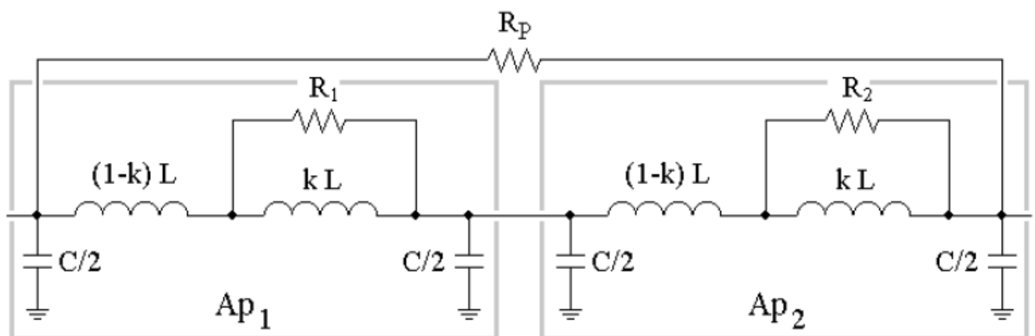


**Figure 2.16:** Circuit representation of Main Dipole

| Component | Value | Units |
|---|---|---|
| $L$ | 49 | mH |
| $C$ | 150 | nF |
| $k$ | 0.75 | - |
| $R_1, R_2$ | 10 | Ω |
| $R_p$ | 100 | Ω |

**Table 2.2:** Values of components in dipole circuit model

From this circuit representation an analytical frequency characteristic of the MB impedance is obtained. The main behaviors modelled are inductive effects, eddy currents, and coil-to-ground parasitic capacitance. [23] According to theory, inductive effects are dominant at low frequencies, manifested as a linear increase in the frequency characteristic of the impedance. At around $30 - 50$ Hz, IFCL become effective by imposing a flattening of the transfer function. These AC losses are represented as a resistor in parallel with an inductor for each aperture in the circuit model. A resonance occurs between the inductances and coil-to-ground capacitance, before the capacitive effects become dominant at higher frequencies. The parallel resistor $R_p$ is added to smooth transient voltage oscillations and $k$ is a constant which is proportional to the inductance decrease, due to losses. [23] The phenomena of inductive effects, AC losses, parallel resistor, resonance peak and capacitive effects are visible in the dipole measurements of Figure 2.17.

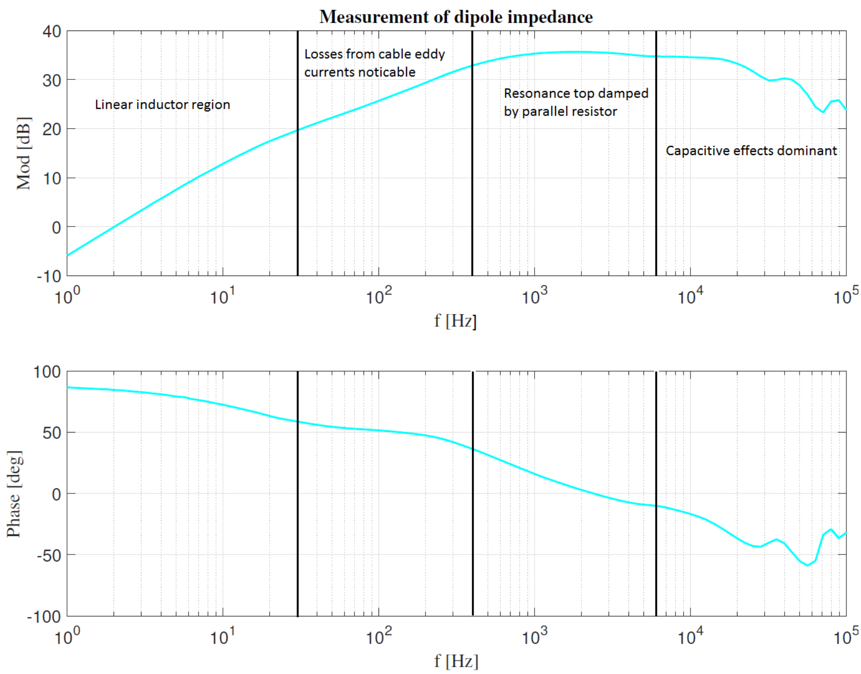


**Figure 2.17:** Measurement of dipole A31L2

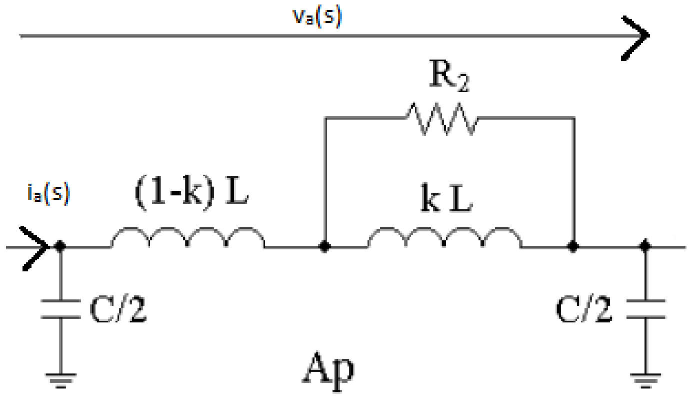


**Figure 2.18:** Equivalent circuit model of the aperture

Based on the equivalent circuit model of the apertures in Figure 2.18 with the given definitions of $i_a$ and $v_a$,, the transfer function of its impedance is [23]

$$Z_a = \frac{v_a(s)}{i_a(s)} = \frac{sL(1+\frac{sk(1-k)L}{R_a})}{(1+\frac{sk(1-k)L}{R_a})(1+R_a\frac{C}{4}s+(1-k)L\frac{C}{4}s^2)}. \qquad \Omega \quad (2.11)$$

### 2.3.2 Dipole magnet chain

A dipole magnet chain in the LHC consists of 154 dipole magnets, each having an inductance of approximately 98.7 $mH$ at nominal values of 11850 A and 8.33 T. [23] The current is fed through a power converter, which is connected in parallel with a crowbar that activates when the power converter is turned off. Additionally, the magnet chain is equipped with a low-pass filter and two energy extraction units. The two energy extraction units consist of electromechanical switches, an extraction resistor of 148 mΩ in parallel with a 53 mF snubber capacitor. [23] One energy extractor is located in the middle of the chain, while the other is at the end. The whole dipole magnet chain circuit is shown in Figure 2.19

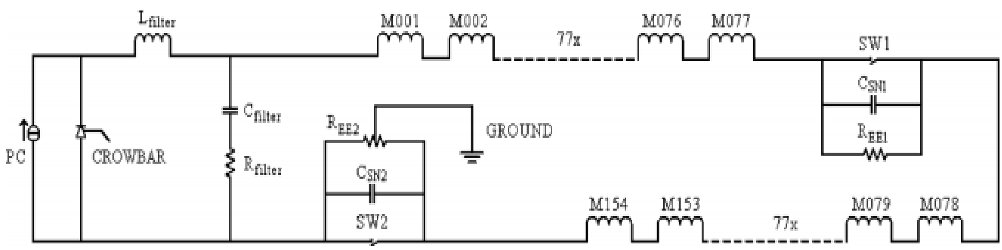


**Figure 2.19:** Circuit representation of dipole magnet chain [23]

## 2.4 Quench and quench detection

Given a critical surface for a material, such as in Figure 2.9, a quench is defined as "the transition from the superconducting to the normal conducting state. Such a transition will invariably occur if any of the three parameters temperature, magnetic field or current density exceeds its critical value" [7, p. 2] Additionally, a quench is a special phenomena such that it can occur at any point in the given material exceeding critical values. The quench is either suppressed or propagated, depending on the heat deposition created. Without any protection, the point at which the quench occurs will have a hot-spot temperature, which will be considerably higher than its surroundings. There are several causes of quench among others flux jumps, AC losses and heat leaks.[11, p. 34] However, the most important ones are heating due to Lorentz forces acting on the coil and causing friction between components, cryogenic malfunction and beam loss.[11, p. 34] At high currents, such as in the LHC only a tiny energy deposition is needed to heat the magnet beyond critical temperature, which is caused by the low heat capacity of materials at cryogenic temperatures. [7, p. 2] When a magnet quenches, the magnetic energy stored in the volume of magnet turns into Ohmic losses and as a consequence more heat is generated. The high temperature resulting from an uncontrolled quench can damage the insulation material and even melt the cable. Other dangers are electric discharges destroying the magnet due to overvoltages. Also, high Lorentz forces and temperature gradients can create large variations in stress and degradation, resulting in an overall reduction of current-carrying capability. [3]

### 2.4.1 Quench protection system

Considering these potential damages, it is important for the operation of the LHC to have a well-functioning Quench Protection System (QPS). To ensure a reliable level of certainty of a quench, quench detectors for each magnet consist of iQPS and nQPS systems. iQPS measures the voltage difference between the two apertures of a dipole, while nQPS compares the voltage across each dipole with the voltage of two electrically adjacent dipoles. [24] Under normal operating conditions without quenching, these voltage differences are approximately zero. Filling the accelerator with particles requires ramping up current in the magnets. After reaching the desired energy, particles are made to collide and magnets operate with constant current. Once collisions are terminated, either due to decrease of their luminosity or as a result of a fault in the machine, the magnets are ramped down or discharged with energy extraction systems and individual quench heaters respectively. In general, the voltage across a magnet or aperture is

$$U = L\frac{\partial I}{\partial t} + RI. \qquad \text{V} \quad (2.12)$$

With zero resistance and steady-state operation the total voltage is equal to zero. For ramp-up or -down there will be an inductive voltage component that will cancel when comparing it with another magnet or aperture:

$$\Delta U = L_1\frac{\partial I}{\partial t} - L_2\frac{\partial I}{\partial t} = 0 \qquad \text{V} \quad (2.13)$$

However, when a quench occurs the voltage builds up as a result of the increased resistance in the magnet. “If one of the two systems measures a difference beyond the threshold for more than the discrimination time, it triggers the firing of the quench heaters.” [24] Hence, a quench is detected even if both apertures in a dipole are quenching, a so-called symmetric quench. Moreover, the motivation for having both nQPS and iQPS is to enable detection of all quenches. A symmetric quench gives a zero difference in aperture voltage

$$\Delta U_{ap} = (R_{1,ap} - R_{2,ap})I \approx 0 \qquad \text{V} \quad (2.14)$$

while the difference in magnet voltage is

$$\Delta U_{mag} = (R_{1,mag} - R_{2,mag})I \neq 0. \qquad \text{V} \quad (2.15)$$

When it comes to determining the discrimination time, the time between the voltage threshold is reached to the protection is triggered, there is a trade-off between having it short enough to prevent damages and sufficiently long as to be certain of the quench. For any upgrade of the LHC, this has to be reevaluated in conjunction with the voltage threshold.

### 2.4.2 Triggering of quench protection

Once the QPS has detected a quench, a sequence of events, to protect against damages described earlier in section 2.4, are executed. First the beam is dumped and an Fast Power Abort (FPA) is triggered. This consists in turning off the power converter and opening the two energy extraction switches of Figure 2.19, allowing the current to flow through the extraction resistors in the dipole magnet chain, hence resulting in current decrease. [2] [23] Next the quench heaters are triggered, spreading the quench over the entire magnet by heating up large fractions of coil. As a consequence, this mechanism dissipates the stored magnetic energy over a larger volume and results in lower hot-spot temperatures. [3] Due to increase in voltage over the quenched magnet the by-pass diode starts to conduct. The entire magnet chain is completely discharged after a few hundred seconds after detection. [3] Figure 2.20 illustrates the LHC main dipole magnet chain when extraction resistors and by-pass diode are conducting, bypassing the quenched dipole.

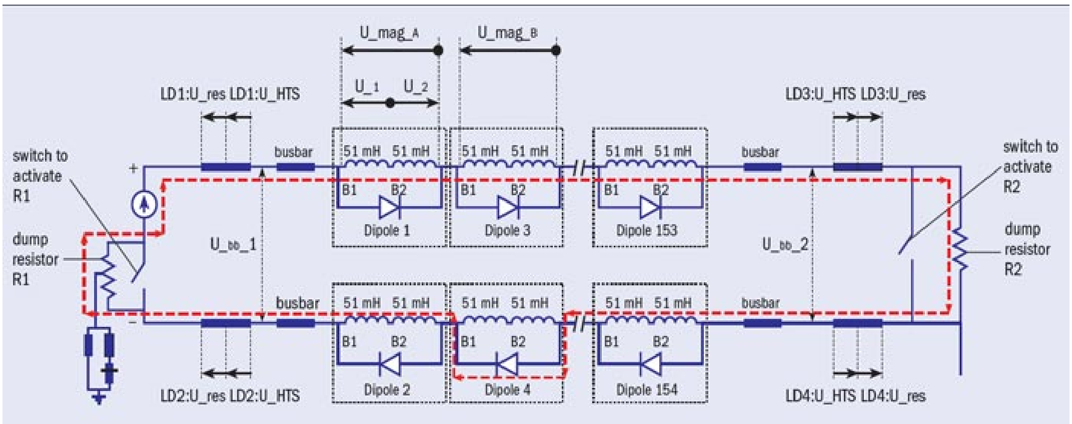


**Figure 2.20:** Schematic of the LHC main dipole magnet chain with energy extractors and by-pass diode (Diode 4) conducting [3]

[2]The two switches do not open simultaneously

Chapter 3

# Calculation of Parasitic Capacitance to Ground

*This chapter deals with obtaining the parasitic capacitance between coils and ground, which is the parameter C in Figure 2.16. Such a value will be incorporated into the analytical transfer function of the MB impedance. According to Figure 2.17, capacitive effects become dominant in the range of around* 10 $kHz$ *and above. Despite MBs being operated in DC, faults such as short circuit to ground and fuse blow-up as well as a Fast Power Aborts may occur. If one wishes to simulate and analyze these frequency dependent events, reliable models of parasitic capacitances become necessary. From such values, the crucial understanding of transient phenomena in the magnet for protection and operation is achieved.*

*Furthermore, the inaccuracy of Frequency Response Measurements make such estimates of capacitance unreliable. Thus, Finite Element Method (FEM) was chosen to calculate this parameter of the equivalent MB circuit model.*

*Currently, there are capacitance to ground measurements from High Voltage Tests of the MB in addition to analytical equations given by Equation 3.7 that are an accurate approximation of the parasitic capacitance. However, in the case of analyzing new magnet designs and automating such calculations, Finite Element Analysis (FEA) is a powerful and fast tool. Hence, for this instance where measurements exist, this will be a proof of concept for the method.*

## 3.1 Parasitic capacitance in the MB

In the presence of a dielectric material with a physical extension, there will be a capacitance given a difference in voltage on each side of the specimen. Capacitance being the ability by a specimen to store charge is defined as

$$C = \frac{Q}{\Delta V}, \qquad \text{F} \quad (3.1)$$

where $Q$ [C] is the total charge and $\Delta V$ [V] is the voltage difference between the two terminals. For a dielectric this ability is compared to vacuum with the parameter, relative permittivity, $\epsilon_r$ for a capacitor with the same geometry and electric field $\mathbf{E}$ [V/m] , assuming it is a linear one

$$\epsilon_0 \cdot \epsilon_r \oint \mathbf{E}\, ds = Q. \qquad \text{C} \quad (3.2)$$

In the MB there is parasitic capacitance due to insulation around the turns, blocks, wedges and cold bore. The parasitic capacitance to ground has been included in the equivalent MB circuit model, and is equivalent to the $C$ in Figure 2.16. Turn-to-turn capacitances are ignored in the model. They are referred to as parasitic as they are relatively small and an unwanted effect. However, the parasitic capacitance to ground is not negligible considering that the magnets are 14.32 m long and acts as a transmission line, exhibiting voltage waves and the effects of superposition.

A simple manner to evaluate this capacitance analytically is through Gauss' Law, assuming a linear dielectric plate capacitance

$$\oint \mathbf{D}\, ds = Q, \qquad \text{C} \quad (3.3)$$

meaning that the displacement field $\mathbf{D}$ [C/$m^2$]is proportional to $\mathbf{E}$

$$\mathbf{D} = \epsilon \cdot \mathbf{E}. \qquad \text{C}/m^2 \quad (3.4)$$

$$\mathbf{E} = -\nabla V = -\frac{V}{d}\hat{\mathbf{z}}. \qquad \text{V/m} \quad (3.5)$$

Combining Equation 3.3, Equation 3.4 and Equation 3.5 yields

$$Q = \epsilon \cdot \mathbf{E} \cdot S, \qquad \text{C} \quad (3.6)$$

implying that

$$C = \frac{\epsilon \cdot S}{d}. \qquad \text{C} \quad (3.7)$$

Here $S$ is the surface area of the capacitor [$m^2$] and $d$ is the distance between the plates [m].

## 3.2 Introduction to FEM calculations of parasitic capacitance

Overall, the goal for this stage of circuit modelling, is to evaluate the total parasitic capacitance to ground of the MB and compare this to measured and analytically calculated values. Considering the complexity of the geometry, a FEM model has been developed in COMSOL. The FEM is a numeric technique which provides an approximated model solution to problems described by sets of Partial Differential Equations (PDE)s. The domain is discretized, and a suitable discretization function defined over elements reduce the PDE to a set of algebraic equations. The size of the mesh depends on the physical phenomena, and accuracy of results desired. For example, when studying a phenomena such as the skin effect, a too coarse mesh would completely neglect such behavior.

### Boundary conditions for parasitic capacitance to ground

The challenge with calculating parasitic capacitances utilizing a FEM solver, is that the thickness of the insulation is one order of magnitude smaller than the width of the narrow side of the turns, causing high computational cost due to excessive meshing of the model. In order to avoid such excessive meshing, a boundary condition is imposed where there is insulation instead of explicitly modelling it in a 2D domain. These boundary conditions are an interpretation of Gauss' Law for a dielectric which is thin enough to assume that the electric potential is linear in the dielectric. Starting with the general form of Gauss' Law

$$\nabla \cdot \mathbf{D} = \rho. \qquad \mathrm{C}/m^3 \quad (3.8)$$

For an electrostatic hypothesis the magnetic flux density is constant, implying that the Faraday's Law is

$$\frac{\mathbf{B}}{dt} = \nabla \times \mathbf{E} = 0. \qquad \mathrm{V/m} \quad (3.9)$$

This gives a curl free field, which is conservative. In turn this leads to

$$\mathbf{E} = -\nabla V + c. \qquad \mathrm{V/m} \quad (3.10)$$

c is the Coulomb gauge and is set to zero. For a linear dielectric

$$\mathbf{D} = \epsilon \mathbf{E}, \qquad \mathrm{C}/m^2 \quad (3.11)$$

such that

$$\epsilon(\nabla \cdot \mathbf{E}) = \rho \qquad \mathrm{C}/m^2 \quad (3.12)$$
$$\Downarrow$$
$$\epsilon(-\nabla \cdot V) = \rho. \qquad \mathrm{C}/m^2 \quad (3.13)$$

In a charge-free region of space with a medium that is isotropic and homogeneous, assuming the distance $d$ is much smaller than the dimensions of the plates, Laplace's equation is obtained

$$\nabla^2 \cdot V = 0. \qquad \mathrm{V}/m^2 \quad (3.14)$$

[25, p. 33] Thus, integrating twice results in

$$V(z) = k_1 \cdot z + k_2, \qquad \mathrm{V} \quad (3.15)$$

where V(0)=$k_2$ and V(d)= $k_1 \cdot$ d. The electrical field becomes

$$\mathbf{E} = -\nabla V = -\frac{V}{d}\mathbf{e}. \qquad \mathrm{V/m} \quad (3.16)$$

Incorporating this back into Gauss' Law gives

$$\nabla \cdot \mathbf{D} = \nabla \cdot (\epsilon \frac{\Delta V}{d}) = \rho. \qquad \mathrm{C}/m^3 \quad (3.17)$$

Furthermore, the Divergence Theorem states that

$$\int_v \nabla \cdot \mathbf{D} \cdot dv = \int_S \nabla \cdot (\epsilon \frac{\Delta V}{d}) \cdot d\mathbf{S} = Q, \qquad \mathrm{C} \quad (3.18)$$

where $v$ is the volume of integration and $\mathbf{S}$ is the surface encompassing the volume $v$. In order to determine the displacement inside the thin layer an integration cylinder V is defined as described in Figure 3.1, while letting $\delta$ approach zero

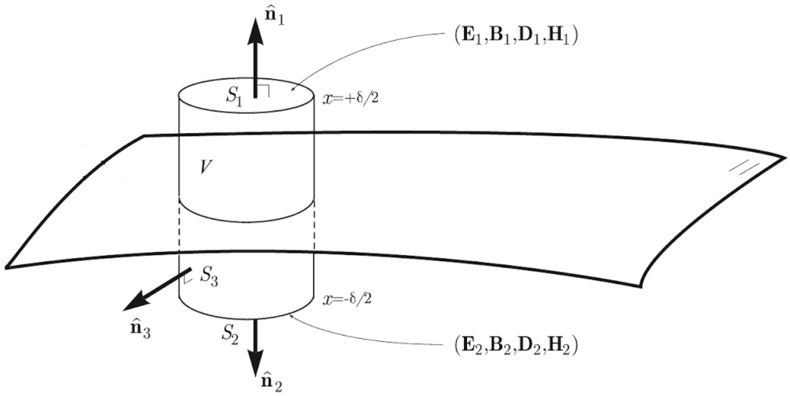


**Figure 3.1:** Derivation of electrostatic boundary conditions across a thin layer dipole magnet chain[p. 62]rothwell2008electromagnetics

Gauss' law for this volume is

$$\int_{S1} \mathbf{D}_1 \cdot \hat{\mathbf{n_1}} \cdot dS + \int_{S2} \mathbf{D}_2 \cdot \hat{\mathbf{n2}} \cdot dS + \int_{S3} \mathbf{D}_3 \cdot \hat{\mathbf{n_3}} \cdot dS = \int_V \rho dV, \qquad \mathrm{C} \quad (3.19)$$

where

$$\int_{S3} \mathbf{D}_3 \cdot \hat{\mathbf{n_3}} \cdot dS = 0 \quad (for \quad \delta \to 0) \qquad \mathrm{C} \quad (3.20)$$

Seeing as

$$\begin{aligned} \hat{\mathbf{n_1}} = -\hat{\mathbf{n_2}} = \hat{\mathbf{n_{12}}} \\ \mathbf{S}_1 = \mathbf{S}_2 \end{aligned} \qquad (3.21)$$

implies

$$\int_{S1} (\mathbf{D}_1 - \mathbf{D}_2) \cdot \hat{\mathbf{n_{12}}} \cdot dS = \int_V \rho dV. \qquad \mathrm{C} \quad (3.22)$$

Hence

$$(\mathbf{D}_1 - \mathbf{D}_2) \cdot \hat{\mathbf{n_{12}}} = \rho_s. \qquad \mathrm{C/m^2} \quad (3.23)$$

[26, p. 62] Indeed in COMSOL electrostatics, the feature Distributed Capacitance follows the boundary condition according to

$$\mathbf{n} \cdot (\mathbf{D_1} - \mathbf{D_2}) = \epsilon_0 \epsilon_r \cdot \frac{V_{ref} - V}{d}, \qquad \mathrm{C} \quad (3.24)$$

which is the same interpretation of Gauss' Law combining Equation 3.11, Equation 3.16 with Equation 3.23. [27] Here, $V_{ref} - V$ is the voltage difference between the plates and $d$ is the distance. Thus the thin-layer in COMSOL is a direct interpretation of Gauss Law for a a linear electric potential.

## 3.3 Geometry of MB model in COMSOL

In order to parametrize the insulation of the MB, the design drawings of a quadrant of the MB, wedges and cold bore have been scrutinized. Exerpts of these drawings can be found in Figure 3.2, Figure 3.3 and Figure 3.5. Materials and component names are given in Table 3.1 for the former.

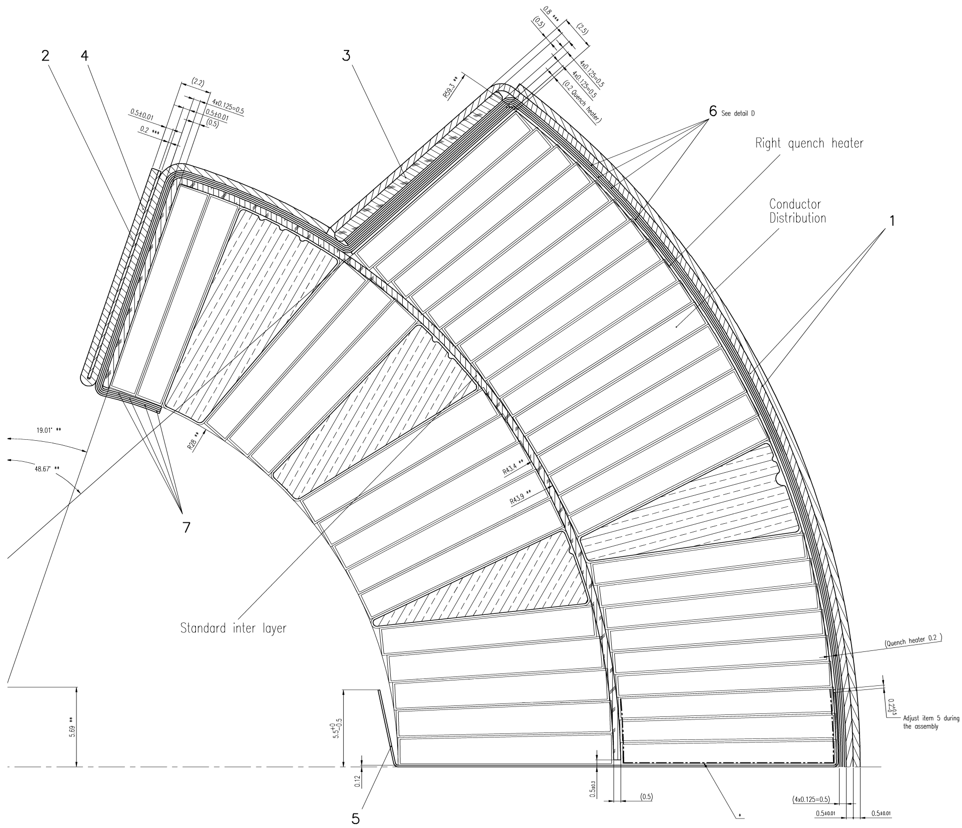


**Figure 3.2:** Insulation for a quadrant of the main dipole

| Competent name | Number in design drawing | Material |
|---|---|---|
| Insulation sheets | 5-7 | Polyimide film |
| Shim retainer | 4 | Austelinic steel |
| Shim outer layer | 3 | Polyimide G10 |
| Shim inner layer | 2 | Polyimide G10 |
| Coil protection sheet | 1 | Austelinic steel |

**Table 3.1:** Materials of components (MB)

The two layers of coil protection sheet, protect the coil insulation against any potential sharp edges of the steel collar. Since this is also made of steel and in contact with the grounded steel collar, it is assumed to be grounded. The same applies to the shim retainer.

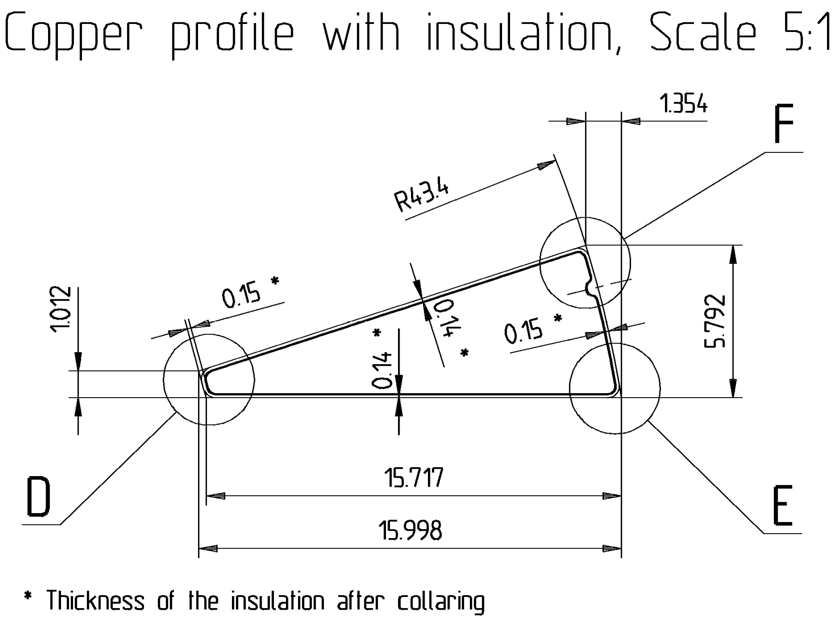


**Figure 3.3:** Insulation around copper wedges

Figure 3.3 shows that the wedges have a 0.15 mm insulation thickness, which is made of Kapton.

The cold bore is the pipe where the beam travels. Figure 3.4 highlights its position in orange in relation to the coils and gives a longitudinal view of the cold bore.

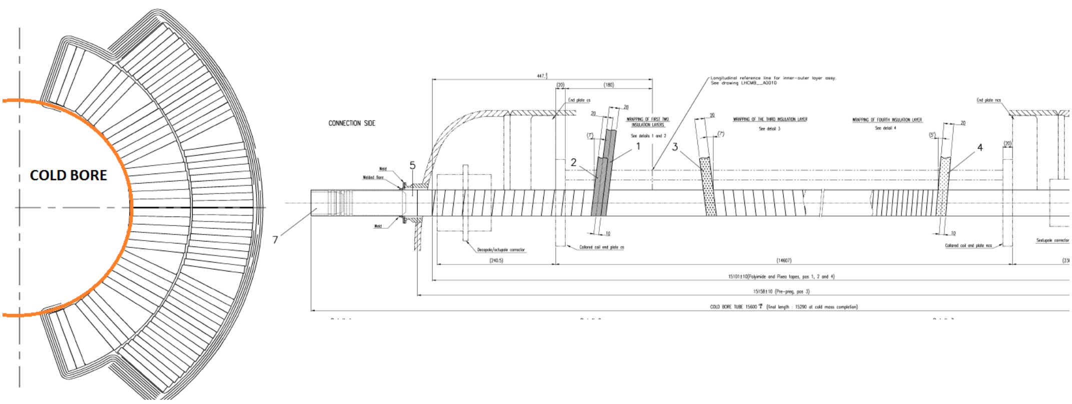


**Figure 3.4:** Cross-sectional and longitudinal view of cold bore

The coils are insulated from the metallic cold bore with 5 layers of insulation measuring a total thickness of 0.51 [mm]. This insulation follows the whole inner arc of the first layer of the MB.

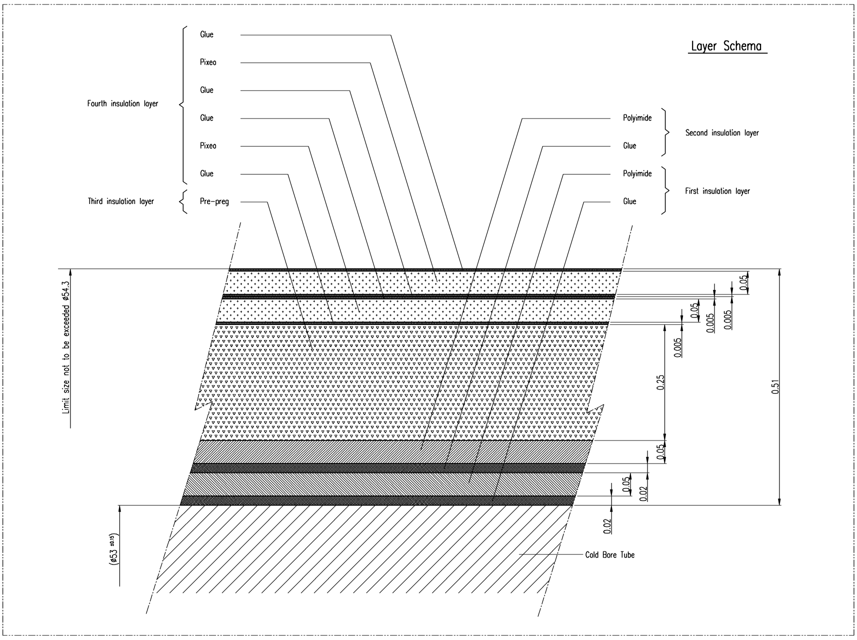


**Figure 3.5:** Insulation around cold bore

A summary of the insulation thickness at different locations of the MB is disclosed in Table 3.2

| Competent name | Insulation thickness [mm] |
|---|---|
| Inner layer top | 1.125 |
| Inner layer left | 0.635 (1.135 for the uppermost coil and 0.755 for lowermost coil) |
| Outer layer top | 2.125 |
| Outer layer right | 0.825 |

**Table 3.2:** Materials of components (cold bore)

Reviewing Table 3.2, the average thickness of mesh is around 1 mm. Simultaneously, the diameter of the full MB is 0.5 m, which means that if the insulation is resolved with 5 points, it would result in 250 0000 points along a line across the width of a 2D model. Even though the number of nodes depends on the problem at hand, this implies an unmanageable amount easily exceeding 1 million. Hence, the boundary condition implemented is expected to reduce computation cost considerably.

Finally, the geometry as implemented in COMSOL is presented in Figure 3.6.

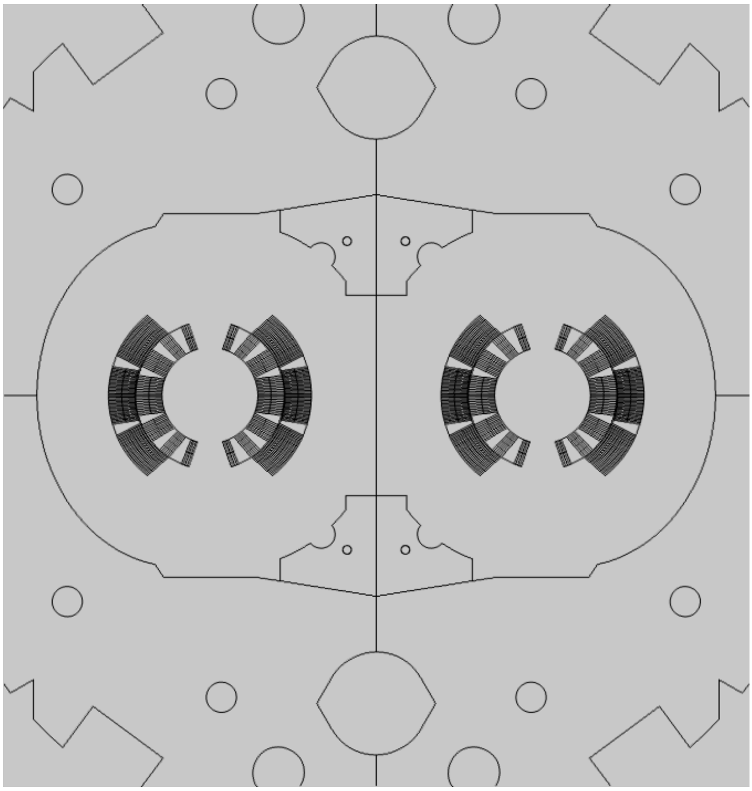

**Figure 3.6:** COMSOL geometry of MB with steel collar, cold bore and iron yoke

### 3.3.1 Assumptions for FEM calculation

The insulation is assumed to have the relative permittivity $\epsilon_r$ of 3. Polyimide has a relative permittivity between 2.8-3.8 depending on if it is are completely immersed in helium and completely dry, but also depends on the residual humidity from the industrial process of manufacturing. In addition, there is a certain amount of liquid helium in the insulation with a relative permittivity $\epsilon_r$ of 1.05. [28] Furthermore the steel, copper and iron materials utilized are from the COMSOL material library, and do not necessarily exhibit the same properties as the actual materials in the LHC. However, looking at Equation 3.24 these materials do not influence the solution. Lastly, the geometry has been adapted to COMSOL, hence simplification have been made. Also, it has been assumed that the parasitic capacitances of the busbars are negligible.

## 3.4 Method for FEA

From electrostatics capacitance is per definition

$$C = \frac{Q}{\Delta V}, \qquad \text{F} \quad (3.25)$$

where Q is the charge on the terminal and $\Delta V$ is the voltage difference between the plates considered. The next example provides as a template to calculate capacitance when there is more than two plates , such as in Figure 3.7. Here there are three metallic plates, where one is grounded.

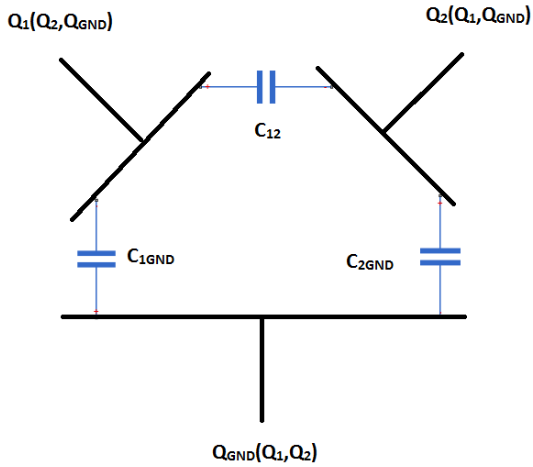


**Figure 3.7:** Example with three charged metallic plates

Wanting to evaluate $C_{1,GND}$, from charge of conservation it is deduced that

$$Q_1 = C_{1,2} * \Delta V_{12} + C_{1,GND} * \Delta V_{1,GND} \qquad \mathrm{C} \tag{3.26}$$

$$Q_2 = C_{1,2} * \Delta V_{12} + C_{2,GND} * \Delta V_{2,GND} \qquad \mathrm{C} \tag{3.27}$$

$$Q_{GND} = C_{1,GND} * \Delta V_{1,GND} + C_{2,GND} * \Delta V_{2,GND} \qquad \mathrm{C} \tag{3.28}$$

To solve Equation 3.26 the boundary condition $V_2 = V_{GND} = 0\ V$ is imposed, resulting in

$$C_{1,GND} = \frac{Q_{GND}}{\Delta V_{1,GND}}. \qquad \mathrm{C} \tag{3.29}$$

Thus if $\Delta V_{1,2}$=0, $V_1$ and $V_2$ are equipontential and $C_{1,2}$ does not accumulate charge on $Q_1$. From this simple example, it is clear that it is vital to enforce conservation of charge within the cross-section evaluated and have all terminals accessible numerically for FEA. If influence of a terminal is to be mitigated it must be put to zero.

### 3.4.1 Grounding terminals in FEM model

The metallic wedges are floating and effect the distribution of parasitic capacitance to ground, so they are explicitly grounded. Both figures depict a quadrant of an aperture, as the magnet is symmetric. Notice that the standard inter-layer is left floating, as it is part of the insulation and evaluated in terms of material properties in COMSOL.

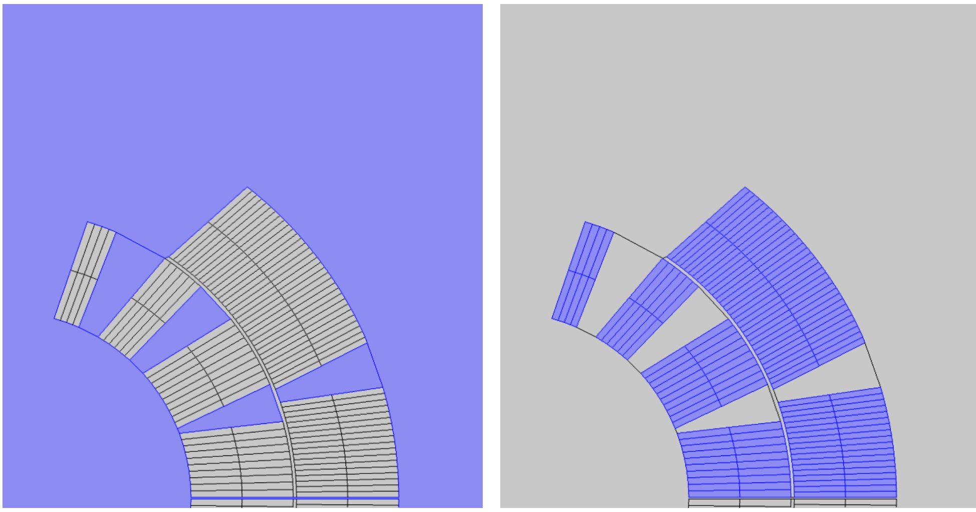

(a) Domains grounded during simulation

(b) Domains at 10 [V] during simulation

### 3.4.2 Mesh of FEM model

The mesh used to calculate parasitic capacitance is as shown in Figure 3.9. Notice that only one of the quadrants of coils have been meshes, so to decrease computational cost. Within the coils the meshing is heavy as the geometry is relatively complex, compared to the cold bore and steel collar where the mesh is larger. To avoid tile shaped **E**-fields and discontinuities a quadratic discretization function was chosen.

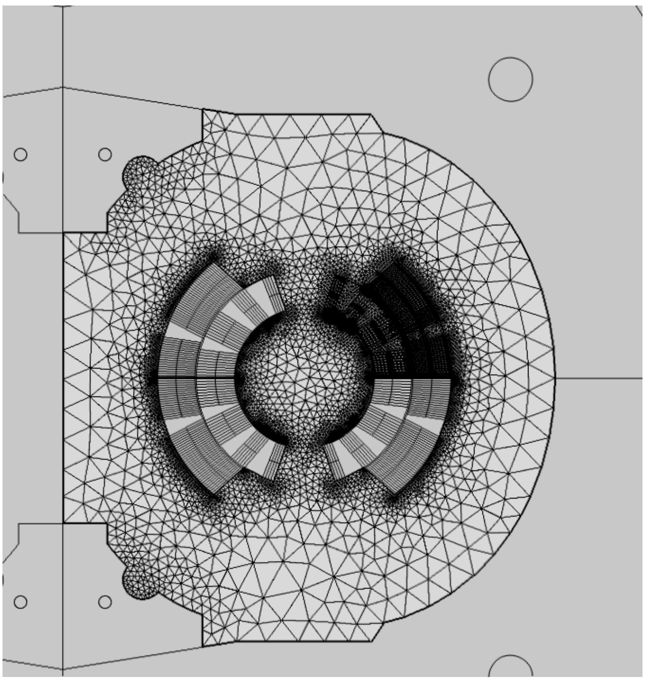

**Figure 3.9:** Meshing of Geometry

#### Mesh sensitivity analysis

In order to validate the mesh utilized, a dedicated sensitivity analysis was performed. The result of using a varying number of elements can be seen in Table 3.3. The number of elements indicates the fineness of the mesh, while the average element quality is a value from zero to one, according to how equilateral each meshing triangle is. [1] This, together with the mesh size, is directly proportional to the accuracy of the the solution. On the other hand, low quality elements can be tolerated as long as they occur at the periphery of the model, not at crucial points of computation. The element quality for each triangle for each mesh level is depicted in Appendix E. For some of the coarser meshes a low element quality within the coil and at the edge of the steel collar is seen. The former leads to an expectation of low accuracy results.

| Mesh level | Number of elements | Average element quality | $C$ [F] |
|---|---|---|---|
| Extremely fine | 40476 | 0.9484 | 3.709699E-7 |
| Fine | 14878 | 0.907 | 3.709698E-7 |
| Coarse | 8896 | 0.8747 | 3.709691E-7 |
| Extremely coarse | 3843 | 0.7191 | 3.709691E-7 |
| Manually coarse | 3321 | 0.7208 | 3.709691E-7 |

**Table 3.3:** Mesh sensitivity

According to Table 3.3 the COMSOL model is almost insensitive to the mesh. This is because the capacitance is calculated from the electric field displacement at the boundary condition between the coils and the surroundings, and thus independent of any spacial gradients.

## 3.5 Results of FEA

### 3.5.1 Electric field

The electrical field resulting from applying a voltage to one of the coils of the MB can be studied in Figure 3.10. The only domain floating is the inter-layer and thus exhibits different values than 0 and 10 V.

[1] An average element quality of one is called an Ideal Delaunay Mesh

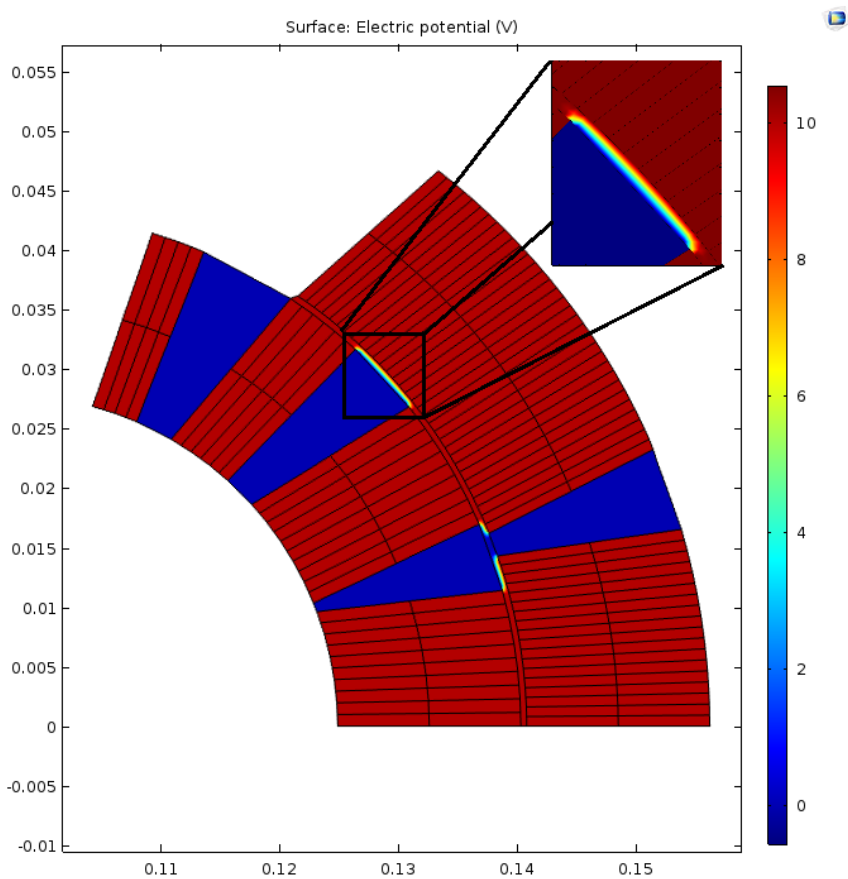


**Figure 3.10:** Electric potential of MB quadrant with zoom-in on insulation

## 3.6 Comparing parasitic capacitance from FEA and measurements

As a proof of concept of the FEA, a parallel analytical calculation will subsequently be performed using Equation 3.7. Here $S$ is surface area of capacitor and $d$ is the distance between plates

| $C_{collar-ground}$ | | |
|---|---|---|
| Parameter | Value | Unit |
| S | 6.2 | $[m^2]$ |
| $\epsilon_r$ | 3 | - |
| d | 0.825 | [mm] |
| C | 2E-07 | [F] |

**Table 3.4:** Analytical calculation of $C_{collar-ground}$

| $C_{coldbore-ground}$ | | |
|---|---|---|
| Parameter | Value | Unit |
| S | 4.6 | $[m^2]$ |
| $\epsilon_r$ | 3 | - |
| d | 0.75 | [mm] |
| C | 1.64E-07 | [F] |

**Table 3.5:** Analytic calculation of $C_{coldbore-ground}$

Hence the total parasitic capacitance to ground is 364 nF. This validates the value of 370 nF calculated from the FEM method. Furthermore, the measured value is 300 nF. Considering that the materials of the MB shrink when cooled down to cryogenic temperatures with about 10 %, while the dimensions given from design drawings are at room temperature, this further supports the proposed FEM method. [29]

## 3.7 Conclusion of FEM calculation of parasitic capacitance to ground

In conclusion, conserving charge within the geometry of the model, is vital to calculating capaciticances in a FEM solver such as COMSOL. Furthermore, it is necessary to equalize all the floating parts in the geometry, so their charge does not accumulate on the parasitic capacitance to ground. Taking these two aspects into account, while using the equations in section 3.4 and putting all metallic parts to zero potential, one can obtain the parasitic capacitance to ground in a model of complex geometry.

Chapter 4

# Method for fitting of MB parameters

*Having obtained the parameter C for the equivalent MB circuit model in the previous chapter, one wishes to estimate L by measurements. Through an optimization technique, the difference between the analytical frequency transfer function and measurements will be minimized. This determines $R_1$,$R_2$ and $k$.*

*To obtain $R_1$,$R_2$ and $k$, it is necessary to study how these parameter's chain value influence a single MB measurement. More specifically, simulations have been run where $R_1$,$R_2$ and $k$ seperately are relatively high for 153 MBs, while the measured magnet parameter value is much lower. If this influence is minimal this implies that each magnet in the dipole magnet chain can be fitted individually, without having to resort to a more advanced approach for obtaining all the fits for 154 MBs. Thus, a verdict on the modularity of fitting the MBs on the chain is concluded.*

*In its totality, this chapter is about methods and all the techniques presented will be utilized in Chapter 6 to fit the impedance of the MB based on FRMs from April 2017.*

## 4.1 Dipole magnet chain during measurements

During the measurements presented, the dipole magnet chain was disconnected from its usual power converter and filter. Also, the energy extractor at the end of the chain was short-circuited, while each end of the dipole magnet chain was connected to a HTS current lead [1] such that the chain could be grounded. For this thesis measurements from November 2016 and April 2017 will be studied, though these have a slightly different measurement configuration. Both measurement configurations are presented in Figure 4.1 and Figure 4.2.

[1]a device providing the electrical link between the room temperature power cables and the cold bus-bars [30]

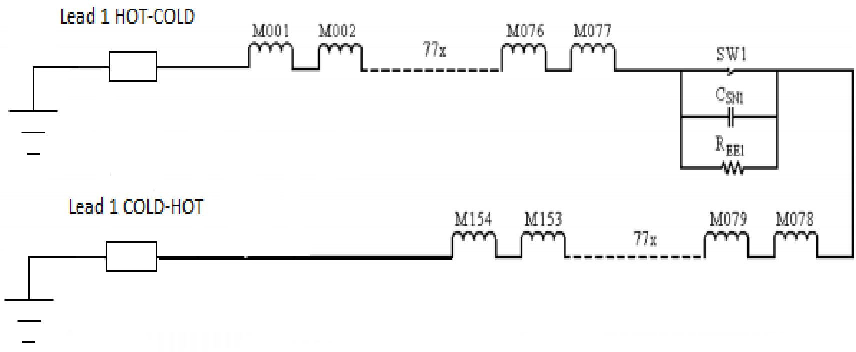


**Figure 4.1:** Circuit diagram of dipole magnet chain during November 2016 measurements (whole chain)

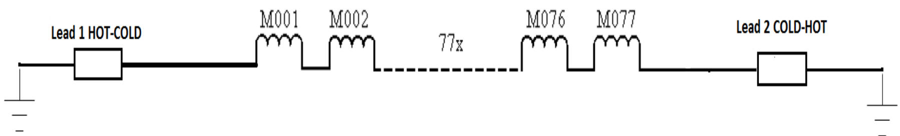


**Figure 4.2:** Circuit diagram of dipole magnet chain during April 2017 measurements (half chain)

For the two configurations, the chain was grounded and the generator floating. The main difference between the two are that for the November measurements the whole chain of 154 dipoles was included, while for the April measurements only half of the MBs were connected in series. Also, the 'whole chain configuration' includes an energy extractor, while the 'half chain configuration' does not. However, during measurements from November 2016 the switch was closed, meaning that it had no effect on the chain.

The measurement set-up for all measurements was type normal, which is discussed at lengths in the report "Multi-scale Analysis of Electro-Thermal Transients in the LHC Main Dipole Circuit". [31] The idea behind the type normal measurement configuration is to study the magnet characteristics of the dipole on multiple levels. Therefore this configuration is flexible enough to measure the whole dipole, both apertures as well as each pole. Referring to Figure 4.3, the voltage taps of Channel 2 can be connected across any single inductance or adjacent inductances.

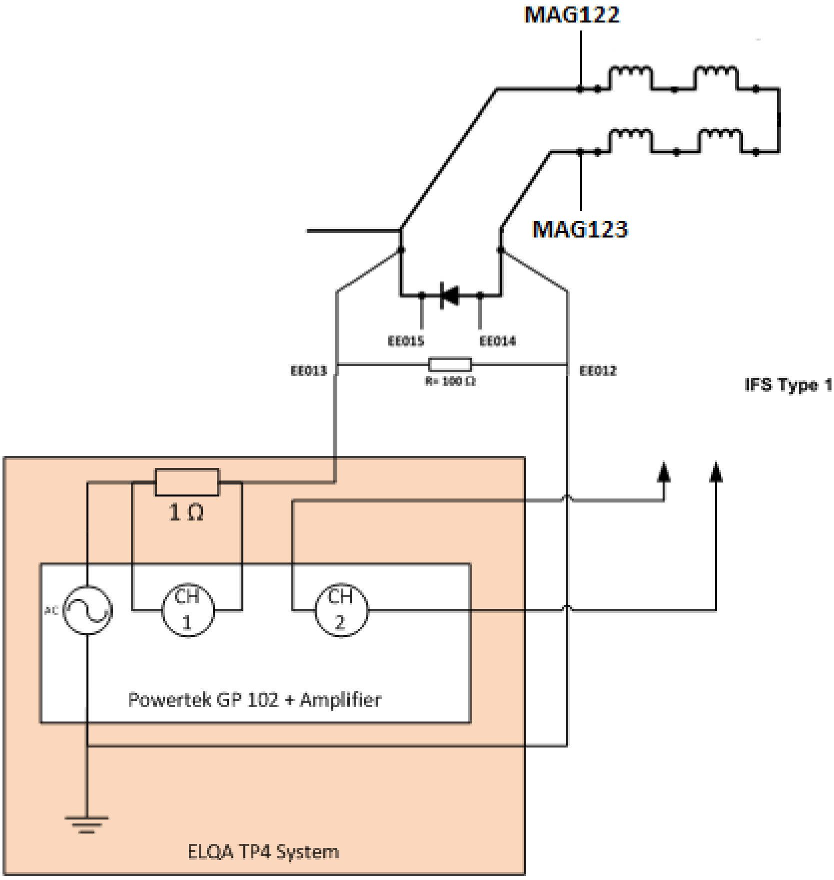


**Figure 4.3:** Type normal measurement configuration [32]

The inductances in the figures represent the four poles of the twin-aperture dipole. Channel 1 (CH1) represents the current measurement, while Channel 2 (CH2) gives the voltage measurements. Feeding the main dipole with an AC voltage makes it possible to do a frequency sweep and measure the resulting current and voltage. Defining a transfer function as a ratio between input and output, the transfer function of the MB impedances become:

$$z(j\omega) = \frac{u(j\omega)}{i(j\omega)} \quad \Omega \qquad (4.1)$$

After two campaigns of magnet measurements in Section 1-2, there is considerable available amount of data for analysis. Specifically, eight magnets measured November 2016 and 41 magnets in April 2017. The available magnets with the corresponding measurement campaign and series are given in Table 4.1 and Table 4.2.

| Measurement Campaign | Electrical position of magnets |
| --- | --- |
| November 2016 | 33, 34, 36, 118, 121, 122, 123, 124 |
| April 2017 | 1, 2 ,3,17 ,18, 19, 20, 21, 22, 40, 42, 43, 44, 45, 46, 47, 48, 49, 50, 51, 55,101, 104, 105, 107, 108, 109, 111, 112, 112, 114, 115, 116, 133, 134, 135, 136, 137, 138, 152, 153, 154 |

**Table 4.1:** MB measurement overview

| Series | Electrical position of magnets |
| --- | --- |
| 1000 (Alstom) | 17, 21, 36, 44, 45, 49, 104, 113, 114, 118, 121, 122, 124, 136, 152, 153 |
| 2000 (Ansaldo) | 1, 3, 18, 19, 20, 22,33, 34, 40, 42, 43, 46, 47, 48, 50, 55, 105, 107, 108, 109, 111, 115, 116, 123, 133, 134, 135, 137 |
| 3000 (Noell) | 2, 51, 138 |

**Table 4.2:** MB measurement by series

The amount of data makes it possible to study differences across magnet series, and conclude if the parameter fittings of transfer function of the MBimpedance should be grouped. For example the fittings could be according to magnet series number, individually or otherwise. Unfortunately, the same magnet was not measured twice for each campaign, which would have provided a point of comparison.

## 4.2 Fitting parameters to measurements

Figure 4.4 shows the comparison between measurements of the first aperture in A31L2 and C30L2 and Pspice simulations of an aperture with the parameters of Table 2.2, both performed in the dipole magnet chain. Certain discrepancies between measurements and simulations exist, which poses a need to improve the fit. By adjusting $L$ the constant offset present below 30 Hz is eliminated, while fitting $R_1$, $R_2$ and $k$ will reduce the error for higher frequencies.

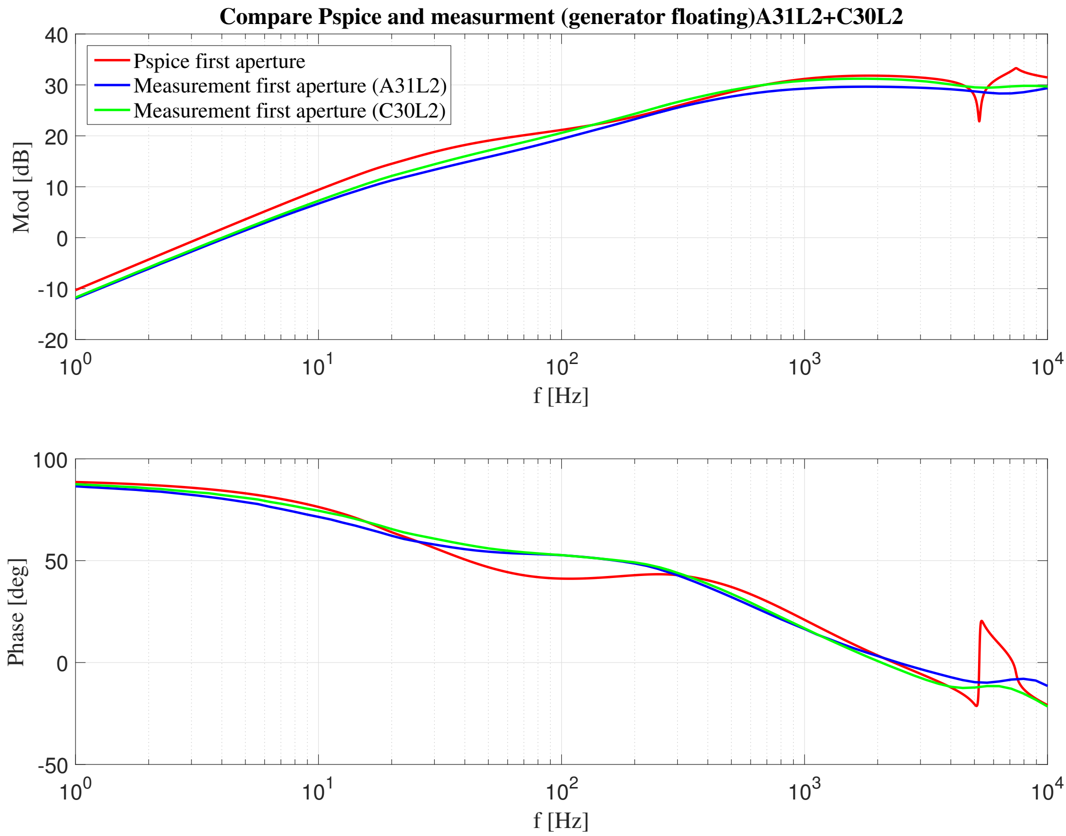


**Figure 4.4:** Comparing measurements of dipoles A31L2 and C20L2 to Pspice simulation with present parameter fit

Here, it is important to note that the resistances of the apertures $R_1$, $R_2$ can be balanced or unbalanced. However, in many instances the average value in the dipole is a more convenient measure, as it simplifies the analytical transfer function of the whole MBequivalent circuit. This value will be referred to as $R_a$. To deduce the values of $R_1$ and $R_2$ it is enough to look up the difference between the two for each MB, which is available in the present Pspice model among others. See Listing A.6.

### 4.2.1 Fitting L

Considering that inductive effects are dominant for low frequencies in the dipole, it is possible to find $L$. The transfer function of the dipole impedance can be approximated to

$$Z_{di}(s) = Ls, \qquad \Omega \quad (4.2)$$

which implies that the curve will intercept the 0-dB line at

$$\omega_c = (1/L), \qquad \text{rad/s} \quad (4.3)$$

where $\omega_c$ is the crossover frequency. With Equation 4.3, obtaining $L$ becomes a matter of simple interpolation from measurement data. The code in Listing A.1 was used to evaluate $L$.

### 4.2.2 Sensitivity analysis

One approach to fitting $k$ and $R_a$ for a magnet, is to understand the sensitivity of each parameter and how the change influences the characteristic of the transfer function of the impedance. Such an analysis can be studied in Figure 4.5 and Figure 4.6

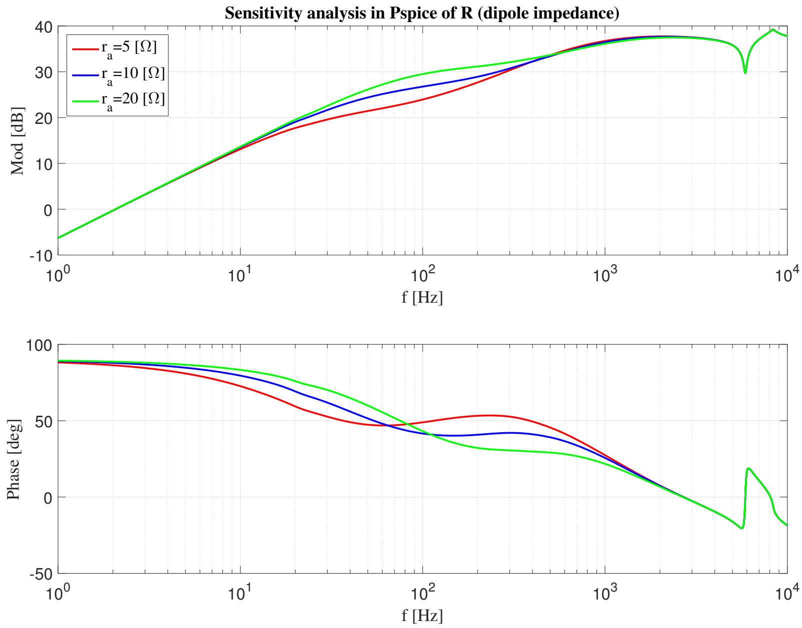


**Figure 4.5:** Sensitivity analysis - change in $R_a$

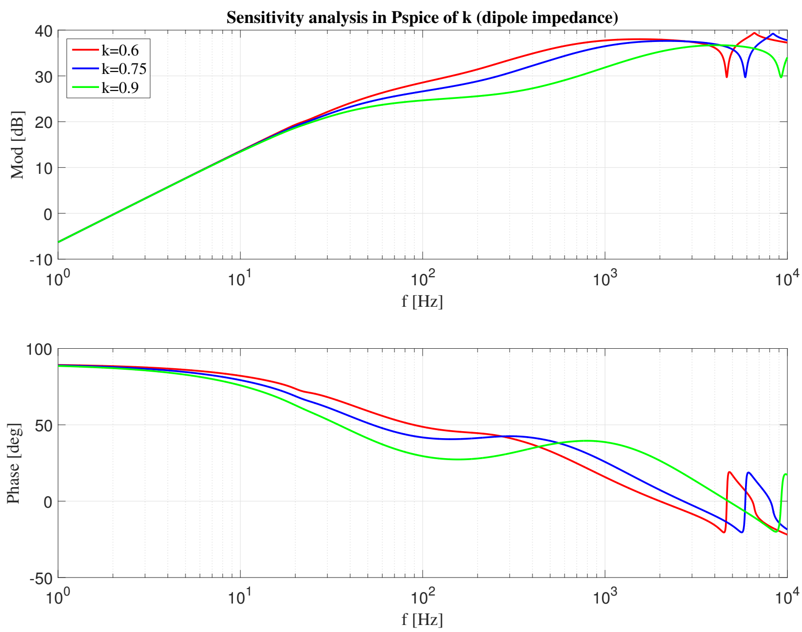


**Figure 4.6:** Sensitivity analysis - change in $k$

From Figure 4.5, it is noticeable that changing $R_a$, is inversely proportional to the time constant of IFCL, described in section 4.2. Figure 4.6 shows that $k$ is proportional to IFCL. The complexity of manual tuning necessitates an optimization technique. Also, a method for comparing fits is necessary. PSO with a suitable objective function addresses both these needs.

### 4.2.3 Method for $\mathbf{R_a}$ and $k$ fit: Particle Swarm Optimization

The method for fitting parameters utilized is called PSO, which is an iterative method inspired by the movement of flocks of birds. The method is initiated by assigning a population of candidate solutions, called particles, random values within the bounds specified. [33] For each iteration, the objective function is evaluated at each particle location, and determines the best (lowest) function value and the best location. Subsequently, the algorithm chooses new velocities, based on the current velocity, the particles' individual best locations, and the best locations of their neighbors. The update of the velocity **v** from the last velocity

$$\mathbf{v} = W\mathbf{v_{last}} + \mathbf{y1}\cdot\mathbf{u1}\cdot(\mathbf{p}\text{-}\mathbf{x}) + \mathbf{y2}\cdot\mathbf{u2}\cdot(\mathbf{g}\text{-}\mathbf{x}), \tag{4.4}$$

where W is the inertia of the movement, **y1** is the weighting of the self-adjustment, **y2** is the weighting of the social-adjustment, **p-x** is the difference between the current position and the best position the particle has seen, **g-x** is the difference between the current position and the best position in the current neighborhood and **u1** and **u2** are uniformly (0,1) distributed random vectors with the same length as the number of variables.[33]

This is expected to move the swarm toward the best solutions, by iteratively updating the particle locations (the new location is the old one plus the velocity, modified to keep particles within bounds), velocities, and neighbors, according to

$$\mathbf{x_{new}} = \mathbf{x} + \mathbf{v}. \tag{4.5}$$

[33] Iterations proceed until the algorithm reaches a stopping criterion. These criteria include reaching tolerances, the maximum of allowed iterations, or time. [33]

#### Particle Swarm Optimization using total vector error

When evaluating error of impedances, both magnitude and phase must be condensed into a single parameter. A neat manner of doing just this is Total Vector Error (TVE). The expression for the TVE is given by

$$TVE(\omega) = \frac{|Z_{tf}(\omega) - Z_{tf,meas}(\omega)|}{|Z_{tf,meas}(\omega)|}, \tag{4.6}$$

where $Z_{tf}$ is the impedance of the dipole for a certain frequency given analytically, while $Z_{tf,meas}$ is the measured impedance at the same frequency.

In order to minimize the TVE between measurements and the analytical transfer function, the method of PSO was implemented. The code implementing this method is given in Listing A.5, and the objective function is defined as the mean of TVE$^2$. As the PSO function in Matlab is stochastic it may give different results each run, having a large influence on the objective function value. Thus, the code implemented loops through 100 iteration to extract the best fit.

When implementing the PSO there are various approaches to defining the objective function. The main objective function minimizes the mean of TVE$^2$, such that:

$$e = \frac{\overline{|\mathbf{Z_{tf}} - \mathbf{Z_{tf,meas}}|^2}}{\overline{|\mathbf{Z_{tf,meas}}|^2}}, \tag{4.7}$$

where bars indicate averaged values. This was chosen as the main expression as it gives greater weight to larger errors. Alternatively the mean of the TVE can be used as an objective function

$$e = \frac{\overline{|\mathbf{Z_{tf}} - \mathbf{Z_{tf,meas}}|}}{\overline{|\mathbf{Z_{tf,meas}}|}}. \tag{4.8}$$

In order to add more emphasize on higher frequencies the objective function can be defined as

$$e = \overline{\omega} \cdot \frac{\overline{|\mathbf{Z_{tf}} - \mathbf{Z_{tf,meas}}|^2}}{\overline{|\mathbf{Z_{tf,meas}}|^2}}. \tag{4.9}$$

In the case where the measurements are logarithmically spaced, creating a bias towards lower frequencies, it could also be an idea to integrate the area of the TVE

$$e = \int \left(\frac{|\mathbf{Z_{tf}} - \mathbf{Z_{tf,meas}}|}{|\mathbf{Z_{tf,meas}}|}\right) d\omega. \tag{4.10}$$

The fitting will be done using mean of TVE$^2$ of Equation 4.7, as the objective function, provided that it gives a satisfactory fit at high frequencies. If this proves unattainable the TVE will be integrated like in Equation 4.10.

### 4.2.4 Influence of the chain's $\mathbf{R_a}$ and $k$ on A31L2

The values of $R_a$ and $k$ differ along the chain, and therefore need to be fitted to each magnet. One wants to study if the fitting of $R_a$ and $k$ can be done independently magnet by magnet without having to resort to a more advanced approach. In order to verify this, the MB impedance of A31L2 was simulated for different $R_a$'s in the rest of the chain, and Figure 4.7 shows the result. The same was done for $k$, which is presented in Figure 4.8.

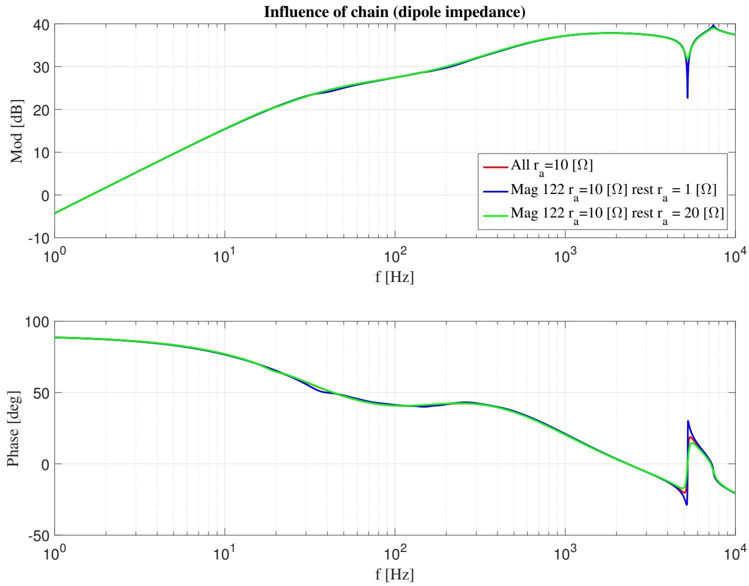


**Figure 4.7:** Dipole impedance for several values of $R_a$ in the rest of the chain

As is observable in Figure 4.7 the influence of the other aperture resistances on the dipole impedance in question is negligible and only become pressing at resonance frequencies. Thus $R_a$ can be tuned individually.

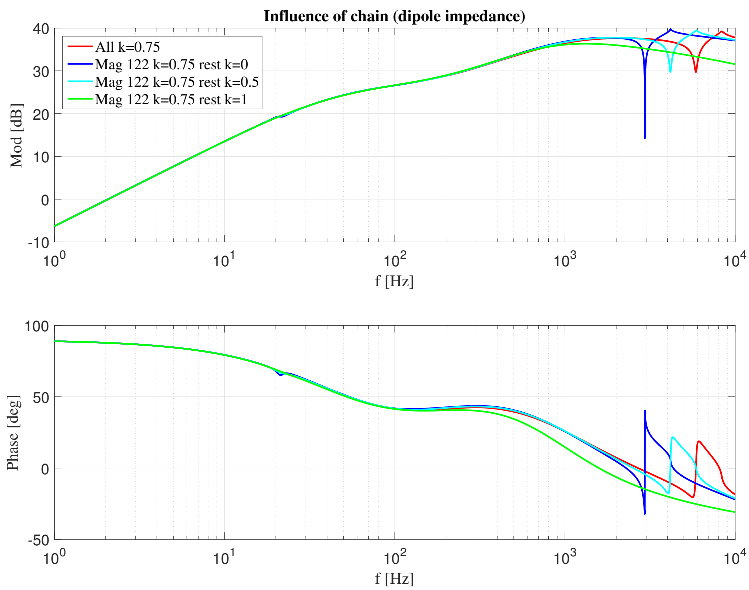


**Figure 4.8:** Dipole impedance for several values of $k$ in the rest of the chain

In Figure 4.8 one can see that $k$ in the rest of the chain has a noticeable influence at high frequencies. This is not significant since the discrepancy is mostly for $k$ equal to one, which is an unphysical fit. Therefore, the $k$-value of a magnet will be fitted individually like with $R_a$.

Chapter 5

# Preliminary investigations for fitting MB parameters

*In November 2016 measurements of 8 MBs in sector 1-2 of the LHC were conducted. Based on these measurements the report "Multi-scale Analysis of Electro-Thermal Transients in the LHC Main Dipole Circuit" discusses various measurement configurations and concludes with a strong recommendation. The recommendation is for grounding each end of the dipole chain and leaving the generator floating. [31] Subsequently, there have been additional measurements made on more magnets in sector 1-2 in April 2017. Despite having a different configuration than the ones from November, the recommended grounding points were followed. Before any fitting of parameters of the MB transfer function impedance is conducted, it is desirable to conclude on the preferable measurement technique. Thus the difference between available measurements will be treated.*

*Measurements were conducted on dipole magnets connected to the rest of the chain, while its associated analytical impedance expression is for a stand-alone magnet. Thus, the next step will be to study the influence of the rest of the chain on the MB measured. Based on this influence, measures of reducing discrepancies devised.*

*Another topic of interest is the influence of the electrical position of an MB on impedance. The concept of symmetrical impedances created by grounding lines aid this discussion. Also, limitations to representing capacitance to ground as lumped elements is expanded upon.*

*Lastly, the issue of low measured inductance values is investigated. Recent MB measurements during cool-down will indicate if these values are due to superconducting phenomena. Subsequently, data from during LHC operating during ramp-up of current will conclude if the low inductance values are justified by the Meissner phase. COMSOL simulations quantify magnetizing effects at* $1\ A$ *and its influence on inductance.*

*Overall, this chapter presents solutions deemed necessary, before the PSO-algorithm can be performed to find the parameters* $R_a$ *and* $k$

## 5.1 Influence of chain

Before fitting the parameters $k$ and $R_a$, the inter-dependencies in the dipole magnet chain must be clarified. More specifically, it must be concluded if one should fit the transfer function to measurements of the single or double aperture impedance. Here single and double aperture refers to the equivalent circuit in Figure 2.18 and Figure 2.16 respectively. This fitting depends on which circuit gives the best overlap with the stand-alone equivalent. A key realization when comprehending the influence the rest of the chain, is that the measurements can be modelled either as a single or double aperture in parallel with the rest of the chain. This is illustrated in Figure 5.1a and Figure 5.1b respectively. Hence, if the single or double aperture is disconnected from the rest of the chain, it is possible to simulate the impedance of the chain and compare it with the simulated stand-alone impedance of the single or double aperture.

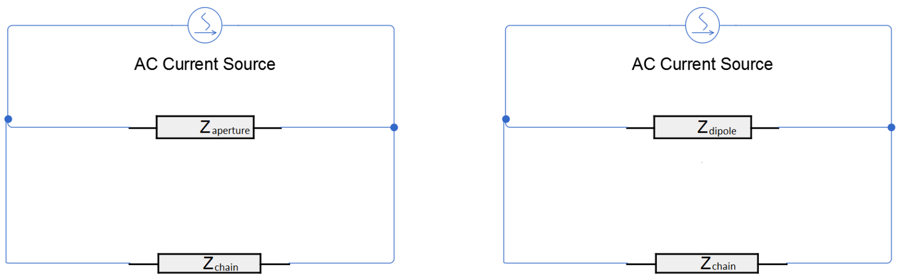


**(a)** Aperture **(b)** Dipole

**Figure 5.1:** Schematic of measurement configuration

When the impedance of the chain is much larger than the impedance of the singe or double aperture, the measurement will be close to the impedance of the latter. This is because the total impedance will always be smaller than the smallest impedance in a parallel connection. Moreover, the larger the largest impedance is, the closer the total value will be to the smallest impedance. However, for the frequencies where the impedance of the chain and the impedance of the single or double aperture are comparable, the total impedance is about half the size of the chain impedance. See Equation 5.1

$$
\begin{aligned}
Z_{eq}(\omega) &= \frac{Z_1(\omega)\cdot Z_2(\omega)}{Z_1(\omega)+Z_2(\omega)} \\
&\text{for} \\
Z_1 = Z_2 \Rightarrow Z_{eq} &= \frac{Z_1}{2}. \\
&\text{for} \\
Z_1 << Z_2 \Rightarrow Z_{eq} &\approx Z_1.
\end{aligned}
\qquad \Omega \quad (5.1)
$$

At the point where the impedances are equal, the inter-dependency between the chain and the circuit studied becomes too strong. The results of simulating the impedance for the rest of the chain simulated with the single and double aperture disconnected in PSpice are given in Figure 5.2 and Figure 5.3 respectively.

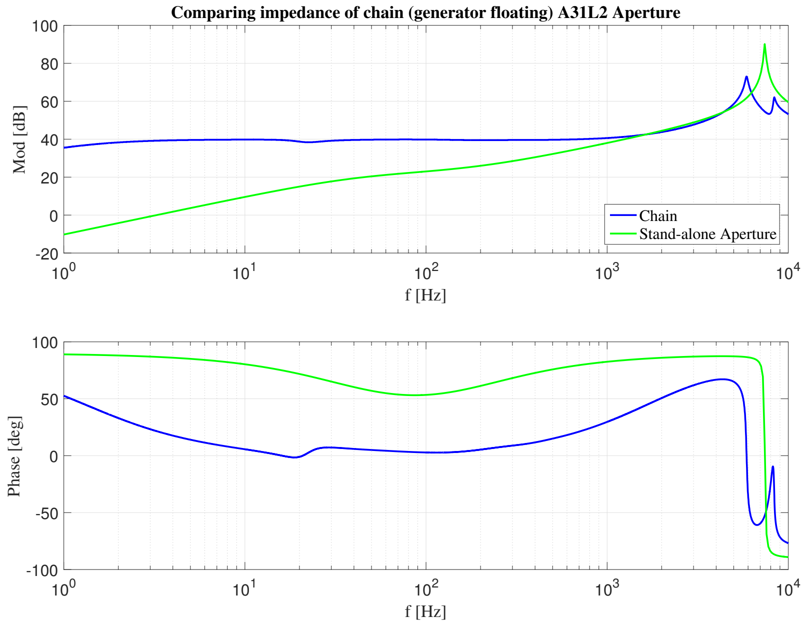


**Figure 5.2:** Impedance of chain - disconnecting aperture

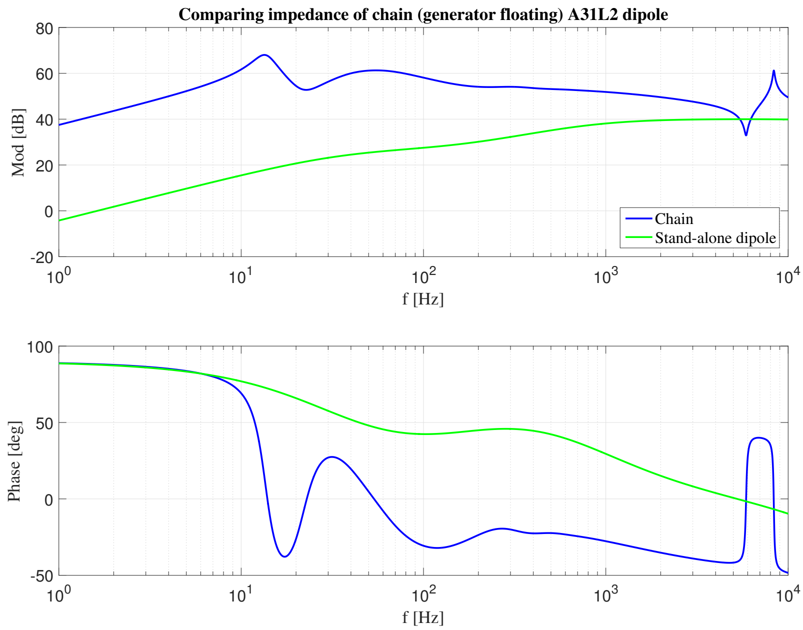


**Figure 5.3:** Impedance of chain - disconnecting double aperture

Comparing Figure 5.2 and Figure 5.3, we see that the chain impedance stays higher calculated from the double aperture than single. While the chain and aperture impedance are equal at around 1 kHz, the chain and double aperture impedance only intercept at around 8 kHz. Hence, measurements should be fitted to the transfer function of the double aperture impedance.

From the analysis in Figure 5.3 the impedances become equal at 8 kHz, at which the measured impedance is equal to half of the magnet impedance. As a criterion, it was decided to ignore frequencies when the chain impedance is less than one order of magnitude larger than the double aperture impedance. Therefore frequencies up to 1 kHz will be included for PSO analysis. This limits the influence of the rest of dipole magnet chain sufficiently.

### 5.1.1 Analytic transfer function of the double aperture

Since the parameters $k$ and $R_a$ shall be fitted against the analytical transfer function of the double aperture impedance its expression must be obtained. This required a y-$\Delta$ transformation of the equivalent circuit schematic, as visualized in Figure 5.4. The actual expression for the transfer function of the double aperture impedance was achieved by using the symbolic tool in Matlab and the code in Listing A.2, with the explicit expression in Listing A.3.

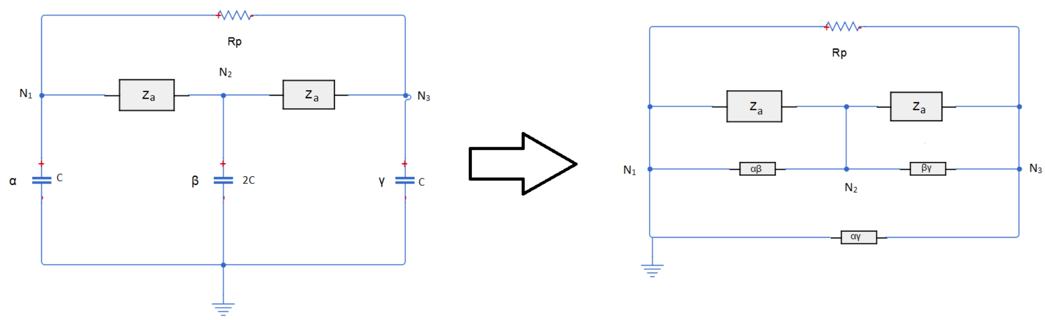


**Figure 5.4:** y-$\Delta$ transformation of double aperture equivalent circuit

Looking at Figure 5.4, the transfer function of the double aperture impedance is deduced. Here, $Z_a$ is the series connection between $(1-k)L$ and $kL$ and $R_a$ in parallel, meaning that:

$$Z_a(s) = L(1-k)s + \frac{LR_aks}{R_a + Lks}. \qquad \Omega \quad (5.2)$$

The expressions for the impedance of capacitances to ground before the transformation are

$$\alpha(s) = \frac{2}{Cs}, \beta(s) = \frac{1}{Cs} \quad \text{and} \gamma(s) = \frac{2}{Cs}. \qquad \Omega \quad (5.3)$$

After the y-$\Delta$ transformation the expressions become:

$$\alpha\beta(s) = \frac{\alpha\beta + \alpha\gamma + \beta\gamma}{\gamma}, \qquad \Omega \quad (5.4)$$

$$\beta\gamma(s) = \frac{\alpha\beta + \alpha\gamma + \beta\gamma}{\alpha} \quad \text{and} \qquad \Omega \quad (5.5)$$

$$\alpha\gamma(s) = \frac{\alpha\beta + \alpha\gamma + \beta\gamma}{\beta}. \qquad \Omega \quad (5.6)$$

Thus, the transfer functions

$$\alpha\beta(s) = \beta\gamma(s) = \frac{4}{Cs} \quad \text{and} \qquad \Omega \quad (5.7)$$

$$\alpha\gamma(s) = \frac{8}{Cs} \qquad \Omega \quad (5.8)$$

is obtained. Each $Z_a$ is in parallel to either $\alpha\beta$ or $\beta\gamma$, which again are connected in series with one another

$$Z_1 = \frac{Z_a * \alpha\beta}{Z_a + \alpha\beta}, \quad Z_2 = \frac{Z_a * \beta\gamma}{Z_a + \beta\gamma} \quad \text{and} \quad Z_{series} = Z_1 + Z_2. \qquad \Omega \quad (5.9)$$

The resulting transfer function is evaluated to

$$Z_{series} = \frac{-(8(Ls(k-1) - \frac{LR_a ks}{R_a + Lks})}{Cs(\frac{4}{Cs} - Ls(k-1) + \frac{LR_a ks}{R_a + Lks})}. \qquad \Omega \quad (5.10)$$

$Z_{series}$ is according to Figure 5.4 in parallel with $R_p$ and $\alpha\gamma$. Finally, the total impedance becomes

$$Z_{tot} = \frac{Z_{series}\alpha\gamma R_p}{Z_{series}\alpha\gamma + Z_{series}R_p + \alpha\gamma R_p}. \qquad \Omega \quad (5.11)$$

## 5.2 Evaluating measurement configuration

Although, there are only eight magnet measurements with the 'whole chain configuration' available, while there are 41 magnet measurements with the 'half chain configuration' it is relevant to compare the two configurations. Based on such a comparison, future measurements can be standardized. A comparison between the impedance of the dipole magnet chain for Magnet 122 with the 'whole' and 'half chain' configuration is found in Figure 5.5.

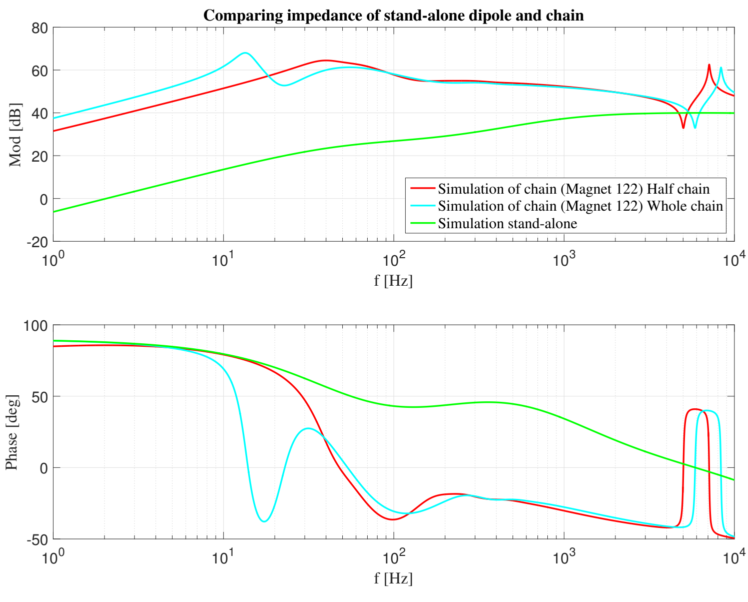


**Figure 5.5:** Comparing chain impedance for 'half' and 'whole chain configuration'

The simulations show a difference with the 'whole chain configuration' staying higher for a wider range of frequencies than the 'half chain'. The crossing of impedances occurs at 5496 Hz and 4677 Hz, for the 'whole chain' and 'half chain configuration' respectively. Thus the 'whole chain configuration' is preferable to the 'half chain'.

Another aspect that influences the chain impedance of a magnet is its electrical position, and Figure 5.6 displays the chain impedance of Magnet 1 and 19.

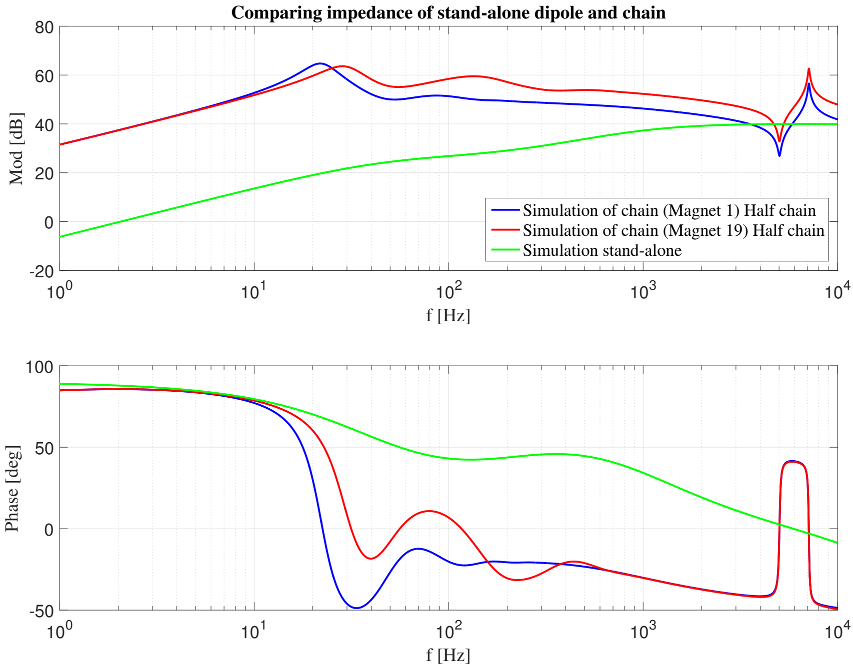


**Figure 5.6:** Comparing chain impedance for different electrical positions

Mainly the magnets on each end of the dipole magnet chain have a significantly lower intercept frequency between impedance of stand-alone double aperture and chain, which is illustrated in Figure 5.6. Magnet 1 has an intercept frequency 3467 Hz compared to Magnet 19 with a 4677 Hz intercept frequency. This supports the argument that care should be taken when fitting the first and last magnet.

## 5.3 Distributed Capacitance

A consistent issue when comparing measurement and simulations is that perturbations around 8 kHz in simulations is observed that are not present in measurements. Measurements and simulations are compared in Figure 5.7.

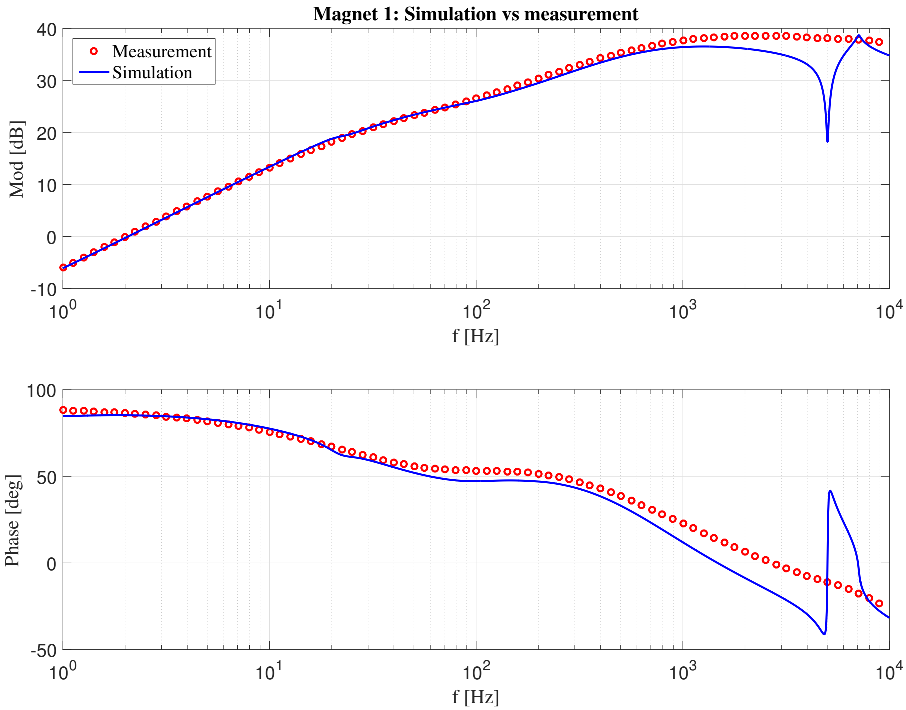


**Figure 5.7:** Comparing simulation and measurement of Magnet 1

When comparing the two in Figure 5.7 it becomes apparent that this is not due to a low sampling frequency of measurements. An hypothesis to the discrepancy is that the equivalent circuit model utilized in PSpice is not valid for high frequencies. This could be due to the simplification of a distributed capacitance in the MB design to a lumped element in the circuit model not being able to capture behavior above 1 kHz.

In order to investigate the issue of distributed capacitance, additional simulations have been performed on Magnet 122. One where the MB model is extended with 7 capacitances and one with 9 capacitances according to Listing A, Listing A and Listing A with circuit models depicted in Figure D.1, Figure D.2 and Figure D.3 of Appendix D. A limitation to the present model, in terms of the $1-10$ kHz range is that the capacitances are placed at the edges of the circuit creating a large influence on impedance, which can be seen as perturbations. Thus all circuit models simulated in this section have been modified such that the capacitances are places at the interior of the circuit and not at the same node as the parallel resistor. Still, the total capacitance values remains the same. The comparison between the three models can be studied in Figure 5.8 for Magnet 122.

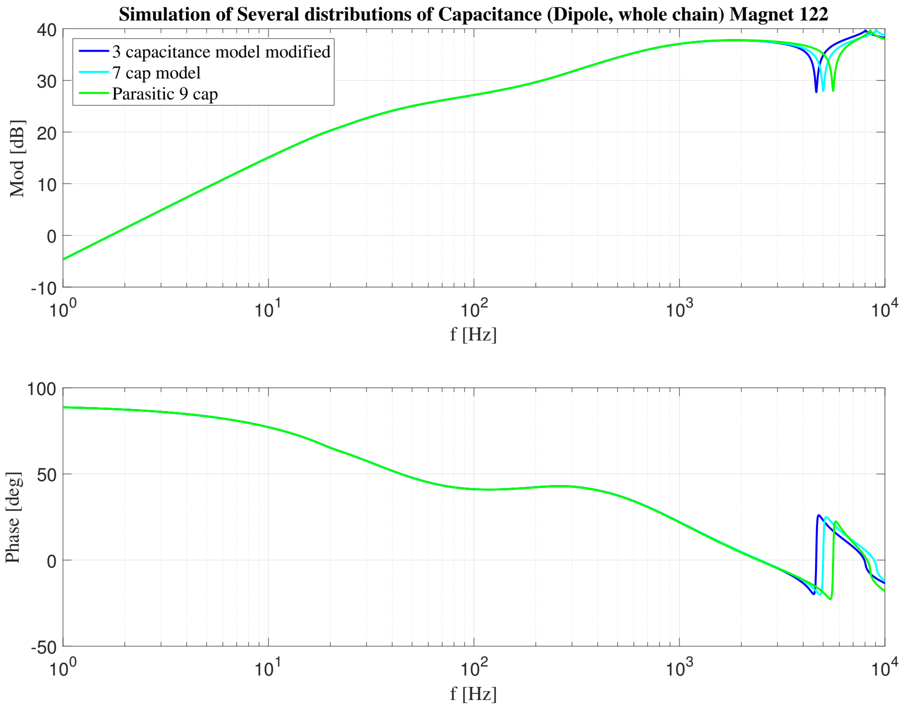


**Figure 5.8:** Simulation of Magnet 1 with three different MB models ('whole chain')

In Figure 5.8 the frequency of the dip, originally at 8 kHz, increases with increasingly distributed capacitance in the circuit. For a circuit with infinitely many capacitances accumulating to a total capacitance of 300 nF would mean that the perturbation would not appear at all. Hence a lumped element model is not be able to capture the behavior of distributed capacitance.

## 5.4 Grounding line and symmetries

For the cryostat to be at zero voltage, a grounding network has been constructed. This grounding line has a certain impedance, and influences the frequency transfer function of the impedance depending on the magnet's position. The grounding line has an influence on impedance depending on the magnet's electrical position. To understand such influences simulations in Pspice were performed. With the 'half chain configuration' symmetries are created. Not around the middle point of the chain as with the whole chain, but such that the first position of the first chain overlaps with the last position of the second chain and vice versa. This is plotted in Figure 5.9 and Figure 5.10. Figure 5.11 shows a simulation with the same measurement configuration if the grounding line was removed. Without the grounding line the 'half chain' is again symmetric around the middle point of the dipole chain.

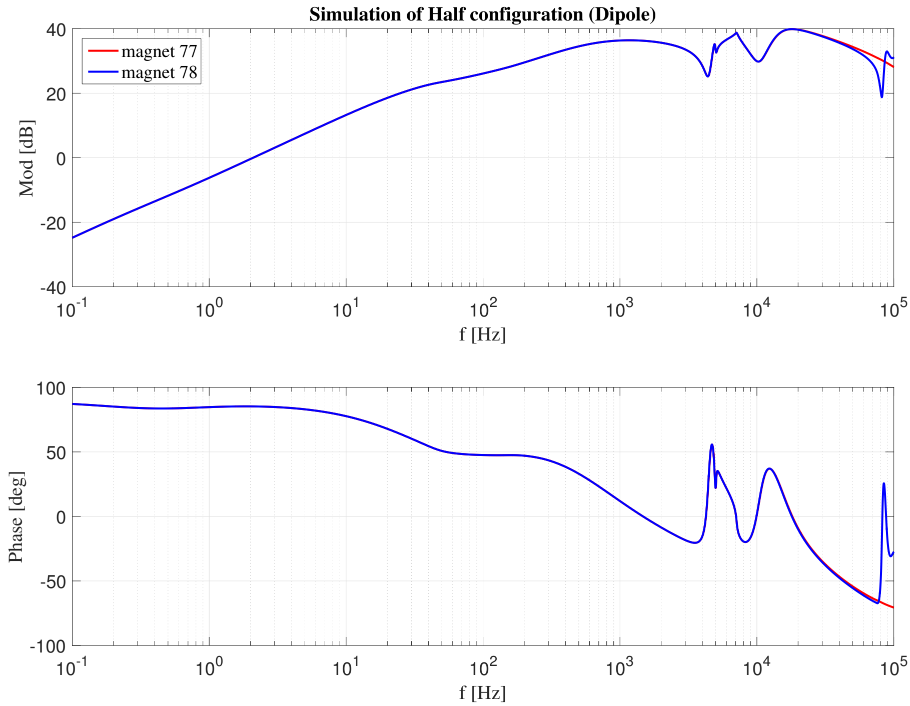


**Figure 5.9:** Simulation of Magnet 77 and 78 for 'half-chain configuration'

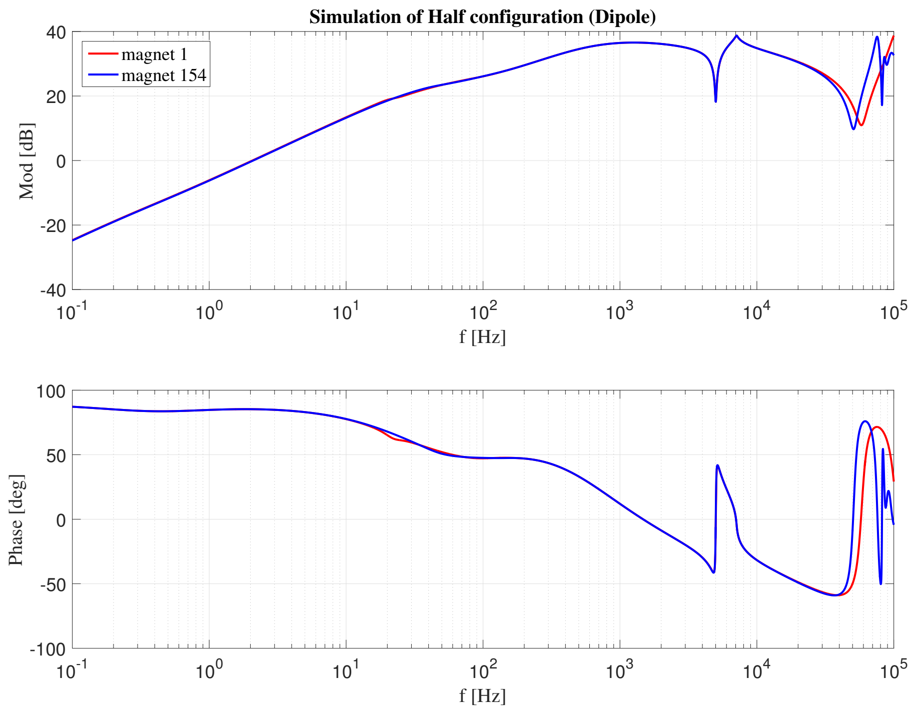


**Figure 5.10:** Simulation of Magnet 1 and 154 for 'half chain configuration'

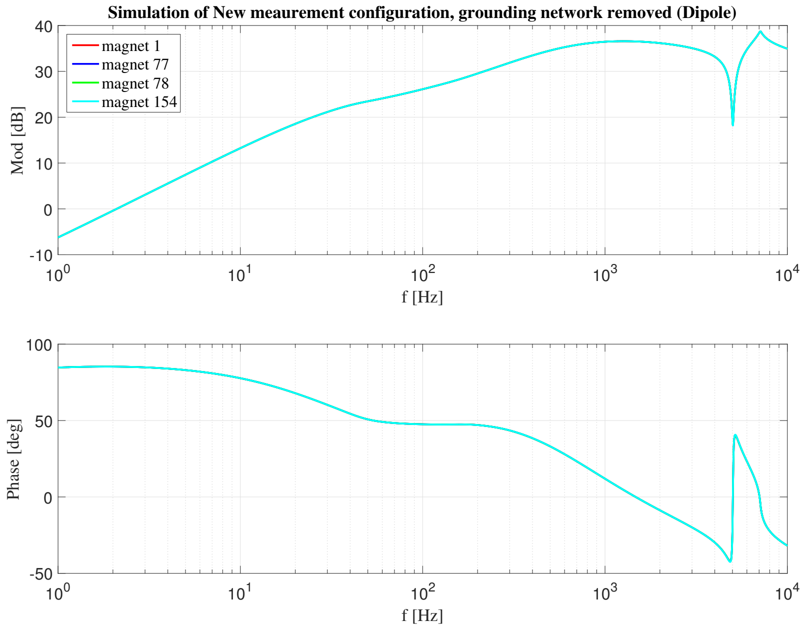


**Figure 5.11:** Simulation of Magnet 1, 77, 78 and 154 for 'half chain configuration' without Grounding Network

To further examine the symmetries created by grounding lines, measurements of symmetrically equal magnets have been plotted together, which is presented in Figure 5.12. Subsequently, a simulation of symmetrically opposite magnets was plotted in Figure 5.13

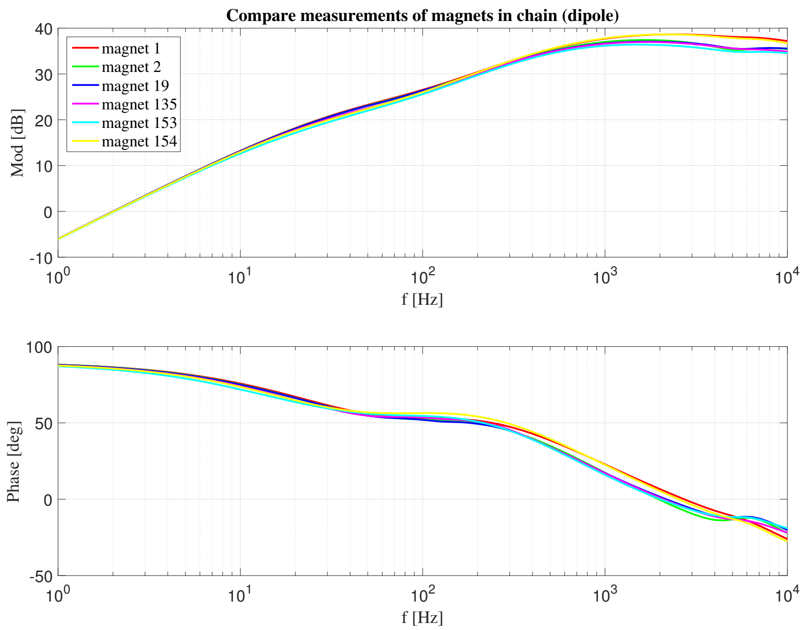


**Figure 5.12:** Measurements of mangets 1,2,19, 153,154 (dipoles)

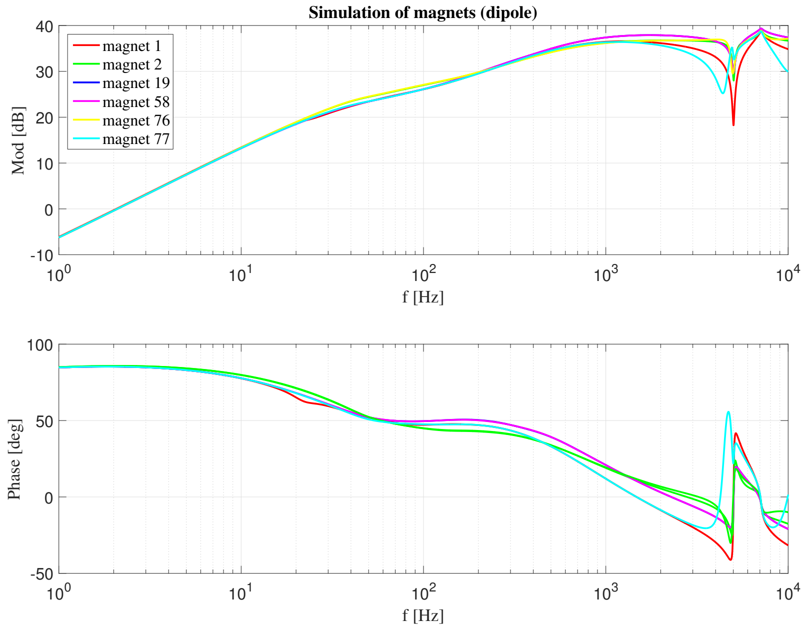


**Figure 5.13:** Measurements of mangets 1,2,19, 153,154 (dipoles)

According to measurements of Figure 5.12, the symmetries for the rest of the chain is less apparent. Due to the approximation of distributed capacitance discussed in section 5.3, Figure 5.13 exhibits symmetries. Based on the limited on the measurements of symmetrical magnets, the result indicates that symmetry is only valid for the first and last magnet of the chain.

## 5.5 Low inductance values from Frequency Response Measurements

Compared to the nominal inductance of 98.7 mH, the results from the November 2016 measurements of eight magnets in Sector 1-2 were showing low inductance values. See Figure 4.4. After getting 41 additional magnet measurements in April 2017, it was verified that this also was the case for these new measurements. As is seen from Figure 5.14, the inductance values range from $77 - 81$ mH. Thus there is a systematic phenomena causing such a low reading.

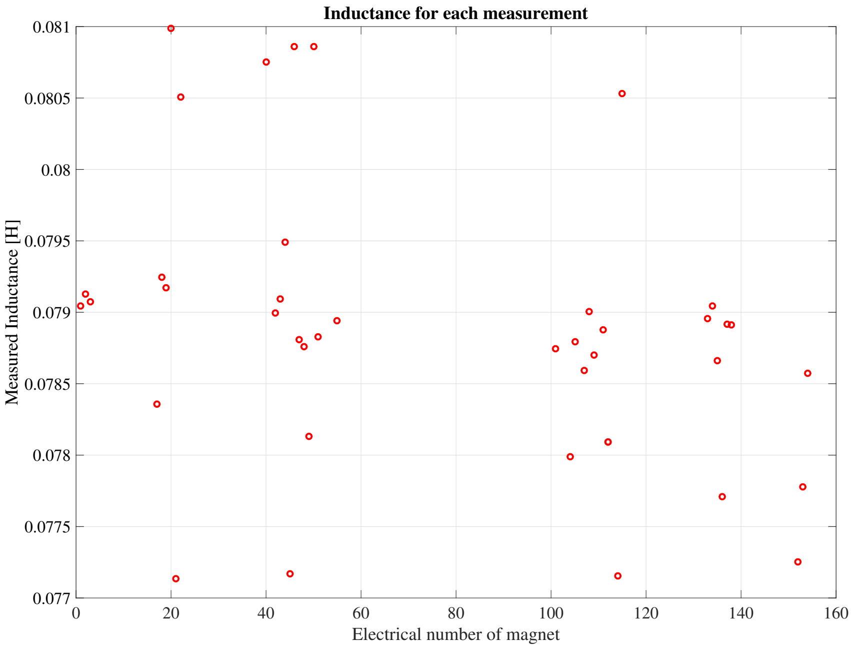


**Figure 5.14:** Inductance for April 2017 MB measurements

A hypothesis from [22] is that for FRMs at 1 A the magnet is in the Meissner region, meaning its expelling all flux from the conductor. Once the magnet reaches a magnetic flux density over $B_{c1}$ an additional volume is available for the flux, resulting in a higher inductance. [22] Similar behavior has been described in [34]. When ramping the MB at 10 A/s, the initial inductance obtained at comparable current levels was 85 % of nominal value, which is attributed to residual positive magnetization. [34] During similar measurements of MB prototypes, the same phenomena was observed. [29] Figure 5.15 shows the calculated differential inductance during two current cycles between -600 and 600 A.

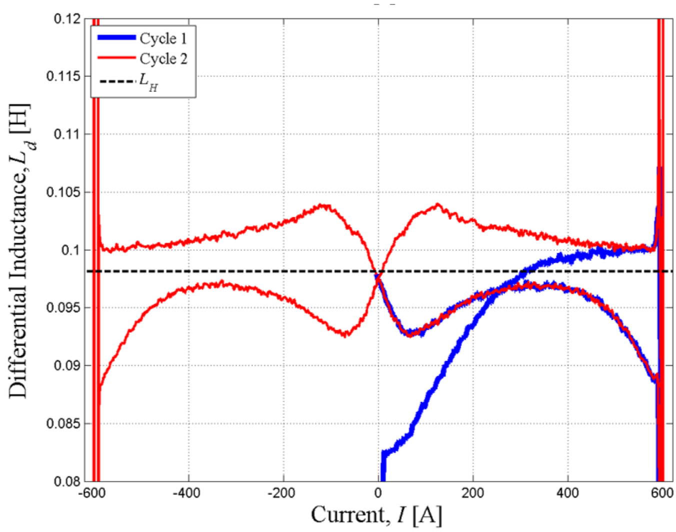


**Figure 5.15:** Calculated differential inductance Ld (Cycles 1 and 2) [34]

To explain the low inductance values, a sensitivity analysis focusing on temperature, current and frequency will be executed. Therefore, this section studies $L$ as function of these three parameters independently. The former is studied from a cool-down process of a stand-alone MB over the period 9th-11th of June 2017. Inductance as a function of current will be obtained, through calculation of the differential inductance of the MB during operation. The data is from the 3rd of May 2017 during ramping of current. Lastly, inductance as a function of frequency is studied through a COMSOL model of the MB. This study concludes the largest contributors to inductance decrease at 1 A and 2.15 Hz. From these efforts it will be possible to not only conclude on the sensitivity of temperature, current and frequency to inductance, but also provide an explanation to the behaviour.

An important distinction is between the concepts of differential inductance $L_{diff}$ and apparent inductance $L_{\text{ap}}$. All estimations of inductance in this thesis, whether from measurements or simulation, are either differential or apparent. Differential inductance and apparent inductance are defined as

$$\begin{aligned} L_{diff} &= \frac{d\phi}{di} \\ L_{ap} &= \frac{\phi}{i}. \end{aligned} \quad \text{H} \qquad (5.12)$$

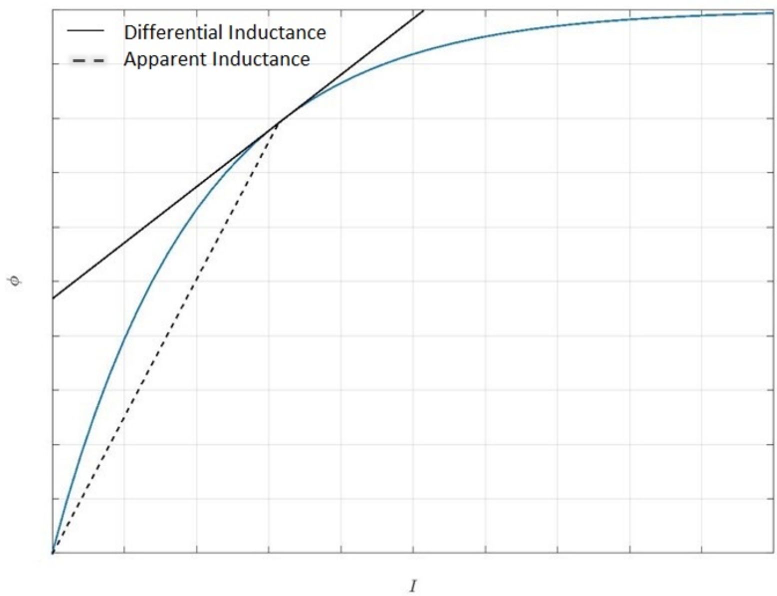


**Figure 5.16:** Distinction apparent and differential inductance: Flux vs current

Figure 5.16 of flux vs current, illustrate that for for some intervals of current a constant change in current does not induce a proportional change in magnetic field. This causes a change in $L_{diff}$ and $L_{\text{ap}}$. Moreover, from Figure 5.16 it is clear that these values are not the same in all cases. However, with no saturation, only the linear range for double aperture impedance is considered. Hence apparent and differential inductance will be the same, and inductance will be calculated based on the available data.

### 5.5.1 Apparent inductance at cool-down

The first approach to the case of sensitivity of inductance is investigating the apparent inductance during cool-down of an MB. Between 9th-11th of June 2017, a stand-alone MB was cooled down from $80-4.5$ K. Simultaneously, FRMs of impedance were conducted every 10 minutes. The result when estimating $L_{\mathrm{ap}}$ at 2.15 Hz is rendered in Figure 5.17.

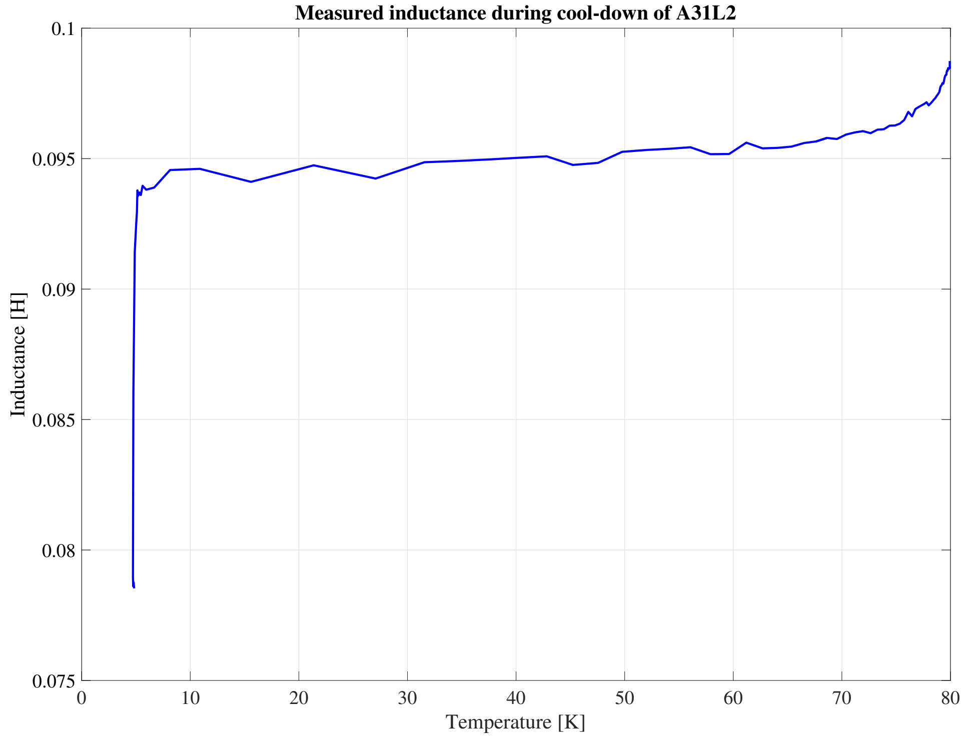


**Figure 5.17:** Differential inductance vs Temperature

As the MB temperature drops below critical temperature, there is a dramatic drop in inductance. Therefore, the drop in inductance must be due to superconducting effects.

### 5.5.2 Differential inductance at current ramp-up

With the aid of data from LHC operation, it is possible to study the sensitivity of inductance to the current level. The equation for calculating differential inductance is

$$L_{diff} = \frac{U_{mag} - R_{splice} \cdot I}{di/dt}, \qquad \mathrm{H} \quad (5.13)$$

where the splice resistance $R_{splice}$ is 1 [n$\Omega$] and represents the resistance from interconnections in the circuit. $U_{mag}$ is the voltage across the MB A12R1 in Sector 1-2.

The data from Figure 5.18a, Figure 5.18b and Figure 5.19 are from a ramp-up from $1-100$ A. Up until about 11 s, the voltage is saw-tooth shaped and thus $di/dt$ is challenging to evaluate, which is reflected in Figure 5.19. Hence the resulting differential inductance values are unreliable. However, the differential inductance stabilizes at around 30 A as the voltage reaches a plateau, and inductance values are observed at around 0.09 H between

$30 - 100$ A in Figure 5.19. Equation 2.2 states that the penetration depth in the Meissner region is proportional to the field, which explains the linear increase in differential inductance with current in Figure 5.19.

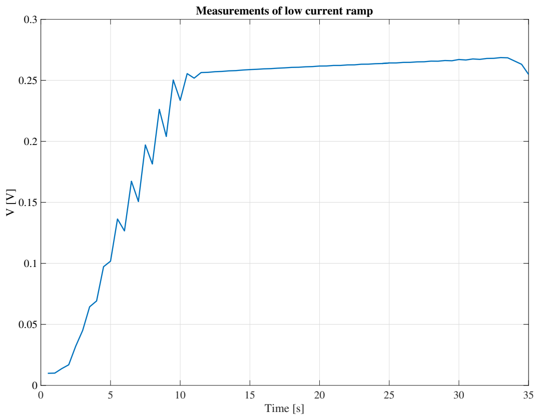


(a) Voltage over magnet

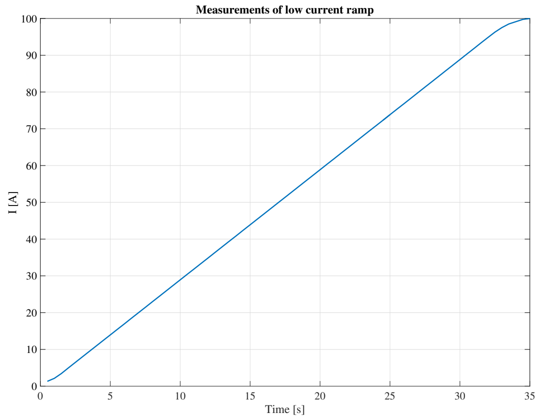


(b) Current through magnet

**Figure 5.18:** Measurement of Current ramp from LHC during operation

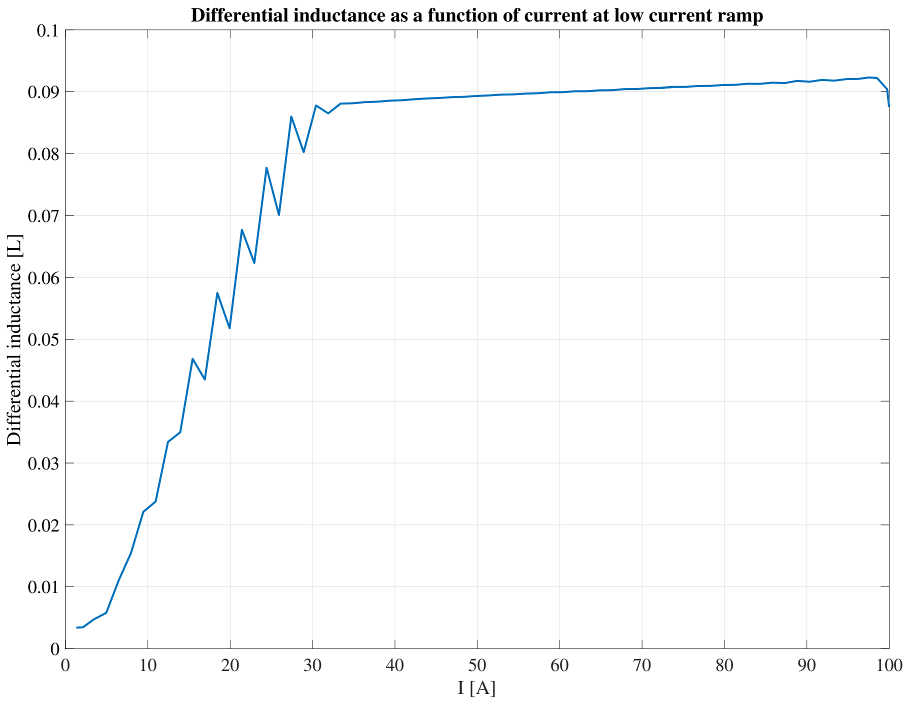


**Figure 5.19:** Calculation of Differential Inductance from Measurement of Current ramp from LHC during operation

Looking at a current ramp from $2 - 11$ kA in Figure 5.20a, Figure 5.20b and Figure 5.21, the voltage and differential inductance remains relatively stable. Furthermore, the inductance value is close to nominal value, which is expected for such high current values.

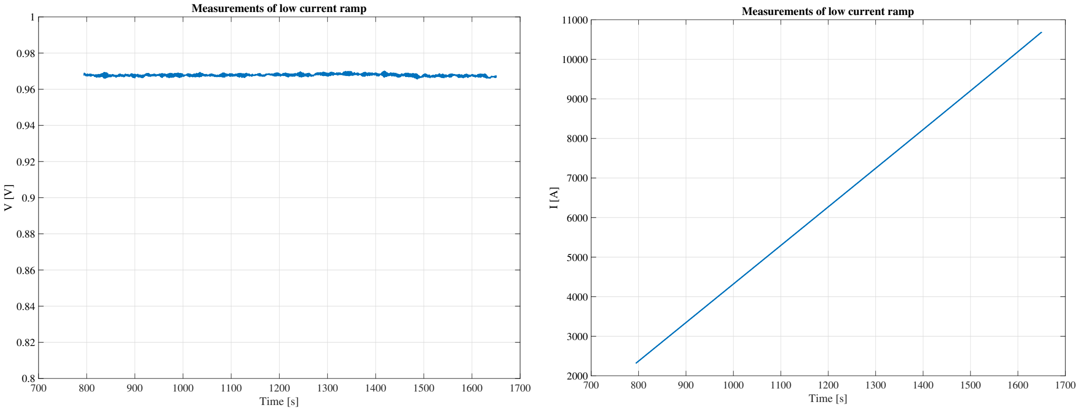


**(a)** Voltage over magnet

**(b)** Current through magnet

**Figure 5.20:** Measurement of Current ramp from LHC during operation

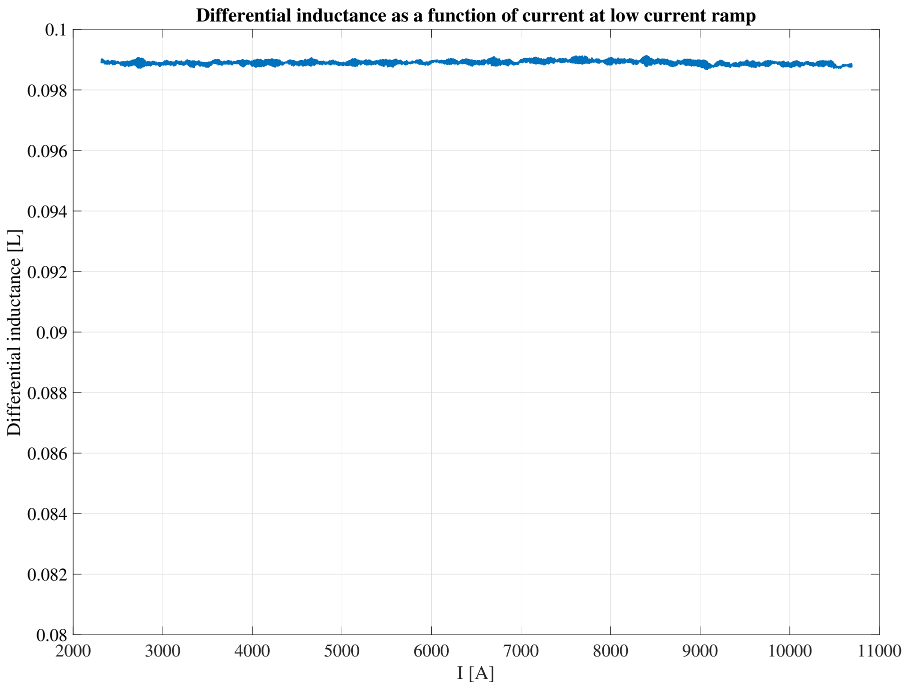


**Figure 5.21:** Calculation of Differential Inductance from Measurement of Current ramp from LHC during operation

Based on calculations in Appendix C, the Meissner region extends until about 223.5 A for a single strand, which means that a significant difference in differential inductance for the intervals $30 - 100$ A and $2 - 11$ kA is expected. To conclude, these measurements validate the theory of lower differential inductance in the Meissner phase.

From subsection 5.5.1 and subsection 5.5.2, it is clear that low inductance values are due to superconducting effects, which show behavior according to the Meissner phase at low currents. Next, the superconducting effect that gives the largest contribution to drop in $L_{diff}$,for the case of operating in the Meissner phase, will be determined.

### 5.5.3 FEA of magnetizing effects

In order to study the contribution of persistent magnetization and induced eddy-currents in the cable and copper wedges, a simulation has been run in a COMSOL model of the MB. The geometry is as for the FEM calculation for parasitic capacitance, except now only a quadrant has been considered. See Figure 3.6. According to Ravaioli, persistent magnetization, eddy currents in wedges, ISCC and IFCC contribute to magnetization at low current. [34] [35] These effects all decrease inductance. Moreover, the MB model in COMSOL has the ability to isolate each effect, such that they can be studied both independently and combined. The model has been simulated in the frequency domain with 1 A Root Mean Square (RMS) as current input. It is resolved at the half-turn level with homogenized material properties and physical laws over such an area. [35]

Figure 5.22a- Figure 5.22f depict the magnetic flux density and magnetic vector potential for the various isolated effects, as well as all the combined effects at 2.15 Hz.

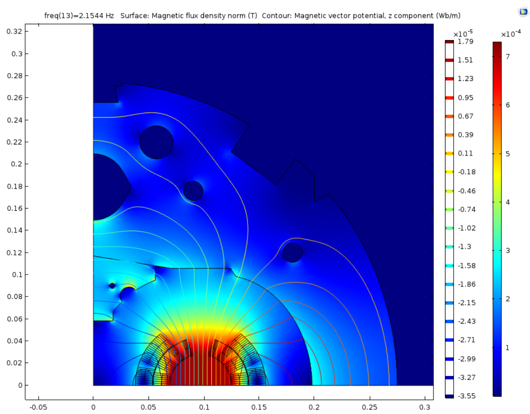


**(a)** No effects reducing differential inductance

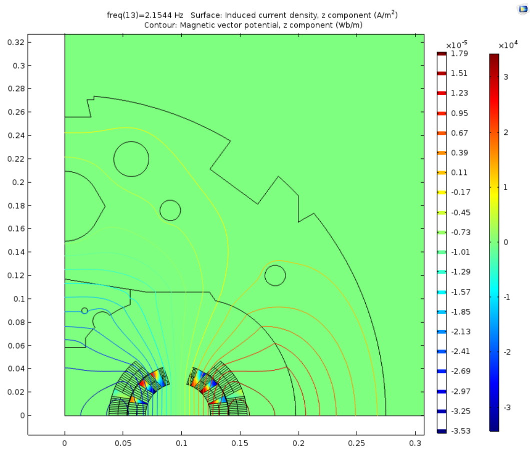


**(b)** Eddy currents in copper wedges

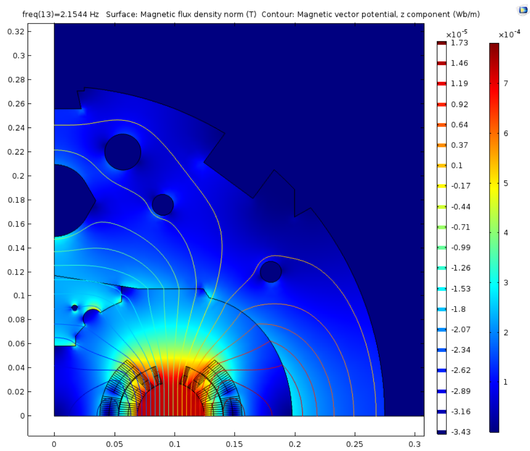


**(c)** ISCC

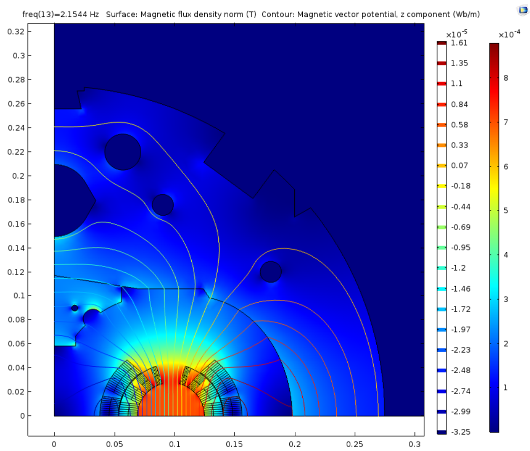


**(d)** IFCC

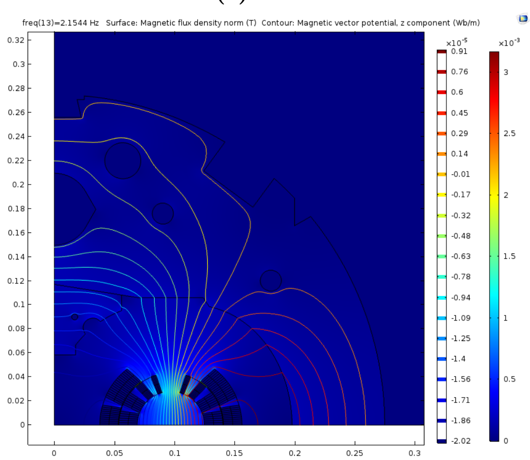


**(e)** Persistant magnetization

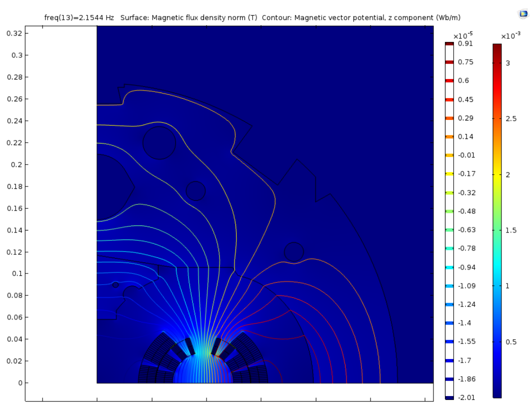


**(f)** All phenomena combined

**Figure 5.22:** Magnetic flux density and magnetic vector potential

Due to the Meissner effect, the flux lines are expelled from the coils in Figure 5.22e and

Figure 5.22f. Figure 5.22b show a small eddy current at the edge of the copper wedges of the inner layer.

Finally, Figure 5.23 shows $L$ as a function of frequency when each magnetization effect is isolated and combined.

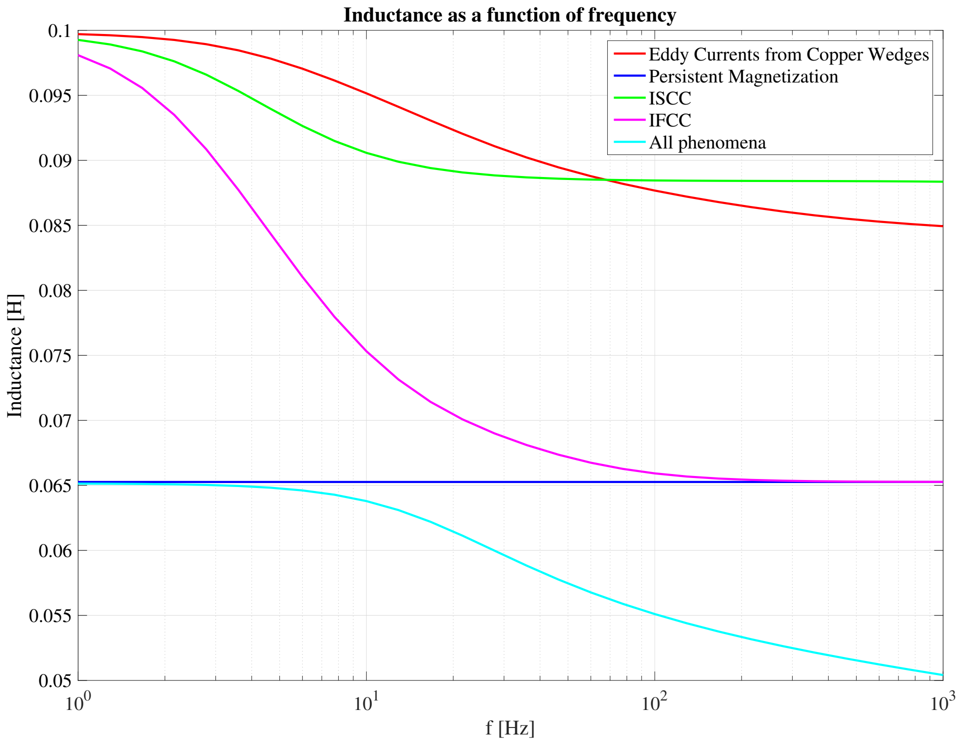


**Figure 5.23:** L vs Omega from COMSOL model of MB, isolating various effects to study contribution on magnetization at 1 A

As seen in Figure 5.23, eddy currents and ISCC hardly effect inductance at low frequencies, where the inductance has been estimated. IFCC have some effect on the decrease in L at low frequencies. On the other hand, the persistent magnetization is independent of frequency and has a large impact at 1 A.

When all phenomena are combined, the effects of persistent magnetization and eddy currents in the copper wedges superimpose, while coupling currents from strands and filaments are suppressed. Another relevant observation from Figure 5.23, is that $L$ only including magnetizing effects from IFCC obtains the same value at high frequencies as $L$ from persistent magnetization. To understand these results, the behavior of each magnetizing effect must be understood. According to

$$\mathbf{M}_{\text{IFCC}} \propto \mathbf{M}_{\text{ISCC}} \propto \frac{d\mathbf{B}}{dt} \qquad \text{A/m} \quad (5.14)$$

$$M_{\text{pers}} \propto J_c. \qquad \text{A/m} \quad (5.15)$$

[35] Hence at a high frequency $\mathbf{M}_{\text{IFCC}}$ expels all flux from the coils when the behavior of the IFCCs are isolated. This is why $L$ only including magnetizing effects from IFCC overlaps at

high frequencies with the $L$-value only considering persistent magnetization. Since persistent magnetization is such a strong effect at low currents it expels all the flux in the coils and $\mathbf{M}_{\mathrm{IFCC}}$ and $\mathbf{M}_{\mathrm{ISCC}}$ experiences a zero constant field, meaning that they are both zero. In other words, as persistent magnetization expels all flux there is no more flux to be expelled by IFCC and ISCC in the coils. Thus we do not see their effect in the combined simulation of all phenomena. However, eddy currents in the copper wedges have the ability to magnetize wedges and reduce the overall inductance, which is observed in the combined simulation.

An inductance of 0.065 H is considerably lower than the measured 0.08 H. Figure 5.22e provides a plausible explanation. Seeing as the MB is operated in the Meissner phase, a behavior described in subsection 2.1.5, the coils are expelling all external fields according to Equation 2.7. This expulsion of flux can clearly be seen in Figure 5.22e. However, the MB coils are only partially made of superconducting material, which is illustrated in Figure 5.24. Instead of considering the copper and the Nb-Ti separately in the COMSOL model, persistent magnetization is scaled according to the fraction of superconducting material in the strand and ratio of strand to cable cross-sectional area, which is inaccurate in the Meissner phase. In reality some flux lines will concatenate the coils when MBs are operated in this manner. This in turn gives a larger inductance than obtained from COMSOL simulations.

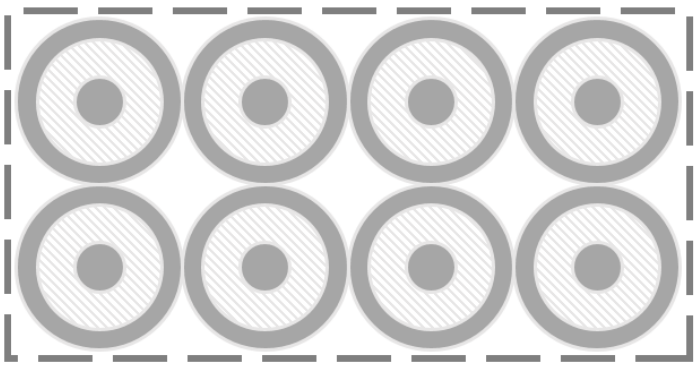

**Figure 5.24:** Cable cross section; the light- and dark-grey domains refer respectively to the superconducting and the copper domains; the remaining white domain represents the cable's voids, here considered as filled with epoxy resin [35]

In addition, the current distribution implemented in the simulation are given by the CSM covered in subsection 2.1.6, although this model ignores the Meissner phase. [7, p. 23] Moreover, it is challenging to model the current paths taken in the MB at such low currents, in the superconducting state. Being far from the critical current density and without resistance, the current is not equally distributing, creating large variations in local field quality. To get a more accurate evaluation of inductance at 1 A, a model incorporating current distribution at these values must be included in the FEM model.

To study the magnetizing effects dependency on current, the same simulation has been performed at 1 kA, and $L$ as a function of $\omega$ has been plotted in Figure 5.25.

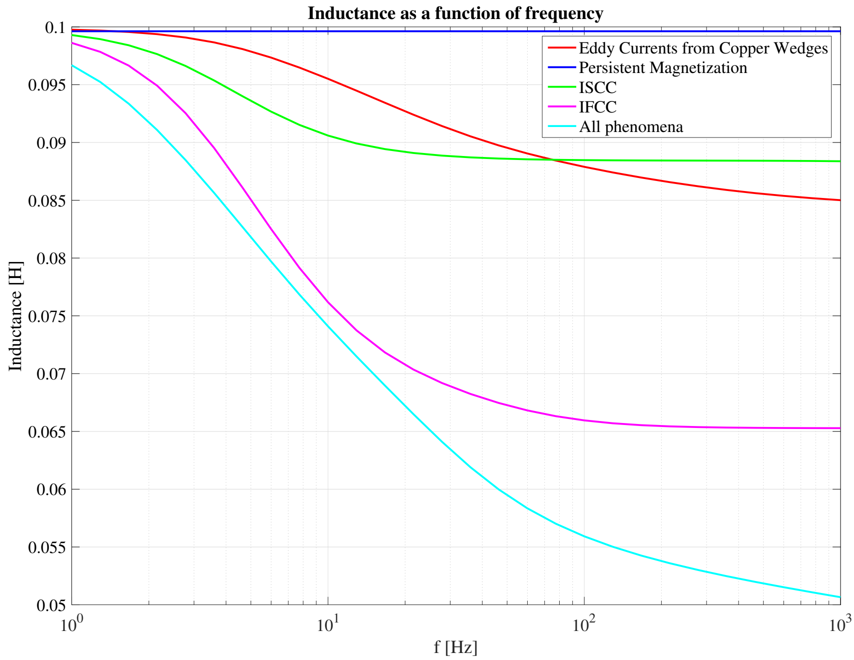


**Figure 5.25:** L vs Omega from COMSOL model of MB, isolating various effects to study contribution on magnetization at 1 $kA$

Here, in Figure 5.25 the effect of persistent magnetization drops drastically from the case of 1 A. As expected the effects of eddy currents in copper wedges, IFCC and ISCC stay the same with the same time constants. Due to weak persistent magnetization flux lines penetrate the coils and the magnetization effects superimpose for the combined simulation.

What we can conclude from these simulations, is that persistent magnetization is the largest contributor to the reduction of inductance in the Meissner phase. For 1 A at 2.15 Hz it accounts for 99.7 % of the decrease in inductance. Now that the discrepancy in inductance has been accounted for, the fitting of parameters will be conducted with an average inductance value and it will be assumed that this has a negligible effect on parameters.

In the light of results from Figure 5.23, there is a need to discuss the quality of results from fitting the transfer function of the double aperture impedance to measurements performed at around 1 A.

Chapter 6

# Results from fitting of MB parameters

*The fitting of the parameters $R_a$ and $k$ necessitated the study of the influence of the rest of the chain on single and double aperture measurements. Both of which have been conducted in a dipole magnet chain. It was concluded that the double aperture measurements contained the least influence from the rest of the chain. Furthermore, the frequency range of fitting was limited to under* 1 kHz. *Hence all the fits are based on double aperture measurements below* 1 kHz.

*With MB measurements available in a chain and stand-alone it is possible to deduce the influence of the rest of the chain on magnet measurements, through comparison. Simultaneously, an inherent challenge to fitting measurements to analytic transfer functions is highlighted. Hence the discrepancy in PSO fits will be discussed.*

*Next, data analysis is conducted on the 41 MB measurements from April 2017, all from the 'half chain measurement configuration'. Deviation from the mean of all measurements is studied for each MB. Based on this analysis, an approach to grouping magnets for common fits is devised according to this deviation.*

*From such groupings, a PSO-algorithm is utilized and the parameter fittings of $k$ and $R_a$ determined.*

## 6.1 Comparing measurements from stand-alone and chain

The comparison between stand-alone and chained MB measurements is presented in Figure 6.1.

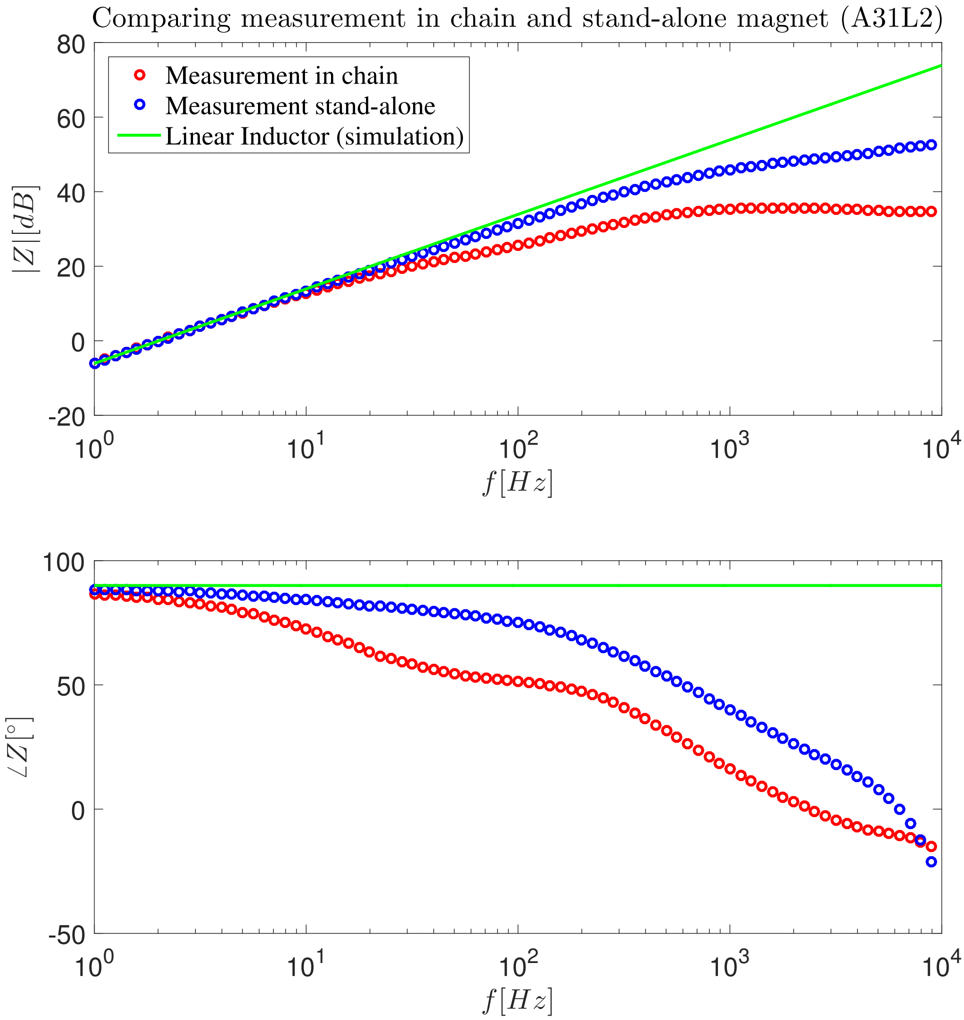


**Figure 6.1:** Comparison between stand-alone and chained measurements

An important distinction between the measurements, is that the stand-alone magnet was removed of its 100 Ω parallel resistor $R_p$. To account for this the stand-alone measurements were modified as if they had a parallel resistor

$$\mathbf{Z}_{\text{fit,meas}} = \frac{\mathbf{Z}_{\text{meas}} \cdot R_p}{\mathbf{Z}_{\text{meas}} + R_p}, \qquad \Omega \quad (6.1)$$

where $\mathbf{Z}_{\text{fit,meas}}$ is the modified measurement impedance equivalent to $Z_{tf,meas}$ in Equation 4.6, while $\mathbf{Z}_{\text{meas}}$ is the raw measurement impedance. The comparison between the modified stand-alone measurement and raw chained MB measurements is given in Figure 6.2

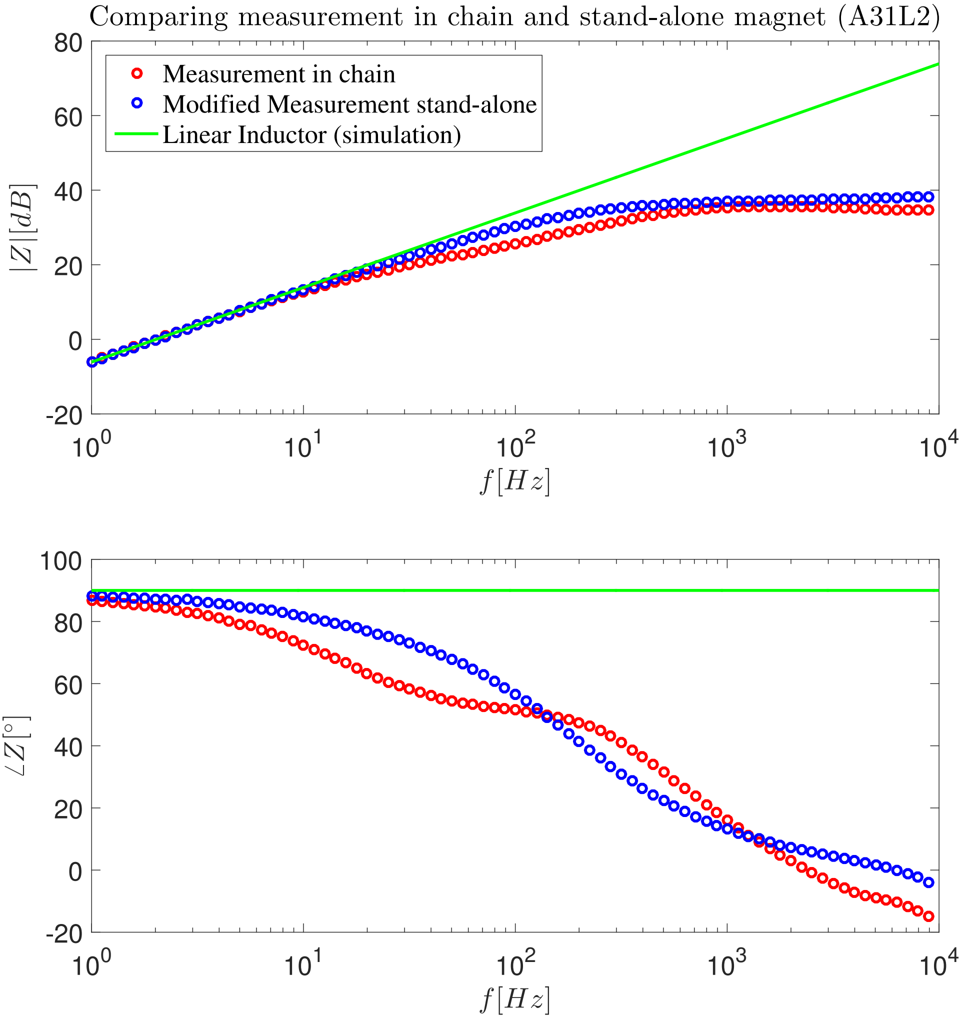


**Figure 6.2:** Comparison between stand-alone (modified) and chained measurements

From this comparison, the modified stand-alone measurement and raw chained MB measurements exhibit different time constants, in addition to a noticeable shift in phase. Hence a certain discrepancy in the parameter fit is expected.

## 6.2 Comparing fits from stand-alone and chain

12th of June 2017 there were measurements performed of a stand-alone MB magnet. From these measurements it is possible to compare the fitting of parameters stand-alone and chain, and to investigate how reliable measurements of magnets in chains are. The comparison between measurements, simulations and the analytical transfer function of the double aperture is given in Figure 6.3 for Magnet 122 in the chain. The linear inductor is for comparison.

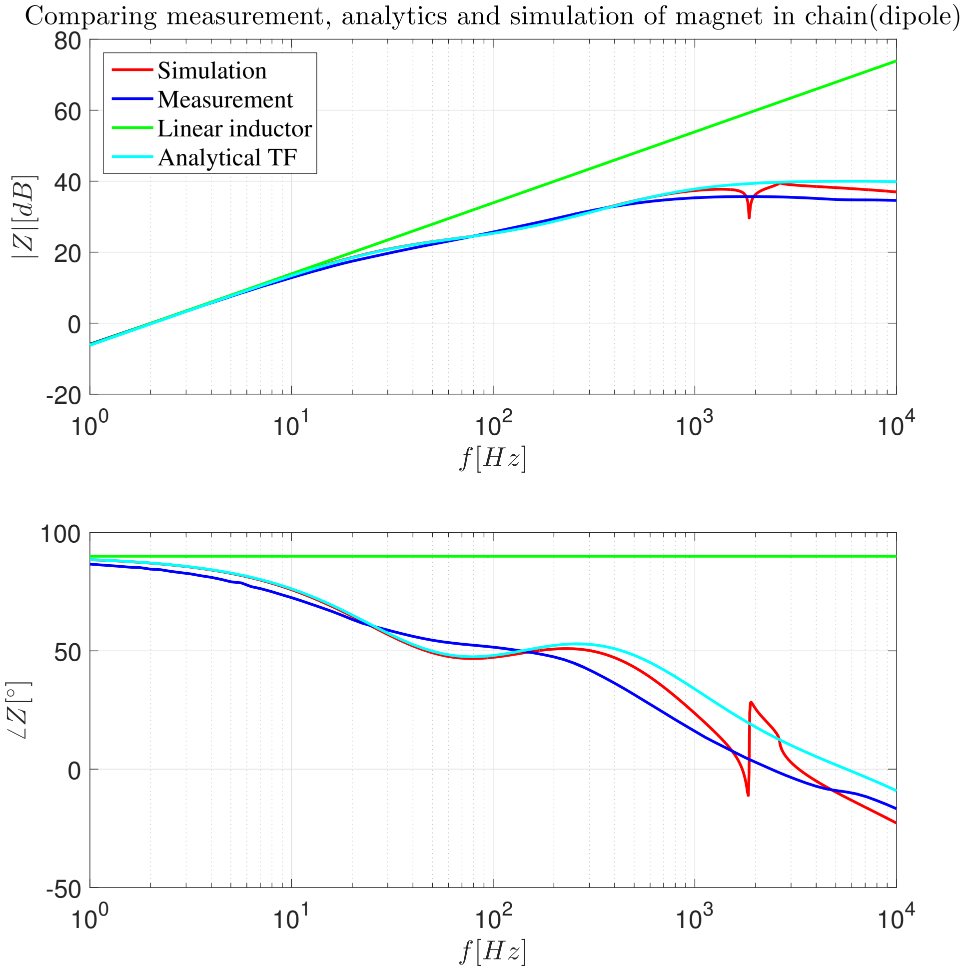


**Figure 6.3:** Comparison between measurements, simulations and analytical transfer function (chained double aperture)

Figure 6.3 shows a satisfactory overlap between simulation, measurement and analytical transfer function until around 600 Hz. While simulations exhibit a perturbation at high frequency, amplitude measurements stay below the 100 Ω-value of $R_p$ and its associated analytic transfer function. These are possible sources of error in the fitting.

With the removal of $R_p$ in mind, the stand-alone measurements were fitted under three different premises. The first was done implementing the transfer function of the MB without $R_p$. The result is shown in Figure 6.4. Here $k$=0.758 and $R_a$=47.93 Ω.

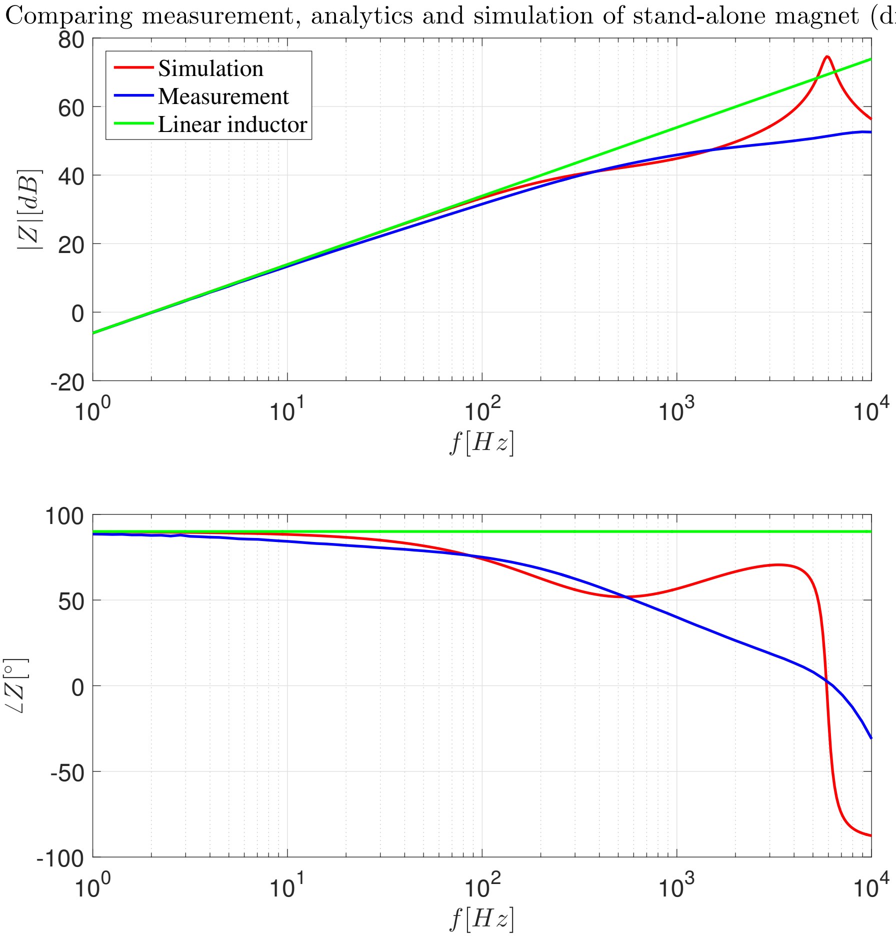


**Figure 6.4:** Comparison between measurements, simulations and analytical transfer function (stand-alone double aperture)

When fitting the same magnet in the chain it produced the fit $k$=0.727 $R_a$=6.41 Ω. Considering the large discrepancy in $R_a$, it was decided to modify the measurements such that it would have a parallel resistor, according to Equation 6.1.

The subsequent fit was $k$=0.669 and $R_a$=29.71 Ω., and the fit can be studied in Figure 6.5.

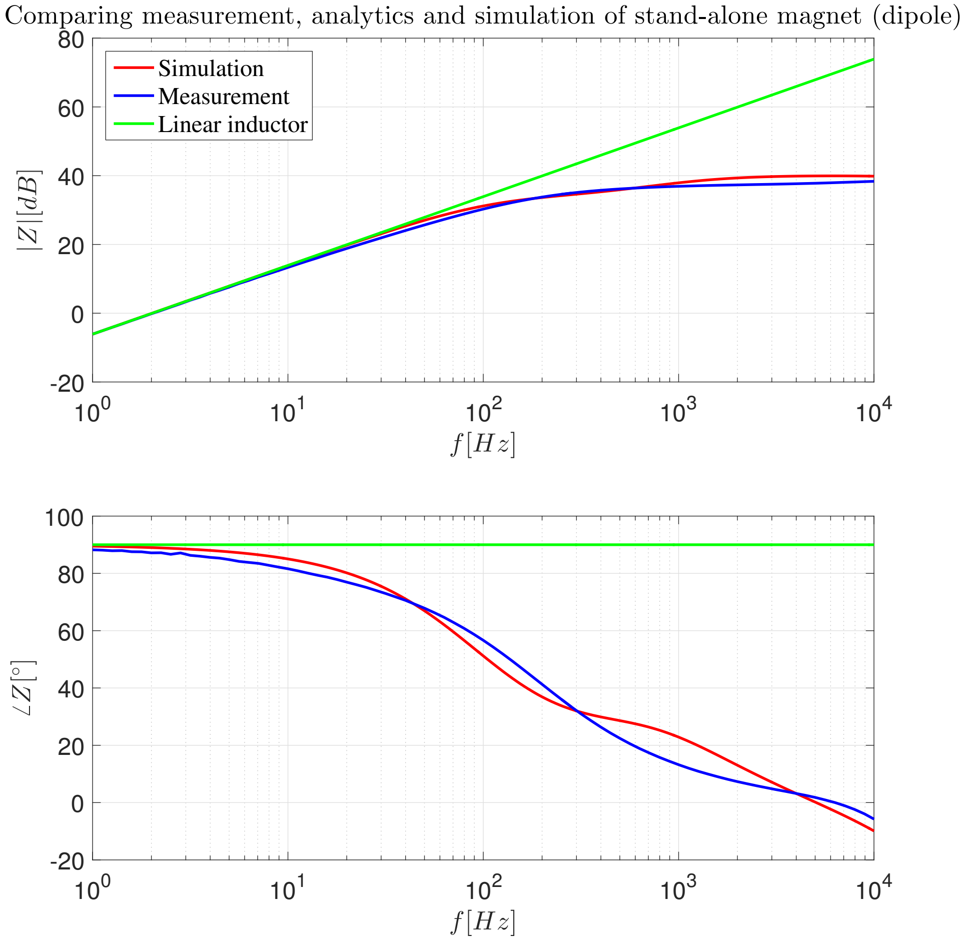


**Figure 6.5:** Comparison between modified measurements and simulations (stand-alone dipole)

Next, the same procedure of modifying the measurements were conducted, only now $R_a$ was constrained in the PSO-algorithm to be smaller than 11.11 Ω. The result can be viewed in Figure 6.6, with the PSO-fit of $k$=0.499 and $R_a$=11.11 Ω. A summary is given in Table 6.1

| Fitting | $k$ | $R_a$ [Ω] |
|---|---|---|
| Magnet 122 chained | 0.727 | 6.41 |
| Raw stand-alone | 0.758 | 47.93 |
| Modified stand-alone | 0.669 | 29.71 |
| Modified stand-alone with limited $R_a$ | 0.499 | 11.11 |

**Table 6.1:** Comparing of PSO-fits

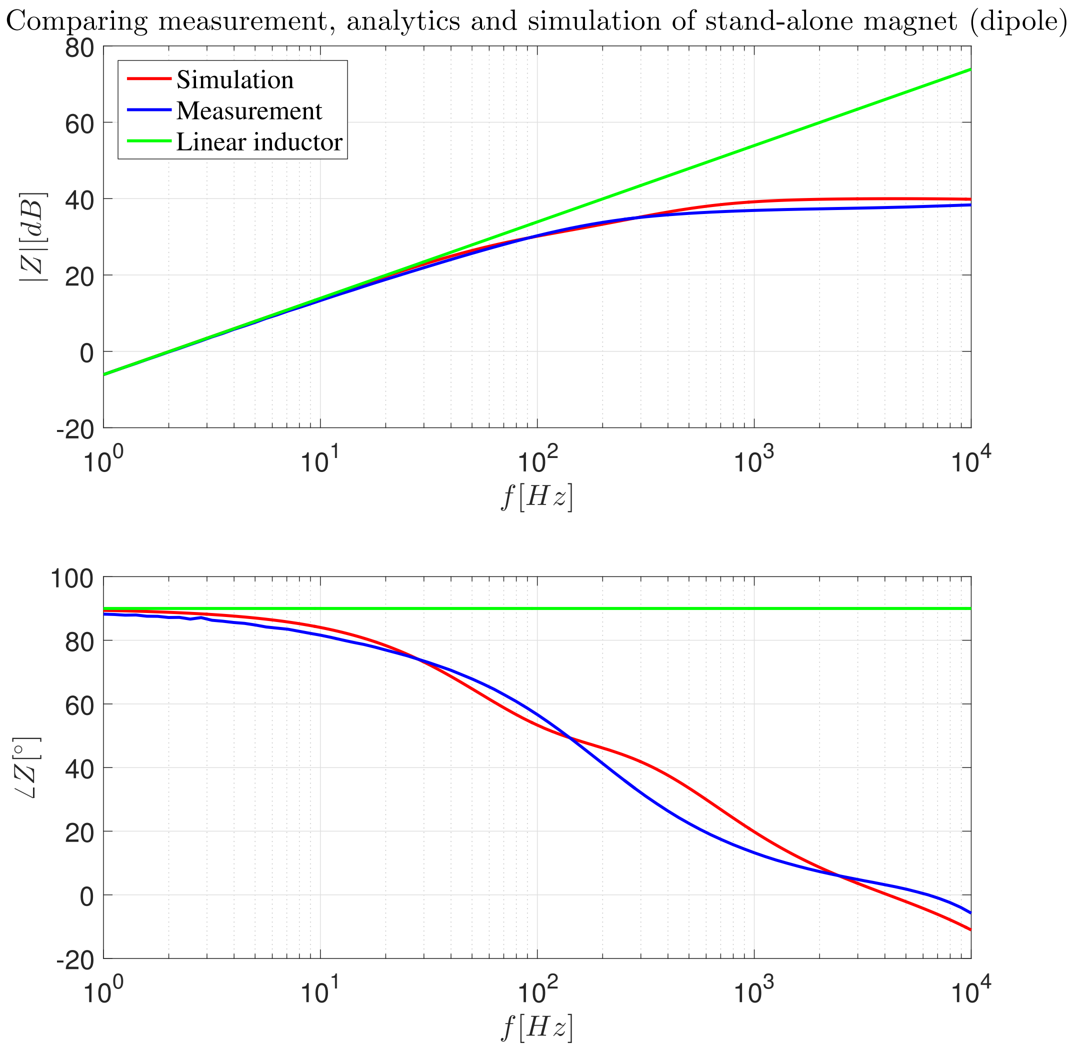


**Figure 6.6:** Comparison between measurements and simulations

Figure 6.3-Figure 6.6, illustrate the difficulty of fitting parameters to measurement. Moreover, the analytical impedance transfer function curves according to the power of $s$ in the expression, while measurements do not manage to curve in the same manner. Thus, the fit stays slightly above and slightly below during these curved parts. This creates big discrepancies in $R_a$, which defines the time constant at which the curve diverges from the linear slope of the linear inductor. Therefore, it is unsurprising that fitting parameters to measurements from a stand-alone and chain results in different values of parameters.

## 6.3 Results from Data Analysis

With the available FRMs of 41 dipoles from April 2017, these are compared in Figure 6.8. Here it is clear that all double apertures follow the same trend.

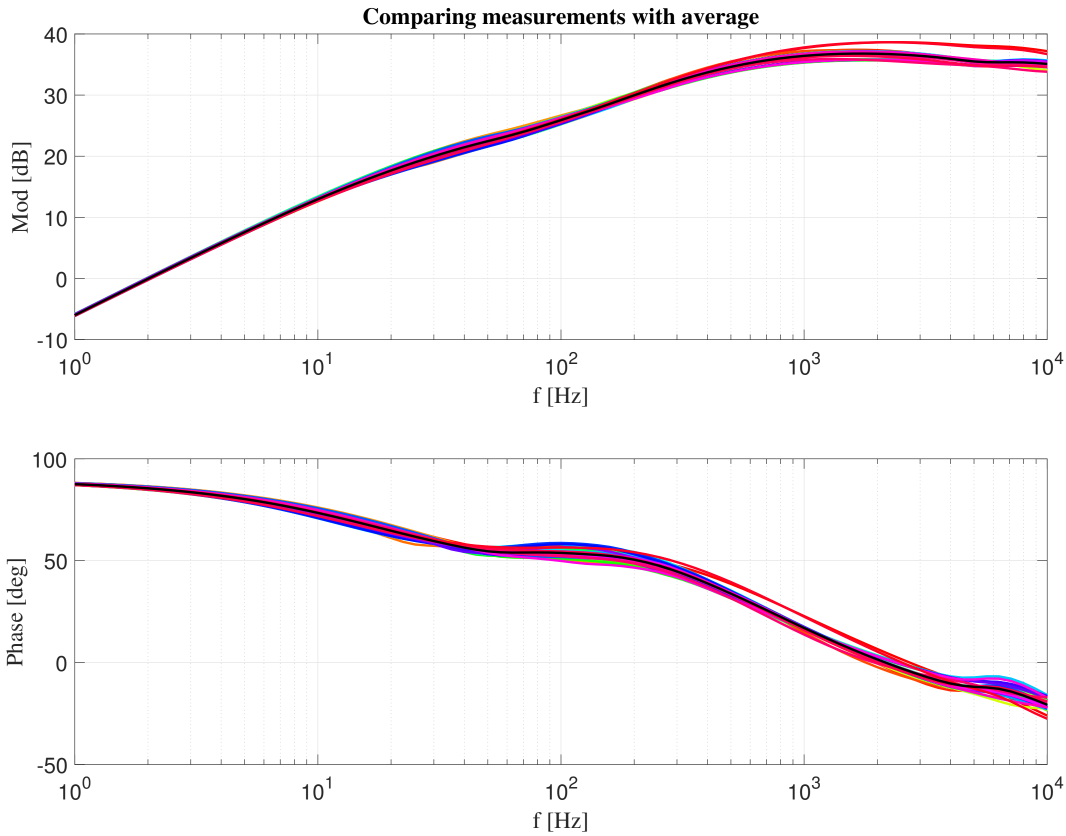


**Figure 6.7:** Comparison between MB measurements and average

In order to compare each double aperture's deviation from average impedance taken into account that these are complex values, the modulus of vector difference is calculated, according to

$$\mathbf{d}_\mathrm{z} = |\mathbf{Z}_\mathrm{n} - \mathbf{mean}_\mathrm{z}|, \qquad \Omega \quad (6.2)$$

where $\mathbf{Z}_\mathrm{n}$ equals the impedance of magnet of electrical number n, $\mathbf{mean}_\mathrm{z}$ is the average impedance per frequency and $\mathbf{d}_\mathrm{z}$ denotes the deviation from average impedance per frequency for a double aperture. With Equation 6.2 all deviation in modulus and phase condenses into one vector. The result is shown in Figure 6.8

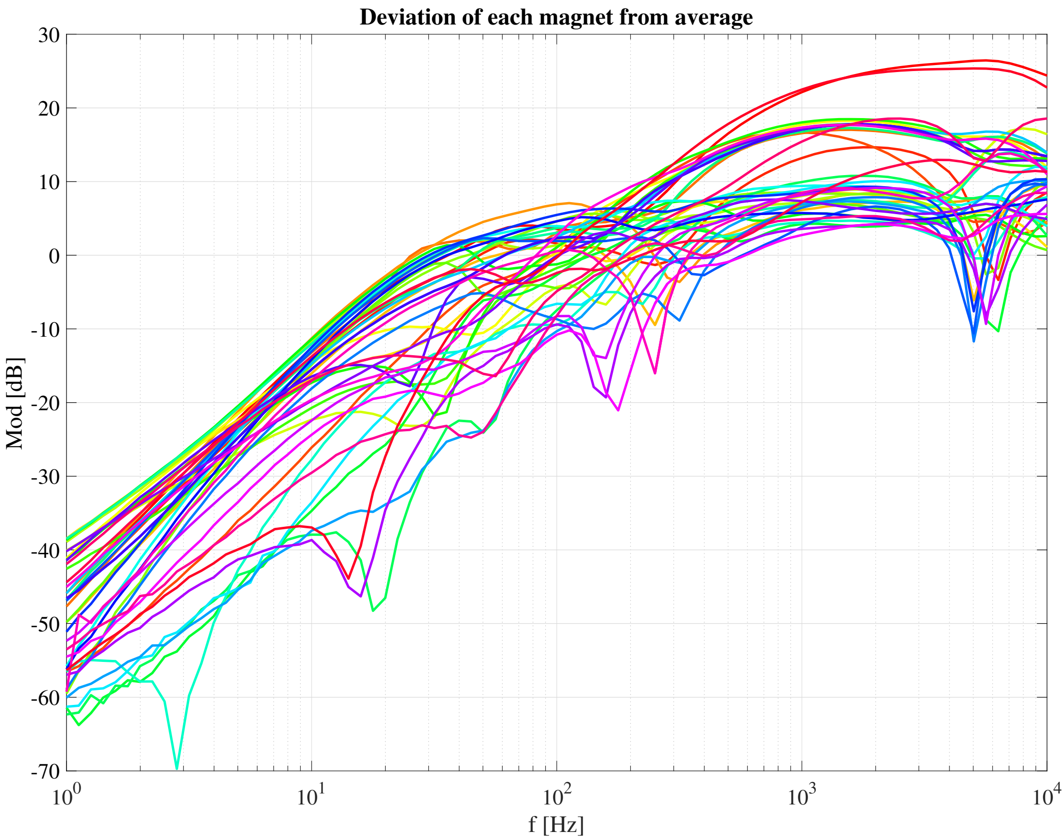


**Figure 6.8:** Deviation from average impedance per frequency for a double aperture

In Figure 6.8 the deviation increases with higher frequencies. The trend is due to different AC characteristics for different electrical positions and manufacturers, but similar inductance.

Subsequently, the average deviation from the magnet average across all frequencies has been compared and grouped according to their series number. The data points in Figure 6.9 of the same color are of the same series and thus manufacturer, as given in Table 4.2.

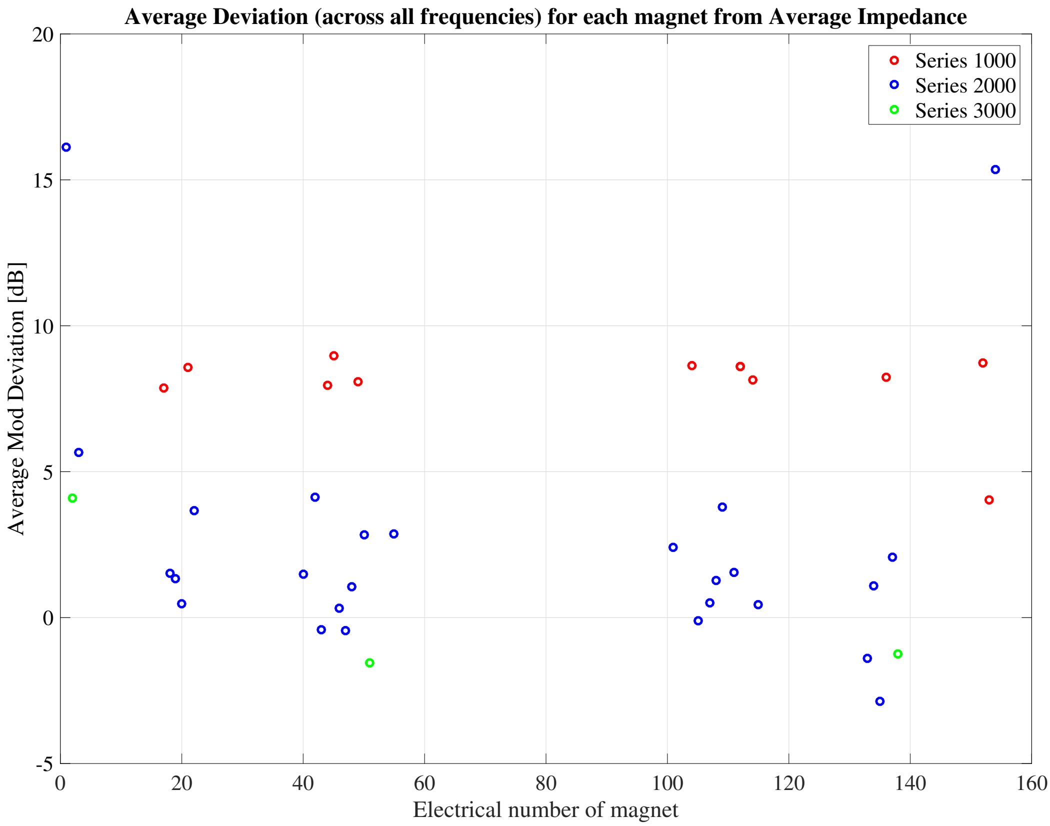


**Figure 6.9:** Average deviation from magnet average by electrical position

Ignoring the first and last magnet, which experience a large influence from the chain, there is a clear trend for series 1000 and 2000, where series 2000 has a smaller deviation from average than series 1000. There are too few measurements of series 3000 to say anything conclusive about any pattern in deviation from average impedance. Based on these observations it has been concluded to fit parameters according to series, for series 1000 and series 2000, except for magnet 1 and magnet 154. Magnet 1, Magnet 154 and all magnets of series 3000 will be fitted separately.

## 6.4 Results from PSO-fitting

Now that the approach to fitting has been determined, the PSO-fits can be performed. Only the fits of series 1000 and 2000 are presented graphically here in Figure 6.10-Figure 6.13, while the rest are depicted in Appendix B. A summary of all fits are given in Table 6.2

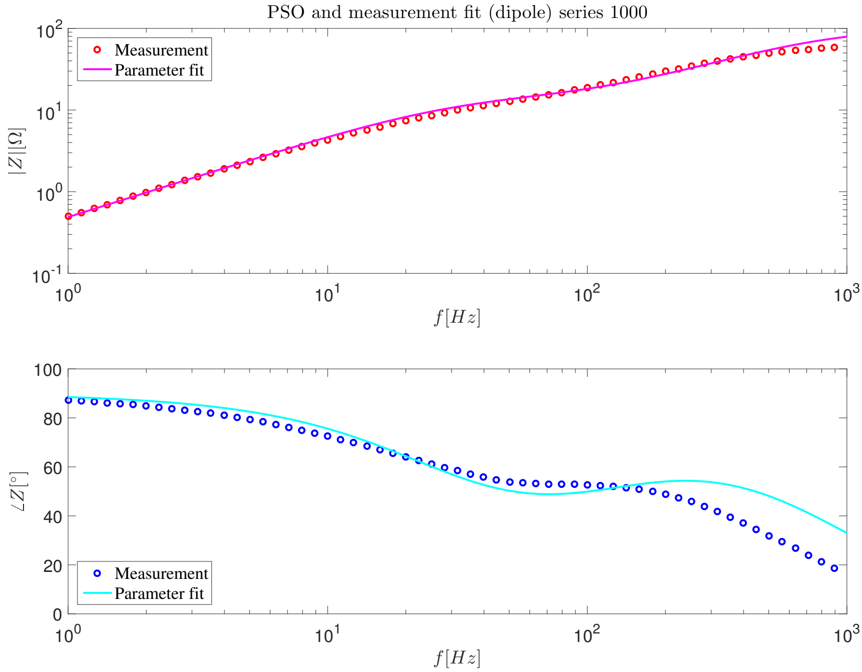


**Figure 6.10:** PSO fit of parameters for Series 1000

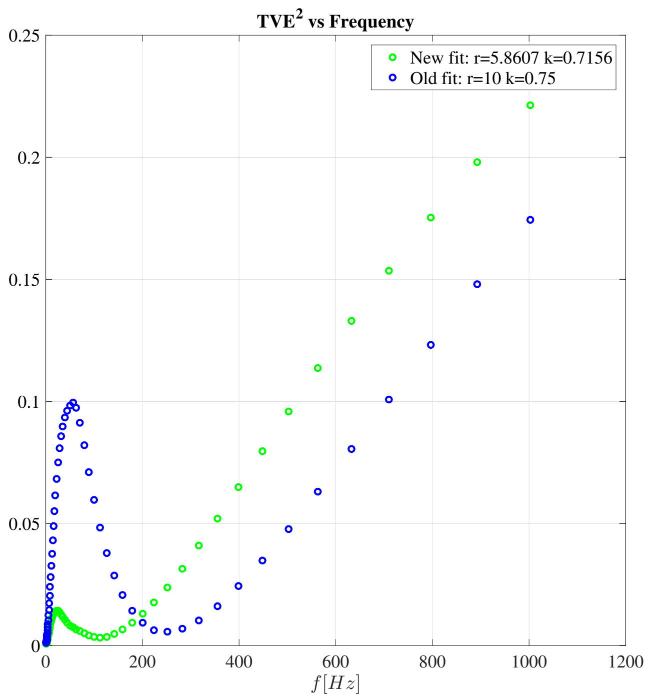


**Figure 6.11:** $TVE^2$ for PSO fit of Series 1000

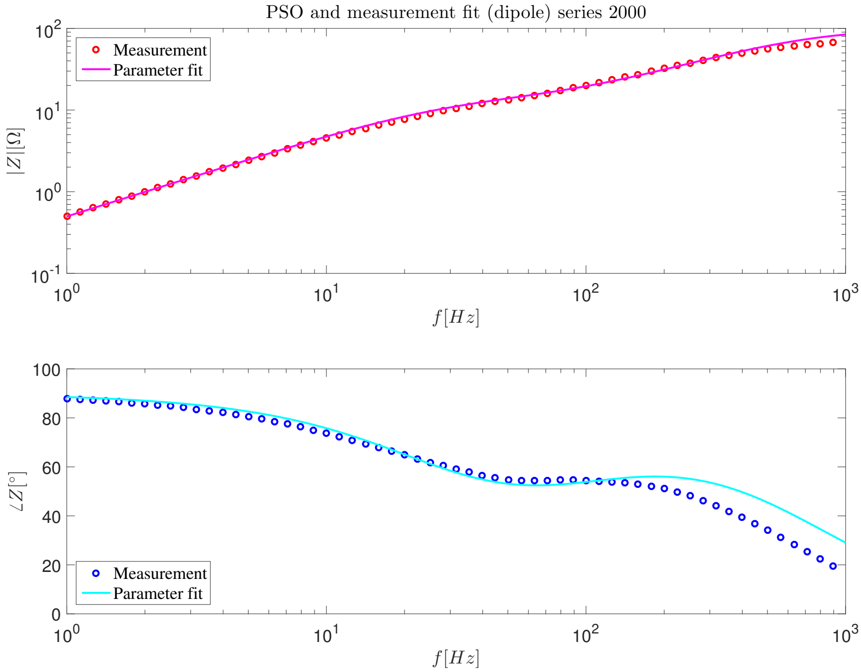


**Figure 6.12:** PSO fit of parameters for Series 2000

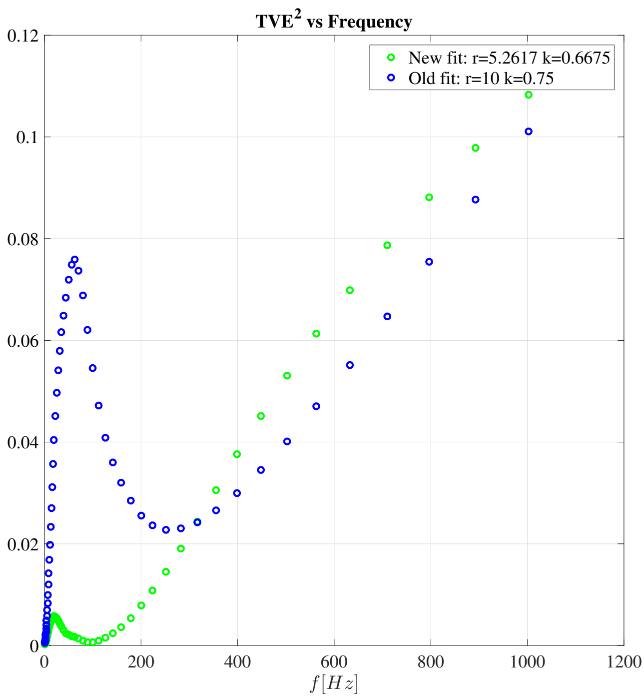


**Figure 6.13:** $TVE^2$ for PSO fit of Series 2000

In Figure 6.10 and Figure 6.12 the largest deviation from the fit is between $100 - 1000$ Hz in the phase, which is caused by the large difference in behaviour for the phase defined analytically and in measurements. See phase plot of Figure 6.3.

| Fitting | $k$ | $R_a$ [$\Omega$] | $\overline{TVE^2}$ [1] |
|---|---|---|---|
| Series 1000 | 0.7156 | 5.8607 | 0.0281 |
| Series 2000 | 0.6675 | 5.2617 | 0.0141 |
| Series 3000 | 0.6853 | 5.8002 | 0.0162 |
| Magnet 1 | 0.6539 | 5.8892 | 0.004 |
| Magnet 154 | 0.6452 | 4.4463 | 0.0044 |
| Magnet 2 | 0.6706 | 6.2058 | 0.0107 |
| Magnet 51 | 0.6917 | 5.4399 | 0.0192 |
| Magnet 138 | 0.6934 | 5.8035 | 0.0194 |
| All | 0.6895 | 5.6098 | 0.0191 |

**Table 6.2:** Results of PSO-fits

When looking at the fitting from Table 6.2 the values of $k$ and $R_a$ are relatively similar. As expected the fit of Magnet 1 and 154 differ largely in $R_a$ from the Series 2000 fit, even though they belong to this series, due to large influence from chain. Also, Magnet 51 differ in $R_a$ from its series fit, which is Series 3000. This discrepancy is attributed to the lack of double aperture measurements of Series 3000. Overall, this tells us that a sound approach to fitting has been chosen.

The old fit of $k$=0.75 and $R_a$=10 $\Omega$ had a $\overline{TVE^2}$ value of 0.0389. Thus all fits show at least a 30 % reduction in $\overline{TVE^2}$.

### 6.4.1 Testing for modified objective function

According to Figure 6.11 and Figure 6.13, $TVE^2$ is only reduced below $200 - 300$ Hz over a frequency range of 1 kHz of fitting. This is a clear effect of logarithmic spacing of measurements, creating a bias towards low frequencies. For the sake of testing the parameter fit and addressing this bias, the objective function has been modified such that it is the integrated TVE and not the mean, as given in Equation 4.10. The result is given in Table 6.3

| Fitting | $k$ | $R_a$ [$\Omega$] | $\int TVE d\omega$ |
|---|---|---|---|
| Series 1000 | 0.7685 | 17.0982 | 1.4418e+03 |
| Series 2000 | 0.6863 | 9.9919 | 1.1431e+03 |

**Table 6.3:** Results of PSO-fits with integrated TVE

[1] Mean of TVE$^2$

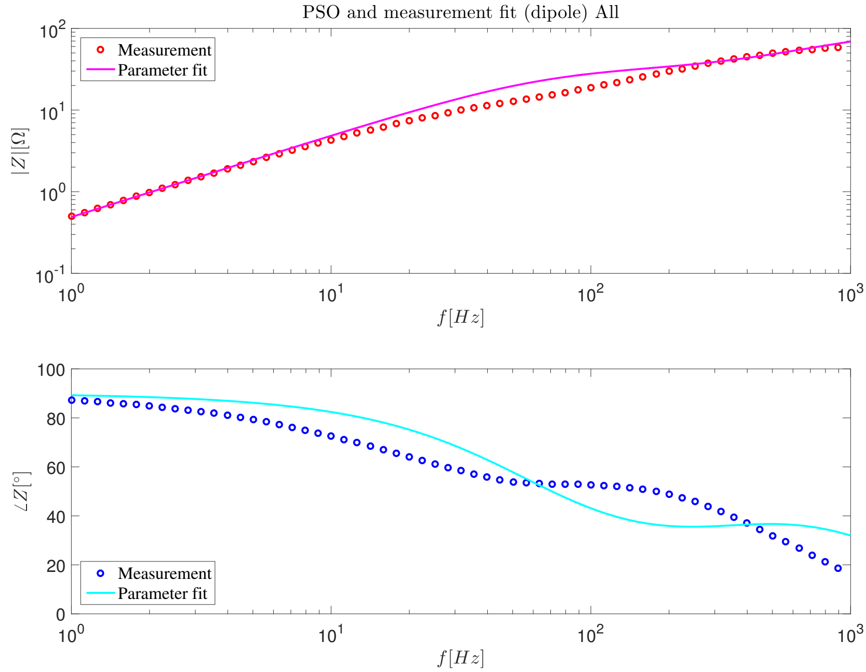


**Figure 6.14:** PSO fit of parameters for Series 1000 (integrated objective function)

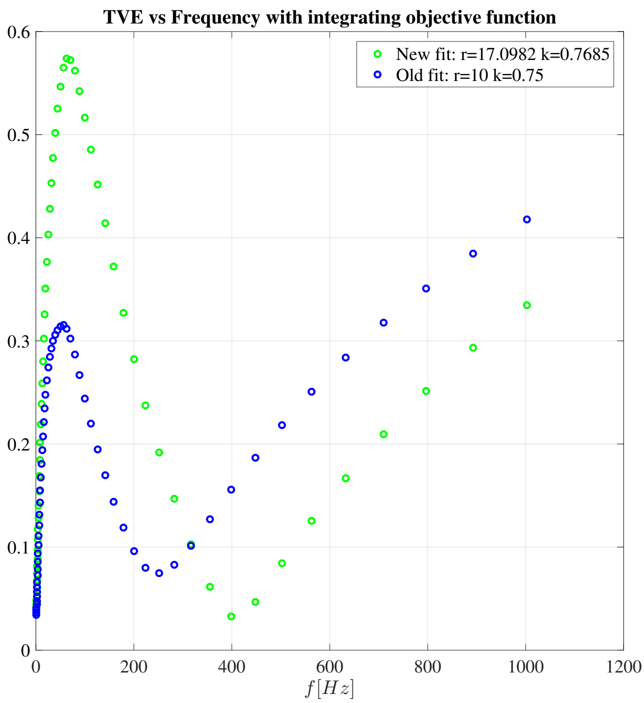


**Figure 6.15:** $TVE^2$ for PSO fit of Series 1000 (integrated objective function)

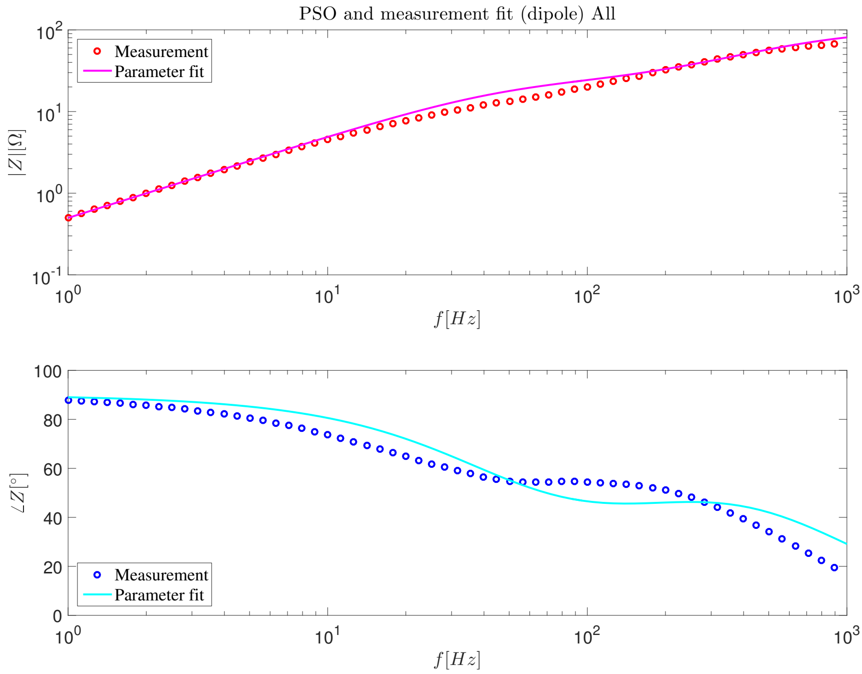


**Figure 6.16:** PSO fit of parameters for Series 2000 (integrated objective function)

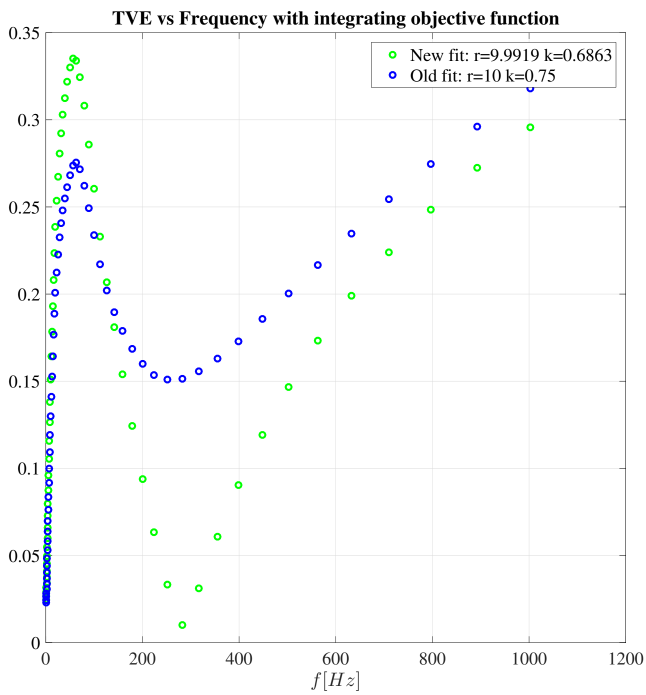


**Figure 6.17:** $TVE^2$ for PSO fit of Series 2000 (integrated objective function)

Indeed with the integrated TVE the range for which TVE is lower for the new fit over the present fit is increased. However, the fit is deteriorated for the frequency range $10 - 100$ Hz, which is the frequency range where AC characteristics of $R_a$ and $k$ are dominant. This implies a worse fit than for $\overline{TVE^2}$ as an objective function. With this test in modification of objective function, $\overline{TVE^2}$ is validated as the preferred objective function for PSO parameter fitting, despite the two objective function's error being incomparable numerically.

Chapter 7

# Discussion

*So far, this thesis has reached the aim of outlining a method to fit the analytic impedance transfer function to FRMs. In addition, this method is suitable for measurements performed in the dipole magnet chain. Together with Chapter 8, this chapter fulfills the second aim of the thesis, which is to evaluate the method outlined by focusing on limitations and pinpoint possible solutions to such limitations.*

## 7.1 Discussion on PSO parameter fit to measurements

This section discusses the most relevant points on parameter fitting using the PSO algorithm based on FRMs. These include evaluating measurement configurations, the PSO method itself. The influence of magnet series number and its electrical position on impedance measurements as well as the fitting approach chosen is also discussed. Lastly, the limitations of the present equivalent circuit model is presented.

### 7.1.1 Evaluation of measurement configuration

All the results presented in Chapter 6 are based on measurements from April 2017 which were achieved with a 'half chain configuration'. Simultaneously, the study from Figure 5.5 shows that the 'whole chain configuration' is better at limiting the influence of the chain on the measured MB. Since the difference in frequency is relatively small, a big discrepancy in measurements for the same double aperture is not expected. However, the exact difference is unknown, as the two measurement configurations have not been executed on the same double aperture. Furthermore, the 'half chain configuration' is faster to execute, provided that it is possible to disconnect the busbar at the mid-point of the chain, as each half chain can be measured in parallel. If there is a time constraint in performing measurements, as there usually is during technical stops in the LHC, increased quality can be sacrificed for obtaining more magnet measurements.

### 7.1.2 Evaluation of PSO method

An advantage of the PSO algorithm is that it is independent of the analytical expression and thus circuit. This makes it flexible to circuit modifications. However, the algorithm does not rely on physical laws and therefore it might produce invalid results. By enforcing limits to the upper and lower bounds of the parameters, the physical limitations of the circuit will be restored. Since the PSO algorithm is stochastic it gives slightly different results each run, that have a considerable influence on the value of the objective function. Hence it was necessary to loop through the algorithm multiple times to achieve a minimal value, and thus achieving confidence of a suitable fit.

When utilizing the PSO algorithm, it is necessary to consider which types of errors are to be minimized, and define the objective function accordingly. For example, it could be more important to obtain a good fit for a certain frequency range, high or low, or it could be a priority to eliminate large errors. For this case, it was desirable to reduce large errors and fit the range under 1 kHz , and therefore the mean of $TVE^2$ was chosen as an initial objective function. With logarithmic spacing of measurements, there is a clear bias towards low frequencies in this definition. To reduce this bias the objective function was altered to an integration of the TVE. Compared to the first implementation, this gives a worse fit at $10 - 100$ Hz where the most important AC characteristics are dominant. To more accurately estimate $R_a$ and $k$, the mean of $TVE^2$ was concluded to be the preferred objective function. A limitation here, is that there is no way to directly compare objective functions when they are defined differently. It is only possible to look at the outcome of the fit under different implementations of the objective function, and visually evaluate the improvement.

### 7.1.3 Evaluation of influence on impedance measurements from series number and electrical position

When measurements are performed in a magnet chain, there are several sources of influence that are not encompassed by the analytical expression of the double aperture. These effects include magnet series number and electrical position. Moreover, Figure 6.9 and Figure 5.6 illustrate how series number and electrical position influence double aperture impedance in a chain respectively. Of these two, the series number has the biggest influence on impedance double aperture measurements, except for the first and last electrically positioned double aperture in the magnet chain. Also, the electrical position was found to have negligible influence on measurements not positioned first or last.

### 7.1.4 Evaluation of fitting approach

From Figure 6.7, the measurements of 41 MBs are very similar, with the largest discrepancy from average being 27 %. Furthermore, the deviation from the average impedance at every frequency has been evaluated for each magnet, according to Equation 6.2. Based on an averaged deviation over all frequencies a grouping of magnets for common fitting was decided. Here, a clear pattern has been observed for series 1000 and 2000, implying that the series number effects AC characteristics and thus the double aperture impedance.

One can imagine the data analysis of the deviation from all measurements averaged at every frequency, being performed with a different reference point. For example a more generic analytical transfer function or even a constant. The averaged deviation would still show the same pattern of grouping. Thus there is a high level of confidence in the result.

### 7.1.5 Limitations to the present equivalent circuit model

Overall, there is an inherent challenge to fitting parameters, whether it is from chained or stand-alone measurements. This is due to analytical transfer functions, expressed in the frequency domain, curve in a manner that the measurements do not follow. Figure 7.1 shows the comparison between measurements and its associated fitted analytic transfer function for the appropriate frequency range.

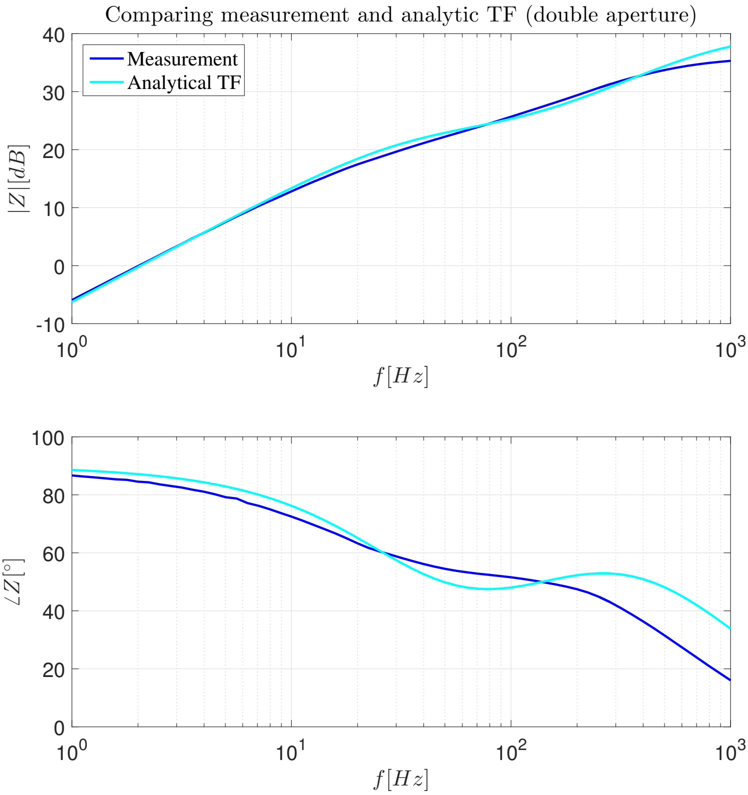


**Figure 7.1:** Comparison between measurements and fitted analytic TF (double aperture)

As can be seen in Figure 7.1 this results in the impedance of the fitted analytic transfer function for some frequencies to stay above and sometime below measurements. For reasons discussed in section 7.2, the kink associated with IFCL becomes more pronounced at higher current levels. Thus, this is expected to be less of an issue for higher current level measurements.

The fitting of the MB assumes it can be represented as an equivalent circuit, although the parameter $C$ refers to a distributed capacitance of a parasitic nature and not a physical capacitor of a classical RLC circuit. Due to this limitation in the model, perturbations are observed at high frequencies that are not present in measurement. See Figure 5.7.

With some amplitude maximums values just above 60 Ω, none of the measurement amplitudes reached the 100 Ω-value of $R_p$ in Figure 6.3. This is startling considering that this resistor only has a ±10% tolerance. Possible reasons include the distributed capacitance being modelled as a lumped element, unmodelled parasitic effects that become dominant around 1 kHz or influences by the measurement device. The two first reasons seem the most likely as impedance in the measurement device are accounted for in the measurement data presented in this report.

## 7.2 Implications from low inductance value study on parameter fitting

Through COMSOL simulations of magnetization effects in the MB, insight has been gained into the non-linearities of the transfer function of the MB impedance created by the Meissner phase. For the simulation at 1 A, presented in Figure 5.23, the magnetization effect of IFCC is suppressed. In reality, not all flux will be expelled by persistent magnetization due to normal conducting regions in the cable, though it will be considerably damped at 1 A. Moreover, $R_a$ is inversely proportional to the time constant, while $k$ is proportional to IFCL. This means that fitting FRMs at 1 A will be inaccurate compared to operating point conditions.

On the other hand, performing FRMs at operating conditions on an MB is challenging for practical reasons. One challenge is to obtain a device that can supply a 12 kA DC signal and provide an AC ripple of 1 A to a reasonable level of accuracy. In addition, there is a risk of triggering the QPS at high frequency. Thus, the most feasible solution would be to conduct the measurements at an operating point above the Meissner phase, which is approximately above 0.18 T for Nb-Ti. As the magnetic flux density is not uniform throughout the magnet, it should be determined at which current level most of the magnet, for example 80 %, is out of the Meissner phase. At such a current level, it is certain that persistent magnetization has a negligible influence, and the other magnetizing discussed effects would superimpose with the same relative magnitude and time constants as for the operating point. See Figure 5.25. However, magnetization from saturation in the iron yoke would differ from the operating point.

Chapter 8

# Conclusion

*In the Large Hadron Collider counter-circulating beams of hadrons collide, guided by the magnetic field of 1232 Main Dipole Magnets. These magnets are connected in chains of 154 Main Dipole Magnets. For the purpose of simulations of failure scenarios and the quench protection system a Main Dipole Magnet is often represented as an equivalent circuit composed of lumped elements. The parameters of this circuit need to be accurately determined, ensuring reliable results.*

*The starting point for this research was Frequency Response Measurements of Main Dipole Magnet impedance from the dipole magnet chain of Sector 1-2 from November 2016 and April 2017. For reliable fault analysis and simulations of frequency dependent phenomena it is necessary to fit the parameter* $L$, $R_a$, $k$ *and* $C$ *from the analytic transfer function of the Main Dipole Magnet impedance to these measurements.*

*The parameter* $C$*, which represents the parasitic capacitance to ground was determined using the Finite Element Method in COMSOL. Inductance* $L$*, describing the inductive effects of the equivalent model, was extracted analytically from the cross-over frequency of measurements. Inductance values were surprisingly low, and subsequent studies, through COMSOL simulations, attributed this to persistent magnetization.*

*Last but not least, the Particle Swarm Optimization was performed to determine* $R_a$ *and* $k$*, which account for Inter Filament Coupling Loss. Particle Swarm Optimization is an iterative algorithm inspired by the movement of flocks of birds. Several considerations had to be made with this method. Firstly, it has to be determined if aperture or double aperture measurements should be utilized for fitting. Since double aperture measurements proved to contain the least influence from the rest of the chain, this was chosen. Secondly, measurement deviations from average values were analyzed to seek patterns. It was found that there was a pattern in the deviation according to series number. Thus it was decided to group fits according to series.*

At the beginning of this thesis the following research questions were formulated

1. Is it possible to accurately calculate parasitic capacitance to ground with a Finite Element Method approach and thus obtain the parameter $C$?
2. Is the Particle Swarm Optimization algorithm an adequate method to fit Main Dipole Magnet parameters from analytic transfer functions of impedance to Frequency Response Measurements?
   - In particular, is the method suitable for fitting Main Dipole Magnet parameters to Frequency Response Measurements performed while connected to the dipole magnet chain?
3. What requirements should be specified of measurements designed for parameter fitting?

Comparing analytical and experimental results with results from the COMSOL simulation it is clear that it is possible to calculate parasitic capacitance to ground using Finite Element Method. When doing so it is essential to equalize equipotential metallic terminals to mitigate their influence. Although there are analytical formulations that can accurately calculate parasitic capacitance to ground, Finite Element Method automates this procedure and makes it more efficient for complex models. Another important point is that the insulation shrinks by 10 % when cooled down from room to cryogenic temperatures, which influences the capacitance. Therefore, any analysis based on room temperature analysis should be scaled. The results from this analysis serve as a proof of concept for calculating parasitic capacitance to ground using Finite Element Method.

The Particle Swarm Optimization algorithm is flexible and can be performed on any equivalent circuit, provided its impedance has an analytic transfer function formulation. In other words, as the equivalent model of the Main Dipole Magnet is updated and modified its parameters can still be obtained through Particle Swarm Optimization. Despite inherent challenges to fitting parameters from measurements, this thesis shows promising results as the Particle Swarm Optimization algorithm produce similar enough results for chained and stand-alone Main Dipole Magnet measurements, where $k$=0.73 $R_a$=6.4 Ω for stand-alone measurements and $k$=0.67 and $R_a$=29.7 1 Ω for chained measurements. Following the recommendations for measurements in subsection 8.1.2 these discrepancies will most likely be decreased further.

Both series number and electrical position, influence the impedance of the Main Dipole Magnet. The former is an inherent feature of the magnet, and means that Particle Swarm Optimization fittings of magnets can be grouped according to series number, if they are of the 1000 or 2000 series. Since there were only 3 magnet measurements of series 3000, the pattern of this series is inconclusive and therefore fitted individually. The Main Dipole Magnet impedance dependence on electrical position is due to the influence of chain impedance on magnet measurements. This is only relevant for the magnets on each end of the dipole magnet chain. Thus, these fits should be ignored and instead its series fit should be applied to these magnets.

With these consideration, I conclude that the Particle Swarm Optimization algorithm is indeed an adequate method to fit Main Dipole Magnet parameters from analytic transfer functions of impedance to Frequency Response Measurements, even for Main Dipole Magnet measurements performed in the dipole magnet chain. The method for fitting parameters outlined in this thesis can be seen as a template for determining parameters of accelerator magnets in general, provided that they have an analytic transfer function formulation for impedance.

In light of results from subsection 5.5.3, it is clear that the magnetizing effects of Inter Strand Coupling Currents and Inter Filament Coupling Currents are suppressed by persistent magnetization at 1 A. At 1 kA results exhibit a superposition of all magnetizing effects with the expected time constants of around 30 Hz as shown in Figure 5.25. This implies that Frequency Response Measurements of double aperture impedance should be performed outside of the Meissner phase in order to recreate the AC characteristics at the operating point of the Main Dipole Magnet. As mentioned in section 5.2, the 'whole chain configuration' is preferable to the 'half chain' one, and the dipole magnet chain should be grounded at each end of the chain, while the generator is left floating.

## 8.1 Recommendations for Future Work

The combination of further simulations and measurements will aid the understanding of the AC behavior of the Main Dipole Magnet.

### 8.1.1 Recommendations for Simulations

From the two COMSOL models presented in this thesis, there are plenty of opportunities to refine and update these models for more accuracy and new studies.

**Modified Finite Element Method model to accurately quantify persistent magnetization in the Meissner phase** The Finite Element Method model presented in subsection 5.5.3, homogenizes physical laws over each half-turn, resulting in an overestimation of persistent magnetization. The Modified Finite Element Method model would capture effects within a half-turn, such that flux lines are not completely expelled like in the present simulation. However, this would be a detailed and thus computationally heavy simulation. Such that if there exists theories that describe current distribution in the cable in the Meissner phase that could simplify the model it should be prioritized.

**Finite Element Method approach to quantifying inter-turn parasitic capacitance** With more work on the Finite Element Method model presented in Chapter 3 would enable the evaluation inter-turn parasitic capacitance. This will aid understanding of behaviour above 10 kHz.

**Integrated Finite Element Method model with electrodynamic and magnetodynamic effects** As discussed in section 5.3, representing the Main Dipole Magnet with an equivalent circuit, composed of lumped elements, is not able to capture behaviour above 1 kHz, due to parasitic capacitance being distributed throughout the magnet. A Finite Element Method model combining electrodynamic and magnetodynamic effects to characterize the impedance through a frequency sweep, would aid in the development of an equivalent circuit capturing behaviour above 1 kHz.

### 8.1.2 Recommendations for Future Measurements

For future developments of determining Main Dipole Magnet parameters and expanding the equivalent circuit of the Main Dipole Magnet, it is indispensable to have measurements available to validate results from simulations. These measurements should be Frequency Response Measurements of the double aperture impedance for high enough current, such that the operation is not in the Meissner phase. For example, there could be a DC signal of about 500 A with a small added AC signal for the sweep. The limitation here is with the power converter and ensuring accuracy when supplying a 12 kA DC signal with an AC ripple of 1 A. These measurements would provide reliable data of the AC characteristic of the Main Dipole Magnets that are more feasible practically to obtain than at operating point.

# Bibliography


[1] CERN. *About CERN*. Accessed: 2017-07-09. URL: https://www.comsol.com/blogs/brief-introduction-weak-form/.

[2] CERN. *LHC MACHINE OUTREACH*. Accessed: 2016-11-29. URL: http://lhc-machine-outreach.web.cern.ch/lhc-machine-outreach/.

[3] Andrzej Siemko. *Safeguarding the superconducting magnets*. Accessed: 2016-11-29. URL: http://cerncourier.com/cws/article/cern/54383.

[4] CERN. *faq LHC: the guide*. Accessed: 2016-12-14. URL: https://cds.cern.ch/record/1092437/files/CERN-Brochure-2008-001-Eng.pdf.

[5] Martin N. Wilson. *Superconducting magnets*. Monographs on Cryogenics 2. Clarendon Press, 1983. ISBN: 0198548052.

[6] CERN. *Superconductivity*. Accessed: 2016-11-29. URL: https://home.cern/about/engineering/superconductivity.

[7] Karl-Hubert Mess, Siegfried Wolff, and Peter Schmüser. *Superconducting Accelerator Magnets*. World Scientific Publishing CO. Pte. Ltd., 1996. ISBN: 978-981-02-2790-6.

[8] J. File and R. G. Mills. "Observation of Persistent Current in a Superconducting Solenoid". In: *Phys. Rev. Lett.* 10 (3 1963), pp. 93–96. DOI: 10.1103/PhysRevLett.10.93.

[9] Yukikazu Iwasa. *Case studies in superconducting magnets : design and operational issues*. Selected topics in superconductivity. Plenum Press, 1994. ISBN: 0306448815. DOI: 10.1007/b115039.

[10] C. Kittel. *Introduction to Solid State Physics, 8th ed.* Wiley, 2004. ISBN: 9780471415268.

[11] Jonas Blomberg Ghini. "SPECIALIZATION REPORT WINTER 2015: PROTECTING THE SUPERCONDUCTING 11T HI–LUMI LHC DIPOLE WITH THE NEW COUPLING–LOSS INDUCED QUENCH PROTECTION SYSTEM". In: (2015). DOI: https://twiki.cern.ch/twiki/pub/TEMPEPE/SectionThesis/SpecializationReport_GHINI_2015.pdf.

[12] Kozo Osamura. *Composite superconductors*. Vol. 3. CRC Press, 1993.

[13] CERN. *LHC Machine Outreach: Super conducting cable*. Accessed: 2016-11-29. URL: http://lhc-machine-outreach.web.cern.ch/lhc-machine-outreach/components/cable.htm.

[14] Martin N. Wilson. "NbTi superconductors with low ac loss: A review". In: *Cryogenics* 48.7–8 (2008). Special Issue: Low-Tc Superconducting Materials, pp. 381 –395. ISSN: 0011-2275. DOI: http://dx.doi.org/10.1016/j.cryogenics.2008.04.008. URL: http://www.sciencedirect.com/science/article/pii/S0011227508000507.

[15] Arjan Peter Verweij. *Electrodynamics of Superconducting Cables in Accelerator Magnets*. University of Twente, 1995. ISBN: 90–9008555–6.

[16] O. Brüning, P. Collier, P. Lebrun, S. Myers, R. Ostojic, J. Poole, and P. Proudlock. *LHC Design Report: Volume 1 The LHC Main Ring*. CERN - Scientific Information Service, 2004. ISBN: 9290832240.

[17] A.P. Verweij H H J ten Kate Ravaioli Emmanuele. *CLIQ. A new quench protection technology for superconducting magnets*. University of Twente, 1984. ISBN: 9789036539081.

[18] Stephan Russenschuck. *Field Computation for Accelerator Magnets*. WILEY-VCH Verlag GmbH & Co. KGaA, 2010. ISBN: 978-3-527-40769-9.

[19] E. Ravaioli, B. Auchmann, and A. P. Verweij. "Fast Method to Quantify the Collective Magnetization in Superconducting Magnets". In: *IEEE Transactions on Applied Superconductivity* 23.3 (2013), pp. 4700204–4700204. ISSN: 1051-8223. DOI: 10.1109/TASC.2012.2227649.

[20] S. Russenschuck. *Field Computation for Accelerator Magnets: Analytical and Numerical Methods for Electromagnetic Design and Optimization*. Wiley, 2011. ISBN: 9783527635474. URL: https://books.google.ch/books?id=tA4VxZvoiJUC.

[21] Maury Tigner Frank Zimmermann Alexander Wu Chao Karl Hubert Mess. *Handbook of accelerator physics and engineering, 2nd ed.* World Scientific Publishing CO. Pte. Ltd., 2013. ISBN: 978-81-7758-519-3.

[22] K. M. Smedley and R. E. Shafer. "Experimental determination of electrical characteristics and circuit models of superconducting dipole magnets". In: *IEEE Transactions on Magnetics* 30.5 (1994), pp. 2708–2712. ISSN: 0018-9464. DOI: 10.1109/20.312510.

[23] E. Ravaioli, K. Dahlerup-Petersen, F. Formenti, J. Steckert, H. Thiesen, and A. Verweij. "Modeling of the voltage waves in the LHC main dipole circuits". In: *IEEE Transactions on Applied Superconductivity* 22.3 (2012), pp. 9002704 –9002704. DOI: http://ieeexplore.ieee.org/document/6082398/.

[24] E. Ravaioli et al. "Impact of the voltage transients after a fast power abort on the quench detection system in the LHC main dipole chain". In: *IEEE Transactions on Applied Superconductivity* 22.3 (2012), pp. 9002504 –9002504. DOI: http://ieeexplore.ieee.org/abstract/document/6126021/.

[25] J. Skaar. *Elektromagnetisme*. Department of Electronic Systems at Norwegian University of Science and Technology, 2013.

[26] E.J. Rothwell and M.J. Cloud. *Electromagnetics, Second Edition*. Electrical Engineering Textbook Series. CRC Press, 2008. ISBN: 9781420064483. URL: `https://books.google.ch/books?id=7AHLBQAAQBAJ`.

[27] COMSOL AB. "COMSOL Multiphysics reference guide: The Heat Transfer Interfaces". In: (2015).

[28] Inc. Chip One Stop. *Relative permittivity*. 2015. URL: `http://www.chip1stop.com/web/VNM/en/tutorialContents.do?page=008` (visited on 06/29/2015).

[29] K. Dahlerup and F. Schmidt. "Impedance Measurements and Modeling of the Ten Meter Prototype LHC Dipole Magnet". In: (1995). LHC Project Note. DOI: `http://cds.cern.ch/record/692033/files/project-note-11.pdf`.

[30] Dr. Amalia Ballarino (AT-MEI-SD CERN). *HTS at CERN: Introduction*. Accessed: 2016-12-05. URL: `http://at-mel-cf.web.cern.ch/at-mel-cf/html/index.htm`.

[31] Sara Ambjørndalen. "Multi-scale Analysis of Electro-Thermal Transients in the LHC Main Dipole Circuit". In: (2016). Specialization Report at Norwegian University of Science and Technology.

[32] Mateusz Jakub Bednarek. "Investigation of A31L2 dipole problem – Local Transfer Function Measurement". In: (2016). See appendix H of 'Multi-scale Analysis of Electro-Thermal Transients in the LHC Main Dipole Circuit'.

[33] Inc The MathWorks. "Matlab Documentation". In: (2015).

[34] E. Ravaioli, B. Auchmann, and A. P. Verweij. "Fast Method to Quantify the Collective Magnetization in Superconducting Magnets". In: *IEEE Transactions on Applied Superconductivity* 23.3 (2013), pp. 4700204–4700204. ISSN: 1051-8223. DOI: `10.1109/TASC.2012.2227649`.

[35] Lorenzo Bortot et al. "A 2-D Finite-Element Model for Electro-Thermal Transients in Accelerator Magnets". In: *Paper submitted in 21st International Conference on the Computation of Electromagnetic Fields, (June 18-22, 2017, Daejeon, Korea)* (). This paper is up for peer review.

[36] P. Mangin and R. Kahn. *Superconductivity: An introduction*. Springer International Publishing, 2016. ISBN: 9783319505275. URL: `https://books.google.ch/books?id=ogDGDQAAQBAJ`.

Appendix A

# Sample of Matlab and Pspice code

```
    % Calculating inductance from frequency transfer meausrement of ith magnet
    mod=allMagnetInfo{1,2}{1,i}{1,1}.mod;
     freq=allMagnetInfo{1,2}{1,i}{1,1}.freq;
     [modLow, ind1]=max(mod(mod<0)); % Extract frequencies around 0 [dB]
     [modHigh, ind2]=min(mod(mod>0));
    y = [modLow modHigh];
    x = [freq(ind1) freq(ind1+1)];
    frq_0dB = interp1(y,x,0)*2*pi; %convert to [rad/s]
    L(i)=1/frq_0dB; % Calculate inductance for each magnet
```

**Listing A.1:** Code to fit L

```

syms s R L C Rp k

%% RL apertures
z_par=R*k*L*s/(k*L*s+R);
z_l=(1-k)*L*s;
 z_series_rl=z_par+z_l;

%% Capacitances
z_a=2/(C*s);
z_b=1/(C*s);
z_c=2/(C*s);

%% Y to deltastar transformation
z_ab=(z_a*z_b+z_a*z_c+z_b*z_c)/z_c;
z_bc=(z_a*z_b+z_a*z_c+z_b*z_c)/z_a;
z_ac=(z_a*z_b+z_a*z_c+z_b*z_c)/z_b;

z1=z_series_rl*z_ab/(z_series_rl+z_ab);
z2=z_series_rl*z_bc/(z_series_rl+z_bc);
 z_series =z1+z2;

z_tot=z_series*z_ac*Rp/(z_series*z_ac+z_series*Rp+z_ac*Rp)
```

**Listing A.2:** Symolic tool to obtain expression for dipole impedance

```
function Ztf = TrFun(w,L,R,k,C,Rp)

```

```
%whole dipole
Ztf =(64*Rp*(L*w*i*(k - 1) - (L*R*k*w*i)/(R + L*k*w*i)))/(C^2*(w*i)^2*(4/(C*w*
    i) - L*w*i*(k - 1) + (L*R*k*w*i)/(R + L*k*w*i))*((64*(L*w*i*(k - 1) - (L*R
    *k*w*i)/(R + L*k*w*i)))/(C^2*(w*i)^2*(4/(C*w*i) - L*w*i*(k - 1) + (L*R*k*w
    *i)/(R + L*k*w*i))) - (8*Rp)/(C*w*i) + (8*Rp*(L*w*i*(k - 1) - (L*R*k*w*i)
    /(R + L*k*w*i)))/(C*w*i*(4/(C*w*i) - L*w*i*(k - 1) + (L*R*k*w*i)/(R + L*k*
    w*i)))));

end
```

**Listing A.3:** Transfer function of dipole impedance

```
function e = f_obj(x)

% x(1)=k
% x(2)=R

global w $Ztf_meas$ $L_ap$ $C_Gnd$ Rp

wlength=length(w);

Ztf=zeros(wlength,1);
for m=1:wlength
      Ztf(m) = TrFun(w(m),$L_ap$, x(2),x(1),$C_Gnd$,Rp);
end

e = mean( (abs(Ztf-$Ztf_meas$)./abs($Ztf_meas$)).^2 ); % mean TVE^2

end
```

**Listing A.4:** Objective function calculating the mean $TVE^2$

```
%% Initialization

close all
clear
clc

freq=Q(:,1);
z_mag=(Q(:,2));
z_phase=unwrap((pi/180)*Q(:,3))*(180/pi);

%% Fit of the TF

global w Ztf_meas L_ap Rp C_Gnd

w = 2*pi*freq;
L_ap = 0.0388; % L_ap is fixed to fit the first part of the TF
Ztf_meas = z_mag.*exp(1i*z_phase*pi/180);
C_Gnd= 150e-9;
Rp = 100;

x(1) = 0; % k % First attempt values
x(2) = 10; % R1
%x(3) = 1; % R2
%x(4) = 150e-9; % C_gnd

lb=x*0.01;
ub=x/0.01;

lb(1)=0;
ub(1)=1;
```

```
x_fit=zeros(100,2);
tve_av=zeros(100,1);
for i=1:100
fun = @f_obj;
x_fit_op(i,:) = particleswarm(fun,2,lb,ub);
tve_av(i)=f_obj(x_fit_op);
end

% [tve_av_sqrd,x]=min(tve_av);
[tve_av_sim,x]=min(tve_av);
x_fit=x_fit_op(x,:)

f_fit=logspace( floor(log10(freq(1))), ceil(log10(freq(end))), 100);
w_fit=2*pi*f_fit;
w_fitlength=length(w_fit);

Ztf_fit=zeros(w_fitlength,1);
for m=1:w_fitlength
  Ztf_fit(m) = TrFun(w_fit(m),L_ap, x_fit(2),x_fit(1),C_Gnd, Rp);
end

z_mag_fit=abs(Ztf_fit);
z_phase_fit=angle(Ztf_fit)*180/pi;
```

**Listing A.5:** Code to obtain optimal fit for k and R

```
* PSPICE RB Standard Simulation File
* 2016/09/30 CERN


* Pspice custom components Libraries
.LIB "C:\gitlab\PSpice\RB\Library\Items\RB\RB_Diodes.lib"
.LIB "C:\gitlab\PSpice\RB\Library\Items\RB\RB_Thyristors.lib"
.LIB "C:\gitlab\PSpice\RB\Library\Items\RB\RB_Switches.lib"
.LIB "C:\gitlab\PSpice\RB\Library\Items\RB\RB_PC.lib"
*.LIB "C:\gitlab\PSpice\RB\Library\Items\RB\RB_MB.lib"
.LIB "\\cern.ch\dfs\Users\s\sambjorn\Documents\Pspice\RB_MB.lib"
.LIB "C:\gitlab\PSpice\RB\Library\Items\RB\RB_EE.lib"
*
* Two PCs in parallel
*x1_PC ( 1 2 ) RB_PC_Full
*v1_PH_filter ( 2 3 ) 0
*v2_PH_filter ( 21 1 ) 0
*

* PC grounding point 1
VPC_gnd1 (3 0) 0


* HTS lead 1 HOT-COLD
*r_fakeGnd (3 0) 100MEG
r1_warm ( 3 4 ) 378.5u
v1_warm ( 4 5 ) 50m
l1_warm ( 5 6 ) 10u
v1_fake ( 6 MAG1 ) 0
*
* HTS lead 2 COLD-HOT
v2_fake ( MAG77_Out 7 ) 0
r2_warm ( 7 8 ) 69.5u
v2_warm ( 8 9 ) 50m
l2_warm ( 9 10 ) 10u
*
```

```
* Energy Extractor 1
x1_RB_EE1 ( 10 11 ) RB_EE1_1poleEq
*
* HTS lead 3 HOT-COLD
r3_warm ( 11 12 ) 69.5u
v3_warm ( 12 13 ) 50m
l3_warm ( 13 14 ) 10u
v3_fake ( 14 MAG78 ) 0

v4_fake ( MAG154_Out 15 ) 0
r4_warm ( 15 16 ) 428.5u
v4_warm ( 16 17 ) 50m
l4_warm ( 17 18 ) 10u

* PC grounding point 2
VPC_gnd2 (18 0) 0

*
* Energy Extractor 2
*x1_RB_EE2 ( 18 19 ) RB_EE2_1poleEq
*
* Bus bar to PC
*r5_warm ( 19 20 ) 54u
*l5_warm ( 20 21 ) 10u

* Frequency measurement unit
i1 ( freqMid freqNeg ) ac 1
rMeas (freqMid freqPos) 1
*rGnd (freqNeg 0) 0.1
rGnd (freqNeg 0) 100MEG
* Connection to magnets
VfreqNeg (freqNeg MAG123) 0
VfreqMid (freqMiddle MAG_Mid122) 0
VfreqPos (freqPos MAG122) 0


x_MB1 ( MAG1 MAG_Mid1 MAG2 MAG_Gnd1 ) RB_MB_Dipole
+ PARAMS: r1=9.7 r2=10.0 rGnd1=1.1E7 rGnd2=1.1E7 rGnd3=1.1E7 rGnd4=1.1E7
x_MB2 ( MAG2 MAG_Mid2 MAG3 MAG_Gnd2 ) RB_MB_Dipole
+ PARAMS: r1=9.6 r2=10.0 rGnd1=1.1E7 rGnd2=1.1E7 rGnd3=1.1E7 rGnd4=1.1E7
x_MB3 ( MAG3 MAG_Mid3 MAG4 MAG_Gnd3 ) RB_MB_Dipole
+ PARAMS: r1=9.6 r2=10.0 rGnd1=1.1E7 rGnd2=1.1E7 rGnd3=1.1E7 rGnd4=1.1E7
x_MB4 ( MAG4 MAG_Mid4 MAG5 MAG_Gnd4 ) RB_MB_Dipole
+ PARAMS: r1=9.0 r2=10.0 rGnd1=1.1E7 rGnd2=1.1E7 rGnd3=1.1E7 rGnd4=1.1E7
x_MB5 ( MAG5 MAG_Mid5 MAG6 MAG_Gnd5 ) RB_MB_Dipole
+ PARAMS: r1=10.0 r2=10.0 rGnd1=1.1E7 rGnd2=1.1E7 rGnd3=1.1E7 rGnd4=1.1E7
x_MB6 ( MAG6 MAG_Mid6 MAG7 MAG_Gnd6 ) RB_MB_Dipole
+ PARAMS: r1=10.0 r2=10.0 rGnd1=1.1E7 rGnd2=1.1E7 rGnd3=1.1E7 rGnd4=1.1E7
x_MB7 ( MAG7 MAG_Mid7 MAG8 MAG_Gnd7 ) RB_MB_Dipole
+ PARAMS: r1=10.0 r2=10.0 rGnd1=1.1E7 rGnd2=1.1E7 rGnd3=1.1E7 rGnd4=1.1E7
x_MB8 ( MAG8 MAG_Mid8 MAG9 MAG_Gnd8 ) RB_MB_Dipole
+ PARAMS: r1=10.0 r2=10.0 rGnd1=1.1E7 rGnd2=1.1E7 rGnd3=1.1E7 rGnd4=1.1E7
x_MB9 ( MAG9 MAG_Mid9 MAG10 MAG_Gnd9 ) RB_MB_Dipole
+ PARAMS: r1=10.0 r2=10.0 rGnd1=1.1E7 rGnd2=1.1E7 rGnd3=1.1E7 rGnd4=1.1E7
x_MB10 ( MAG10 MAG_Mid10 MAG11 MAG_Gnd10 ) RB_MB_Dipole
+ PARAMS: r1=8.2 r2=10.0 rGnd1=1.1E7 rGnd2=1.1E7 rGnd3=1.1E7 rGnd4=1.1E7
x_MB11 ( MAG11 MAG_Mid11 MAG12 MAG_Gnd11 ) RB_MB_Dipole
+ PARAMS: r1=9.0 r2=10.0 rGnd1=1.1E7 rGnd2=1.1E7 rGnd3=1.1E7 rGnd4=1.1E7
x_MB12 ( MAG12 MAG_Mid12 MAG13 MAG_Gnd12 ) RB_MB_Dipole
+ PARAMS: r1=10.0 r2=10.0 rGnd1=1.1E7 rGnd2=1.1E7 rGnd3=1.1E7 rGnd4=1.1E7
x_MB13 ( MAG13 MAG_Mid13 MAG14 MAG_Gnd13 ) RB_MB_Dipole
+ PARAMS: r1=9.1 r2=10.0 rGnd1=1.1E7 rGnd2=1.1E7 rGnd3=1.1E7 rGnd4=1.1E7
```

```
x_MB14 ( MAG14 MAG_Mid14 MAG15 MAG_Gnd14 ) RB_MB_Dipole
+ PARAMS: r1=8.1 r2=10.0 rGnd1=1.1E7 rGnd2=1.1E7 rGnd3=1.1E7 rGnd4=1.1E7
x_MB15 ( MAG15 MAG_Mid15 MAG16 MAG_Gnd15 ) RB_MB_Dipole
+ PARAMS: r1=9.2 r2=10.0 rGnd1=1.1E7 rGnd2=1.1E7 rGnd3=1.1E7 rGnd4=1.1E7
x_MB16 ( MAG16 MAG_Mid16 MAG17 MAG_Gnd16 ) RB_MB_Dipole
+ PARAMS: r1=8.1 r2=10.0 rGnd1=1.1E7 rGnd2=1.1E7 rGnd3=1.1E7 rGnd4=1.1E7
x_MB17 ( MAG17 MAG_Mid17 MAG18 MAG_Gnd17 ) RB_MB_Dipole
+ PARAMS: r1=9.15 r2=10.0 rGnd1=1.1E7 rGnd2=1.1E7 rGnd3=1.1E7 rGnd4=1.1E7
x_MB18 ( MAG18 MAG_Mid18 MAG19 MAG_Gnd18 ) RB_MB_Dipole
+ PARAMS: r1=10.0 r2=10.0 rGnd1=1.1E7 rGnd2=1.1E7 rGnd3=1.1E7 rGnd4=1.1E7
x_MB19 ( MAG19 MAG_Mid19 MAG20 MAG_Gnd19 ) RB_MB_Dipole
+ PARAMS: r1=9.2 r2=10.0 rGnd1=1.1E7 rGnd2=1.1E7 rGnd3=1.1E7 rGnd4=1.1E7
x_MB20 ( MAG20 MAG_Mid20 MAG21 MAG_Gnd20 ) RB_MB_Dipole
+ PARAMS: r1=8.1 r2=10.0 rGnd1=1.1E7 rGnd2=1.1E7 rGnd3=1.1E7 rGnd4=1.1E7
x_MB21 ( MAG21 MAG_Mid21 MAG22 MAG_Gnd21 ) RB_MB_Dipole
+ PARAMS: r1=9.0 r2=10.0 rGnd1=1.1E7 rGnd2=1.1E7 rGnd3=1.1E7 rGnd4=1.1E7
x_MB22 ( MAG22 MAG_Mid22 MAG23 MAG_Gnd22 ) RB_MB_Dipole
+ PARAMS: r1=8.4 r2=10.0 rGnd1=1.1E7 rGnd2=1.1E7 rGnd3=1.1E7 rGnd4=1.1E7
x_MB23 ( MAG23 MAG_Mid23 MAG24 MAG_Gnd23 ) RB_MB_Dipole
+ PARAMS: r1=9.2 r2=10.0 rGnd1=1.1E7 rGnd2=1.1E7 rGnd3=1.1E7 rGnd4=1.1E7
x_MB24 ( MAG24 MAG_Mid24 MAG25 MAG_Gnd24 ) RB_MB_Dipole
+ PARAMS: r1=10.0 r2=10.0 rGnd1=1.1E7 rGnd2=1.1E7 rGnd3=1.1E7 rGnd4=1.1E7
x_MB25 ( MAG25 MAG_Mid25 MAG26 MAG_Gnd25 ) RB_MB_Dipole
+ PARAMS: r1=8.1 r2=10.0 rGnd1=1.1E7 rGnd2=1.1E7 rGnd3=1.1E7 rGnd4=1.1E7
x_MB26 ( MAG26 MAG_Mid26 MAG27 MAG_Gnd26 ) RB_MB_Dipole
+ PARAMS: r1=10.0 r2=10.0 rGnd1=1.1E7 rGnd2=1.1E7 rGnd3=1.1E7 rGnd4=1.1E7
x_MB27 ( MAG27 MAG_Mid27 MAG28 MAG_Gnd27 ) RB_MB_Dipole
+ PARAMS: r1=10.0 r2=10.0 rGnd1=1.1E7 rGnd2=1.1E7 rGnd3=1.1E7 rGnd4=1.1E7
x_MB28 ( MAG28 MAG_Mid28 MAG29 MAG_Gnd28 ) RB_MB_Dipole
+ PARAMS: r1=10.0 r2=10.0 rGnd1=1.1E7 rGnd2=1.1E7 rGnd3=1.1E7 rGnd4=1.1E7
x_MB29 ( MAG29 MAG_Mid29 MAG30 MAG_Gnd29 ) RB_MB_Dipole
+ PARAMS: r1=9.0 r2=10.0 rGnd1=1.1E7 rGnd2=1.1E7 rGnd3=1.1E7 rGnd4=1.1E7
x_MB30 ( MAG30 MAG_Mid30 MAG31 MAG_Gnd30 ) RB_MB_Dipole
+ PARAMS: r1=8.6 r2=10.0 rGnd1=1.1E7 rGnd2=1.1E7 rGnd3=1.1E7 rGnd4=1.1E7
x_MB31 ( MAG31 MAG_Mid31 MAG32 MAG_Gnd31 ) RB_MB_Dipole
+ PARAMS: r1=8.7 r2=10.0 rGnd1=1.1E7 rGnd2=1.1E7 rGnd3=1.1E7 rGnd4=1.1E7
x_MB32 ( MAG32 MAG_Mid32 MAG33 MAG_Gnd32 ) RB_MB_Dipole
+ PARAMS: r1=8.6 r2=10.0 rGnd1=1.1E7 rGnd2=1.1E7 rGnd3=1.1E7 rGnd4=1.1E7
x_MB33 ( MAG33 MAG_Mid33 MAG34 MAG_Gnd33 ) RB_MB_Dipole
+ PARAMS: r1=8.5 r2=10.0 rGnd1=1.1E7 rGnd2=1.1E7 rGnd3=1.1E7 rGnd4=1.1E7
x_MB34 ( MAG34 MAG_Mid34 MAG35 MAG_Gnd34 ) RB_MB_Dipole
+ PARAMS: r1=8.8 r2=10.0 rGnd1=1.1E7 rGnd2=1.1E7 rGnd3=1.1E7 rGnd4=1.1E7
x_MB35 ( MAG35 MAG_Mid35 MAG36 MAG_Gnd35 ) RB_MB_Dipole
+ PARAMS: r1=10.0 r2=10.0 rGnd1=1.1E7 rGnd2=1.1E7 rGnd3=1.1E7 rGnd4=1.1E7
x_MB36 ( MAG36 MAG_Mid36 MAG37 MAG_Gnd36 ) RB_MB_Dipole
+ PARAMS: r1=9.0 r2=10.0 rGnd1=1.1E7 rGnd2=1.1E7 rGnd3=1.1E7 rGnd4=1.1E7
x_MB37 ( MAG37 MAG_Mid37 MAG38 MAG_Gnd37 ) RB_MB_Dipole
+ PARAMS: r1=9.4 r2=10.0 rGnd1=1.1E7 rGnd2=1.1E7 rGnd3=1.1E7 rGnd4=1.1E7
x_MB38 ( MAG38 MAG_Mid38 MAG39 MAG_Gnd38 ) RB_MB_Dipole
+ PARAMS: r1=9.0 r2=10.0 rGnd1=1.1E7 rGnd2=1.1E7 rGnd3=1.1E7 rGnd4=1.1E7
x_MB39 ( MAG39 MAG_Mid39 MAG40 MAG_Gnd39 ) RB_MB_Dipole
+ PARAMS: r1=10.0 r2=10.0 rGnd1=1.1E7 rGnd2=1.1E7 rGnd3=1.1E7 rGnd4=1.1E7
x_MB40 ( MAG40 MAG_Mid40 MAG41 MAG_Gnd40 ) RB_MB_Dipole
+ PARAMS: r1=10.0 r2=10.0 rGnd1=1.1E7 rGnd2=1.1E7 rGnd3=1.1E7 rGnd4=1.1E7
x_MB41 ( MAG41 MAG_Mid41 MAG42 MAG_Gnd41 ) RB_MB_Dipole
+ PARAMS: r1=10.0 r2=10.0 rGnd1=1.1E7 rGnd2=1.1E7 rGnd3=1.1E7 rGnd4=1.1E7
x_MB42 ( MAG42 MAG_Mid42 MAG43 MAG_Gnd42 ) RB_MB_Dipole
+ PARAMS: r1=10.0 r2=10.0 rGnd1=1.1E7 rGnd2=1.1E7 rGnd3=1.1E7 rGnd4=1.1E7
x_MB43 ( MAG43 MAG_Mid43 MAG44 MAG_Gnd43 ) RB_MB_Dipole
+ PARAMS: r1=10.0 r2=10.0 rGnd1=1.1E7 rGnd2=1.1E7 rGnd3=1.1E7 rGnd4=1.1E7
x_MB44 ( MAG44 MAG_Mid44 MAG45 MAG_Gnd44 ) RB_MB_Dipole
+ PARAMS: r1=9.5 r2=10.0 rGnd1=1.1E7 rGnd2=1.1E7 rGnd3=1.1E7 rGnd4=1.1E7
```

```
x_MB45 ( MAG45 MAG_Mid45 MAG46 MAG_Gnd45 ) RB_MB_Dipole
+ PARAMS: r1=10.0 r2=10.0 rGnd1=1.1E7 rGnd2=1.1E7 rGnd3=1.1E7 rGnd4=1.1E7
x_MB46 ( MAG46 MAG_Mid46 MAG47 MAG_Gnd46 ) RB_MB_Dipole
+ PARAMS: r1=10.0 r2=10.0 rGnd1=1.1E7 rGnd2=1.1E7 rGnd3=1.1E7 rGnd4=1.1E7
x_MB47 ( MAG47 MAG_Mid47 MAG48 MAG_Gnd47 ) RB_MB_Dipole
+ PARAMS: r1=8.8 r2=10.0 rGnd1=1.1E7 rGnd2=1.1E7 rGnd3=1.1E7 rGnd4=1.1E7
x_MB48 ( MAG48 MAG_Mid48 MAG49 MAG_Gnd48 ) RB_MB_Dipole
+ PARAMS: r1=8.6 r2=10.0 rGnd1=1.1E7 rGnd2=1.1E7 rGnd3=1.1E7 rGnd4=1.1E7
x_MB49 ( MAG49 MAG_Mid49 MAG50 MAG_Gnd49 ) RB_MB_Dipole
+ PARAMS: r1=8.8 r2=10.0 rGnd1=1.1E7 rGnd2=1.1E7 rGnd3=1.1E7 rGnd4=1.1E7
x_MB50 ( MAG50 MAG_Mid50 MAG51 MAG_Gnd50 ) RB_MB_Dipole
+ PARAMS: r1=9.5 r2=10.0 rGnd1=1.1E7 rGnd2=1.1E7 rGnd3=1.1E7 rGnd4=1.1E7
x_MB51 ( MAG51 MAG_Mid51 MAG52 MAG_Gnd51 ) RB_MB_Dipole
+ PARAMS: r1=8.7 r2=10.0 rGnd1=1.1E7 rGnd2=1.1E7 rGnd3=1.1E7 rGnd4=1.1E7
x_MB52 ( MAG52 MAG_Mid52 MAG53 MAG_Gnd52 ) RB_MB_Dipole
+ PARAMS: r1=10.0 r2=10.0 rGnd1=1.1E7 rGnd2=1.1E7 rGnd3=1.1E7 rGnd4=1.1E7
x_MB53 ( MAG53 MAG_Mid53 MAG54 MAG_Gnd53 ) RB_MB_Dipole
+ PARAMS: r1=9.6 r2=10.0 rGnd1=1.1E7 rGnd2=1.1E7 rGnd3=1.1E7 rGnd4=1.1E7
x_MB54 ( MAG54 MAG_Mid54 MAG55 MAG_Gnd54 ) RB_MB_Dipole
+ PARAMS: r1=9.6 r2=10.0 rGnd1=1.1E7 rGnd2=1.1E7 rGnd3=1.1E7 rGnd4=1.1E7
x_MB55 ( MAG55 MAG_Mid55 MAG56 MAG_Gnd55 ) RB_MB_Dipole
+ PARAMS: r1=10.0 r2=10.0 rGnd1=1.1E7 rGnd2=1.1E7 rGnd3=1.1E7 rGnd4=1.1E7
x_MB56 ( MAG56 MAG_Mid56 MAG57 MAG_Gnd56 ) RB_MB_Dipole
+ PARAMS: r1=10.0 r2=10.0 rGnd1=1.1E7 rGnd2=1.1E7 rGnd3=1.1E7 rGnd4=1.1E7
x_MB57 ( MAG57 MAG_Mid57 MAG58 MAG_Gnd57 ) RB_MB_Dipole
+ PARAMS: r1=10.0 r2=10.0 rGnd1=1.1E7 rGnd2=1.1E7 rGnd3=1.1E7 rGnd4=1.1E7
x_MB58 ( MAG58 MAG_Mid58 MAG59 MAG_Gnd58 ) RB_MB_Dipole
+ PARAMS: r1=9.7 r2=10.0 rGnd1=1.1E7 rGnd2=1.1E7 rGnd3=1.1E7 rGnd4=1.1E7
x_MB59 ( MAG59 MAG_Mid59 MAG60 MAG_Gnd59 ) RB_MB_Dipole
+ PARAMS: r1=8.7 r2=10.0 rGnd1=1.1E7 rGnd2=1.1E7 rGnd3=1.1E7 rGnd4=1.1E7
x_MB60 ( MAG60 MAG_Mid60 MAG61 MAG_Gnd60 ) RB_MB_Dipole
+ PARAMS: r1=9.0 r2=10.0 rGnd1=1.1E7 rGnd2=1.1E7 rGnd3=1.1E7 rGnd4=1.1E7
x_MB61 ( MAG61 MAG_Mid61 MAG62 MAG_Gnd61 ) RB_MB_Dipole
+ PARAMS: r1=10.0 r2=10.0 rGnd1=1.1E7 rGnd2=1.1E7 rGnd3=1.1E7 rGnd4=1.1E7
x_MB62 ( MAG62 MAG_Mid62 MAG63 MAG_Gnd62 ) RB_MB_Dipole
+ PARAMS: r1=8.45 r2=10.0 rGnd1=1.1E7 rGnd2=1.1E7 rGnd3=1.1E7 rGnd4=1.1E7
x_MB63 ( MAG63 MAG_Mid63 MAG64 MAG_Gnd63 ) RB_MB_Dipole
+ PARAMS: r1=9.1 r2=10.0 rGnd1=1.1E7 rGnd2=1.1E7 rGnd3=1.1E7 rGnd4=1.1E7
x_MB64 ( MAG64 MAG_Mid64 MAG65 MAG_Gnd64 ) RB_MB_Dipole
+ PARAMS: r1=10.0 r2=10.0 rGnd1=1.1E7 rGnd2=1.1E7 rGnd3=1.1E7 rGnd4=1.1E7
x_MB65 ( MAG65 MAG_Mid65 MAG66 MAG_Gnd65 ) RB_MB_Dipole
+ PARAMS: r1=10.0 r2=10.0 rGnd1=1.1E7 rGnd2=1.1E7 rGnd3=1.1E7 rGnd4=1.1E7
x_MB66 ( MAG66 MAG_Mid66 MAG67 MAG_Gnd66 ) RB_MB_Dipole
+ PARAMS: r1=10.0 r2=10.0 rGnd1=1.1E7 rGnd2=1.1E7 rGnd3=1.1E7 rGnd4=1.1E7
x_MB67 ( MAG67 MAG_Mid67 MAG68 MAG_Gnd67 ) RB_MB_Dipole
+ PARAMS: r1=8.9 r2=10.0 rGnd1=1.1E7 rGnd2=1.1E7 rGnd3=1.1E7 rGnd4=1.1E7
x_MB68 ( MAG68 MAG_Mid68 MAG69 MAG_Gnd68 ) RB_MB_Dipole
+ PARAMS: r1=9.1 r2=10.0 rGnd1=1.1E7 rGnd2=1.1E7 rGnd3=1.1E7 rGnd4=1.1E7
x_MB69 ( MAG69 MAG_Mid69 MAG70 MAG_Gnd69 ) RB_MB_Dipole
+ PARAMS: r1=10.0 r2=10.0 rGnd1=1.1E7 rGnd2=1.1E7 rGnd3=1.1E7 rGnd4=1.1E7
x_MB70 ( MAG70 MAG_Mid70 MAG71 MAG_Gnd70 ) RB_MB_Dipole
+ PARAMS: r1=8.8 r2=10.0 rGnd1=1.1E7 rGnd2=1.1E7 rGnd3=1.1E7 rGnd4=1.1E7
x_MB71 ( MAG71 MAG_Mid71 MAG72 MAG_Gnd71 ) RB_MB_Dipole
+ PARAMS: r1=10.0 r2=10.0 rGnd1=1.1E7 rGnd2=1.1E7 rGnd3=1.1E7 rGnd4=1.1E7
x_MB72 ( MAG72 MAG_Mid72 MAG73 MAG_Gnd72 ) RB_MB_Dipole
+ PARAMS: r1=9.1 r2=10.0 rGnd1=1.1E7 rGnd2=1.1E7 rGnd3=1.1E7 rGnd4=1.1E7
x_MB73 ( MAG73 MAG_Mid73 MAG74 MAG_Gnd73 ) RB_MB_Dipole
+ PARAMS: r1=9.2 r2=10.0 rGnd1=1.1E7 rGnd2=1.1E7 rGnd3=1.1E7 rGnd4=1.1E7
x_MB74 ( MAG74 MAG_Mid74 MAG75 MAG_Gnd74 ) RB_MB_Dipole
+ PARAMS: r1=9.2 r2=10.0 rGnd1=1.1E7 rGnd2=1.1E7 rGnd3=1.1E7 rGnd4=1.1E7
x_MB75 ( MAG75 MAG_Mid75 MAG76 MAG_Gnd75 ) RB_MB_Dipole
+ PARAMS: r1=9.3 r2=10.0 rGnd1=1.1E7 rGnd2=1.1E7 rGnd3=1.1E7 rGnd4=1.1E7
```

```
x_MB76 ( MAG76 MAG_Mid76 MAG77 MAG_Gnd76 ) RB_MB_Dipole
+ PARAMS: r1=10.0 r2=10.0 rGnd1=1.1E7 rGnd2=1.1E7 rGnd3=1.1E7 rGnd4=1.1E7
x_MB77 ( MAG77 MAG_Mid77 MAG77_Out MAG_Gnd77 ) RB_MB_Dipole
+ PARAMS: r1=10.0 r2=10.0 rGnd1=1.1E7 rGnd2=1.1E7 rGnd3=1.1E7 rGnd4=1.1E7
x_MB78 ( MAG78 MAG_Mid78 MAG79 MAG_Gnd78 ) RB_MB_Dipole
+ PARAMS: r1=10.0 r2=10.0 rGnd1=1.1E7 rGnd2=1.1E7 rGnd3=1.1E7 rGnd4=1.1E7
x_MB79 ( MAG79 MAG_Mid79 MAG80 MAG_Gnd79 ) RB_MB_Dipole
+ PARAMS: r1=10.0 r2=10.0 rGnd1=1.1E7 rGnd2=1.1E7 rGnd3=1.1E7 rGnd4=1.1E7
x_MB80 ( MAG80 MAG_Mid80 MAG81 MAG_Gnd80 ) RB_MB_Dipole
+ PARAMS: r1=10.0 r2=10.0 rGnd1=1.1E7 rGnd2=1.1E7 rGnd3=1.1E7 rGnd4=1.1E7
x_MB81 ( MAG81 MAG_Mid81 MAG82 MAG_Gnd81 ) RB_MB_Dipole
+ PARAMS: r1=10.0 r2=10.0 rGnd1=1.1E7 rGnd2=1.1E7 rGnd3=1.1E7 rGnd4=1.1E7
x_MB82 ( MAG82 MAG_Mid82 MAG83 MAG_Gnd82 ) RB_MB_Dipole
+ PARAMS: r1=9.6 r2=10.0 rGnd1=1.1E7 rGnd2=1.1E7 rGnd3=1.1E7 rGnd4=1.1E7
x_MB83 ( MAG83 MAG_Mid83 MAG84 MAG_Gnd83 ) RB_MB_Dipole
+ PARAMS: r1=10.0 r2=10.0 rGnd1=1.1E7 rGnd2=1.1E7 rGnd3=1.1E7 rGnd4=1.1E7
x_MB84 ( MAG84 MAG_Mid84 MAG85 MAG_Gnd84 ) RB_MB_Dipole
+ PARAMS: r1=10.0 r2=10.0 rGnd1=1.1E7 rGnd2=1.1E7 rGnd3=1.1E7 rGnd4=1.1E7
x_MB85 ( MAG85 MAG_Mid85 MAG86 MAG_Gnd85 ) RB_MB_Dipole
+ PARAMS: r1=9.7 r2=10.0 rGnd1=1.1E7 rGnd2=1.1E7 rGnd3=1.1E7 rGnd4=1.1E7
x_MB86 ( MAG86 MAG_Mid86 MAG87 MAG_Gnd86 ) RB_MB_Dipole
+ PARAMS: r1=10.0 r2=10.0 rGnd1=1.1E7 rGnd2=1.1E7 rGnd3=1.1E7 rGnd4=1.1E7
x_MB87 ( MAG87 MAG_Mid87 MAG88 MAG_Gnd87 ) RB_MB_Dipole
+ PARAMS: r1=9.3 r2=10.0 rGnd1=1.1E7 rGnd2=1.1E7 rGnd3=1.1E7 rGnd4=1.1E7
x_MB88 ( MAG88 MAG_Mid88 MAG89 MAG_Gnd88 ) RB_MB_Dipole
+ PARAMS: r1=10.0 r2=10.0 rGnd1=1.1E7 rGnd2=1.1E7 rGnd3=1.1E7 rGnd4=1.1E7
x_MB89 ( MAG89 MAG_Mid89 MAG90 MAG_Gnd89 ) RB_MB_Dipole
+ PARAMS: r1=10.0 r2=10.0 rGnd1=1.1E7 rGnd2=1.1E7 rGnd3=1.1E7 rGnd4=1.1E7
x_MB90 ( MAG90 MAG_Mid90 MAG91 MAG_Gnd90 ) RB_MB_Dipole
+ PARAMS: r1=9.6 r2=10.0 rGnd1=1.1E7 rGnd2=1.1E7 rGnd3=1.1E7 rGnd4=1.1E7
x_MB91 ( MAG91 MAG_Mid91 MAG92 MAG_Gnd91 ) RB_MB_Dipole
+ PARAMS: r1=9.5 r2=10.0 rGnd1=1.1E7 rGnd2=1.1E7 rGnd3=1.1E7 rGnd4=1.1E7
x_MB92 ( MAG92 MAG_Mid92 MAG93 MAG_Gnd92 ) RB_MB_Dipole
+ PARAMS: r1=9.6 r2=10.0 rGnd1=1.1E7 rGnd2=1.1E7 rGnd3=1.1E7 rGnd4=1.1E7
x_MB93 ( MAG93 MAG_Mid93 MAG94 MAG_Gnd93 ) RB_MB_Dipole
+ PARAMS: r1=9.0 r2=10.0 rGnd1=1.1E7 rGnd2=1.1E7 rGnd3=1.1E7 rGnd4=1.1E7
x_MB94 ( MAG94 MAG_Mid94 MAG95 MAG_Gnd94 ) RB_MB_Dipole
+ PARAMS: r1=10.0 r2=10.0 rGnd1=1.1E7 rGnd2=1.1E7 rGnd3=1.1E7 rGnd4=1.1E7
x_MB95 ( MAG95 MAG_Mid95 MAG96 MAG_Gnd95 ) RB_MB_Dipole
+ PARAMS: r1=9.7 r2=10.0 rGnd1=1.1E7 rGnd2=1.1E7 rGnd3=1.1E7 rGnd4=1.1E7
x_MB96 ( MAG96 MAG_Mid96 MAG97 MAG_Gnd96 ) RB_MB_Dipole
+ PARAMS: r1=9.1 r2=10.0 rGnd1=1.1E7 rGnd2=1.1E7 rGnd3=1.1E7 rGnd4=1.1E7
x_MB97 ( MAG97 MAG_Mid97 MAG98 MAG_Gnd97 ) RB_MB_Dipole
+ PARAMS: r1=8.9 r2=10.0 rGnd1=1.1E7 rGnd2=1.1E7 rGnd3=1.1E7 rGnd4=1.1E7
x_MB98 ( MAG98 MAG_Mid98 MAG99 MAG_Gnd98 ) RB_MB_Dipole
+ PARAMS: r1=10.0 r2=10.0 rGnd1=1.1E7 rGnd2=1.1E7 rGnd3=1.1E7 rGnd4=1.1E7
x_MB99 ( MAG99 MAG_Mid99 MAG100 MAG_Gnd99 ) RB_MB_Dipole
+ PARAMS: r1=10.0 r2=10.0 rGnd1=1.1E7 rGnd2=1.1E7 rGnd3=1.1E7 rGnd4=1.1E7
x_MB100 ( MAG100 MAG_Mid100 MAG101 MAG_Gnd100 ) RB_MB_Dipole
+ PARAMS: r1=9.3 r2=10.0 rGnd1=1.1E7 rGnd2=1.1E7 rGnd3=1.1E7 rGnd4=1.1E7
x_MB101 ( MAG101 MAG_Mid101 MAG102 MAG_Gnd101 ) RB_MB_Dipole
+ PARAMS: r1=9.1 r2=10.0 rGnd1=1.1E7 rGnd2=1.1E7 rGnd3=1.1E7 rGnd4=1.1E7
x_MB102 ( MAG102 MAG_Mid102 MAG103 MAG_Gnd102 ) RB_MB_Dipole
+ PARAMS: r1=10.0 r2=10.0 rGnd1=1.1E7 rGnd2=1.1E7 rGnd3=1.1E7 rGnd4=1.1E7
x_MB103 ( MAG103 MAG_Mid103 MAG104 MAG_Gnd103 ) RB_MB_Dipole
+ PARAMS: r1=10.0 r2=10.0 rGnd1=1.1E7 rGnd2=1.1E7 rGnd3=1.1E7 rGnd4=1.1E7
x_MB104 ( MAG104 MAG_Mid104 MAG105 MAG_Gnd104 ) RB_MB_Dipole
+ PARAMS: r1=10.0 r2=10.0 rGnd1=1.1E7 rGnd2=1.1E7 rGnd3=1.1E7 rGnd4=1.1E7
x_MB105 ( MAG105 MAG_Mid105 MAG106 MAG_Gnd105 ) RB_MB_Dipole
+ PARAMS: r1=9.2 r2=10.0 rGnd1=1.1E7 rGnd2=1.1E7 rGnd3=1.1E7 rGnd4=1.1E7
x_MB106 ( MAG106 MAG_Mid106 MAG107 MAG_Gnd106 ) RB_MB_Dipole
+ PARAMS: r1=10.0 r2=10.0 rGnd1=1.1E7 rGnd2=1.1E7 rGnd3=1.1E7 rGnd4=1.1E7
```

```
x_MB107 ( MAG107 MAG_Mid107 MAG108 MAG_Gnd107 ) RB_MB_Dipole
+ PARAMS: r1=9.6 r2=10.0 rGnd1=1.1E7 rGnd2=1.1E7 rGnd3=1.1E7 rGnd4=1.1E7
x_MB108 ( MAG108 MAG_Mid108 MAG109 MAG_Gnd108 ) RB_MB_Dipole
+ PARAMS: r1=10.0 r2=10.0 rGnd1=1.1E7 rGnd2=1.1E7 rGnd3=1.1E7 rGnd4=1.1E7
x_MB109 ( MAG109 MAG_Mid109 MAG110 MAG_Gnd109 ) RB_MB_Dipole
+ PARAMS: r1=10.0 r2=10.0 rGnd1=1.1E7 rGnd2=1.1E7 rGnd3=1.1E7 rGnd4=1.1E7
x_MB110 ( MAG110 MAG_Mid110 MAG111 MAG_Gnd110 ) RB_MB_Dipole
+ PARAMS: r1=9.5 r2=10.0 rGnd1=1.1E7 rGnd2=1.1E7 rGnd3=1.1E7 rGnd4=1.1E7
x_MB111 ( MAG111 MAG_Mid111 MAG112 MAG_Gnd111 ) RB_MB_Dipole
+ PARAMS: r1=10.0 r2=10.0 rGnd1=1.1E7 rGnd2=1.1E7 rGnd3=1.1E7 rGnd4=1.1E7
x_MB112 ( MAG112 MAG_Mid112 MAG113 MAG_Gnd112 ) RB_MB_Dipole
+ PARAMS: r1=10.0 r2=10.0 rGnd1=1.1E7 rGnd2=1.1E7 rGnd3=1.1E7 rGnd4=1.1E7
x_MB113 ( MAG113 MAG_Mid113 MAG114 MAG_Gnd113 ) RB_MB_Dipole
+ PARAMS: r1=9.6 r2=10.0 rGnd1=1.1E7 rGnd2=1.1E7 rGnd3=1.1E7 rGnd4=1.1E7
x_MB114 ( MAG114 MAG_Mid114 MAG115 MAG_Gnd114 ) RB_MB_Dipole
+ PARAMS: r1=9.4 r2=10.0 rGnd1=1.1E7 rGnd2=1.1E7 rGnd3=1.1E7 rGnd4=1.1E7
x_MB115 ( MAG115 MAG_Mid115 MAG116 MAG_Gnd115 ) RB_MB_Dipole
+ PARAMS: r1=9.35 r2=10.0 rGnd1=1.1E7 rGnd2=1.1E7 rGnd3=1.1E7 rGnd4=1.1E7
x_MB116 ( MAG116 MAG_Mid116 MAG117 MAG_Gnd116 ) RB_MB_Dipole
+ PARAMS: r1=10.0 r2=10.0 rGnd1=1.1E7 rGnd2=1.1E7 rGnd3=1.1E7 rGnd4=1.1E7
x_MB117 ( MAG117 MAG_Mid117 MAG118 MAG_Gnd117 ) RB_MB_Dipole
+ PARAMS: r1=10.0 r2=10.0 rGnd1=1.1E7 rGnd2=1.1E7 rGnd3=1.1E7 rGnd4=1.1E7
x_MB118 ( MAG118 MAG_Mid118 MAG119 MAG_Gnd118 ) RB_MB_Dipole
+ PARAMS: r1=9.05 r2=10.0 rGnd1=1.1E7 rGnd2=1.1E7 rGnd3=1.1E7 rGnd4=1.1E7
x_MB119 ( MAG119 MAG_Mid119 MAG120 MAG_Gnd119 ) RB_MB_Dipole
+ PARAMS: r1=9.3 r2=10.0 rGnd1=1.1E7 rGnd2=1.1E7 rGnd3=1.1E7 rGnd4=1.1E7
x_MB120 ( MAG120 MAG_Mid120 MAG121 MAG_Gnd120 ) RB_MB_Dipole
+ PARAMS: r1=9.45 r2=10.0 rGnd1=1.1E7 rGnd2=1.1E7 rGnd3=1.1E7 rGnd4=1.1E7
x_MB121 ( MAG121 MAG_Mid121 MAG122 MAG_Gnd121 ) RB_MB_Dipole
+ PARAMS: r1=9.3 r2=10.0 rGnd1=1.1E7 rGnd2=1.1E7 rGnd3=1.1E7 rGnd4=1.1E7
*x_MB122 ( MAG122 MAG_Mid122 MAG123 MAG_Gnd122 MAG122_pSh MAG122_nSh )
    RB_MB_Dipole_Short_Refined
x_MB122 ( MAG122 MAG_Mid122 MAG123 MAG_Gnd122 ) RB_MB_Dipole
+ PARAMS: r1=9.4 r2=10 rGnd1=1.1E7 rGnd2=1.1E7 rGnd3=1.1E7 rGnd4=1.1E7
x_MB123 ( MAG123 MAG_Mid123 MAG124 MAG_Gnd123 ) RB_MB_Dipole
+ PARAMS: r1=9.4 r2=10.0 rGnd1=1.1E7 rGnd2=1.1E7 rGnd3=1.1E7 rGnd4=1.1E7
x_MB124 ( MAG124 MAG_Mid124 MAG125 MAG_Gnd124 ) RB_MB_Dipole
+ PARAMS: r1=9.4 r2=10.0 rGnd1=1.1E7 rGnd2=1.1E7 rGnd3=1.1E7 rGnd4=1.1E7
x_MB125 ( MAG125 MAG_Mid125 MAG126 MAG_Gnd125 ) RB_MB_Dipole
+ PARAMS: r1=9.35 r2=10.0 rGnd1=1.1E7 rGnd2=1.1E7 rGnd3=1.1E7 rGnd4=1.1E7
x_MB126 ( MAG126 MAG_Mid126 MAG127 MAG_Gnd126 ) RB_MB_Dipole
+ PARAMS: r1=9.45 r2=10.0 rGnd1=1.1E7 rGnd2=1.1E7 rGnd3=1.1E7 rGnd4=1.1E7
x_MB127 ( MAG127 MAG_Mid127 MAG128 MAG_Gnd127 ) RB_MB_Dipole
+ PARAMS: r1=9.2 r2=10.0 rGnd1=1.1E7 rGnd2=1.1E7 rGnd3=1.1E7 rGnd4=1.1E7
x_MB128 ( MAG128 MAG_Mid128 MAG129 MAG_Gnd128 ) RB_MB_Dipole
+ PARAMS: r1=9.37 r2=10.0 rGnd1=1.1E7 rGnd2=1.1E7 rGnd3=1.1E7 rGnd4=1.1E7
x_MB129 ( MAG129 MAG_Mid129 MAG130 MAG_Gnd129 ) RB_MB_Dipole
+ PARAMS: r1=10.0 r2=10.0 rGnd1=1.1E7 rGnd2=1.1E7 rGnd3=1.1E7 rGnd4=1.1E7
x_MB130 ( MAG130 MAG_Mid130 MAG131 MAG_Gnd130 ) RB_MB_Dipole
+ PARAMS: r1=9.6 r2=10.0 rGnd1=1.1E7 rGnd2=1.1E7 rGnd3=1.1E7 rGnd4=1.1E7
x_MB131 ( MAG131 MAG_Mid131 MAG132 MAG_Gnd131 ) RB_MB_Dipole
+ PARAMS: r1=9.35 r2=10.0 rGnd1=1.1E7 rGnd2=1.1E7 rGnd3=1.1E7 rGnd4=1.1E7
x_MB132 ( MAG132 MAG_Mid132 MAG133 MAG_Gnd132 ) RB_MB_Dipole
+ PARAMS: r1=10.0 r2=10.0 rGnd1=1.1E7 rGnd2=1.1E7 rGnd3=1.1E7 rGnd4=1.1E7
x_MB133 ( MAG133 MAG_Mid133 MAG134 MAG_Gnd133 ) RB_MB_Dipole
+ PARAMS: r1=8.6 r2=10.0 rGnd1=1.1E7 rGnd2=1.1E7 rGnd3=1.1E7 rGnd4=1.1E7
x_MB134 ( MAG134 MAG_Mid134 MAG135 MAG_Gnd134 ) RB_MB_Dipole
+ PARAMS: r1=10.0 r2=10.0 rGnd1=1.1E7 rGnd2=1.1E7 rGnd3=1.1E7 rGnd4=1.1E7
x_MB135 ( MAG135 MAG_Mid135 MAG136 MAG_Gnd135 ) RB_MB_Dipole
+ PARAMS: r1=10.0 r2=10.0 rGnd1=1.1E7 rGnd2=1.1E7 rGnd3=1.1E7 rGnd4=1.1E7
x_MB136 ( MAG136 MAG_Mid136 MAG137 MAG_Gnd136 ) RB_MB_Dipole
+ PARAMS: r1=10.0 r2=10.0 rGnd1=1.1E7 rGnd2=1.1E7 rGnd3=1.1E7 rGnd4=1.1E7
```

```
x_MB137 ( MAG137 MAG_Mid137 MAG138 MAG_Gnd137 ) RB_MB_Dipole
+ PARAMS: r1=9.3 r2=10.0 rGnd1=1.1E7 rGnd2=1.1E7 rGnd3=1.1E7 rGnd4=1.1E7
x_MB138 ( MAG138 MAG_Mid138 MAG139 MAG_Gnd138 ) RB_MB_Dipole
+ PARAMS: r1=8.65 r2=10.0 rGnd1=1.1E7 rGnd2=1.1E7 rGnd3=1.1E7 rGnd4=1.1E7
x_MB139 ( MAG139 MAG_Mid139 MAG140 MAG_Gnd139 ) RB_MB_Dipole
+ PARAMS: r1=10.0 r2=10.0 rGnd1=1.1E7 rGnd2=1.1E7 rGnd3=1.1E7 rGnd4=1.1E7
x_MB140 ( MAG140 MAG_Mid140 MAG141 MAG_Gnd140 ) RB_MB_Dipole
+ PARAMS: r1=9.45 r2=10.0 rGnd1=1.1E7 rGnd2=1.1E7 rGnd3=1.1E7 rGnd4=1.1E7
x_MB141 ( MAG141 MAG_Mid141 MAG142 MAG_Gnd141 ) RB_MB_Dipole
+ PARAMS: r1=9.4 r2=10.0 rGnd1=1.1E7 rGnd2=1.1E7 rGnd3=1.1E7 rGnd4=1.1E7
x_MB142 ( MAG142 MAG_Mid142 MAG143 MAG_Gnd142 ) RB_MB_Dipole
+ PARAMS: r1=10.0 r2=10.0 rGnd1=1.1E7 rGnd2=1.1E7 rGnd3=1.1E7 rGnd4=1.1E7
x_MB143 ( MAG143 MAG_Mid143 MAG144 MAG_Gnd143 ) RB_MB_Dipole
+ PARAMS: r1=9.25 r2=10.0 rGnd1=1.1E7 rGnd2=1.1E7 rGnd3=1.1E7 rGnd4=1.1E7
x_MB144 ( MAG144 MAG_Mid144 MAG145 MAG_Gnd144 ) RB_MB_Dipole
+ PARAMS: r1=8.7 r2=10.0 rGnd1=1.1E7 rGnd2=1.1E7 rGnd3=1.1E7 rGnd4=1.1E7
x_MB145 ( MAG145 MAG_Mid145 MAG146 MAG_Gnd145 ) RB_MB_Dipole
+ PARAMS: r1=8.8 r2=10.0 rGnd1=1.1E7 rGnd2=1.1E7 rGnd3=1.1E7 rGnd4=1.1E7
x_MB146 ( MAG146 MAG_Mid146 MAG147 MAG_Gnd146 ) RB_MB_Dipole
+ PARAMS: r1=8.6 r2=10.0 rGnd1=1.1E7 rGnd2=1.1E7 rGnd3=1.1E7 rGnd4=1.1E7
x_MB147 ( MAG147 MAG_Mid147 MAG148 MAG_Gnd147 ) RB_MB_Dipole
+ PARAMS: r1=8.65 r2=10.0 rGnd1=1.1E7 rGnd2=1.1E7 rGnd3=1.1E7 rGnd4=1.1E7
x_MB148 ( MAG148 MAG_Mid148 MAG149 MAG_Gnd148 ) RB_MB_Dipole
+ PARAMS: r1=8.32 r2=10.0 rGnd1=1.1E7 rGnd2=1.1E7 rGnd3=1.1E7 rGnd4=1.1E7
x_MB149 ( MAG149 MAG_Mid149 MAG150 MAG_Gnd149 ) RB_MB_Dipole
+ PARAMS: r1=10.0 r2=10.0 rGnd1=1.1E7 rGnd2=1.1E7 rGnd3=1.1E7 rGnd4=1.1E7
x_MB150 ( MAG150 MAG_Mid150 MAG151 MAG_Gnd150 ) RB_MB_Dipole
+ PARAMS: r1=8.9 r2=10.0 rGnd1=1.1E7 rGnd2=1.1E7 rGnd3=1.1E7 rGnd4=1.1E7
x_MB151 ( MAG151 MAG_Mid151 MAG152 MAG_Gnd151 ) RB_MB_Dipole
+ PARAMS: r1=8.65 r2=10.0 rGnd1=1.1E7 rGnd2=1.1E7 rGnd3=1.1E7 rGnd4=1.1E7
x_MB152 ( MAG152 MAG_Mid152 MAG153 MAG_Gnd152 ) RB_MB_Dipole
+ PARAMS: r1=10.0 r2=10.0 rGnd1=1.1E7 rGnd2=1.1E7 rGnd3=1.1E7 rGnd4=1.1E7
x_MB153 ( MAG153 MAG_Mid153 MAG154 MAG_Gnd153 ) RB_MB_Dipole
+ PARAMS: r1=8.65 r2=10.0 rGnd1=1.1E7 rGnd2=1.1E7 rGnd3=1.1E7 rGnd4=1.1E7
x_MB154 ( MAG154 MAG_Mid154 MAG154_Out MAG_Gnd154 ) RB_MB_Dipole
+ PARAMS: r1=8.8 r2=10.0 rGnd1=1.1E7 rGnd2=1.1E7 rGnd3=1.1E7 rGnd4=1.1E7
*Short in block 6
*x_MB122_short ( MAG122_pSh MAG122_nSh ) R_Short_MB
v_fakeGND ( GND1 0 ) 0
x_MbGND1 ( MAG_Gnd1 MAG_Gnd154 GND1 GND2 ) RB_Gnd_Cell2MB
x_MbGND2 ( MAG_Gnd2 MAG_Gnd153 GND2 GND3 ) RB_Gnd_Cell2MB
x_MbGND3 ( MAG_Gnd3 MAG_Gnd152 GND3 GND4 ) RB_Gnd_Cell2MB
x_MbGND4 ( MAG_Gnd4 MAG_Gnd151 GND4 GND5 ) RB_Gnd_Cell2MB
x_MbGND5 ( MAG_Gnd5 MAG_Gnd150 MAG_Gnd6 GND5 GND6 ) RB_Gnd_Cell3MB
x_MbGND6 ( MAG_Gnd149 MAG_Gnd7 MAG_Gnd148 GND6 GND7 ) RB_Gnd_Cell3MB
x_MbGND7 ( MAG_Gnd8 MAG_Gnd147 MAG_Gnd9 GND7 GND8 ) RB_Gnd_Cell3MB
x_MbGND8 ( MAG_Gnd146 MAG_Gnd10 MAG_Gnd145 GND8 GND9 ) RB_Gnd_Cell3MB
x_MbGND9 ( MAG_Gnd11 MAG_Gnd144 MAG_Gnd12 GND9 GND10 ) RB_Gnd_Cell3MB
x_MbGND10 ( MAG_Gnd143 MAG_Gnd13 MAG_Gnd142 GND10 GND11 ) RB_Gnd_Cell3MB
x_MbGND11 ( MAG_Gnd14 MAG_Gnd141 MAG_Gnd15 GND11 GND12 ) RB_Gnd_Cell3MB
x_MbGND12 ( MAG_Gnd140 MAG_Gnd16 MAG_Gnd139 GND12 GND13 ) RB_Gnd_Cell3MB
x_MbGND13 ( MAG_Gnd17 MAG_Gnd138 MAG_Gnd18 GND13 GND14 ) RB_Gnd_Cell3MB
x_MbGND14 ( MAG_Gnd137 MAG_Gnd19 MAG_Gnd136 GND14 GND15 ) RB_Gnd_Cell3MB
x_MbGND15 ( MAG_Gnd20 MAG_Gnd135 MAG_Gnd21 GND15 GND16 ) RB_Gnd_Cell3MB
x_MbGND16 ( MAG_Gnd134 MAG_Gnd22 MAG_Gnd133 GND16 GND17 ) RB_Gnd_Cell3MB
x_MbGND17 ( MAG_Gnd23 MAG_Gnd132 MAG_Gnd24 GND17 GND18 ) RB_Gnd_Cell3MB
x_MbGND18 ( MAG_Gnd131 MAG_Gnd25 MAG_Gnd130 GND18 GND19 ) RB_Gnd_Cell3MB
x_MbGND19 ( MAG_Gnd26 MAG_Gnd129 MAG_Gnd27 GND19 GND20 ) RB_Gnd_Cell3MB
x_MbGND20 ( MAG_Gnd128 MAG_Gnd28 MAG_Gnd127 GND20 GND21 ) RB_Gnd_Cell3MB
x_MbGND21 ( MAG_Gnd29 MAG_Gnd126 MAG_Gnd30 GND21 GND22 ) RB_Gnd_Cell3MB
x_MbGND22 ( MAG_Gnd125 MAG_Gnd31 MAG_Gnd124 GND22 GND23 ) RB_Gnd_Cell3MB
x_MbGND23 ( MAG_Gnd32 MAG_Gnd123 MAG_Gnd33 GND23 GND24 ) RB_Gnd_Cell3MB
```

```
x_MbGND24 ( MAG_Gnd122 MAG_Gnd34 MAG_Gnd121 GND24 GND25 ) RB_Gnd_Cell3MB
x_MbGND25 ( MAG_Gnd35 MAG_Gnd120 MAG_Gnd36 GND25 GND26 ) RB_Gnd_Cell3MB
x_MbGND26 ( MAG_Gnd119 MAG_Gnd37 MAG_Gnd118 GND26 GND27 ) RB_Gnd_Cell3MB
x_MbGND27 ( MAG_Gnd38 MAG_Gnd117 MAG_Gnd39 GND27 GND28 ) RB_Gnd_Cell3MB
x_MbGND28 ( MAG_Gnd116 MAG_Gnd40 MAG_Gnd115 GND28 GND29 ) RB_Gnd_Cell3MB
x_MbGND29 ( MAG_Gnd41 MAG_Gnd114 MAG_Gnd42 GND29 GND30 ) RB_Gnd_Cell3MB
x_MbGND30 ( MAG_Gnd113 MAG_Gnd43 MAG_Gnd112 GND30 GND31 ) RB_Gnd_Cell3MB
x_MbGND31 ( MAG_Gnd44 MAG_Gnd111 MAG_Gnd45 GND31 GND32 ) RB_Gnd_Cell3MB
x_MbGND32 ( MAG_Gnd110 MAG_Gnd46 MAG_Gnd109 GND32 GND33 ) RB_Gnd_Cell3MB
x_MbGND33 ( MAG_Gnd47 MAG_Gnd108 MAG_Gnd48 GND33 GND34 ) RB_Gnd_Cell3MB
x_MbGND34 ( MAG_Gnd107 MAG_Gnd49 MAG_Gnd106 GND34 GND35 ) RB_Gnd_Cell3MB
x_MbGND35 ( MAG_Gnd50 MAG_Gnd105 MAG_Gnd51 GND35 GND36 ) RB_Gnd_Cell3MB
x_MbGND36 ( MAG_Gnd104 MAG_Gnd52 MAG_Gnd103 GND36 GND37 ) RB_Gnd_Cell3MB
x_MbGND37 ( MAG_Gnd53 MAG_Gnd102 MAG_Gnd54 GND37 GND38 ) RB_Gnd_Cell3MB
x_MbGND38 ( MAG_Gnd101 MAG_Gnd55 MAG_Gnd100 GND38 GND39 ) RB_Gnd_Cell3MB
x_MbGND39 ( MAG_Gnd56 MAG_Gnd99 MAG_Gnd57 GND39 GND40 ) RB_Gnd_Cell3MB
x_MbGND40 ( MAG_Gnd98 MAG_Gnd58 MAG_Gnd97 GND40 GND41 ) RB_Gnd_Cell3MB
x_MbGND41 ( MAG_Gnd59 MAG_Gnd96 MAG_Gnd60 GND41 GND42 ) RB_Gnd_Cell3MB
x_MbGND42 ( MAG_Gnd95 MAG_Gnd61 MAG_Gnd94 GND42 GND43 ) RB_Gnd_Cell3MB
x_MbGND43 ( MAG_Gnd62 MAG_Gnd93 MAG_Gnd63 GND43 GND44 ) RB_Gnd_Cell3MB
x_MbGND44 ( MAG_Gnd92 MAG_Gnd64 MAG_Gnd91 GND44 GND45 ) RB_Gnd_Cell3MB
x_MbGND45 ( MAG_Gnd65 MAG_Gnd90 MAG_Gnd66 GND45 GND46 ) RB_Gnd_Cell3MB
x_MbGND46 ( MAG_Gnd89 MAG_Gnd67 MAG_Gnd88 GND46 GND47 ) RB_Gnd_Cell3MB
x_MbGND47 ( MAG_Gnd68 MAG_Gnd87 MAG_Gnd69 GND47 GND48 ) RB_Gnd_Cell3MB
x_MbGND48 ( MAG_Gnd86 MAG_Gnd70 MAG_Gnd85 GND48 GND49 ) RB_Gnd_Cell3MB
x_MbGND49 ( MAG_Gnd71 MAG_Gnd84 MAG_Gnd72 GND49 GND50 ) RB_Gnd_Cell3MB
x_MbGND50 ( MAG_Gnd83 MAG_Gnd73 MAG_Gnd82 GND50 GND51 ) RB_Gnd_Cell3MB
x_MbGND51 ( MAG_Gnd74 MAG_Gnd81 GND51 GND52 ) RB_Gnd_Cell2MB
x_MbGND52 ( MAG_Gnd75 MAG_Gnd80 GND52 GND53 ) RB_Gnd_Cell2MB
x_MbGND53 ( MAG_Gnd76 MAG_Gnd79 GND53 GND54 ) RB_Gnd_Cell2MB
x_MbGND54 ( MAG_Gnd77 MAG_Gnd78 GND54 GND54_Float ) RB_Gnd_Cell2MB
r1_VF1 ( MAG1 v_vf1 ) 20e06
r2_VF1 ( v_vf1 0 ) 24e03
r1_VF2 ( MAG3 v_vf2 ) 20e06
r2_VF2 ( v_vf2 0 ) 24e03
r1_VF3 ( MAG5 v_vf3 ) 20e06
r2_VF3 ( v_vf3 0 ) 24e03
r1_VF4 ( MAG8 v_vf4 ) 20e06
r2_VF4 ( v_vf4 0 ) 24e03
r1_VF5 ( MAG11 v_vf5 ) 20e06
r2_VF5 ( v_vf5 0 ) 24e03
r1_VF6 ( MAG14 v_vf6 ) 20e06
r2_VF6 ( v_vf6 0 ) 24e03
r1_VF7 ( MAG17 v_vf7 ) 20e06
r2_VF7 ( v_vf7 0 ) 24e03
r1_VF8 ( MAG20 v_vf8 ) 20e06
r2_VF8 ( v_vf8 0 ) 24e03
r1_VF9 ( MAG23 v_vf9 ) 20e06
r2_VF9 ( v_vf9 0 ) 24e03
r1_VF10 ( MAG26 v_vf10 ) 20e06
r2_VF10 ( v_vf10 0 ) 24e03
r1_VF11 ( MAG29 v_vf11 ) 20e06
r2_VF11 ( v_vf11 0 ) 24e03
r1_VF12 ( MAG32 v_vf12 ) 20e06
r2_VF12 ( v_vf12 0 ) 24e03
r1_VF13 ( MAG35 v_vf13 ) 20e06
r2_VF13 ( v_vf13 0 ) 24e03
r1_VF14 ( MAG38 v_vf14 ) 20e06
r2_VF14 ( v_vf14 0 ) 24e03
r1_VF15 ( MAG41 v_vf15 ) 20e06
r2_VF15 ( v_vf15 0 ) 24e03
r1_VF16 ( MAG44 v_vf16 ) 20e06
```

```
r2_VF16 ( v_vf16 0 ) 24e03
r1_VF17 ( MAG47 v_vf17 ) 20e06
r2_VF17 ( v_vf17 0 ) 24e03
r1_VF18 ( MAG50 v_vf18 ) 20e06
r2_VF18 ( v_vf18 0 ) 24e03
r1_VF19 ( MAG53 v_vf19 ) 20e06
r2_VF19 ( v_vf19 0 ) 24e03
r1_VF20 ( MAG56 v_vf20 ) 20e06
r2_VF20 ( v_vf20 0 ) 24e03
r1_VF21 ( MAG59 v_vf21 ) 20e06
r2_VF21 ( v_vf21 0 ) 24e03
r1_VF22 ( MAG62 v_vf22 ) 20e06
r2_VF22 ( v_vf22 0 ) 24e03
r1_VF23 ( MAG65 v_vf23 ) 20e06
r2_VF23 ( v_vf23 0 ) 24e03
r1_VF24 ( MAG68 v_vf24 ) 20e06
r2_VF24 ( v_vf24 0 ) 24e03
r1_VF25 ( MAG71 v_vf25 ) 20e06
r2_VF25 ( v_vf25 0 ) 24e03
r1_VF26 ( MAG74 v_vf26 ) 20e06
r2_VF26 ( v_vf26 0 ) 24e03
r1_VF27 ( MAG76 v_vf27 ) 20e06
r2_VF27 ( v_vf27 0 ) 24e03
r1_VF28 ( MAG78 v_vf28 ) 20e06
r2_VF28 ( v_vf28 0 ) 24e03
r1_VF29 ( MAG81 v_vf29 ) 20e06
r2_VF29 ( v_vf29 0 ) 24e03
r1_VF30 ( MAG82 v_vf30 ) 20e06
r2_VF30 ( v_vf30 0 ) 24e03
r1_VF31 ( MAG85 v_vf31 ) 20e06
r2_VF31 ( v_vf31 0 ) 24e03
r1_VF32 ( MAG88 v_vf32 ) 20e06
r2_VF32 ( v_vf32 0 ) 24e03
r1_VF33 ( MAG91 v_vf33 ) 20e06
r2_VF33 ( v_vf33 0 ) 24e03
r1_VF34 ( MAG94 v_vf34 ) 20e06
r2_VF34 ( v_vf34 0 ) 24e03
r1_VF35 ( MAG97 v_vf35 ) 20e06
r2_VF35 ( v_vf35 0 ) 24e03
r1_VF36 ( MAG100 v_vf36 ) 20e06
r2_VF36 ( v_vf36 0 ) 24e03
r1_VF37 ( MAG103 v_vf37 ) 20e06
r2_VF37 ( v_vf37 0 ) 24e03
r1_VF38 ( MAG106 v_vf38 ) 20e06
r2_VF38 ( v_vf38 0 ) 24e03
r1_VF39 ( MAG109 v_vf39 ) 20e06
r2_VF39 ( v_vf39 0 ) 24e03
r1_VF40 ( MAG112 v_vf40 ) 20e06
r2_VF40 ( v_vf40 0 ) 24e03
r1_VF41 ( MAG115 v_vf41 ) 20e06
r2_VF41 ( v_vf41 0 ) 24e03
r1_VF42 ( MAG118 v_vf42 ) 20e06
r2_VF42 ( v_vf42 0 ) 24e03
r1_VF43 ( MAG121 v_vf43 ) 20e06
r2_VF43 ( v_vf43 0 ) 24e03
r1_VF44 ( MAG124 v_vf44 ) 20e06
r2_VF44 ( v_vf44 0 ) 24e03
r1_VF45 ( MAG127 v_vf45 ) 20e06
r2_VF45 ( v_vf45 0 ) 24e03
r1_VF46 ( MAG130 v_vf46 ) 20e06
r2_VF46 ( v_vf46 0 ) 24e03
r1_VF47 ( MAG133 v_vf47 ) 20e06
```

```
r2_VF47 ( v_vf47 0 ) 24e03
r1_VF48 ( MAG136 v_vf48 ) 20e06
r2_VF48 ( v_vf48 0 ) 24e03
r1_VF49 ( MAG139 v_vf49 ) 20e06
r2_VF49 ( v_vf49 0 ) 24e03
r1_VF50 ( MAG142 v_vf50 ) 20e06
r2_VF50 ( v_vf50 0 ) 24e03
r1_VF51 ( MAG145 v_vf51 ) 20e06
r2_VF51 ( v_vf51 0 ) 24e03
r1_VF52 ( MAG148 v_vf52 ) 20e06
r2_VF52 ( v_vf52 0 ) 24e03
r1_VF53 ( MAG151 v_vf53 ) 20e06
r2_VF53 ( v_vf53 0 ) 24e03
r1_VF54 ( MAG153 v_vf54 ) 20e06
r2_VF54 ( v_vf54 0 ) 24e03
r_filter1 ( v_mag1 v_magf1 ) 10e03
c_filter1 ( v_magf1 0 ) 100e-09
r_filter2 ( v_mag2 v_magf2 ) 10e03
c_filter2 ( v_magf2 0 ) 100e-09
r_filter3 ( v_mag3 v_magf3 ) 10e03
c_filter3 ( v_magf3 0 ) 100e-09
r_filter4 ( v_mag4 v_magf4 ) 10e03
c_filter4 ( v_magf4 0 ) 100e-09
r_filter5 ( v_mag5 v_magf5 ) 10e03
c_filter5 ( v_magf5 0 ) 100e-09
r_filter6 ( v_mag6 v_magf6 ) 10e03
c_filter6 ( v_magf6 0 ) 100e-09
r_filter7 ( v_mag7 v_magf7 ) 10e03
c_filter7 ( v_magf7 0 ) 100e-09
r_filter8 ( v_mag8 v_magf8 ) 10e03
c_filter8 ( v_magf8 0 ) 100e-09
r_filter9 ( v_mag9 v_magf9 ) 10e03
c_filter9 ( v_magf9 0 ) 100e-09
r_filter10 ( v_mag10 v_magf10 ) 10e03
c_filter10 ( v_magf10 0 ) 100e-09
r_filter11 ( v_mag11 v_magf11 ) 10e03
c_filter11 ( v_magf11 0 ) 100e-09
r_filter12 ( v_mag12 v_magf12 ) 10e03
c_filter12 ( v_magf12 0 ) 100e-09
r_filter13 ( v_mag13 v_magf13 ) 10e03
c_filter13 ( v_magf13 0 ) 100e-09
r_filter14 ( v_mag14 v_magf14 ) 10e03
c_filter14 ( v_magf14 0 ) 100e-09
r_filter15 ( v_mag15 v_magf15 ) 10e03
c_filter15 ( v_magf15 0 ) 100e-09
r_filter16 ( v_mag16 v_magf16 ) 10e03
c_filter16 ( v_magf16 0 ) 100e-09
r_filter17 ( v_mag17 v_magf17 ) 10e03
c_filter17 ( v_magf17 0 ) 100e-09
r_filter18 ( v_mag18 v_magf18 ) 10e03
c_filter18 ( v_magf18 0 ) 100e-09
r_filter19 ( v_mag19 v_magf19 ) 10e03
c_filter19 ( v_magf19 0 ) 100e-09
r_filter20 ( v_mag20 v_magf20 ) 10e03
c_filter20 ( v_magf20 0 ) 100e-09
r_filter21 ( v_mag21 v_magf21 ) 10e03
c_filter21 ( v_magf21 0 ) 100e-09
r_filter22 ( v_mag22 v_magf22 ) 10e03
c_filter22 ( v_magf22 0 ) 100e-09
r_filter23 ( v_mag23 v_magf23 ) 10e03
c_filter23 ( v_magf23 0 ) 100e-09
r_filter24 ( v_mag24 v_magf24 ) 10e03
```

```
c_filter24 ( v_magf24 0 ) 100e-09
r_filter25 ( v_mag25 v_magf25 ) 10e03
c_filter25 ( v_magf25 0 ) 100e-09
r_filter26 ( v_mag26 v_magf26 ) 10e03
c_filter26 ( v_magf26 0 ) 100e-09
r_filter27 ( v_mag27 v_magf27 ) 10e03
c_filter27 ( v_magf27 0 ) 100e-09
r_filter28 ( v_mag28 v_magf28 ) 10e03
c_filter28 ( v_magf28 0 ) 100e-09
r_filter29 ( v_mag29 v_magf29 ) 10e03
c_filter29 ( v_magf29 0 ) 100e-09
r_filter30 ( v_mag30 v_magf30 ) 10e03
c_filter30 ( v_magf30 0 ) 100e-09
r_filter31 ( v_mag31 v_magf31 ) 10e03
c_filter31 ( v_magf31 0 ) 100e-09
r_filter32 ( v_mag32 v_magf32 ) 10e03
c_filter32 ( v_magf32 0 ) 100e-09
r_filter33 ( v_mag33 v_magf33 ) 10e03
c_filter33 ( v_magf33 0 ) 100e-09
r_filter34 ( v_mag34 v_magf34 ) 10e03
c_filter34 ( v_magf34 0 ) 100e-09
r_filter35 ( v_mag35 v_magf35 ) 10e03
c_filter35 ( v_magf35 0 ) 100e-09
r_filter36 ( v_mag36 v_magf36 ) 10e03
c_filter36 ( v_magf36 0 ) 100e-09
r_filter37 ( v_mag37 v_magf37 ) 10e03
c_filter37 ( v_magf37 0 ) 100e-09
r_filter38 ( v_mag38 v_magf38 ) 10e03
c_filter38 ( v_magf38 0 ) 100e-09
r_filter39 ( v_mag39 v_magf39 ) 10e03
c_filter39 ( v_magf39 0 ) 100e-09
r_filter40 ( v_mag40 v_magf40 ) 10e03
c_filter40 ( v_magf40 0 ) 100e-09
r_filter41 ( v_mag41 v_magf41 ) 10e03
c_filter41 ( v_magf41 0 ) 100e-09
r_filter42 ( v_mag42 v_magf42 ) 10e03
c_filter42 ( v_magf42 0 ) 100e-09
r_filter43 ( v_mag43 v_magf43 ) 10e03
c_filter43 ( v_magf43 0 ) 100e-09
r_filter44 ( v_mag44 v_magf44 ) 10e03
c_filter44 ( v_magf44 0 ) 100e-09
r_filter45 ( v_mag45 v_magf45 ) 10e03
c_filter45 ( v_magf45 0 ) 100e-09
r_filter46 ( v_mag46 v_magf46 ) 10e03
c_filter46 ( v_magf46 0 ) 100e-09
r_filter47 ( v_mag47 v_magf47 ) 10e03
c_filter47 ( v_magf47 0 ) 100e-09
r_filter48 ( v_mag48 v_magf48 ) 10e03
c_filter48 ( v_magf48 0 ) 100e-09
r_filter49 ( v_mag49 v_magf49 ) 10e03
c_filter49 ( v_magf49 0 ) 100e-09
r_filter50 ( v_mag50 v_magf50 ) 10e03
c_filter50 ( v_magf50 0 ) 100e-09
r_filter51 ( v_mag51 v_magf51 ) 10e03
c_filter51 ( v_magf51 0 ) 100e-09
r_filter52 ( v_mag52 v_magf52 ) 10e03
c_filter52 ( v_magf52 0 ) 100e-09
r_filter53 ( v_mag53 v_magf53 ) 10e03
c_filter53 ( v_magf53 0 ) 100e-09
r_filter54 ( v_mag54 v_magf54 ) 10e03
c_filter54 ( v_magf54 0 ) 100e-09
r_filter55 ( v_mag55 v_magf55 ) 10e03
```

```
c_filter55 ( v_magf55 0 ) 100e-09
r_filter56 ( v_mag56 v_magf56 ) 10e03
c_filter56 ( v_magf56 0 ) 100e-09
r_filter57 ( v_mag57 v_magf57 ) 10e03
c_filter57 ( v_magf57 0 ) 100e-09
r_filter58 ( v_mag58 v_magf58 ) 10e03
c_filter58 ( v_magf58 0 ) 100e-09
r_filter59 ( v_mag59 v_magf59 ) 10e03
c_filter59 ( v_magf59 0 ) 100e-09
r_filter60 ( v_mag60 v_magf60 ) 10e03
c_filter60 ( v_magf60 0 ) 100e-09
r_filter61 ( v_mag61 v_magf61 ) 10e03
c_filter61 ( v_magf61 0 ) 100e-09
r_filter62 ( v_mag62 v_magf62 ) 10e03
c_filter62 ( v_magf62 0 ) 100e-09
r_filter63 ( v_mag63 v_magf63 ) 10e03
c_filter63 ( v_magf63 0 ) 100e-09
r_filter64 ( v_mag64 v_magf64 ) 10e03
c_filter64 ( v_magf64 0 ) 100e-09
r_filter65 ( v_mag65 v_magf65 ) 10e03
c_filter65 ( v_magf65 0 ) 100e-09
r_filter66 ( v_mag66 v_magf66 ) 10e03
c_filter66 ( v_magf66 0 ) 100e-09
r_filter67 ( v_mag67 v_magf67 ) 10e03
c_filter67 ( v_magf67 0 ) 100e-09
r_filter68 ( v_mag68 v_magf68 ) 10e03
c_filter68 ( v_magf68 0 ) 100e-09
r_filter69 ( v_mag69 v_magf69 ) 10e03
c_filter69 ( v_magf69 0 ) 100e-09
r_filter70 ( v_mag70 v_magf70 ) 10e03
c_filter70 ( v_magf70 0 ) 100e-09
r_filter71 ( v_mag71 v_magf71 ) 10e03
c_filter71 ( v_magf71 0 ) 100e-09
r_filter72 ( v_mag72 v_magf72 ) 10e03
c_filter72 ( v_magf72 0 ) 100e-09
r_filter73 ( v_mag73 v_magf73 ) 10e03
c_filter73 ( v_magf73 0 ) 100e-09
r_filter74 ( v_mag74 v_magf74 ) 10e03
c_filter74 ( v_magf74 0 ) 100e-09
r_filter75 ( v_mag75 v_magf75 ) 10e03
c_filter75 ( v_magf75 0 ) 100e-09
r_filter76 ( v_mag76 v_magf76 ) 10e03
c_filter76 ( v_magf76 0 ) 100e-09
r_filter77 ( v_mag77 v_magf77 ) 10e03
c_filter77 ( v_magf77 0 ) 100e-09
r_filter78 ( v_mag78 v_magf78 ) 10e03
c_filter78 ( v_magf78 0 ) 100e-09
r_filter79 ( v_mag79 v_magf79 ) 10e03
c_filter79 ( v_magf79 0 ) 100e-09
r_filter80 ( v_mag80 v_magf80 ) 10e03
c_filter80 ( v_magf80 0 ) 100e-09
r_filter81 ( v_mag81 v_magf81 ) 10e03
c_filter81 ( v_magf81 0 ) 100e-09
r_filter82 ( v_mag82 v_magf82 ) 10e03
c_filter82 ( v_magf82 0 ) 100e-09
r_filter83 ( v_mag83 v_magf83 ) 10e03
c_filter83 ( v_magf83 0 ) 100e-09
r_filter84 ( v_mag84 v_magf84 ) 10e03
c_filter84 ( v_magf84 0 ) 100e-09
r_filter85 ( v_mag85 v_magf85 ) 10e03
c_filter85 ( v_magf85 0 ) 100e-09
r_filter86 ( v_mag86 v_magf86 ) 10e03
```

```
c_filter86 ( v_magf86 0 ) 100e-09
r_filter87 ( v_mag87 v_magf87 ) 10e03
c_filter87 ( v_magf87 0 ) 100e-09
r_filter88 ( v_mag88 v_magf88 ) 10e03
c_filter88 ( v_magf88 0 ) 100e-09
r_filter89 ( v_mag89 v_magf89 ) 10e03
c_filter89 ( v_magf89 0 ) 100e-09
r_filter90 ( v_mag90 v_magf90 ) 10e03
c_filter90 ( v_magf90 0 ) 100e-09
r_filter91 ( v_mag91 v_magf91 ) 10e03
c_filter91 ( v_magf91 0 ) 100e-09
r_filter92 ( v_mag92 v_magf92 ) 10e03
c_filter92 ( v_magf92 0 ) 100e-09
r_filter93 ( v_mag93 v_magf93 ) 10e03
c_filter93 ( v_magf93 0 ) 100e-09
r_filter94 ( v_mag94 v_magf94 ) 10e03
c_filter94 ( v_magf94 0 ) 100e-09
r_filter95 ( v_mag95 v_magf95 ) 10e03
c_filter95 ( v_magf95 0 ) 100e-09
r_filter96 ( v_mag96 v_magf96 ) 10e03
c_filter96 ( v_magf96 0 ) 100e-09
r_filter97 ( v_mag97 v_magf97 ) 10e03
c_filter97 ( v_magf97 0 ) 100e-09
r_filter98 ( v_mag98 v_magf98 ) 10e03
c_filter98 ( v_magf98 0 ) 100e-09
r_filter99 ( v_mag99 v_magf99 ) 10e03
c_filter99 ( v_magf99 0 ) 100e-09
r_filter100 ( v_mag100 v_magf100 ) 10e03
c_filter100 ( v_magf100 0 ) 100e-09
r_filter101 ( v_mag101 v_magf101 ) 10e03
c_filter101 ( v_magf101 0 ) 100e-09
r_filter102 ( v_mag102 v_magf102 ) 10e03
c_filter102 ( v_magf102 0 ) 100e-09
r_filter103 ( v_mag103 v_magf103 ) 10e03
c_filter103 ( v_magf103 0 ) 100e-09
r_filter104 ( v_mag104 v_magf104 ) 10e03
c_filter104 ( v_magf104 0 ) 100e-09
r_filter105 ( v_mag105 v_magf105 ) 10e03
c_filter105 ( v_magf105 0 ) 100e-09
r_filter106 ( v_mag106 v_magf106 ) 10e03
c_filter106 ( v_magf106 0 ) 100e-09
r_filter107 ( v_mag107 v_magf107 ) 10e03
c_filter107 ( v_magf107 0 ) 100e-09
r_filter108 ( v_mag108 v_magf108 ) 10e03
c_filter108 ( v_magf108 0 ) 100e-09
r_filter109 ( v_mag109 v_magf109 ) 10e03
c_filter109 ( v_magf109 0 ) 100e-09
r_filter110 ( v_mag110 v_magf110 ) 10e03
c_filter110 ( v_magf110 0 ) 100e-09
r_filter111 ( v_mag111 v_magf111 ) 10e03
c_filter111 ( v_magf111 0 ) 100e-09
r_filter112 ( v_mag112 v_magf112 ) 10e03
c_filter112 ( v_magf112 0 ) 100e-09
r_filter113 ( v_mag113 v_magf113 ) 10e03
c_filter113 ( v_magf113 0 ) 100e-09
r_filter114 ( v_mag114 v_magf114 ) 10e03
c_filter114 ( v_magf114 0 ) 100e-09
r_filter115 ( v_mag115 v_magf115 ) 10e03
c_filter115 ( v_magf115 0 ) 100e-09
r_filter116 ( v_mag116 v_magf116 ) 10e03
c_filter116 ( v_magf116 0 ) 100e-09
r_filter117 ( v_mag117 v_magf117 ) 10e03
```

```
c_filter117 ( v_magf117 0 ) 100e-09
r_filter118 ( v_mag118 v_magf118 ) 10e03
c_filter118 ( v_magf118 0 ) 100e-09
r_filter119 ( v_mag119 v_magf119 ) 10e03
c_filter119 ( v_magf119 0 ) 100e-09
r_filter120 ( v_mag120 v_magf120 ) 10e03
c_filter120 ( v_magf120 0 ) 100e-09
r_filter121 ( v_mag121 v_magf121 ) 10e03
c_filter121 ( v_magf121 0 ) 100e-09
r_filter122 ( v_mag122 v_magf122 ) 10e03
c_filter122 ( v_magf122 0 ) 100e-09
r_filter123 ( v_mag123 v_magf123 ) 10e03
c_filter123 ( v_magf123 0 ) 100e-09
r_filter124 ( v_mag124 v_magf124 ) 10e03
c_filter124 ( v_magf124 0 ) 100e-09
r_filter125 ( v_mag125 v_magf125 ) 10e03
c_filter125 ( v_magf125 0 ) 100e-09
r_filter126 ( v_mag126 v_magf126 ) 10e03
c_filter126 ( v_magf126 0 ) 100e-09
r_filter127 ( v_mag127 v_magf127 ) 10e03
c_filter127 ( v_magf127 0 ) 100e-09
r_filter128 ( v_mag128 v_magf128 ) 10e03
c_filter128 ( v_magf128 0 ) 100e-09
r_filter129 ( v_mag129 v_magf129 ) 10e03
c_filter129 ( v_magf129 0 ) 100e-09
r_filter130 ( v_mag130 v_magf130 ) 10e03
c_filter130 ( v_magf130 0 ) 100e-09
r_filter131 ( v_mag131 v_magf131 ) 10e03
c_filter131 ( v_magf131 0 ) 100e-09
r_filter132 ( v_mag132 v_magf132 ) 10e03
c_filter132 ( v_magf132 0 ) 100e-09
r_filter133 ( v_mag133 v_magf133 ) 10e03
c_filter133 ( v_magf133 0 ) 100e-09
r_filter134 ( v_mag134 v_magf134 ) 10e03
c_filter134 ( v_magf134 0 ) 100e-09
r_filter135 ( v_mag135 v_magf135 ) 10e03
c_filter135 ( v_magf135 0 ) 100e-09
r_filter136 ( v_mag136 v_magf136 ) 10e03
c_filter136 ( v_magf136 0 ) 100e-09
r_filter137 ( v_mag137 v_magf137 ) 10e03
c_filter137 ( v_magf137 0 ) 100e-09
r_filter138 ( v_mag138 v_magf138 ) 10e03
c_filter138 ( v_magf138 0 ) 100e-09
r_filter139 ( v_mag139 v_magf139 ) 10e03
c_filter139 ( v_magf139 0 ) 100e-09
r_filter140 ( v_mag140 v_magf140 ) 10e03
c_filter140 ( v_magf140 0 ) 100e-09
r_filter141 ( v_mag141 v_magf141 ) 10e03
c_filter141 ( v_magf141 0 ) 100e-09
r_filter142 ( v_mag142 v_magf142 ) 10e03
c_filter142 ( v_magf142 0 ) 100e-09
r_filter143 ( v_mag143 v_magf143 ) 10e03
c_filter143 ( v_magf143 0 ) 100e-09
r_filter144 ( v_mag144 v_magf144 ) 10e03
c_filter144 ( v_magf144 0 ) 100e-09
r_filter145 ( v_mag145 v_magf145 ) 10e03
c_filter145 ( v_magf145 0 ) 100e-09
r_filter146 ( v_mag146 v_magf146 ) 10e03
c_filter146 ( v_magf146 0 ) 100e-09
r_filter147 ( v_mag147 v_magf147 ) 10e03
c_filter147 ( v_magf147 0 ) 100e-09
r_filter148 ( v_mag148 v_magf148 ) 10e03
```

```
c_filter148 ( v_magf148 0 ) 100e-09
r_filter149 ( v_mag149 v_magf149 ) 10e03
c_filter149 ( v_magf149 0 ) 100e-09
r_filter150 ( v_mag150 v_magf150 ) 10e03
c_filter150 ( v_magf150 0 ) 100e-09
r_filter151 ( v_mag151 v_magf151 ) 10e03
c_filter151 ( v_magf151 0 ) 100e-09
r_filter152 ( v_mag152 v_magf152 ) 10e03
c_filter152 ( v_magf152 0 ) 100e-09
r_filter153 ( v_mag153 v_magf153 ) 10e03
c_filter153 ( v_magf153 0 ) 100e-09
r_filter154 ( v_mag154 v_magf154 ) 10e03
c_filter154 ( v_magf154 0 ) 100e-09
E_ABM_MAG1 ( v_mag1 0 ) VALUE { V( MAG1,MAG2 ) }
E_ABM_MAG2 ( v_mag2 0 ) VALUE { V( MAG2,MAG3 ) }
E_ABM_MAG3 ( v_mag3 0 ) VALUE { V( MAG3,MAG4 ) }
E_ABM_MAG4 ( v_mag4 0 ) VALUE { V( MAG4,MAG5 ) }
E_ABM_MAG5 ( v_mag5 0 ) VALUE { V( MAG5,MAG6 ) }
E_ABM_MAG6 ( v_mag6 0 ) VALUE { V( MAG6,MAG7 ) }
E_ABM_MAG7 ( v_mag7 0 ) VALUE { V( MAG7,MAG8 ) }
E_ABM_MAG8 ( v_mag8 0 ) VALUE { V( MAG8,MAG9 ) }
E_ABM_MAG9 ( v_mag9 0 ) VALUE { V( MAG9,MAG10 ) }
E_ABM_MAG10 ( v_mag10 0 ) VALUE { V( MAG10,MAG11 ) }
E_ABM_MAG11 ( v_mag11 0 ) VALUE { V( MAG11,MAG12 ) }
E_ABM_MAG12 ( v_mag12 0 ) VALUE { V( MAG12,MAG13 ) }
E_ABM_MAG13 ( v_mag13 0 ) VALUE { V( MAG13,MAG14 ) }
E_ABM_MAG14 ( v_mag14 0 ) VALUE { V( MAG14,MAG15 ) }
E_ABM_MAG15 ( v_mag15 0 ) VALUE { V( MAG15,MAG16 ) }
E_ABM_MAG16 ( v_mag16 0 ) VALUE { V( MAG16,MAG17 ) }
E_ABM_MAG17 ( v_mag17 0 ) VALUE { V( MAG17,MAG18 ) }
E_ABM_MAG18 ( v_mag18 0 ) VALUE { V( MAG18,MAG19 ) }
E_ABM_MAG19 ( v_mag19 0 ) VALUE { V( MAG19,MAG20 ) }
E_ABM_MAG20 ( v_mag20 0 ) VALUE { V( MAG20,MAG21 ) }
E_ABM_MAG21 ( v_mag21 0 ) VALUE { V( MAG21,MAG22 ) }
E_ABM_MAG22 ( v_mag22 0 ) VALUE { V( MAG22,MAG23 ) }
E_ABM_MAG23 ( v_mag23 0 ) VALUE { V( MAG23,MAG24 ) }
E_ABM_MAG24 ( v_mag24 0 ) VALUE { V( MAG24,MAG25 ) }
E_ABM_MAG25 ( v_mag25 0 ) VALUE { V( MAG25,MAG26 ) }
E_ABM_MAG26 ( v_mag26 0 ) VALUE { V( MAG26,MAG27 ) }
E_ABM_MAG27 ( v_mag27 0 ) VALUE { V( MAG27,MAG28 ) }
E_ABM_MAG28 ( v_mag28 0 ) VALUE { V( MAG28,MAG29 ) }
E_ABM_MAG29 ( v_mag29 0 ) VALUE { V( MAG29,MAG30 ) }
E_ABM_MAG30 ( v_mag30 0 ) VALUE { V( MAG30,MAG31 ) }
E_ABM_MAG31 ( v_mag31 0 ) VALUE { V( MAG31,MAG32 ) }
E_ABM_MAG32 ( v_mag32 0 ) VALUE { V( MAG32,MAG33 ) }
E_ABM_MAG33 ( v_mag33 0 ) VALUE { V( MAG33,MAG34 ) }
E_ABM_MAG34 ( v_mag34 0 ) VALUE { V( MAG34,MAG35 ) }
E_ABM_MAG35 ( v_mag35 0 ) VALUE { V( MAG35,MAG36 ) }
E_ABM_MAG36 ( v_mag36 0 ) VALUE { V( MAG36,MAG37 ) }
E_ABM_MAG37 ( v_mag37 0 ) VALUE { V( MAG37,MAG38 ) }
E_ABM_MAG38 ( v_mag38 0 ) VALUE { V( MAG38,MAG39 ) }
E_ABM_MAG39 ( v_mag39 0 ) VALUE { V( MAG39,MAG40 ) }
E_ABM_MAG40 ( v_mag40 0 ) VALUE { V( MAG40,MAG41 ) }
E_ABM_MAG41 ( v_mag41 0 ) VALUE { V( MAG41,MAG42 ) }
E_ABM_MAG42 ( v_mag42 0 ) VALUE { V( MAG42,MAG43 ) }
E_ABM_MAG43 ( v_mag43 0 ) VALUE { V( MAG43,MAG44 ) }
E_ABM_MAG44 ( v_mag44 0 ) VALUE { V( MAG44,MAG45 ) }
E_ABM_MAG45 ( v_mag45 0 ) VALUE { V( MAG45,MAG46 ) }
E_ABM_MAG46 ( v_mag46 0 ) VALUE { V( MAG46,MAG47 ) }
E_ABM_MAG47 ( v_mag47 0 ) VALUE { V( MAG47,MAG48 ) }
E_ABM_MAG48 ( v_mag48 0 ) VALUE { V( MAG48,MAG49 ) }
E_ABM_MAG49 ( v_mag49 0 ) VALUE { V( MAG49,MAG50 ) }
```

```
E_ABM_MAG50 ( v_mag50 0 ) VALUE { V( MAG50,MAG51 ) }
E_ABM_MAG51 ( v_mag51 0 ) VALUE { V( MAG51,MAG52 ) }
E_ABM_MAG52 ( v_mag52 0 ) VALUE { V( MAG52,MAG53 ) }
E_ABM_MAG53 ( v_mag53 0 ) VALUE { V( MAG53,MAG54 ) }
E_ABM_MAG54 ( v_mag54 0 ) VALUE { V( MAG54,MAG55 ) }
E_ABM_MAG55 ( v_mag55 0 ) VALUE { V( MAG55,MAG56 ) }
E_ABM_MAG56 ( v_mag56 0 ) VALUE { V( MAG56,MAG57 ) }
E_ABM_MAG57 ( v_mag57 0 ) VALUE { V( MAG57,MAG58 ) }
E_ABM_MAG58 ( v_mag58 0 ) VALUE { V( MAG58,MAG59 ) }
E_ABM_MAG59 ( v_mag59 0 ) VALUE { V( MAG59,MAG60 ) }
E_ABM_MAG60 ( v_mag60 0 ) VALUE { V( MAG60,MAG61 ) }
E_ABM_MAG61 ( v_mag61 0 ) VALUE { V( MAG61,MAG62 ) }
E_ABM_MAG62 ( v_mag62 0 ) VALUE { V( MAG62,MAG63 ) }
E_ABM_MAG63 ( v_mag63 0 ) VALUE { V( MAG63,MAG64 ) }
E_ABM_MAG64 ( v_mag64 0 ) VALUE { V( MAG64,MAG65 ) }
E_ABM_MAG65 ( v_mag65 0 ) VALUE { V( MAG65,MAG66 ) }
E_ABM_MAG66 ( v_mag66 0 ) VALUE { V( MAG66,MAG67 ) }
E_ABM_MAG67 ( v_mag67 0 ) VALUE { V( MAG67,MAG68 ) }
E_ABM_MAG68 ( v_mag68 0 ) VALUE { V( MAG68,MAG69 ) }
E_ABM_MAG69 ( v_mag69 0 ) VALUE { V( MAG69,MAG70 ) }
E_ABM_MAG70 ( v_mag70 0 ) VALUE { V( MAG70,MAG71 ) }
E_ABM_MAG71 ( v_mag71 0 ) VALUE { V( MAG71,MAG72 ) }
E_ABM_MAG72 ( v_mag72 0 ) VALUE { V( MAG72,MAG73 ) }
E_ABM_MAG73 ( v_mag73 0 ) VALUE { V( MAG73,MAG74 ) }
E_ABM_MAG74 ( v_mag74 0 ) VALUE { V( MAG74,MAG75 ) }
E_ABM_MAG75 ( v_mag75 0 ) VALUE { V( MAG75,MAG76 ) }
E_ABM_MAG76 ( v_mag76 0 ) VALUE { V( MAG76,MAG77 ) }
E_ABM_MAG77 ( v_mag77 0 ) VALUE { V( MAG77,MAG77_Out ) }
E_ABM_MAG78 ( v_mag78 0 ) VALUE { V( MAG78,MAG79 ) }
E_ABM_MAG79 ( v_mag79 0 ) VALUE { V( MAG79,MAG80 ) }
E_ABM_MAG80 ( v_mag80 0 ) VALUE { V( MAG80,MAG81 ) }
E_ABM_MAG81 ( v_mag81 0 ) VALUE { V( MAG81,MAG82 ) }
E_ABM_MAG82 ( v_mag82 0 ) VALUE { V( MAG82,MAG83 ) }
E_ABM_MAG83 ( v_mag83 0 ) VALUE { V( MAG83,MAG84 ) }
E_ABM_MAG84 ( v_mag84 0 ) VALUE { V( MAG84,MAG85 ) }
E_ABM_MAG85 ( v_mag85 0 ) VALUE { V( MAG85,MAG86 ) }
E_ABM_MAG86 ( v_mag86 0 ) VALUE { V( MAG86,MAG87 ) }
E_ABM_MAG87 ( v_mag87 0 ) VALUE { V( MAG87,MAG88 ) }
E_ABM_MAG88 ( v_mag88 0 ) VALUE { V( MAG88,MAG89 ) }
E_ABM_MAG89 ( v_mag89 0 ) VALUE { V( MAG89,MAG90 ) }
E_ABM_MAG90 ( v_mag90 0 ) VALUE { V( MAG90,MAG91 ) }
E_ABM_MAG91 ( v_mag91 0 ) VALUE { V( MAG91,MAG92 ) }
E_ABM_MAG92 ( v_mag92 0 ) VALUE { V( MAG92,MAG93 ) }
E_ABM_MAG93 ( v_mag93 0 ) VALUE { V( MAG93,MAG94 ) }
E_ABM_MAG94 ( v_mag94 0 ) VALUE { V( MAG94,MAG95 ) }
E_ABM_MAG95 ( v_mag95 0 ) VALUE { V( MAG95,MAG96 ) }
E_ABM_MAG96 ( v_mag96 0 ) VALUE { V( MAG96,MAG97 ) }
E_ABM_MAG97 ( v_mag97 0 ) VALUE { V( MAG97,MAG98 ) }
E_ABM_MAG98 ( v_mag98 0 ) VALUE { V( MAG98,MAG99 ) }
E_ABM_MAG99 ( v_mag99 0 ) VALUE { V( MAG99,MAG100 ) }
E_ABM_MAG100 ( v_mag100 0 ) VALUE { V( MAG100,MAG101 ) }
E_ABM_MAG101 ( v_mag101 0 ) VALUE { V( MAG101,MAG102 ) }
E_ABM_MAG102 ( v_mag102 0 ) VALUE { V( MAG102,MAG103 ) }
E_ABM_MAG103 ( v_mag103 0 ) VALUE { V( MAG103,MAG104 ) }
E_ABM_MAG104 ( v_mag104 0 ) VALUE { V( MAG104,MAG105 ) }
E_ABM_MAG105 ( v_mag105 0 ) VALUE { V( MAG105,MAG106 ) }
E_ABM_MAG106 ( v_mag106 0 ) VALUE { V( MAG106,MAG107 ) }
E_ABM_MAG107 ( v_mag107 0 ) VALUE { V( MAG107,MAG108 ) }
E_ABM_MAG108 ( v_mag108 0 ) VALUE { V( MAG108,MAG109 ) }
E_ABM_MAG109 ( v_mag109 0 ) VALUE { V( MAG109,MAG110 ) }
E_ABM_MAG110 ( v_mag110 0 ) VALUE { V( MAG110,MAG111 ) }
E_ABM_MAG111 ( v_mag111 0 ) VALUE { V( MAG111,MAG112 ) }
```

```
E_ABM_MAG112  ( v_mag112 0 )  VALUE {  V( MAG112,MAG113 )  }
E_ABM_MAG113  ( v_mag113 0 )  VALUE {  V( MAG113,MAG114 )  }
E_ABM_MAG114  ( v_mag114 0 )  VALUE {  V( MAG114,MAG115 )  }
E_ABM_MAG115  ( v_mag115 0 )  VALUE {  V( MAG115,MAG116 )  }
E_ABM_MAG116  ( v_mag116 0 )  VALUE {  V( MAG116,MAG117 )  }
E_ABM_MAG117  ( v_mag117 0 )  VALUE {  V( MAG117,MAG118 )  }
E_ABM_MAG118  ( v_mag118 0 )  VALUE {  V( MAG118,MAG119 )  }
E_ABM_MAG119  ( v_mag119 0 )  VALUE {  V( MAG119,MAG120 )  }
E_ABM_MAG120  ( v_mag120 0 )  VALUE {  V( MAG120,MAG121 )  }
E_ABM_MAG121  ( v_mag121 0 )  VALUE {  V( MAG121,MAG122 )  }
E_ABM_MAG122  ( v_mag122 0 )  VALUE {  V( MAG122,MAG123 )  }
E_ABM_MAG123  ( v_mag123 0 )  VALUE {  V( MAG123,MAG124 )  }
E_ABM_MAG124  ( v_mag124 0 )  VALUE {  V( MAG124,MAG125 )  }
E_ABM_MAG125  ( v_mag125 0 )  VALUE {  V( MAG125,MAG126 )  }
E_ABM_MAG126  ( v_mag126 0 )  VALUE {  V( MAG126,MAG127 )  }
E_ABM_MAG127  ( v_mag127 0 )  VALUE {  V( MAG127,MAG128 )  }
E_ABM_MAG128  ( v_mag128 0 )  VALUE {  V( MAG128,MAG129 )  }
E_ABM_MAG129  ( v_mag129 0 )  VALUE {  V( MAG129,MAG130 )  }
E_ABM_MAG130  ( v_mag130 0 )  VALUE {  V( MAG130,MAG131 )  }
E_ABM_MAG131  ( v_mag131 0 )  VALUE {  V( MAG131,MAG132 )  }
E_ABM_MAG132  ( v_mag132 0 )  VALUE {  V( MAG132,MAG133 )  }
E_ABM_MAG133  ( v_mag133 0 )  VALUE {  V( MAG133,MAG134 )  }
E_ABM_MAG134  ( v_mag134 0 )  VALUE {  V( MAG134,MAG135 )  }
E_ABM_MAG135  ( v_mag135 0 )  VALUE {  V( MAG135,MAG136 )  }
E_ABM_MAG136  ( v_mag136 0 )  VALUE {  V( MAG136,MAG137 )  }
E_ABM_MAG137  ( v_mag137 0 )  VALUE {  V( MAG137,MAG138 )  }
E_ABM_MAG138  ( v_mag138 0 )  VALUE {  V( MAG138,MAG139 )  }
E_ABM_MAG139  ( v_mag139 0 )  VALUE {  V( MAG139,MAG140 )  }
E_ABM_MAG140  ( v_mag140 0 )  VALUE {  V( MAG140,MAG141 )  }
E_ABM_MAG141  ( v_mag141 0 )  VALUE {  V( MAG141,MAG142 )  }
E_ABM_MAG142  ( v_mag142 0 )  VALUE {  V( MAG142,MAG143 )  }
E_ABM_MAG143  ( v_mag143 0 )  VALUE {  V( MAG143,MAG144 )  }
E_ABM_MAG144  ( v_mag144 0 )  VALUE {  V( MAG144,MAG145 )  }
E_ABM_MAG145  ( v_mag145 0 )  VALUE {  V( MAG145,MAG146 )  }
E_ABM_MAG146  ( v_mag146 0 )  VALUE {  V( MAG146,MAG147 )  }
E_ABM_MAG147  ( v_mag147 0 )  VALUE {  V( MAG147,MAG148 )  }
E_ABM_MAG148  ( v_mag148 0 )  VALUE {  V( MAG148,MAG149 )  }
E_ABM_MAG149  ( v_mag149 0 )  VALUE {  V( MAG149,MAG150 )  }
E_ABM_MAG150  ( v_mag150 0 )  VALUE {  V( MAG150,MAG151 )  }
E_ABM_MAG151  ( v_mag151 0 )  VALUE {  V( MAG151,MAG152 )  }
E_ABM_MAG152  ( v_mag152 0 )  VALUE {  V( MAG152,MAG153 )  }
E_ABM_MAG153  ( v_mag153 0 )  VALUE {  V( MAG153,MAG154 )  }
E_ABM_MAG154  ( v_mag154 0 )  VALUE {  V( MAG154,MAG154_Out )  }
E_ABM_1stAP_MAG1  ( v_ApA1 0 )  VALUE {  V( MAG1,MAG_Mid1 )  }
E_ABM_1stAP_MAG2  ( v_ApA2 0 )  VALUE {  V( MAG2,MAG_Mid2 )  }
E_ABM_1stAP_MAG3  ( v_ApA3 0 )  VALUE {  V( MAG3,MAG_Mid3 )  }
E_ABM_1stAP_MAG4  ( v_ApA4 0 )  VALUE {  V( MAG4,MAG_Mid4 )  }
E_ABM_1stAP_MAG5  ( v_ApA5 0 )  VALUE {  V( MAG5,MAG_Mid5 )  }
E_ABM_1stAP_MAG6  ( v_ApA6 0 )  VALUE {  V( MAG6,MAG_Mid6 )  }
E_ABM_1stAP_MAG7  ( v_ApA7 0 )  VALUE {  V( MAG7,MAG_Mid7 )  }
E_ABM_1stAP_MAG8  ( v_ApA8 0 )  VALUE {  V( MAG8,MAG_Mid8 )  }
E_ABM_1stAP_MAG9  ( v_ApA9 0 )  VALUE {  V( MAG9,MAG_Mid9 )  }
E_ABM_1stAP_MAG10  ( v_ApA10 0 )  VALUE {  V( MAG10,MAG_Mid10 )  }
E_ABM_1stAP_MAG11  ( v_ApA11 0 )  VALUE {  V( MAG11,MAG_Mid11 )  }
E_ABM_1stAP_MAG12  ( v_ApA12 0 )  VALUE {  V( MAG12,MAG_Mid12 )  }
E_ABM_1stAP_MAG13  ( v_ApA13 0 )  VALUE {  V( MAG13,MAG_Mid13 )  }
E_ABM_1stAP_MAG14  ( v_ApA14 0 )  VALUE {  V( MAG14,MAG_Mid14 )  }
E_ABM_1stAP_MAG15  ( v_ApA15 0 )  VALUE {  V( MAG15,MAG_Mid15 )  }
E_ABM_1stAP_MAG16  ( v_ApA16 0 )  VALUE {  V( MAG16,MAG_Mid16 )  }
E_ABM_1stAP_MAG17  ( v_ApA17 0 )  VALUE {  V( MAG17,MAG_Mid17 )  }
E_ABM_1stAP_MAG18  ( v_ApA18 0 )  VALUE {  V( MAG18,MAG_Mid18 )  }
E_ABM_1stAP_MAG19  ( v_ApA19 0 )  VALUE {  V( MAG19,MAG_Mid19 )  }
```

```
E_ABM_1stAP_MAG20  ( v_ApA20 0 )  VALUE {  V( MAG20,MAG_Mid20 )  }
E_ABM_1stAP_MAG21  ( v_ApA21 0 )  VALUE {  V( MAG21,MAG_Mid21 )  }
E_ABM_1stAP_MAG22  ( v_ApA22 0 )  VALUE {  V( MAG22,MAG_Mid22 )  }
E_ABM_1stAP_MAG23  ( v_ApA23 0 )  VALUE {  V( MAG23,MAG_Mid23 )  }
E_ABM_1stAP_MAG24  ( v_ApA24 0 )  VALUE {  V( MAG24,MAG_Mid24 )  }
E_ABM_1stAP_MAG25  ( v_ApA25 0 )  VALUE {  V( MAG25,MAG_Mid25 )  }
E_ABM_1stAP_MAG26  ( v_ApA26 0 )  VALUE {  V( MAG26,MAG_Mid26 )  }
E_ABM_1stAP_MAG27  ( v_ApA27 0 )  VALUE {  V( MAG27,MAG_Mid27 )  }
E_ABM_1stAP_MAG28  ( v_ApA28 0 )  VALUE {  V( MAG28,MAG_Mid28 )  }
E_ABM_1stAP_MAG29  ( v_ApA29 0 )  VALUE {  V( MAG29,MAG_Mid29 )  }
E_ABM_1stAP_MAG30  ( v_ApA30 0 )  VALUE {  V( MAG30,MAG_Mid30 )  }
E_ABM_1stAP_MAG31  ( v_ApA31 0 )  VALUE {  V( MAG31,MAG_Mid31 )  }
E_ABM_1stAP_MAG32  ( v_ApA32 0 )  VALUE {  V( MAG32,MAG_Mid32 )  }
E_ABM_1stAP_MAG33  ( v_ApA33 0 )  VALUE {  V( MAG33,MAG_Mid33 )  }
E_ABM_1stAP_MAG34  ( v_ApA34 0 )  VALUE {  V( MAG34,MAG_Mid34 )  }
E_ABM_1stAP_MAG35  ( v_ApA35 0 )  VALUE {  V( MAG35,MAG_Mid35 )  }
E_ABM_1stAP_MAG36  ( v_ApA36 0 )  VALUE {  V( MAG36,MAG_Mid36 )  }
E_ABM_1stAP_MAG37  ( v_ApA37 0 )  VALUE {  V( MAG37,MAG_Mid37 )  }
E_ABM_1stAP_MAG38  ( v_ApA38 0 )  VALUE {  V( MAG38,MAG_Mid38 )  }
E_ABM_1stAP_MAG39  ( v_ApA39 0 )  VALUE {  V( MAG39,MAG_Mid39 )  }
E_ABM_1stAP_MAG40  ( v_ApA40 0 )  VALUE {  V( MAG40,MAG_Mid40 )  }
E_ABM_1stAP_MAG41  ( v_ApA41 0 )  VALUE {  V( MAG41,MAG_Mid41 )  }
E_ABM_1stAP_MAG42  ( v_ApA42 0 )  VALUE {  V( MAG42,MAG_Mid42 )  }
E_ABM_1stAP_MAG43  ( v_ApA43 0 )  VALUE {  V( MAG43,MAG_Mid43 )  }
E_ABM_1stAP_MAG44  ( v_ApA44 0 )  VALUE {  V( MAG44,MAG_Mid44 )  }
E_ABM_1stAP_MAG45  ( v_ApA45 0 )  VALUE {  V( MAG45,MAG_Mid45 )  }
E_ABM_1stAP_MAG46  ( v_ApA46 0 )  VALUE {  V( MAG46,MAG_Mid46 )  }
E_ABM_1stAP_MAG47  ( v_ApA47 0 )  VALUE {  V( MAG47,MAG_Mid47 )  }
E_ABM_1stAP_MAG48  ( v_ApA48 0 )  VALUE {  V( MAG48,MAG_Mid48 )  }
E_ABM_1stAP_MAG49  ( v_ApA49 0 )  VALUE {  V( MAG49,MAG_Mid49 )  }
E_ABM_1stAP_MAG50  ( v_ApA50 0 )  VALUE {  V( MAG50,MAG_Mid50 )  }
E_ABM_1stAP_MAG51  ( v_ApA51 0 )  VALUE {  V( MAG51,MAG_Mid51 )  }
E_ABM_1stAP_MAG52  ( v_ApA52 0 )  VALUE {  V( MAG52,MAG_Mid52 )  }
E_ABM_1stAP_MAG53  ( v_ApA53 0 )  VALUE {  V( MAG53,MAG_Mid53 )  }
E_ABM_1stAP_MAG54  ( v_ApA54 0 )  VALUE {  V( MAG54,MAG_Mid54 )  }
E_ABM_1stAP_MAG55  ( v_ApA55 0 )  VALUE {  V( MAG55,MAG_Mid55 )  }
E_ABM_1stAP_MAG56  ( v_ApA56 0 )  VALUE {  V( MAG56,MAG_Mid56 )  }
E_ABM_1stAP_MAG57  ( v_ApA57 0 )  VALUE {  V( MAG57,MAG_Mid57 )  }
E_ABM_1stAP_MAG58  ( v_ApA58 0 )  VALUE {  V( MAG58,MAG_Mid58 )  }
E_ABM_1stAP_MAG59  ( v_ApA59 0 )  VALUE {  V( MAG59,MAG_Mid59 )  }
E_ABM_1stAP_MAG60  ( v_ApA60 0 )  VALUE {  V( MAG60,MAG_Mid60 )  }
E_ABM_1stAP_MAG61  ( v_ApA61 0 )  VALUE {  V( MAG61,MAG_Mid61 )  }
E_ABM_1stAP_MAG62  ( v_ApA62 0 )  VALUE {  V( MAG62,MAG_Mid62 )  }
E_ABM_1stAP_MAG63  ( v_ApA63 0 )  VALUE {  V( MAG63,MAG_Mid63 )  }
E_ABM_1stAP_MAG64  ( v_ApA64 0 )  VALUE {  V( MAG64,MAG_Mid64 )  }
E_ABM_1stAP_MAG65  ( v_ApA65 0 )  VALUE {  V( MAG65,MAG_Mid65 )  }
E_ABM_1stAP_MAG66  ( v_ApA66 0 )  VALUE {  V( MAG66,MAG_Mid66 )  }
E_ABM_1stAP_MAG67  ( v_ApA67 0 )  VALUE {  V( MAG67,MAG_Mid67 )  }
E_ABM_1stAP_MAG68  ( v_ApA68 0 )  VALUE {  V( MAG68,MAG_Mid68 )  }
E_ABM_1stAP_MAG69  ( v_ApA69 0 )  VALUE {  V( MAG69,MAG_Mid69 )  }
E_ABM_1stAP_MAG70  ( v_ApA70 0 )  VALUE {  V( MAG70,MAG_Mid70 )  }
E_ABM_1stAP_MAG71  ( v_ApA71 0 )  VALUE {  V( MAG71,MAG_Mid71 )  }
E_ABM_1stAP_MAG72  ( v_ApA72 0 )  VALUE {  V( MAG72,MAG_Mid72 )  }
E_ABM_1stAP_MAG73  ( v_ApA73 0 )  VALUE {  V( MAG73,MAG_Mid73 )  }
E_ABM_1stAP_MAG74  ( v_ApA74 0 )  VALUE {  V( MAG74,MAG_Mid74 )  }
E_ABM_1stAP_MAG75  ( v_ApA75 0 )  VALUE {  V( MAG75,MAG_Mid75 )  }
E_ABM_1stAP_MAG76  ( v_ApA76 0 )  VALUE {  V( MAG76,MAG_Mid76 )  }
E_ABM_1stAP_MAG77  ( v_ApA77 0 )  VALUE {  V( MAG77,MAG_Mid77 )  }
E_ABM_1stAP_MAG78  ( v_ApA78 0 )  VALUE {  V( MAG78,MAG_Mid78 )  }
E_ABM_1stAP_MAG79  ( v_ApA79 0 )  VALUE {  V( MAG79,MAG_Mid79 )  }
E_ABM_1stAP_MAG80  ( v_ApA80 0 )  VALUE {  V( MAG80,MAG_Mid80 )  }
E_ABM_1stAP_MAG81  ( v_ApA81 0 )  VALUE {  V( MAG81,MAG_Mid81 )  }
```

```
E_ABM_1stAP_MAG82  ( v_ApA82 0 )  VALUE {  V( MAG82,MAG_Mid82 )  }
E_ABM_1stAP_MAG83  ( v_ApA83 0 )  VALUE {  V( MAG83,MAG_Mid83 )  }
E_ABM_1stAP_MAG84  ( v_ApA84 0 )  VALUE {  V( MAG84,MAG_Mid84 )  }
E_ABM_1stAP_MAG85  ( v_ApA85 0 )  VALUE {  V( MAG85,MAG_Mid85 )  }
E_ABM_1stAP_MAG86  ( v_ApA86 0 )  VALUE {  V( MAG86,MAG_Mid86 )  }
E_ABM_1stAP_MAG87  ( v_ApA87 0 )  VALUE {  V( MAG87,MAG_Mid87 )  }
E_ABM_1stAP_MAG88  ( v_ApA88 0 )  VALUE {  V( MAG88,MAG_Mid88 )  }
E_ABM_1stAP_MAG89  ( v_ApA89 0 )  VALUE {  V( MAG89,MAG_Mid89 )  }
E_ABM_1stAP_MAG90  ( v_ApA90 0 )  VALUE {  V( MAG90,MAG_Mid90 )  }
E_ABM_1stAP_MAG91  ( v_ApA91 0 )  VALUE {  V( MAG91,MAG_Mid91 )  }
E_ABM_1stAP_MAG92  ( v_ApA92 0 )  VALUE {  V( MAG92,MAG_Mid92 )  }
E_ABM_1stAP_MAG93  ( v_ApA93 0 )  VALUE {  V( MAG93,MAG_Mid93 )  }
E_ABM_1stAP_MAG94  ( v_ApA94 0 )  VALUE {  V( MAG94,MAG_Mid94 )  }
E_ABM_1stAP_MAG95  ( v_ApA95 0 )  VALUE {  V( MAG95,MAG_Mid95 )  }
E_ABM_1stAP_MAG96  ( v_ApA96 0 )  VALUE {  V( MAG96,MAG_Mid96 )  }
E_ABM_1stAP_MAG97  ( v_ApA97 0 )  VALUE {  V( MAG97,MAG_Mid97 )  }
E_ABM_1stAP_MAG98  ( v_ApA98 0 )  VALUE {  V( MAG98,MAG_Mid98 )  }
E_ABM_1stAP_MAG99  ( v_ApA99 0 )  VALUE {  V( MAG99,MAG_Mid99 )  }
E_ABM_1stAP_MAG100  ( v_ApA100 0 )  VALUE {  V( MAG100,MAG_Mid100 )  }
E_ABM_1stAP_MAG101  ( v_ApA101 0 )  VALUE {  V( MAG101,MAG_Mid101 )  }
E_ABM_1stAP_MAG102  ( v_ApA102 0 )  VALUE {  V( MAG102,MAG_Mid102 )  }
E_ABM_1stAP_MAG103  ( v_ApA103 0 )  VALUE {  V( MAG103,MAG_Mid103 )  }
E_ABM_1stAP_MAG104  ( v_ApA104 0 )  VALUE {  V( MAG104,MAG_Mid104 )  }
E_ABM_1stAP_MAG105  ( v_ApA105 0 )  VALUE {  V( MAG105,MAG_Mid105 )  }
E_ABM_1stAP_MAG106  ( v_ApA106 0 )  VALUE {  V( MAG106,MAG_Mid106 )  }
E_ABM_1stAP_MAG107  ( v_ApA107 0 )  VALUE {  V( MAG107,MAG_Mid107 )  }
E_ABM_1stAP_MAG108  ( v_ApA108 0 )  VALUE {  V( MAG108,MAG_Mid108 )  }
E_ABM_1stAP_MAG109  ( v_ApA109 0 )  VALUE {  V( MAG109,MAG_Mid109 )  }
E_ABM_1stAP_MAG110  ( v_ApA110 0 )  VALUE {  V( MAG110,MAG_Mid110 )  }
E_ABM_1stAP_MAG111  ( v_ApA111 0 )  VALUE {  V( MAG111,MAG_Mid111 )  }
E_ABM_1stAP_MAG112  ( v_ApA112 0 )  VALUE {  V( MAG112,MAG_Mid112 )  }
E_ABM_1stAP_MAG113  ( v_ApA113 0 )  VALUE {  V( MAG113,MAG_Mid113 )  }
E_ABM_1stAP_MAG114  ( v_ApA114 0 )  VALUE {  V( MAG114,MAG_Mid114 )  }
E_ABM_1stAP_MAG115  ( v_ApA115 0 )  VALUE {  V( MAG115,MAG_Mid115 )  }
E_ABM_1stAP_MAG116  ( v_ApA116 0 )  VALUE {  V( MAG116,MAG_Mid116 )  }
E_ABM_1stAP_MAG117  ( v_ApA117 0 )  VALUE {  V( MAG117,MAG_Mid117 )  }
E_ABM_1stAP_MAG118  ( v_ApA118 0 )  VALUE {  V( MAG118,MAG_Mid118 )  }
E_ABM_1stAP_MAG119  ( v_ApA119 0 )  VALUE {  V( MAG119,MAG_Mid119 )  }
E_ABM_1stAP_MAG120  ( v_ApA120 0 )  VALUE {  V( MAG120,MAG_Mid120 )  }
E_ABM_1stAP_MAG121  ( v_ApA121 0 )  VALUE {  V( MAG121,MAG_Mid121 )  }
E_ABM_1stAP_MAG122  ( v_ApA122 0 )  VALUE {  V( MAG122,MAG_Mid122 )  }
E_ABM_1stAP_MAG123  ( v_ApA123 0 )  VALUE {  V( MAG123,MAG_Mid123 )  }
E_ABM_1stAP_MAG124  ( v_ApA124 0 )  VALUE {  V( MAG124,MAG_Mid124 )  }
E_ABM_1stAP_MAG125  ( v_ApA125 0 )  VALUE {  V( MAG125,MAG_Mid125 )  }
E_ABM_1stAP_MAG126  ( v_ApA126 0 )  VALUE {  V( MAG126,MAG_Mid126 )  }
E_ABM_1stAP_MAG127  ( v_ApA127 0 )  VALUE {  V( MAG127,MAG_Mid127 )  }
E_ABM_1stAP_MAG128  ( v_ApA128 0 )  VALUE {  V( MAG128,MAG_Mid128 )  }
E_ABM_1stAP_MAG129  ( v_ApA129 0 )  VALUE {  V( MAG129,MAG_Mid129 )  }
E_ABM_1stAP_MAG130  ( v_ApA130 0 )  VALUE {  V( MAG130,MAG_Mid130 )  }
E_ABM_1stAP_MAG131  ( v_ApA131 0 )  VALUE {  V( MAG131,MAG_Mid131 )  }
E_ABM_1stAP_MAG132  ( v_ApA132 0 )  VALUE {  V( MAG132,MAG_Mid132 )  }
E_ABM_1stAP_MAG133  ( v_ApA133 0 )  VALUE {  V( MAG133,MAG_Mid133 )  }
E_ABM_1stAP_MAG134  ( v_ApA134 0 )  VALUE {  V( MAG134,MAG_Mid134 )  }
E_ABM_1stAP_MAG135  ( v_ApA135 0 )  VALUE {  V( MAG135,MAG_Mid135 )  }
E_ABM_1stAP_MAG136  ( v_ApA136 0 )  VALUE {  V( MAG136,MAG_Mid136 )  }
E_ABM_1stAP_MAG137  ( v_ApA137 0 )  VALUE {  V( MAG137,MAG_Mid137 )  }
E_ABM_1stAP_MAG138  ( v_ApA138 0 )  VALUE {  V( MAG138,MAG_Mid138 )  }
E_ABM_1stAP_MAG139  ( v_ApA139 0 )  VALUE {  V( MAG139,MAG_Mid139 )  }
E_ABM_1stAP_MAG140  ( v_ApA140 0 )  VALUE {  V( MAG140,MAG_Mid140 )  }
E_ABM_1stAP_MAG141  ( v_ApA141 0 )  VALUE {  V( MAG141,MAG_Mid141 )  }
E_ABM_1stAP_MAG142  ( v_ApA142 0 )  VALUE {  V( MAG142,MAG_Mid142 )  }
E_ABM_1stAP_MAG143  ( v_ApA143 0 )  VALUE {  V( MAG143,MAG_Mid143 )  }
```

```
E_ABM_1stAP_MAG144 ( v_ApA144 0 ) VALUE { V( MAG144,MAG_Mid144 ) }
E_ABM_1stAP_MAG145 ( v_ApA145 0 ) VALUE { V( MAG145,MAG_Mid145 ) }
E_ABM_1stAP_MAG146 ( v_ApA146 0 ) VALUE { V( MAG146,MAG_Mid146 ) }
E_ABM_1stAP_MAG147 ( v_ApA147 0 ) VALUE { V( MAG147,MAG_Mid147 ) }
E_ABM_1stAP_MAG148 ( v_ApA148 0 ) VALUE { V( MAG148,MAG_Mid148 ) }
E_ABM_1stAP_MAG149 ( v_ApA149 0 ) VALUE { V( MAG149,MAG_Mid149 ) }
E_ABM_1stAP_MAG150 ( v_ApA150 0 ) VALUE { V( MAG150,MAG_Mid150 ) }
E_ABM_1stAP_MAG151 ( v_ApA151 0 ) VALUE { V( MAG151,MAG_Mid151 ) }
E_ABM_1stAP_MAG152 ( v_ApA152 0 ) VALUE { V( MAG152,MAG_Mid152 ) }
E_ABM_1stAP_MAG153 ( v_ApA153 0 ) VALUE { V( MAG153,MAG_Mid153 ) }
E_ABM_1stAP_MAG154 ( v_ApA154 0 ) VALUE { V( MAG154,MAG_Mid154 ) }
E_ABM_2ndAP_MAG1 ( v_ApB1 0 ) VALUE { V( MAG_Mid1,MAG2 ) }
E_ABM_2ndAP_MAG2 ( v_ApB2 0 ) VALUE { V( MAG_Mid2,MAG3 ) }
E_ABM_2ndAP_MAG3 ( v_ApB3 0 ) VALUE { V( MAG_Mid3,MAG4 ) }
E_ABM_2ndAP_MAG4 ( v_ApB4 0 ) VALUE { V( MAG_Mid4,MAG5 ) }
E_ABM_2ndAP_MAG5 ( v_ApB5 0 ) VALUE { V( MAG_Mid5,MAG6 ) }
E_ABM_2ndAP_MAG6 ( v_ApB6 0 ) VALUE { V( MAG_Mid6,MAG7 ) }
E_ABM_2ndAP_MAG7 ( v_ApB7 0 ) VALUE { V( MAG_Mid7,MAG8 ) }
E_ABM_2ndAP_MAG8 ( v_ApB8 0 ) VALUE { V( MAG_Mid8,MAG9 ) }
E_ABM_2ndAP_MAG9 ( v_ApB9 0 ) VALUE { V( MAG_Mid9,MAG10 ) }
E_ABM_2ndAP_MAG10 ( v_ApB10 0 ) VALUE { V( MAG_Mid10,MAG11 ) }
E_ABM_2ndAP_MAG11 ( v_ApB11 0 ) VALUE { V( MAG_Mid11,MAG12 ) }
E_ABM_2ndAP_MAG12 ( v_ApB12 0 ) VALUE { V( MAG_Mid12,MAG13 ) }
E_ABM_2ndAP_MAG13 ( v_ApB13 0 ) VALUE { V( MAG_Mid13,MAG14 ) }
E_ABM_2ndAP_MAG14 ( v_ApB14 0 ) VALUE { V( MAG_Mid14,MAG15 ) }
E_ABM_2ndAP_MAG15 ( v_ApB15 0 ) VALUE { V( MAG_Mid15,MAG16 ) }
E_ABM_2ndAP_MAG16 ( v_ApB16 0 ) VALUE { V( MAG_Mid16,MAG17 ) }
E_ABM_2ndAP_MAG17 ( v_ApB17 0 ) VALUE { V( MAG_Mid17,MAG18 ) }
E_ABM_2ndAP_MAG18 ( v_ApB18 0 ) VALUE { V( MAG_Mid18,MAG19 ) }
E_ABM_2ndAP_MAG19 ( v_ApB19 0 ) VALUE { V( MAG_Mid19,MAG20 ) }
E_ABM_2ndAP_MAG20 ( v_ApB20 0 ) VALUE { V( MAG_Mid20,MAG21 ) }
E_ABM_2ndAP_MAG21 ( v_ApB21 0 ) VALUE { V( MAG_Mid21,MAG22 ) }
E_ABM_2ndAP_MAG22 ( v_ApB22 0 ) VALUE { V( MAG_Mid22,MAG23 ) }
E_ABM_2ndAP_MAG23 ( v_ApB23 0 ) VALUE { V( MAG_Mid23,MAG24 ) }
E_ABM_2ndAP_MAG24 ( v_ApB24 0 ) VALUE { V( MAG_Mid24,MAG25 ) }
E_ABM_2ndAP_MAG25 ( v_ApB25 0 ) VALUE { V( MAG_Mid25,MAG26 ) }
E_ABM_2ndAP_MAG26 ( v_ApB26 0 ) VALUE { V( MAG_Mid26,MAG27 ) }
E_ABM_2ndAP_MAG27 ( v_ApB27 0 ) VALUE { V( MAG_Mid27,MAG28 ) }
E_ABM_2ndAP_MAG28 ( v_ApB28 0 ) VALUE { V( MAG_Mid28,MAG29 ) }
E_ABM_2ndAP_MAG29 ( v_ApB29 0 ) VALUE { V( MAG_Mid29,MAG30 ) }
E_ABM_2ndAP_MAG30 ( v_ApB30 0 ) VALUE { V( MAG_Mid30,MAG31 ) }
E_ABM_2ndAP_MAG31 ( v_ApB31 0 ) VALUE { V( MAG_Mid31,MAG32 ) }
E_ABM_2ndAP_MAG32 ( v_ApB32 0 ) VALUE { V( MAG_Mid32,MAG33 ) }
E_ABM_2ndAP_MAG33 ( v_ApB33 0 ) VALUE { V( MAG_Mid33,MAG34 ) }
E_ABM_2ndAP_MAG34 ( v_ApB34 0 ) VALUE { V( MAG_Mid34,MAG35 ) }
E_ABM_2ndAP_MAG35 ( v_ApB35 0 ) VALUE { V( MAG_Mid35,MAG36 ) }
E_ABM_2ndAP_MAG36 ( v_ApB36 0 ) VALUE { V( MAG_Mid36,MAG37 ) }
E_ABM_2ndAP_MAG37 ( v_ApB37 0 ) VALUE { V( MAG_Mid37,MAG38 ) }
E_ABM_2ndAP_MAG38 ( v_ApB38 0 ) VALUE { V( MAG_Mid38,MAG39 ) }
E_ABM_2ndAP_MAG39 ( v_ApB39 0 ) VALUE { V( MAG_Mid39,MAG40 ) }
E_ABM_2ndAP_MAG40 ( v_ApB40 0 ) VALUE { V( MAG_Mid40,MAG41 ) }
E_ABM_2ndAP_MAG41 ( v_ApB41 0 ) VALUE { V( MAG_Mid41,MAG42 ) }
E_ABM_2ndAP_MAG42 ( v_ApB42 0 ) VALUE { V( MAG_Mid42,MAG43 ) }
E_ABM_2ndAP_MAG43 ( v_ApB43 0 ) VALUE { V( MAG_Mid43,MAG44 ) }
E_ABM_2ndAP_MAG44 ( v_ApB44 0 ) VALUE { V( MAG_Mid44,MAG45 ) }
E_ABM_2ndAP_MAG45 ( v_ApB45 0 ) VALUE { V( MAG_Mid45,MAG46 ) }
E_ABM_2ndAP_MAG46 ( v_ApB46 0 ) VALUE { V( MAG_Mid46,MAG47 ) }
E_ABM_2ndAP_MAG47 ( v_ApB47 0 ) VALUE { V( MAG_Mid47,MAG48 ) }
E_ABM_2ndAP_MAG48 ( v_ApB48 0 ) VALUE { V( MAG_Mid48,MAG49 ) }
E_ABM_2ndAP_MAG49 ( v_ApB49 0 ) VALUE { V( MAG_Mid49,MAG50 ) }
E_ABM_2ndAP_MAG50 ( v_ApB50 0 ) VALUE { V( MAG_Mid50,MAG51 ) }
E_ABM_2ndAP_MAG51 ( v_ApB51 0 ) VALUE { V( MAG_Mid51,MAG52 ) }
```

```
E_ABM_2ndAP_MAG52 ( v_ApB52 0 ) VALUE { V( MAG_Mid52,MAG53 ) }
E_ABM_2ndAP_MAG53 ( v_ApB53 0 ) VALUE { V( MAG_Mid53,MAG54 ) }
E_ABM_2ndAP_MAG54 ( v_ApB54 0 ) VALUE { V( MAG_Mid54,MAG55 ) }
E_ABM_2ndAP_MAG55 ( v_ApB55 0 ) VALUE { V( MAG_Mid55,MAG56 ) }
E_ABM_2ndAP_MAG56 ( v_ApB56 0 ) VALUE { V( MAG_Mid56,MAG57 ) }
E_ABM_2ndAP_MAG57 ( v_ApB57 0 ) VALUE { V( MAG_Mid57,MAG58 ) }
E_ABM_2ndAP_MAG58 ( v_ApB58 0 ) VALUE { V( MAG_Mid58,MAG59 ) }
E_ABM_2ndAP_MAG59 ( v_ApB59 0 ) VALUE { V( MAG_Mid59,MAG60 ) }
E_ABM_2ndAP_MAG60 ( v_ApB60 0 ) VALUE { V( MAG_Mid60,MAG61 ) }
E_ABM_2ndAP_MAG61 ( v_ApB61 0 ) VALUE { V( MAG_Mid61,MAG62 ) }
E_ABM_2ndAP_MAG62 ( v_ApB62 0 ) VALUE { V( MAG_Mid62,MAG63 ) }
E_ABM_2ndAP_MAG63 ( v_ApB63 0 ) VALUE { V( MAG_Mid63,MAG64 ) }
E_ABM_2ndAP_MAG64 ( v_ApB64 0 ) VALUE { V( MAG_Mid64,MAG65 ) }
E_ABM_2ndAP_MAG65 ( v_ApB65 0 ) VALUE { V( MAG_Mid65,MAG66 ) }
E_ABM_2ndAP_MAG66 ( v_ApB66 0 ) VALUE { V( MAG_Mid66,MAG67 ) }
E_ABM_2ndAP_MAG67 ( v_ApB67 0 ) VALUE { V( MAG_Mid67,MAG68 ) }
E_ABM_2ndAP_MAG68 ( v_ApB68 0 ) VALUE { V( MAG_Mid68,MAG69 ) }
E_ABM_2ndAP_MAG69 ( v_ApB69 0 ) VALUE { V( MAG_Mid69,MAG70 ) }
E_ABM_2ndAP_MAG70 ( v_ApB70 0 ) VALUE { V( MAG_Mid70,MAG71 ) }
E_ABM_2ndAP_MAG71 ( v_ApB71 0 ) VALUE { V( MAG_Mid71,MAG72 ) }
E_ABM_2ndAP_MAG72 ( v_ApB72 0 ) VALUE { V( MAG_Mid72,MAG73 ) }
E_ABM_2ndAP_MAG73 ( v_ApB73 0 ) VALUE { V( MAG_Mid73,MAG74 ) }
E_ABM_2ndAP_MAG74 ( v_ApB74 0 ) VALUE { V( MAG_Mid74,MAG75 ) }
E_ABM_2ndAP_MAG75 ( v_ApB75 0 ) VALUE { V( MAG_Mid75,MAG76 ) }
E_ABM_2ndAP_MAG76 ( v_ApB76 0 ) VALUE { V( MAG_Mid76,MAG77 ) }
E_ABM_2ndAP_MAG77 ( v_ApB77 0 ) VALUE { V( MAG_Mid77,MAG77_Out ) }
E_ABM_2ndAP_MAG78 ( v_ApB78 0 ) VALUE { V( MAG_Mid78,MAG79 ) }
E_ABM_2ndAP_MAG79 ( v_ApB79 0 ) VALUE { V( MAG_Mid79,MAG80 ) }
E_ABM_2ndAP_MAG80 ( v_ApB80 0 ) VALUE { V( MAG_Mid80,MAG81 ) }
E_ABM_2ndAP_MAG81 ( v_ApB81 0 ) VALUE { V( MAG_Mid81,MAG82 ) }
E_ABM_2ndAP_MAG82 ( v_ApB82 0 ) VALUE { V( MAG_Mid82,MAG83 ) }
E_ABM_2ndAP_MAG83 ( v_ApB83 0 ) VALUE { V( MAG_Mid83,MAG84 ) }
E_ABM_2ndAP_MAG84 ( v_ApB84 0 ) VALUE { V( MAG_Mid84,MAG85 ) }
E_ABM_2ndAP_MAG85 ( v_ApB85 0 ) VALUE { V( MAG_Mid85,MAG86 ) }
E_ABM_2ndAP_MAG86 ( v_ApB86 0 ) VALUE { V( MAG_Mid86,MAG87 ) }
E_ABM_2ndAP_MAG87 ( v_ApB87 0 ) VALUE { V( MAG_Mid87,MAG88 ) }
E_ABM_2ndAP_MAG88 ( v_ApB88 0 ) VALUE { V( MAG_Mid88,MAG89 ) }
E_ABM_2ndAP_MAG89 ( v_ApB89 0 ) VALUE { V( MAG_Mid89,MAG90 ) }
E_ABM_2ndAP_MAG90 ( v_ApB90 0 ) VALUE { V( MAG_Mid90,MAG91 ) }
E_ABM_2ndAP_MAG91 ( v_ApB91 0 ) VALUE { V( MAG_Mid91,MAG92 ) }
E_ABM_2ndAP_MAG92 ( v_ApB92 0 ) VALUE { V( MAG_Mid92,MAG93 ) }
E_ABM_2ndAP_MAG93 ( v_ApB93 0 ) VALUE { V( MAG_Mid93,MAG94 ) }
E_ABM_2ndAP_MAG94 ( v_ApB94 0 ) VALUE { V( MAG_Mid94,MAG95 ) }
E_ABM_2ndAP_MAG95 ( v_ApB95 0 ) VALUE { V( MAG_Mid95,MAG96 ) }
E_ABM_2ndAP_MAG96 ( v_ApB96 0 ) VALUE { V( MAG_Mid96,MAG97 ) }
E_ABM_2ndAP_MAG97 ( v_ApB97 0 ) VALUE { V( MAG_Mid97,MAG98 ) }
E_ABM_2ndAP_MAG98 ( v_ApB98 0 ) VALUE { V( MAG_Mid98,MAG99 ) }
E_ABM_2ndAP_MAG99 ( v_ApB99 0 ) VALUE { V( MAG_Mid99,MAG100 ) }
E_ABM_2ndAP_MAG100 ( v_ApB100 0 ) VALUE { V( MAG_Mid100,MAG101 ) }
E_ABM_2ndAP_MAG101 ( v_ApB101 0 ) VALUE { V( MAG_Mid101,MAG102 ) }
E_ABM_2ndAP_MAG102 ( v_ApB102 0 ) VALUE { V( MAG_Mid102,MAG103 ) }
E_ABM_2ndAP_MAG103 ( v_ApB103 0 ) VALUE { V( MAG_Mid103,MAG104 ) }
E_ABM_2ndAP_MAG104 ( v_ApB104 0 ) VALUE { V( MAG_Mid104,MAG105 ) }
E_ABM_2ndAP_MAG105 ( v_ApB105 0 ) VALUE { V( MAG_Mid105,MAG106 ) }
E_ABM_2ndAP_MAG106 ( v_ApB106 0 ) VALUE { V( MAG_Mid106,MAG107 ) }
E_ABM_2ndAP_MAG107 ( v_ApB107 0 ) VALUE { V( MAG_Mid107,MAG108 ) }
E_ABM_2ndAP_MAG108 ( v_ApB108 0 ) VALUE { V( MAG_Mid108,MAG109 ) }
E_ABM_2ndAP_MAG109 ( v_ApB109 0 ) VALUE { V( MAG_Mid109,MAG110 ) }
E_ABM_2ndAP_MAG110 ( v_ApB110 0 ) VALUE { V( MAG_Mid110,MAG111 ) }
E_ABM_2ndAP_MAG111 ( v_ApB111 0 ) VALUE { V( MAG_Mid111,MAG112 ) }
E_ABM_2ndAP_MAG112 ( v_ApB112 0 ) VALUE { V( MAG_Mid112,MAG113 ) }
E_ABM_2ndAP_MAG113 ( v_ApB113 0 ) VALUE { V( MAG_Mid113,MAG114 ) }
```

```
E_ABM_2ndAP_MAG114 ( v_ApB114 0 ) VALUE { V( MAG_Mid114,MAG115 ) }
E_ABM_2ndAP_MAG115 ( v_ApB115 0 ) VALUE { V( MAG_Mid115,MAG116 ) }
E_ABM_2ndAP_MAG116 ( v_ApB116 0 ) VALUE { V( MAG_Mid116,MAG117 ) }
E_ABM_2ndAP_MAG117 ( v_ApB117 0 ) VALUE { V( MAG_Mid117,MAG118 ) }
E_ABM_2ndAP_MAG118 ( v_ApB118 0 ) VALUE { V( MAG_Mid118,MAG119 ) }
E_ABM_2ndAP_MAG119 ( v_ApB119 0 ) VALUE { V( MAG_Mid119,MAG120 ) }
E_ABM_2ndAP_MAG120 ( v_ApB120 0 ) VALUE { V( MAG_Mid120,MAG121 ) }
E_ABM_2ndAP_MAG121 ( v_ApB121 0 ) VALUE { V( MAG_Mid121,MAG122 ) }
E_ABM_2ndAP_MAG122 ( v_ApB122 0 ) VALUE { V( MAG_Mid122,MAG123 ) }
E_ABM_2ndAP_MAG123 ( v_ApB123 0 ) VALUE { V( MAG_Mid123,MAG124 ) }
E_ABM_2ndAP_MAG124 ( v_ApB124 0 ) VALUE { V( MAG_Mid124,MAG125 ) }
E_ABM_2ndAP_MAG125 ( v_ApB125 0 ) VALUE { V( MAG_Mid125,MAG126 ) }
E_ABM_2ndAP_MAG126 ( v_ApB126 0 ) VALUE { V( MAG_Mid126,MAG127 ) }
E_ABM_2ndAP_MAG127 ( v_ApB127 0 ) VALUE { V( MAG_Mid127,MAG128 ) }
E_ABM_2ndAP_MAG128 ( v_ApB128 0 ) VALUE { V( MAG_Mid128,MAG129 ) }
E_ABM_2ndAP_MAG129 ( v_ApB129 0 ) VALUE { V( MAG_Mid129,MAG130 ) }
E_ABM_2ndAP_MAG130 ( v_ApB130 0 ) VALUE { V( MAG_Mid130,MAG131 ) }
E_ABM_2ndAP_MAG131 ( v_ApB131 0 ) VALUE { V( MAG_Mid131,MAG132 ) }
E_ABM_2ndAP_MAG132 ( v_ApB132 0 ) VALUE { V( MAG_Mid132,MAG133 ) }
E_ABM_2ndAP_MAG133 ( v_ApB133 0 ) VALUE { V( MAG_Mid133,MAG134 ) }
E_ABM_2ndAP_MAG134 ( v_ApB134 0 ) VALUE { V( MAG_Mid134,MAG135 ) }
E_ABM_2ndAP_MAG135 ( v_ApB135 0 ) VALUE { V( MAG_Mid135,MAG136 ) }
E_ABM_2ndAP_MAG136 ( v_ApB136 0 ) VALUE { V( MAG_Mid136,MAG137 ) }
E_ABM_2ndAP_MAG137 ( v_ApB137 0 ) VALUE { V( MAG_Mid137,MAG138 ) }
E_ABM_2ndAP_MAG138 ( v_ApB138 0 ) VALUE { V( MAG_Mid138,MAG139 ) }
E_ABM_2ndAP_MAG139 ( v_ApB139 0 ) VALUE { V( MAG_Mid139,MAG140 ) }
E_ABM_2ndAP_MAG140 ( v_ApB140 0 ) VALUE { V( MAG_Mid140,MAG141 ) }
E_ABM_2ndAP_MAG141 ( v_ApB141 0 ) VALUE { V( MAG_Mid141,MAG142 ) }
E_ABM_2ndAP_MAG142 ( v_ApB142 0 ) VALUE { V( MAG_Mid142,MAG143 ) }
E_ABM_2ndAP_MAG143 ( v_ApB143 0 ) VALUE { V( MAG_Mid143,MAG144 ) }
E_ABM_2ndAP_MAG144 ( v_ApB144 0 ) VALUE { V( MAG_Mid144,MAG145 ) }
E_ABM_2ndAP_MAG145 ( v_ApB145 0 ) VALUE { V( MAG_Mid145,MAG146 ) }
E_ABM_2ndAP_MAG146 ( v_ApB146 0 ) VALUE { V( MAG_Mid146,MAG147 ) }
E_ABM_2ndAP_MAG147 ( v_ApB147 0 ) VALUE { V( MAG_Mid147,MAG148 ) }
E_ABM_2ndAP_MAG148 ( v_ApB148 0 ) VALUE { V( MAG_Mid148,MAG149 ) }
E_ABM_2ndAP_MAG149 ( v_ApB149 0 ) VALUE { V( MAG_Mid149,MAG150 ) }
E_ABM_2ndAP_MAG150 ( v_ApB150 0 ) VALUE { V( MAG_Mid150,MAG151 ) }
E_ABM_2ndAP_MAG151 ( v_ApB151 0 ) VALUE { V( MAG_Mid151,MAG152 ) }
E_ABM_2ndAP_MAG152 ( v_ApB152 0 ) VALUE { V( MAG_Mid152,MAG153 ) }
E_ABM_2ndAP_MAG153 ( v_ApB153 0 ) VALUE { V( MAG_Mid153,MAG154 ) }
E_ABM_2ndAP_MAG154 ( v_ApB154 0 ) VALUE { V( MAG_Mid154,MAG154_Out ) }
*
* Solver Options
.OPTION
+ RELTOL=0.01
+ VNTOL=1.0E-6
+ ABSTOL=1.0E-10
+ CHGTOL=1.0E-14
+ GMIN=1.0E-10
+ ITL1=400
+ ITL2=20
+ ITL4=400
+ TNOM=27.0
*
* Autoconverge Options
.AUTOCONVERGE
+ RELTOL=0.05
+ VNTOL=0.001
+ ABSTOL=1.0E-5
+ ITL1=1000
+ ITL2=1000
+ ITL4=1000
```

```
*
* Transient Options
*
* AC Options
.AC DEC 10000 0.1 10kHz

.PROBE

.END
```

**Listing A.6:** Pspice code for RB

```

* PSPICE RB MB-MBGnd components library
* 2015/09/17 CERN
* Lorenzo Bortot

*Subcircuit: RB_MBDipole -- Simulink Schematics Available
.subckt RB_MB_Dipole  1_pIn 1_pMid  1_pOut 1_pGND
+ PARAMS:
+ r1=10 r2=10
+ rGnd1=11e06 rGnd2=11e06 rGnd3=11e06 rGnd4=11e06

.param l_mag      = 98e-3
*.param l_mag      = 100e-3

.param c_mag_gnd = 300e-9
.param k          = 0.75

*Inner Busbar
v1_bbIn_PH (1_pIn 100) 0

*Inductors
l1 (100 101) {(1-k)*l_mag/2}
l2 (101 102) {(k)*l_mag/2}
l3 (102 103) {(1-k)*l_mag/2}
l4 (103 104) {(k)*l_mag/2}

*Resistors associated to Joule losses in the apertures
r1 (101 102) {r1}
r2 (103 104) {r2}

*Midport for picking up voltage across each aperture
v1_bbMid_PH (102 1_pMid) 0

*Resistor in parallel
rp (100 104) 100

*Protecting diode
x_diode1 (100 104) RB_MB_DiodeFwdBypass_6V

*Resistors to GND
rGnd1   (100 1_pGND) {rGnd1}
rGnd2_3 (102 1_pGND) {rGnd2*rGnd3/(rGnd2+rGnd3)}
rGnd4   (104 1_pGND) {rGnd4}

*Capacitors to GND
c1         (100 1_pGND) {c_mag_gnd/4}
c2_3       (102 1_pGND) {c_mag_gnd/2}
c4         (104 1_pGND) {c_mag_gnd/4}

*Outer Busbar
v1_bbOut_PH (104 1_pOut) 0
```

```
.ends
```

```

.subckt RB_MB_Dipole_3capmod  1_pIn 1_pMid  1_pOut 1_pGND
+ PARAMS:
+ r1=10 r2=10
+ rGnd1=11e06 rGnd2=11e06 rGnd3=11e06 rGnd4=11e06

*2*L_measured
*.param l_mag     = 0.0776
*.param l_mag     = 93.7650e-3
.param l_mag     = 93.7650e-3
*k_A
.param c_mag_gnd = 300e-9
.param c_p = 3.5846e-07
.param k         = 0.75
*R=7.4503
*extra
*.param l_p     = 0.4195
*.param r_xtra     = 1.1887

*Inner Busbar
v1_bbIn_PH (1_pIn 100) 0

*Inductors
l1 (100 101) {(1-k)*l_mag/2}
l2 (101 102) {(k)*l_mag/2}
l3 (102 103) {(1-k)*l_mag/2}
l4 (103 104) {(k)*l_mag/2}

*Resistors associated to Joule losses in the apertures
r1 (101 102) {r1}
r2 (103 104) {r2}

*Midport for picking up voltage across each aperture
v1_bbMid_PH (102 1_pMid) 0

*Resistor in parallel
rp (100 104) 100

*Parallel components
*l5 (100 105) {l_p}
*rp2 (105 104) {r_xtra}

*Protecting diode
x_diode1 (100 104) RB_MB_DiodeFwdBypass_6V

*Resistors to GND
rGnd1   (100 1_pGND) {rGnd1}
rGnd2_3 (102 1_pGND) {rGnd2*rGnd3/(rGnd2+rGnd3)}
rGnd4   (104 1_pGND) {rGnd4}



*3 cap
c2       (101 1_pGND) {c_mag_gnd/3}
c2_3     (102 1_pGND) {c_mag_gnd/3}
c3       (103 1_pGND) {c_mag_gnd/3}

*Outer Busbar
v1_bbOut_PH (104 1_pOut) 0
.ends
```

```
*Subcircuit: RB_MBDipole distributed capacitance -- Simulink Schematics
    Available
.subckt RB_MB_Dipole_7cap   1_pIn 1_pMid  1_pOut 1_pGND
+ PARAMS:
+ r1=10 r2=10
+ rGnd1=11e06 rGnd2=11e06 rGnd3=11e06 rGnd4=11e06

*2*L_measured
.param l_mag     = 93.7650e-3

*k_A
.param c_mag_gnd = 300e-9
.param k         = 0.75


*Inner Busbar
v1_bbIn_PH (1_pIn 100) 0

*Inductors
l1 (100 101) {(1-k)*l_mag/4}
l2 (101 102) {(1-k)*l_mag/4}
l3 (102 103) {(k)*l_mag/4}
l4 (103 104) {(k)*l_mag/4}
l5 (104 105) {(1-k)*l_mag/4}
l6 (105 106) {(1-k)*l_mag/4}
l7 (106 107) {(k)*l_mag/4}
l8 (107 108) {(k)*l_mag/4}

*Resistors associated to Joule losses in the apertures
r1 (102 103) {r1/2}
r2 (103 104) {r1/2}
r3 (106 107) {r2/2}
r4 (107 108) {r2/2}

*Midport for picking up voltage across each aperture
v1_bbMid_PH (104 1_pMid) 0

*Resistor in parallel
rp (100 108) 100

*Protecting diode
x_diode1 (100 108) RB_MB_DiodeFwdBypass_6V

*Resistors to GND
rGnd1   (100 1_pGND) {rGnd1}
rGnd2_3 (104 1_pGND) {rGnd2*rGnd3/(rGnd2+rGnd3)}
rGnd4   (108 1_pGND) {rGnd4}

*Capacitors to GND
c2        (101 1_pGND) {c_mag_gnd/8}
c3        (102 1_pGND) {c_mag_gnd/8}
c4        (103 1_pGND) {c_mag_gnd/8}
c5        (104 1_pGND) {c_mag_gnd/4}
c6        (105 1_pGND) {c_mag_gnd/8}
c7        (106 1_pGND) {c_mag_gnd/8}
c8        (107 1_pGND) {c_mag_gnd/8}

*Outer Busbar
v1_bbOut_PH (108 1_pOut) 0
.ends
```

```

```

```
.subckt RB_MB_Dipole9cap  1_pIn 1_pMid  1_pOut 1_pGND
+ PARAMS:
+ r1=10 r2=10
+ rGnd1=11e06 rGnd2=11e06 rGnd3=11e06 rGnd4=11e06

*2*L_measured
.param l_mag     = 93.7650e-3

*k_A
.param c_mag_gnd = 300e-9
.param k         = 0.75



*extra
.param lpar     = 0.1e-6

*Inner Busbar
v1_bbIn_PH (1_pIn 99) 0

*Inductors
l0  (99 100) {lpar}
l1 (100 101) {(1-k)*l_mag/4}
l2 (101 102) {(1-k)*l_mag/4}
l3 (102 103) {(k)*l_mag/4}
l4 (103 104) {(k)*l_mag/4}
l5 (104 105) {(1-k)*l_mag/4}
l6 (105 106) {(1-k)*l_mag/4}
l7 (106 107) {(k)*l_mag/4}
l8 (107 108) {(k)*l_mag/4}
l9  (108 109) {lpar}

*Resistors associated to Joule losses in the apertures
r1 (102 103) {r1/2}
r2 (103 104) {r1/2}
r3 (106 107) {r2/2}
r4 (107 108) {r2/2}

*Midport for picking up voltage across each aperture
v1_bbMid_PH (104 1_pMid) 0

*Resistor in parallel
rp (99 109) 100

*Protecting diode
x_diode1 (99 109) RB_MB_DiodeFwdBypass_6V

*Resistors to GND
rGnd1   (100 1_pGND) {rGnd1}
rGnd2_3 (104 1_pGND) {rGnd2*rGnd3/(rGnd2+rGnd3)}
rGnd4   (108 1_pGND) {rGnd4}

*Capacitors to GND

c1        (100 1_pGND) {c_mag_gnd/10}
c2        (101 1_pGND) {c_mag_gnd/10}
c3        (102 1_pGND) {c_mag_gnd/10}
c4        (103 1_pGND) {c_mag_gnd/10}
c5        (104 1_pGND) {c_mag_gnd/5}
c6        (105 1_pGND) {c_mag_gnd/10}
c7        (106 1_pGND) {c_mag_gnd/10}
c8        (107 1_pGND) {c_mag_gnd/10}
```

```
c9         (108 1_pGND) {c_mag_gnd/10}


*Outer Busbar
v1_bbOut_PH (109 1_pOut) 0
.ends
```

Appendix B

# PSO fits

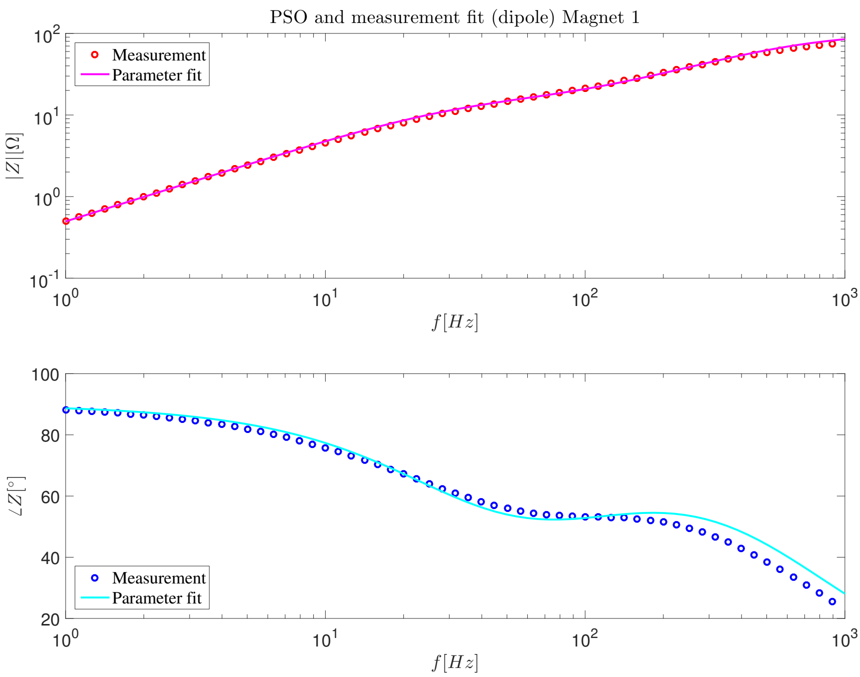


**Figure B.1:** PSO fit of parameters for Magnet 1

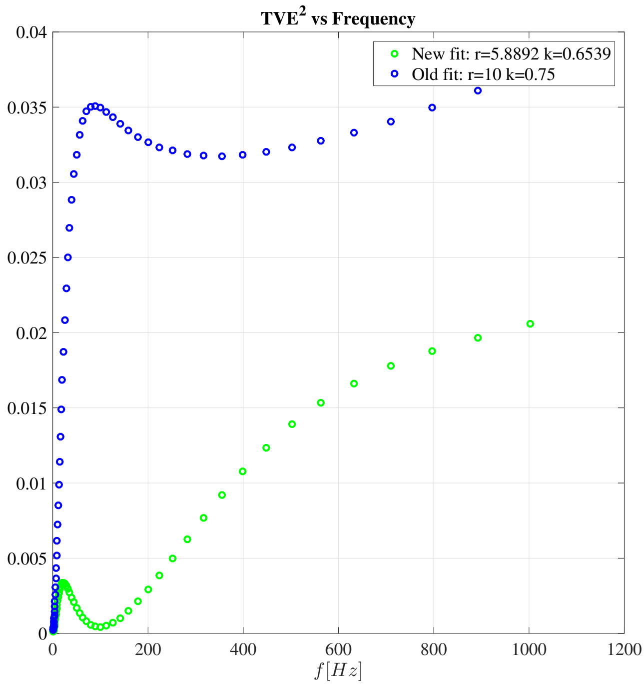


**Figure B.2:** $TVE^2$ for PSO fit of Magnet 1

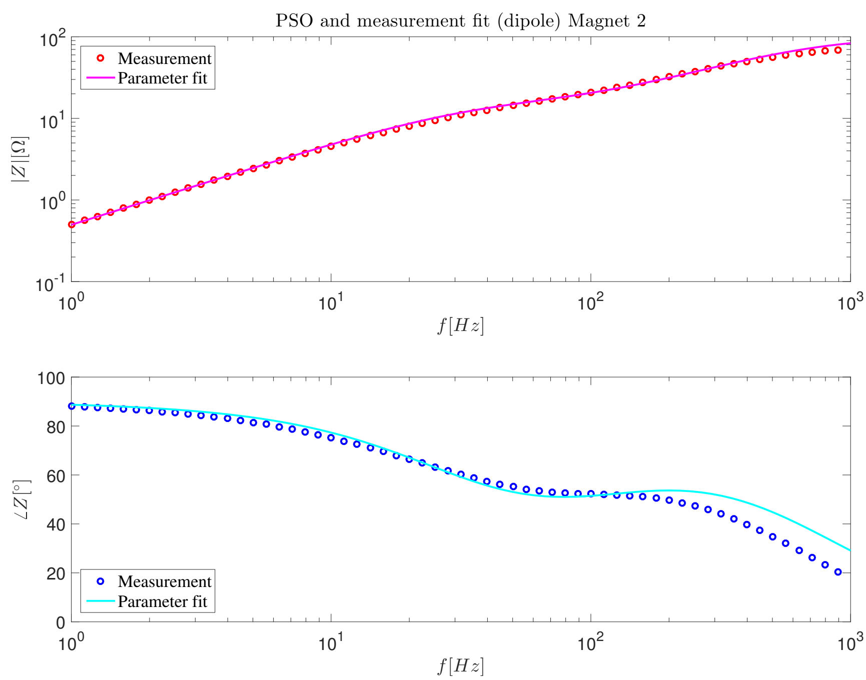


**Figure B.3:** PSO fit of parameters for Magnet 2

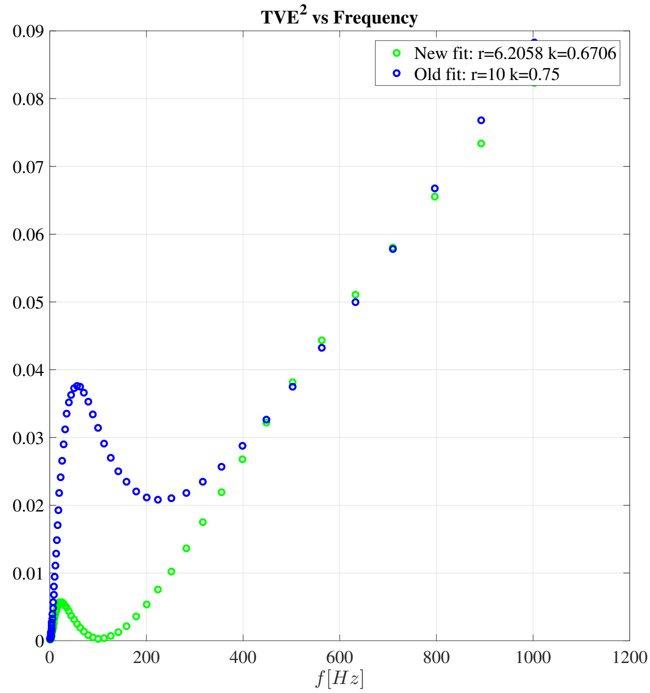


**Figure B.4:** $TVE^2$ for PSO fit of Magnet 2

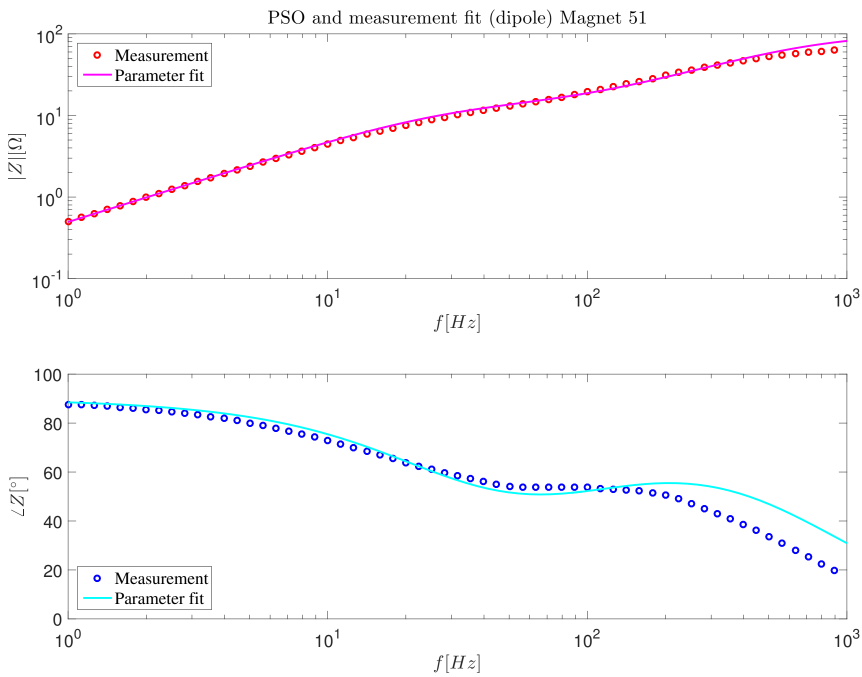


**Figure B.5:** PSO fit of parameters for Magnet 51

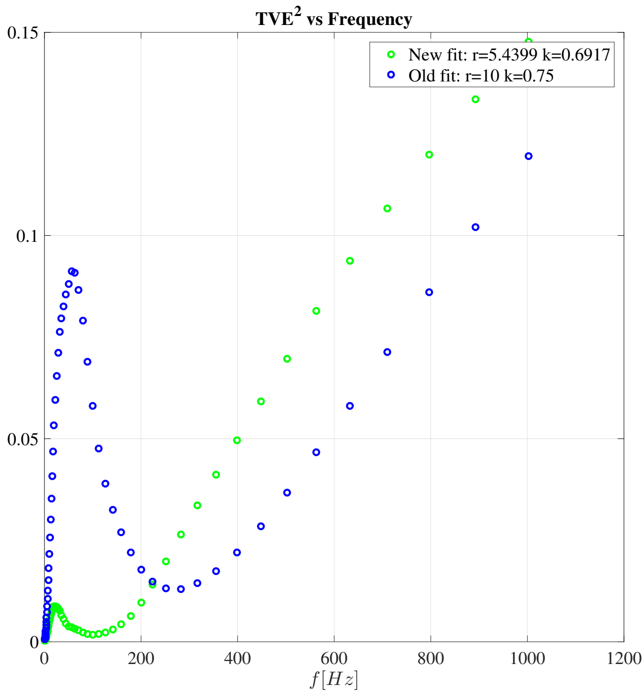


**Figure B.6:** $TVE^2$ for PSO fit of Magnet 51

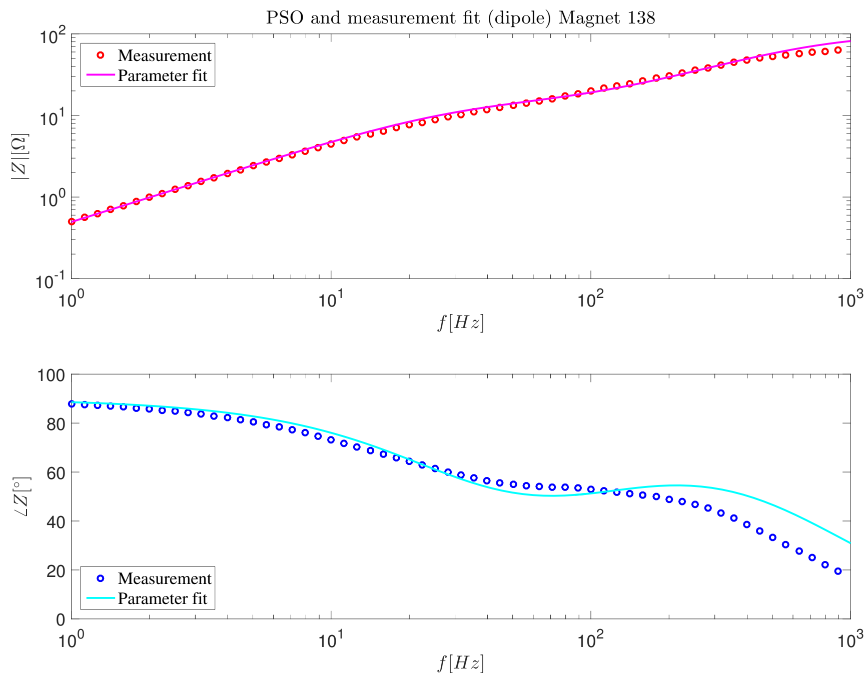


**Figure B.7:** PSO fit of parameters for Magnet 138

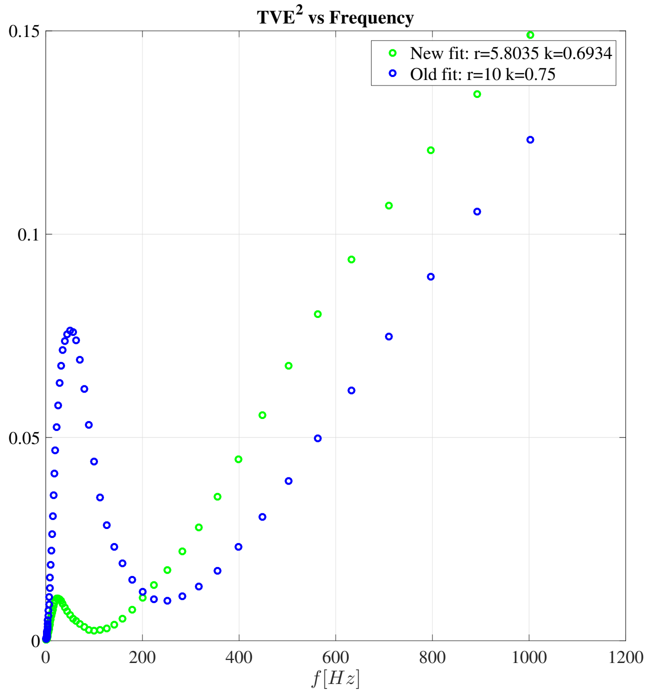


**Figure B.8:** $TVE^2$ for PSO fit of Magnet 138

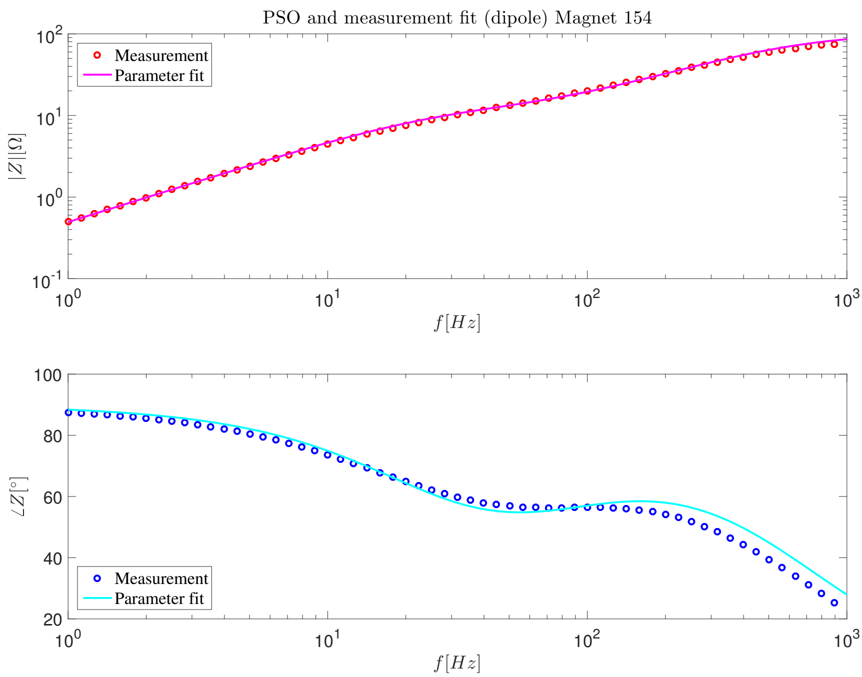


**Figure B.9:** PSO fit of parameters for Magnet 154

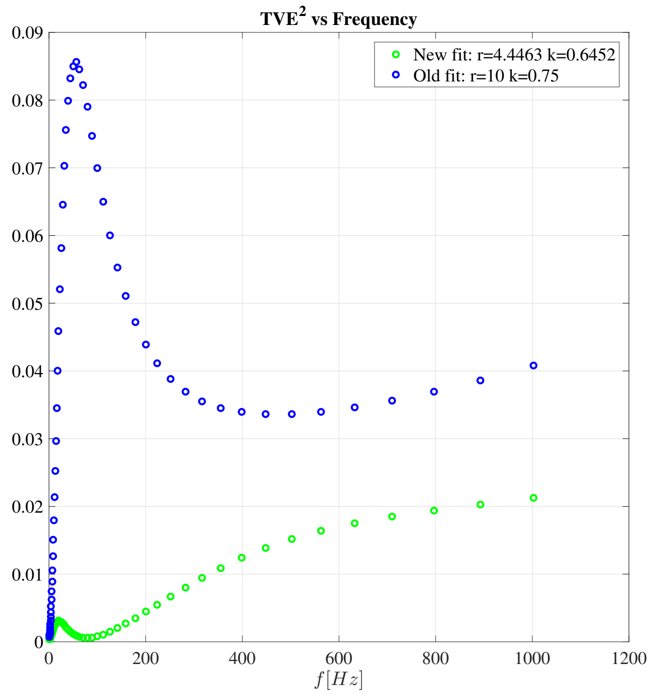


**Figure B.10:** $TVE^2$ for PSO fit of Magnet 154

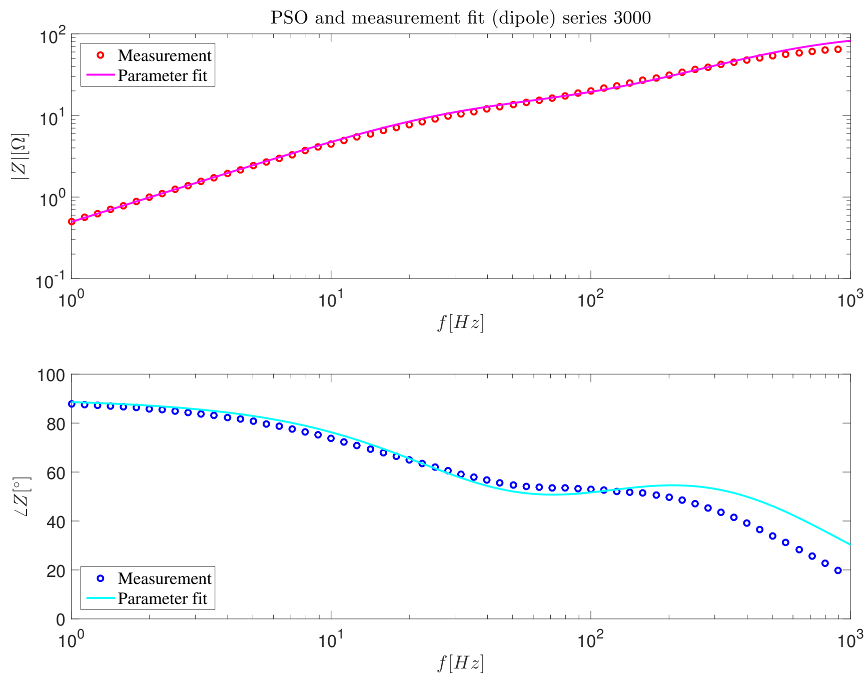


**Figure B.11:** PSO fit of parameters for Series 3000

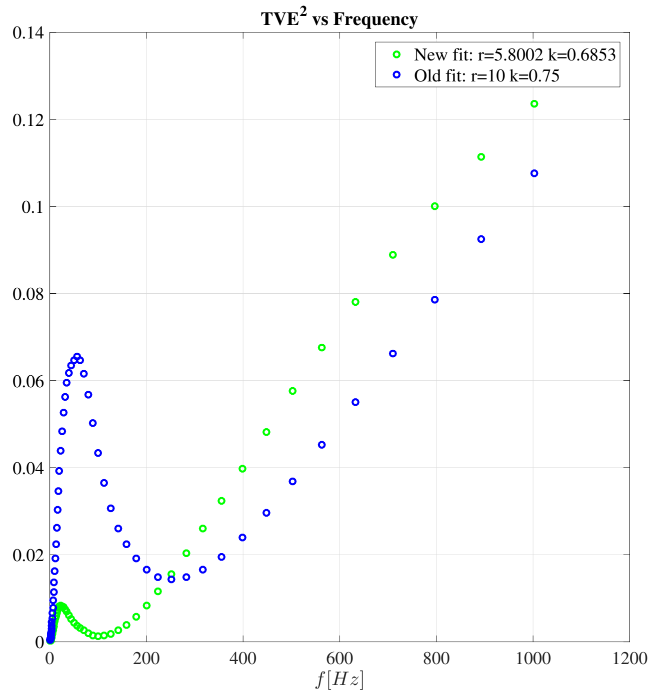


**Figure B.12:** $TVE^2$ for PSO fit of Series 3000

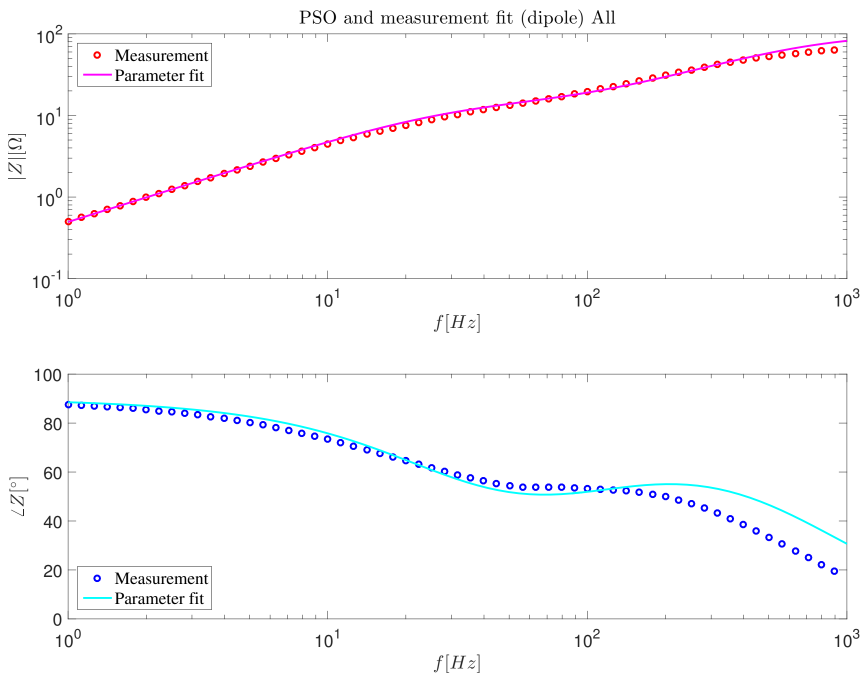


**Figure B.13:** PSO fit of parameters for All Magnets

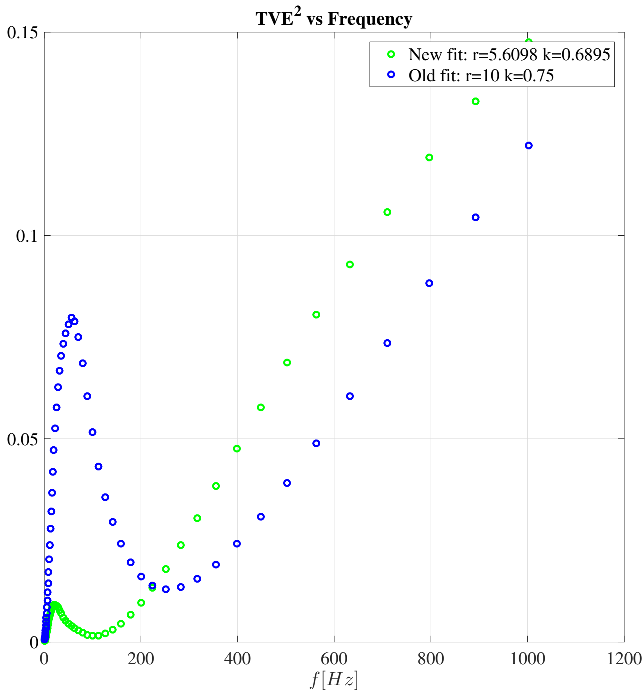


**Figure B.14:** $TVE^2$ for PSO fit of All Magnets

Appendix C

# Meissner region

To evaluate the current range for operating in the Meissner phase for a Type II superconductor it is essential to know the lower critical field $\mathbf{B_{c1}}$. Unfortunately, this data has not been possible to obtain for Nb-Ti. According to Mangin, the critical field for an niobium wire is 0.18 [T]. [36, p. 113] Subsequently, it has been assumes that Nb-Ti takes a similar value of $\mathbf{B_{c1}}$. The lower critical field at 1.9 [K] can be estimated utiziling

$$\mathbf{B_{c1}}(T) = \mathbf{B_{c1}}(0) \cdot \left(1 - \left(\frac{T}{T_c}\right)^2\right), \qquad \mathrm{T} \quad (C.1)$$

which produces the value $\mathbf{B_{c1}}(1.9\ [\mathrm{K}]) = 0.1723$ [T]. Moreover, one assumes a linear relation between magnetic flux density and current. This implies that the Meissner phase follows up to 223.5 [A], and that the field at 1 [A] is evaluated to be

$$\mathbf{B}(1[A]) = 7.7089 \cdot 10^{-4}. \qquad \mathrm{T} \quad (C.2)$$

One can safely conclude that the frequency transfer measurements of the MB impedance have been performed in the Meissner phase.

Appendix D

# Distributed capacitance models

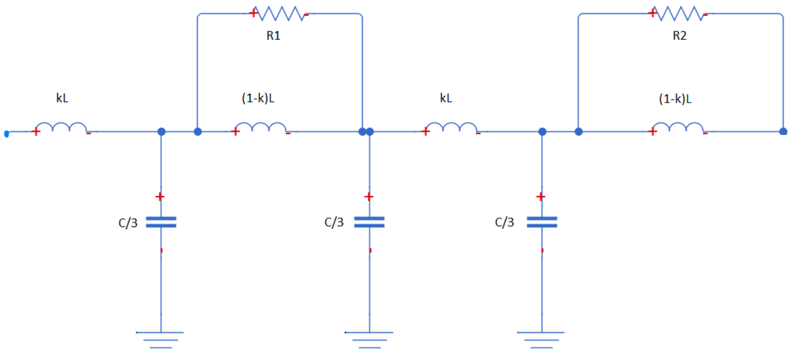


**Figure D.1:** Distributed capacitance model with 3 capacitances as implemented in Pspice

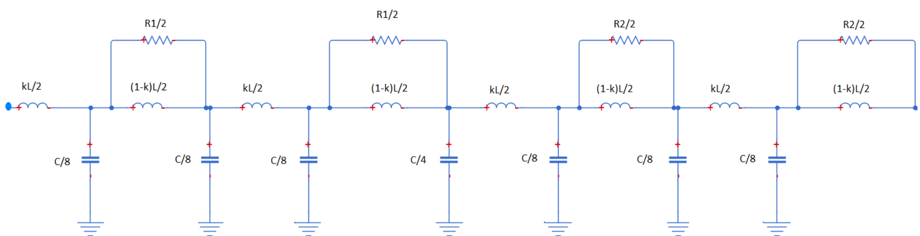


**Figure D.2:** Distributed capacitance model with 7 capacitances as implemented in Pspice

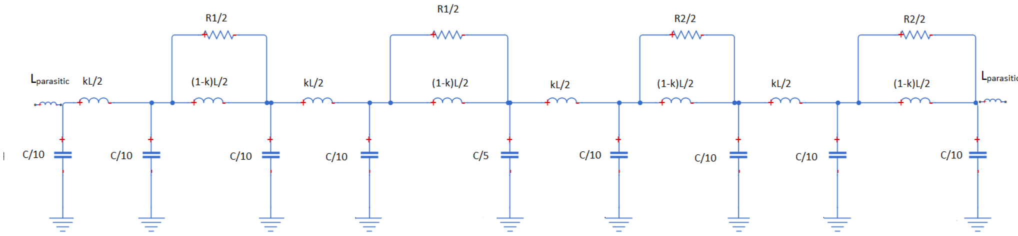


**Figure D.3:** Distributed capacitance model with 9 capacitances as implemented in Pspice

Appendix E

# Element quality by meshing level

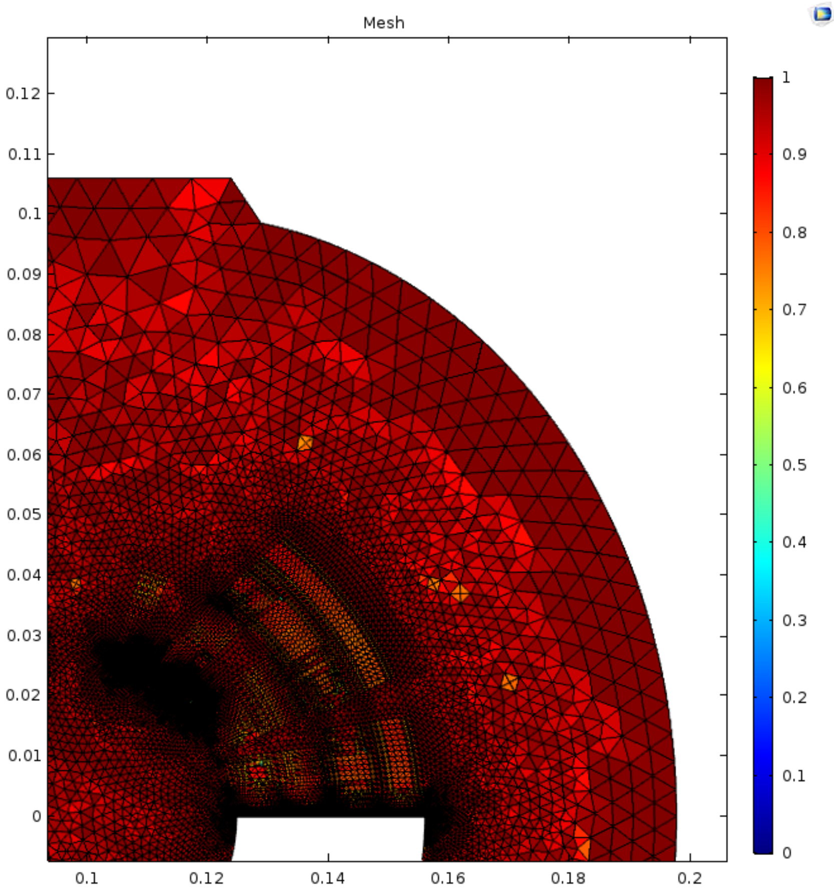


**Figure E.1:** Element quality extreme fine mesh

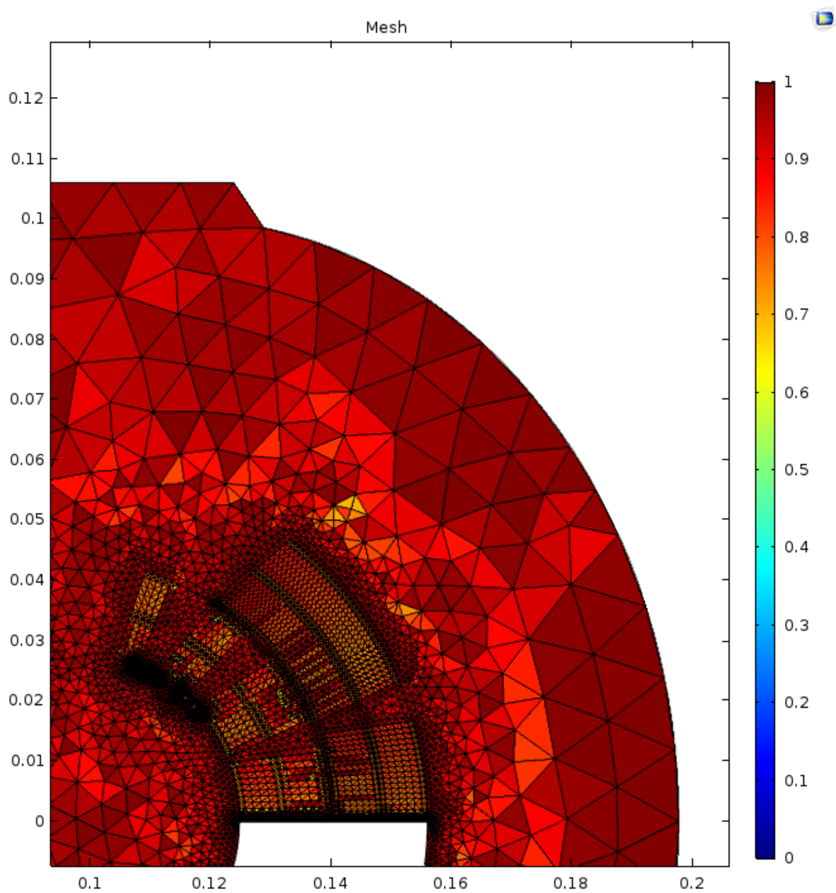


**Figure E.2:** Element quality fine mesh

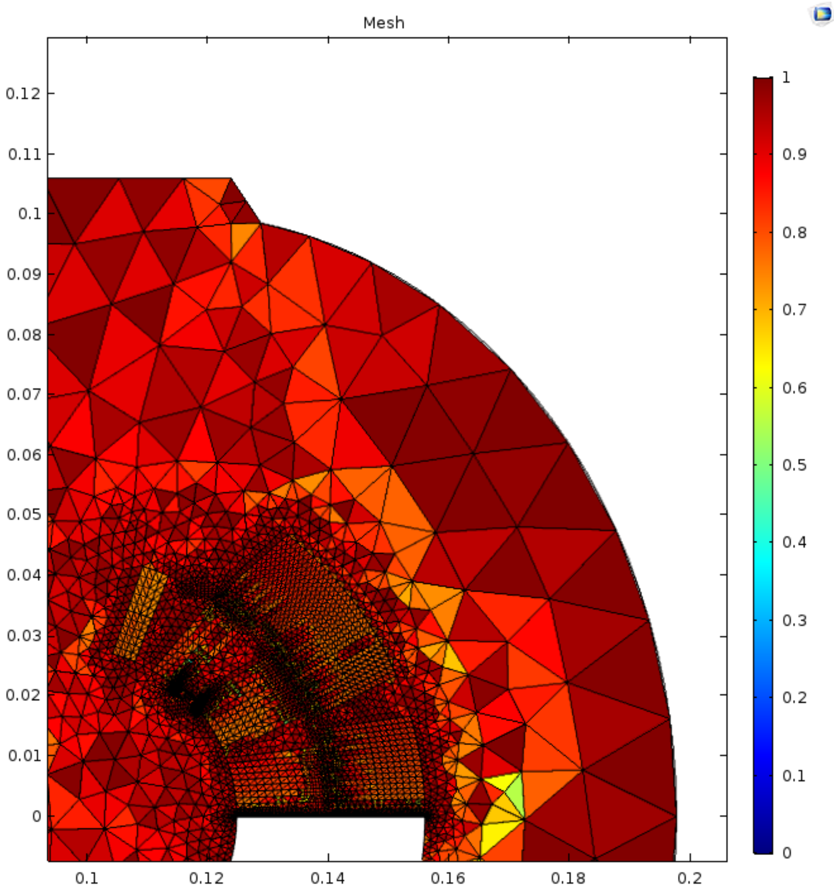


**Figure E.3:** Element quality coarse mesh

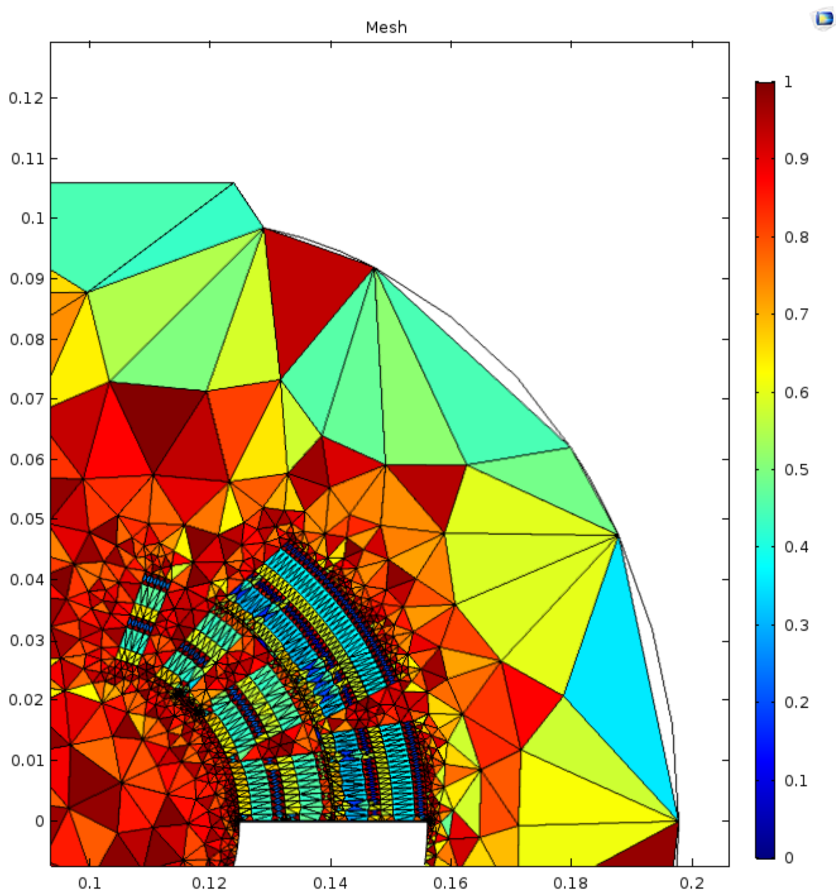


**Figure E.4:** Element quality extreme coarse mesh

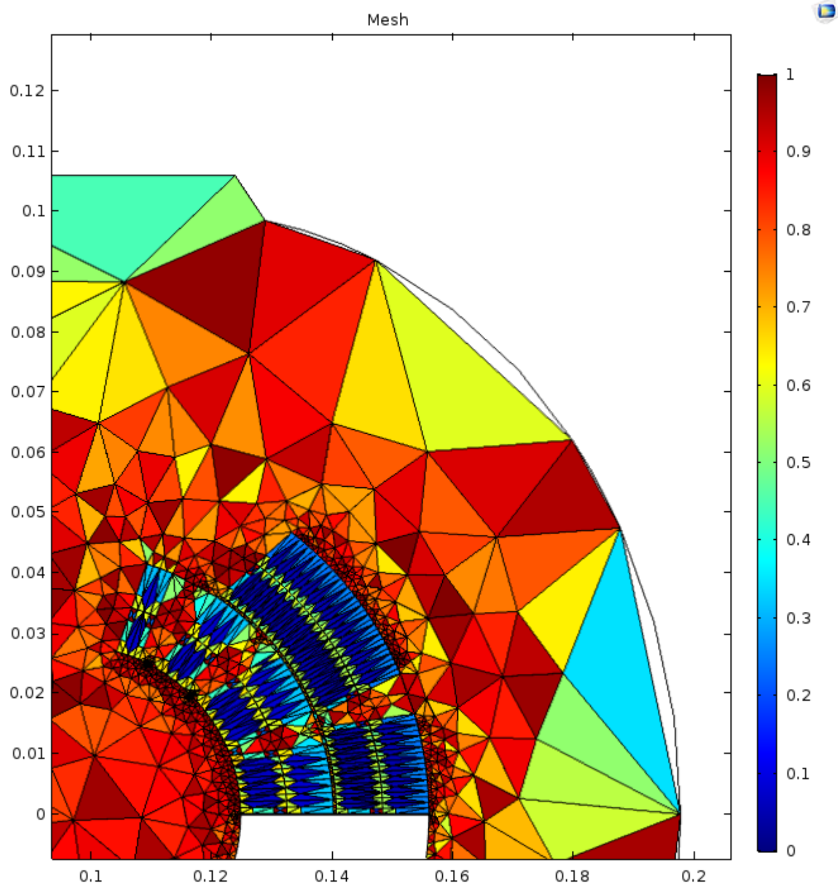


**Figure E.5:** Element quality manually coarse mesh